Investigating Modelling and Inversion Techniques for Overburden Stripping for Uranium Exploration in the Athabasca Basin, Canada

by

© Mehrdad Darijani

A thesis submitted to the School of Graduate Studies in partial fulfilment of the requirements for the degree of Doctor of Philosophy

Department of Earth Sciences

Memorial University of Newfoundland

July, 2019

St. John's, Newfoundland and Labrador

To my family, my homeland and humankind.

Abstract

The major investment in exploration for uranium in Canada is in one of the most important structural corridors of the eastern Athabasca Basin, extending from the Millennium deposit to the McArthur River deposit (called the McArthur-Millennium corridor). This corridor hosts the largest and highest-grade uranium deposits in the world (at a depth of more than 500 m), and it will be the focus of exploration activity by companies (e.g., Cameco) in the Athabasca Basin for many years. In the McArthur-Millennium corridor, people have wondered about how to better detect structures (e.g., alteration zones) associated with the (volumetrically) small uranium mineralization at depth using geophysical methods. But the geophysical responses (e.g., the gravity response) of these structures can be masked by the variation of the overburden thicknesses. Some geophysical attempts have been made to remove the overburden signature and to find the alteration zones, but none of them have got very far. To solve this problem, I investigate developing new methodology as well as new exploration methods in the region to find and remove the overburden signature to explore for new deposits. In this dissertation, I investigate new ways to separate the overburden contribution from geophysical data (via modelling and inversion) so that deeper targets (e.g. an alteration zone) can be detected and delineated by means of an innovative application of new, modern, state-of-the-art modelling and (constrained and joint) inversion of geophysical methods such as seismic refraction, gravity, magnetic and electromagnetic methods. These new methods and investigations (e.g., modelling and constrained joint inversions using the fuzzy c-mean method on tetrahedral meshes) bring us much closer to solving the problem in this corridor. This research project is a part of the CMIC Footprints project, and is a very challenging exploration problem and very useful if successful for many places in Canada, not just the Athabasca Basin and uranium exploration.

The Athabasca Basin is a Proterozoic sedimentary basin which supplies around 20% of the world's uranium. The uranium deposits are surrounded by alteration zones near the unconformity between Proterozoic sedimentary rocks and the Archean and Aphebian metamorphic basement. The sedimentary rocks are covered by Quaternary glacial deposits. Because of the small size of uranium deposits and their location at depth, geophysical

methods look for structures which host the uranium deposits, for example, electromagnetic (EM) methods can locate graphitic faults. The gravity method can potentially detect the alteration zones. The seismic method can image the unconformity and basement faults. And, magnetic data can delineate basement structures. The benefit of using multiple data-types can provide complementary information (e.g. the seismic and gravity). These methods can be used for the overburden stripping as well. In the Athabasca Basin, overburden can be conductive while density and seismic velocity of the overburden is less than the sandstone. Some rocks in unconsolidated glacial deposits have magnetic susceptibilities (e.g. granite), whereas sandstone is non-magnetic. Based on these features, the synthetic modelling and inversion of the geophysical data are performed for (mainly) the overburden characterization as well as reconstructing the geological structure in depth. Magnetic, gravity, first-arrival seismic traveltimes and time- and frequency-domain electromagnetic data are synthetized using forward modelling of 2D and 3D models. For inversion methods, independent, joint and constrained methods are applied for 1D, 2D and 3D cases.

Independent inversions of the seismic refraction data as well as the electromagnetic data are useful methods for reconstructing the base of the overburden, unlike the independent inversions of gravity and magnetic data. The joint inversion of gravity and seismic refraction data is able well to reconstruct the variable thickness of the overburden better and sharper than the independent inversions. After applying the thickness of the overburden (obtained from the joint inversion) in the constrained independent inversion of gravity data, the location of alteration zone is apparent at depths. The joint inversion of magnetic and gravity data was able to reconstruct the basement blocks, the sandstone and the unconformity; furthermore the base of overburden can be detected after using the constrained joint inversion of magnetic and gravity methods. This method cannot show the alteration zone, but it can show the intersection of the fault with the unconformity where the mineralization can occur. For the electromagnetic method, results show that frequency- and time-domain methods can be used for determining the location of the interface between overburden and sandstone and the location of the graphitic faults, respectively.

Acknowledgements

My greatest appreciation goes to my supervisor, Dr. Colin G. Farquharson, for his patience, invaluable advices and continuous support and help throughout this project. And, special thanks go to Dr. Peter Lelièvre for providing the software as well as guidance. I would also like to thank the members of my supervisory committee Dr. Charles Hurich and Dr. Alison Leitch.

I am also grateful for the financial support provided by the Footprints Project and a MUN School of Graduate Studies Fellowship. The Footprints Project is by the Canadian Mining Innovation Council (CMIC; www.cmic-footprints.ca), with funding from lots of industry sponsors and Natural Sciences and Engineering Research Council of Canada (NSERC). This is NSERC-CMIC-Footprints Publication #144. I would also like to thank Dr. Kevin Ansdell (uranium-subproject leader), Dr. Kurt Kyser (uranium-subproject co-leader), Ken Wasyliuk (uranium-subproject research associate) as well as Garnet Wood, Clare O'Dowd and Gerard Zaluski of Cameco Corporation and Robert Hearst (now at Southern Geoscience Consultants) and David Quirt of Orano Canada Inc. (formerly AREVA Resources Canada) for their helpful review and comments on my quarterly reports of the CMIC-Footprints Project and this thesis.

Last but certainly not least, I address my deepest gratitude to my family to whom I owe a great deal; to my late father, Mohammad Darijani, who showed me that the key to life is the knowledge; to my mother, Zahra Jazinizadeh, who has been a constant source of support and encouragement, and has made an untold number of sacrifices for the family; to my sister, Iren, and my brother, Meghdad, for their spiritual supports.

Table of Contents

List of Tables

List of Figures

List of Appendices

Chapter 1

Introduction

One of the primary mineral ores of uranium, containing 50–80 percent of that element, is uraninite (formerly known as pitchblende) which is mostly found in unconformity deposits (more than one third of the uranium resource) where grades can be 3-100 times higher than the other types of deposits (Fayek and Kyser, 1997; Gandhi, 1989; Kyser et al., 2000; Jefferson et al., 2007). Uraninite has mostly a chemical composition of UO_2, but due to oxidation has typically variable proportions of U_3O_8 (www.wikipedia.org). Note that uraninite is the term usually reserved for macrocrystalline (well crystallized) uranium oxide close to the ideal formula of UO_2. The (old) term pitchblende is usually used to refer to microcrystalline to crypto-crystalline or amorphous uranium oxide, often with botryoidal, massive, sooty, or earthy textures which is usually more oxidized.

The main focus in exploration of uranium in Canada is on the Athabasca Basin which hosts uraninite deposits (Figure 1.1; Jefferson et al., 2003; Ramaekers, 1990; Ramaekers and Catuneanu, 2004). In the eastern Athabasca Basin, the McArthur River deposit was discovered in 1988 at a depth of 530 m, started full production in 2000, and is the world's largest high-grade uranium deposit (16.5% U_3O_8 after allowance for dilution), and is the world's largest in terms of annual production (13% of world mine production in 2012;

adapted from www.world-nuclear.org). It is associated with the intersection between moderately-dipping reverse faults, the unconformity, and the contact between conductive, graphite-rich pelitic gneisses and meta-quartzites of the Wollaston Group. In contrast, the Millennium deposit, which was discovered in 2000 at a depth of 650 m, is located in locally graphitic, pelitic to semipelitic gneisses approximately 100 m below the unconformity and in the footwall of the dominant conductive graphitic fault. The McArthur River mine is owned by Cameco (70%) and Orano Canada Inc. (formerly AREVA Resources Canada; 30%), with Cameco being the mine operator. The price of uranium was around US$30 per pound in 2018 (adapted from www.cameco.com).

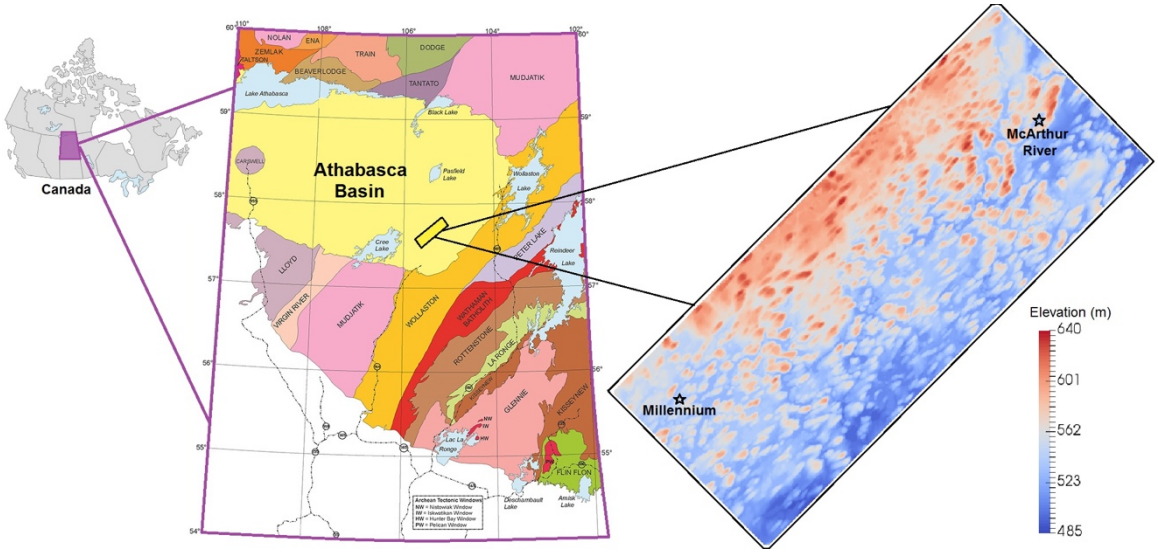

Figure 1.1: Location of the Athabasca Basin in the regional geology map of northern Saskatchewan (taken from www.geotech.ca), and the topography of the McArthur-Millennium corridor. All elevations are relative to mean sea level.

Exploration for uranium in the Athabasca Basin began in the mid-1960's, with companies looking for sandstone-hosted and/or paleochannel-type uranium deposits (Gandhi, 1995). At the beginning, the focus was on the shallower parts of the basin, but recently, it has moved to deeper levels (O'Dowd et al., 2006; Tuncer, 2007). These deeper

deposits, which are associated with the unconformity at the base of the Basin, have traditionally been explored using electromagnetic methods based on detection of a graphitic conductor (Irvine and Witherly, 2006; Tuncer, 2007; Farquharson and Craven, 2009). Seismic methods have begun to be applied for detecting the location of the unconformity and post-Athabasca fault zones (Hajnal et al., 2007; White et al., 2007; Juhojuotti et al., 2012). Seismic data can provide a structural framework from the near surface to a few kilometres below the unconformity (Györfi et al., 2007), calibrated with the aid of borehole geophysics (Mwenifumbo et al., 2004). Airborne magnetic surveys can provide maps of basement geology based on the contrast between different magnetic susceptibilities of rock packages in the basement, for example between Archean gneiss and the Wollaston Supergroup (Pilkington, 1989; Card, 2006; Thomas and McHardy, 2007). Ground and airborne gravity can detect alteration zones as negative gravity anomalies (desilicified zones) or positive anomalies (silicified zones) that surround the small uranium deposits (Wood and Thomas, 2002; Thomas and Wood, 2007; McGill et al., 1993; Matthews et al., 1997; Thomas et al., 2002).

This research is on a corridor between the McArthur River and Millennium areas in the Athabasca Basin, which has a total size of 50×20 km. NE-SW structures in this corridor are associated with the transition between the Wollaston and the Mudjatik domains in the underlying Archean and Paleoproterozoic basement rocks (Yeo and Delaney, 2007; Thomas, 1983; Annesley et al., 2005). Alternating units of quartzite and granitic rocks as well as metamorphosed graphitic pelitic rocks are the main structures in the basement. The late Paleo- to Meso-Proterozoic sedimentary rocks of the Athabasca Basin, which consist of the Manitou Fall formations, rest unconformably on these basement rocks and under the

Late Wisconsinan glacial sediments (Bernier, 2004; Ramaekers et al., 2007; Hoeve and Quirt, 1984). The glacial sediments of the overburden have a variable thickness from 0 up to 100 m and include features such as the drumlins, hummocky moraines, esker complexes, and ground moraines. Unconformity deposits in this corridor are generally found where a fault intersects the unconformity in the vicinity of alteration zones (Figure 1.2; Hoeve and Quirt, 1987; Ramaekers, 1990). The McArthur-Millennium corridor is used in this research not only as a test location for method development but to develop methods for exploration in this corridor as well as to improve the understanding of the area. This research is a part of the larger Canadian Mining Innovation Council Footprints project (CMIC; www.cmic-footprints.ca) which has as one of its three focusses uranium exploration in the Athabasca Basin, but the research has implications for exploration for many different resource types in other locations.

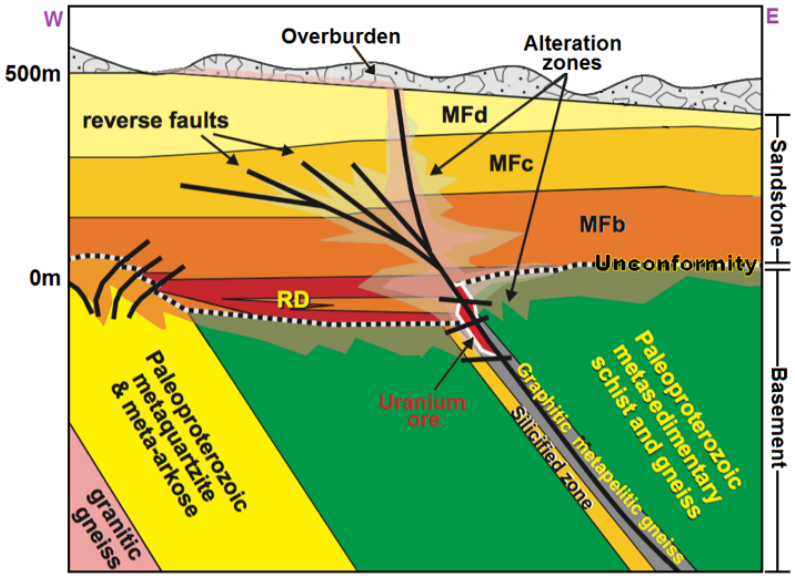

Figure 1.2: Generic model of an unconformity type uranium deposit (adapted from Jefferson et al., 2007). The Athabasca Basin consists of three major strata from top to bottom: overburden (glacial deposits), sandstone (Manitou Falls Formations MFd, MFc, MFb and RD), and metamorphic basement below the unconformity.

Most parts of Canada are covered by overburden especially glacial deposits (Fulton, 1995). The erosion and deposition due to the glacial process have provided a variable thickness in the overburden which can be problematic in a geophysical interpretation. The research problem in this project is a consequence of this variable thickness of glacial deposits, which varies greatly in the eastern Athabasca Basin especially in the McArthur-Millennium corridor (up to 100 m; Schreiner, 1984a; Campbell, 2007). Wood and Thomas (2002) mentioned that since glacial deposits are generally less dense than bedrock, local thickening of these deposits causes an anomalously low gravity response. Such a response can mimic or mask the gravity signature associated with the hydrothermal alteration at depth that can be an important component of the footprint of uranium deposits.

The alteration zones are composed of different types of clay-altered minerals, silicification and desilicification with their distribution in the area being known but not defined accurately. The signature of the alteration zone in the geophysical methods can be seen as a conductive structure (altered clay) in the electromagnetic data, and as mentioned before as negative gravity anomalies (desilicified zones) or positive anomalies (silicified zones) in the gravity data. Highly (altered) silicified zones have higher acoustic impedance which cause them to be seen in the high resolution seismic data. The alteration zones cannot be seen in the magnetic data as they are nonmagnetic. The airborne methods are the most practical methods for the exploration in this large corridor especially the airborne gravity method which is capable of seeing both silicification and desilicification. The high resolution seismic method is not affordable and does not cover the corridor well, also the airborne electromagnetic method has limitations to show the large outspread distribution of the altered clay at depth in the area. In this research, I also consider the gravity method

as the main method for exploration as there are enough available airborne gravity datasets covering the corridor which are not noisy like the available airborne electromagnetic data.

The goal is that the subtle geophysical responses of uranium deposit alteration systems at depth can be confused with or masked by the geophysical response of the overburden. By more accurately modeling the response associated with the overburden, it can be more effectively separated (or stripped) from the geophysical signatures of the deposit. Therefore, in this project I investigate and assess methods for "stripping" off the effect of the glacial cover from geophysical data, primarily from gravity and magnetic data, using new and modern modelling and inversion methods. Since gravity data varies more smoothly than other geophysical data sets it is not always possible to separate the effects of the shallow bodies from the deeper bodies using old and basic methods such as data filtering and the independent inversion which are presented by some researchers such a Kornik (1983) and Sobczak (1983). For the inversion, constrained and joint methods will be investigated over the McArthur-Millennium site. The 2-dimensional (2D) and 3-dimensional (3D) inversions of synthetized data will be performed on the geophysical dataset constrained by sediment cover thickness derived from other geophysical inversions and the physical properties of Quaternary sediments. This helps to reconstruct a model incorporating both sediment cover and the deeper geology including mineralization from geophysical data. And finally, the best inversion methods obtained from the synthetic modelling will be applied to the real data. These new joint inversion methods were never used or applied on any real data before. Thus, a major innovation of the project is new approaches to linking the geophysical signatures of ore systems to their petrophysical and mineralogical attributes by using these attributes as constraints in the inversions. The

research emphasizes the application of new modelling and inversion tools and techniques for recognition of mineralized systems in environments where detection of deposits must rely on few outcrops, few measurements, or muted signals. The emphasis will be on development of new overburden stripping methods for glaciated terrains, which will allow the gravity method to detect alteration footprints below overburden that masks and obscures the gravity signature of the footprint.

Different chapters of this thesis will describe the application of the new approaches to gravity, magnetic, electromagnetic and seismic refraction geophysical methods. The initial chapters will introduce the geology and physical properties of the rocks of the study area as well as geophysical methods and the theory of forward modelling and inversion methods. Synthetic forward modelling of gravity data (free-air and Bouguer anomalies) will be investigated in chapter 5 which assesses the signature of different geological structures in the gravity data of the area. For the seismic refraction method, chapter 6 will show the results related to the 2D modelling and inversion as well as joint inversion with the gravity method in which it can be seen that the overburden stripping can be successfully done and the location of the alteration zone can be determined. In the next chapter (7), in addition to the 3D forward modelling of gravity and magnetic data, the independent, joint and constrained inversions will be done to model the geological structures. There is overlap of the spatial wavelengths of the gravity response of the alteration zones and the overburden thickness variations in the study area but there is more of a separation of the magnetic response of basement features and the magnetic response associated with overburden. This chapter clearly shows that although the alteration zone cannot be defined (as it is too subtle to be detected using gravity and magnetics), the depth to the basement and the large scale

structures in the basement are evident especially where the fault intersects the unconformity in the vicinity of mineralization. In the last chapter (8), for electromagnetic methods, both frequency- and time-domain methods are assessed using 3D forward modelling and 1D inversion codes. It can be seen that the frequency-domain data can be used for reconstructing the base of the overburden while the time-domain data can be used for determining the location of graphitic shear zones at depth. All these results give us a better image of the subsurface of the study area as well as the possibilities for the overburden stripping to see the alteration zone. Therefore, they can be used for the future explorations in the corridor or other regions with similar characters.

Chapter 2

Geological Attributes and Physical Properties in the Millennium-McArthur River Region

2.1 Introduction

The Athabasca Basin is a Proterozoic sedimentary basin which is located in northwest Saskatchewan and northeast Alberta (Figure 2.1; Jefferson et al., 2007). In the Athabasca Basin, the uranium deposits are mostly located close to the unconformity between Proterozoic sedimentary rocks and the Archean and Paleoproterozoic metamorphic basement where the Athabasca Group unconformably overlies the western Wollaston and Wollaston–Mudjatik transition basement domains. The exploration has focused on the unconformities where mineralization is located in the vicinity of graphitic bodies (e.g., in the McArthur River area). However, some mineralization can occur above and below the unconformity at a distance from graphitic bodies (e.g., in the Millennium area). The sedimentary rocks of the Basin are unmetamorphosed strata which are covered by Quaternary glacial deposits and the lakes. Sedimentation began in the Athabasca Basin at

about 1740-1730 Ma. The basement is tectonically interleaved Paleoproterozoic metasedimentary and Archean to Proterozoic granitoid rocks which were last metamorphosed at 1800 Ma by the Trans Hudson Orogen (Jefferson et al., 2007; Alexandre et al., 2007). Paleovalleys and a regolith layer can be seen at the surface of the basement. Uranium deposits in the Athabasca Basin are related to hydrothermal ore-generating events at around 1600 and 1350 Ma which were overprinted by further alteration and uranium remobilization events at around 1176 Ma, 900 Ma and 300 Ma (Fayek et al., 2002a).

Geological structures have different physical properties. Their rock properties provide a quantitative link between geology and geophysics. Physical properties depend on the mineralogy, composition of the rocks, porosity, fractures, material in pores and fractures, geometry of minerals and fractures and alteration, etc (Nur et al., 1998; Schön, 1996). Geophysical data are responsive to variations in physical rock properties in the rocks and minerals in the Earth. Resistivity, density and seismic velocity can also depend on the porosity and the nature of the pore fluid (Mavko, 2009; Schön, 2011). Density and seismic velocity of strata in the Athabasca Basin mostly increase with increasing depth. Resistivity and magnetic susceptibility can vary more widely due to the specific changes in the geological structure. Physical property measurements including resistivity, density, magnetic susceptibility, seismic velocity and porosity have been made on both drill-hole and surface samples (Mwenifumbo et al., 2004).

In this chapter, topics such as the geology and the stratigraphy as well as the quaternary geology (e.g. nature of deposits and stratigraphy) of the McArthur-Millennium region will be discussed. In addition to the investigation of the relationship between uranium

deposition and geological attributes, the main physical properties variations within the region such as density, magnetic susceptibility, conductivity and seismic velocity will be assessed.

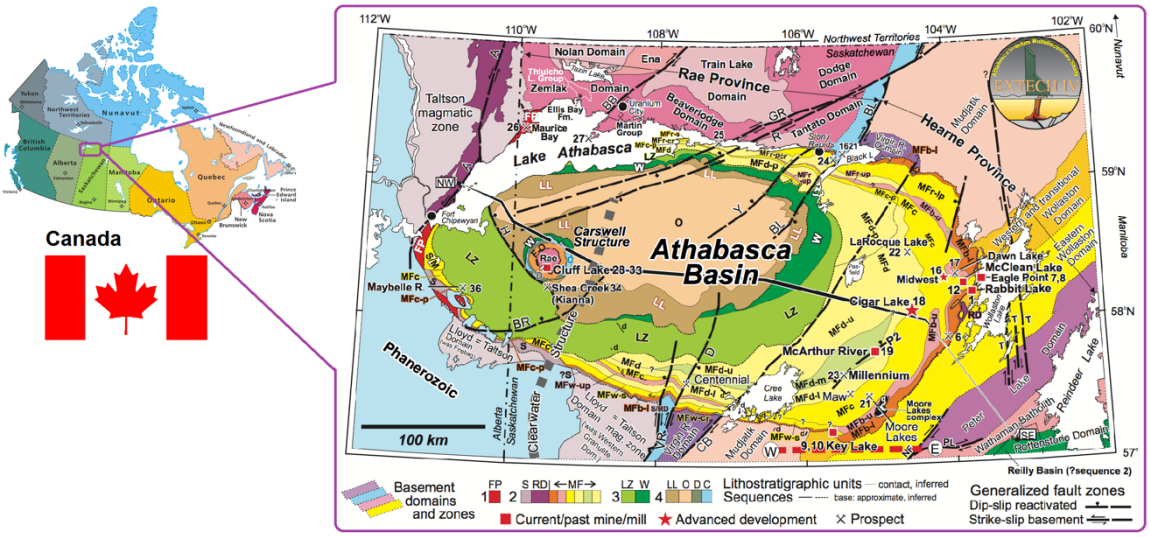

Figure 2.1: Geology of the Athabasca Basin and uranium deposits (adapted from Jefferson et al., 2007).

2.2 Geology and stratigraphy of the McArthur-Millennium corridor

In the McArthur-Millennium area, the near surface structure is overburden comprising Quaternary glacial sediments with a variable thickness (from 0 to more than 100 m; Figures 2.2, 2.3 and 2.4). The underlying layer (see Figure 1.2) is sandstone of late Paleo- to Meso-Proterozoic age (Rainbird et al., 2007) which unconformably overlies Archean and Paleoproterozoic metamorphic basement. At the McArthur River mine, the deposit formed where the reverse P2 fault intersects the unconformity over the basement with an offset up to 80 metres, whereas in the Millennium area the deposit is located below the unconformity in the basement in the vicinity of the B1 fault (see Figures 1.1, 2.3 and 2.4). The age of the

faulting is around 1.8 Ga, and the age of first uranium mineralization is around 1.6 Ga (Jefferson et al., 2007). The basement structure below the unconformity includes two different types of metasedimentary rocks: pelite (making up the hanging-wall rocks of the fault) and quartzite (the footwall rocks; McGill et al., 1993). Alternating units of quartzite and granitic rocks as well as metamorphosed graphitic pelitic rocks are the main lithologies in the basement. Other lithologies which need to be mentioned here are granitoid rocks, pegmatite, psammitic gneiss, chloritic schist, graphitic pelitic schist, quartzo-feldspathic gneiss, albite gneiss, and pelitic and/or psammo-pelitic gneiss, calc-silicate gneiss, metadiorite, metagabbro, and amphibolite (Thomas and Wood, 2007). Most deposits are located near metapelitic rocks. Since the silicification within the sandstone at McArthur River is located above units of basement quartzite, quartzite units are also important for gravity exploration as they are a denser lithology (Marlatt et al., 1992).

In the area, from top to bottom, sandstone consists of the D, C and B units of Manitou Falls formation as well as the Read Formation. Manitou Falls D (MFd) consists of fine grained, well sorted sandstone. Manitou Falls C (MFc) comprises quartzarenite with minor quartz pebbly beds, mudstone interbeds, clay intraclasts and conglomerate interbeds. Manitou Falls D contains the greater abundance of clay intraclasts compared to Manitou Falls C. The Manitou Falls B (MFb) is distinguished by conglomeratic pebble beds (Ramaekers, 1981; McGill et al., 1993; Jefferson et al., 2007). Read Formation (RD), formerly Manitou Falls A (MFa), consists of discontinuous basal conglomerate, intercalated coarse sandstone, conglomerate and red mudstone (McMullan et al., 1987; Mwenifumbo et al., 2004).

Two alteration patterns are observed in the Athabasca (Manitou Falls Formation) sandstones: 1) desilicification and illitization, and 2) silicification, kaolinization and dravitization. Desilicification and silicification mostly occured in the northeast portion and the south portion of the Athabasca Basin, respectively. Strong silicification is quite unique to the McArthur River deposit and it is very restricted to the deposit itself. This silicification, while mostly in the Read formation, is very limited laterally – i.e. especially at the scale of the greater McArthur-Millennium study area (McGill et al., 1993; Matthews et al., 1997). During silicification, silica is deposited by hydrothermal fluids and fills pore spaces and replaces the other minerals. This increases the resistivity and density of the rocks. In contrast, the desilicification (or bleaching) is caused by hydrothermal fluid flow that removes the coloured minerals from the sandstone, and decreases the density of the rocks, leaving behind altered clay minerals such as illite, dravite, kaolinite, chlorite and dickite, which can be seen in the sediments as well as in the upper part of the basement. The clay mineral also shows a low electrical resistivity. In the CMIC-Footprints project, the 3D shells of the distribution of altered clays minerals are identified by researchers with optical remote sensing methods applied to drill core using short-wave infra-red (SWIR) wavelengths (see Section 3.4). Illite is the dominant alteration mineral in the area which can extend laterally for more than 10 kilometres and can also cover the uranium mineralization (Figure 2.2; Earle and Sopuck, 1989). Some linear zones of chlorite and dravite can be seen in the area which cover some of the main mineralization. Illite-kaolinite-chlorite alteration zones are located up at the base of the sandstone and can have up to 400 m width, thousands of metres length and hundreds of metres depth (Wasyliuk, 2002). Mineralization at the eastern Athabasca Basin is more proximal to the zones of silicification

and dravitization. In the case of alteration associated with basement-hosted deposits, the uranium mineralization is surrounded by an outer illitic halo as well as an inner illitic-chloritic halo. Silicification in the McArthur River area is mostly located in the lower RD formation while disilicification in the Millennium area surrounds the reverse faults in the sandstone like a thick cover (Fayek and Kyser, 1997; Alexandre et al., 2007).

Since faults and fracture zones permit the flow of fluids that contain uranium, uranium deposits are mostly formed where the unconformity intersects underlying fold and thrust belts (Jefferson et al., 2007). In these zones, graphite rich faults often underlie uranium deposits. The low electrical resistivity of graphite acts as a good target for electromagnetic exploration methods. Also, the hydrothermal circulation causes alteration of the host rocks including changing their densities which make them a possible target for the gravity exploration method.

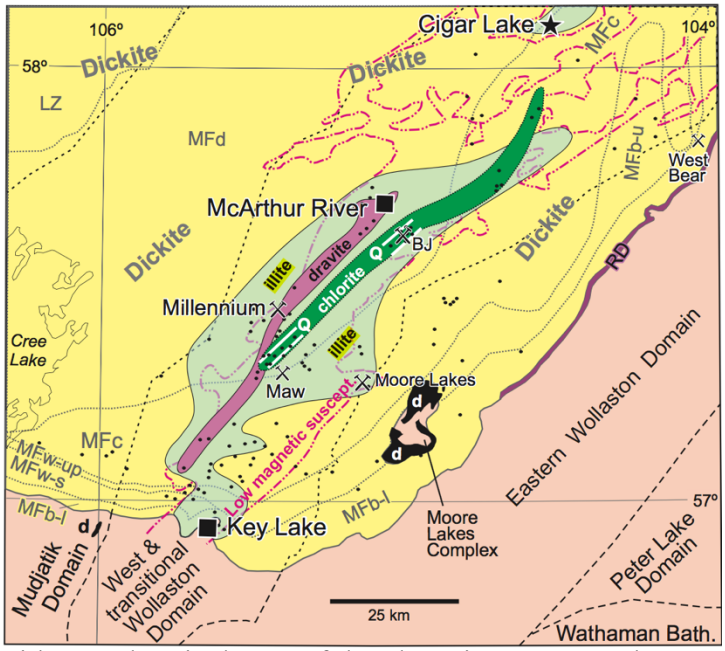

Figure 2.2: Lithogeochemical map of the alteration zones at the eastern part of the Athabasca Basin which shows illite, chlorite, and dravite anomalies in the surficial material and outcrops (Jefferson et al., 2007).

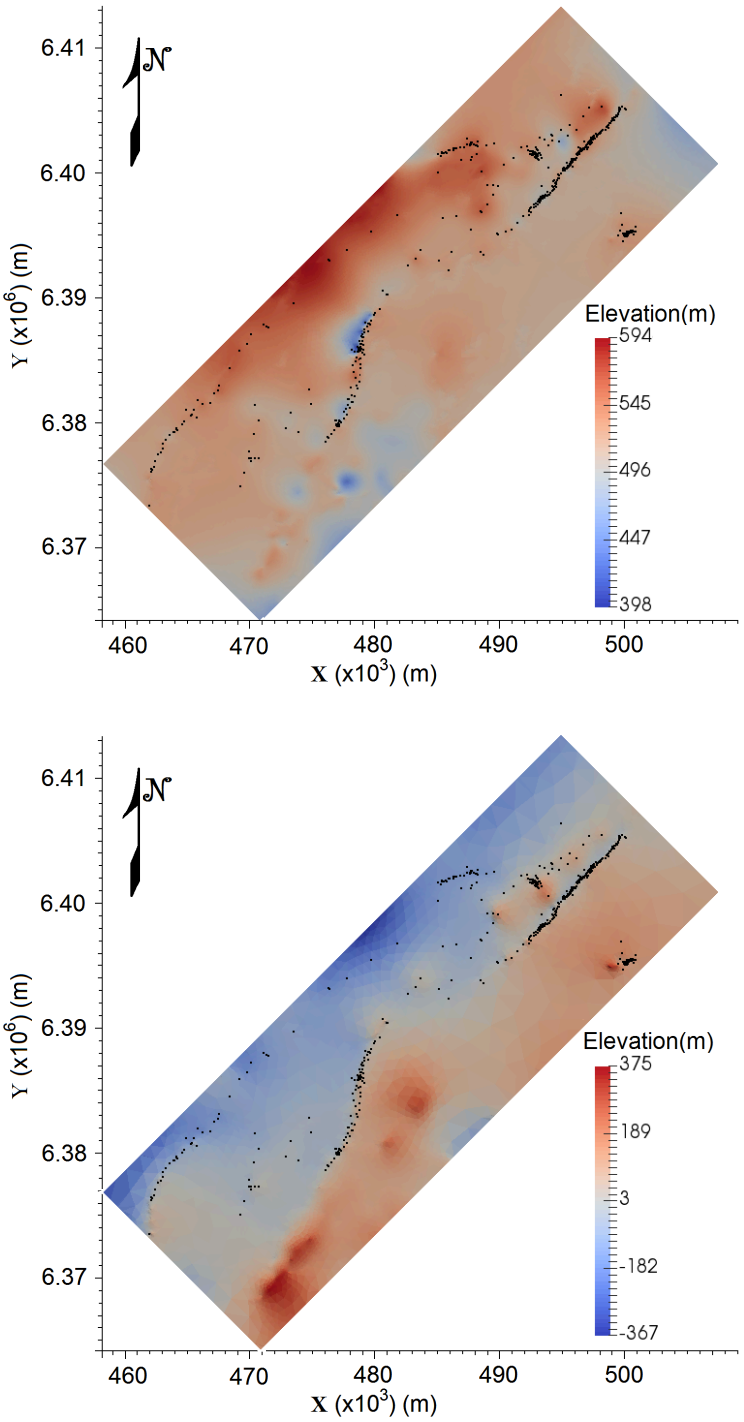

Figure 2.3: Topography of the base of overburden (top) and unconformity (bottom) in the McArthur-Millennium corridor (20×50km) estimated from drill-hole data (adapted from CMIC-Footprints project; made by Mohamed Gouiza and Mira Geoscience Ltd.; see Figure 1.1 for surface topography). Some of the drill-holes in the area are shown by black dots which show that the resolution is only good at places with more drill-holes because the interpolation was coarse as it was simply done between the scattered drill-holes.

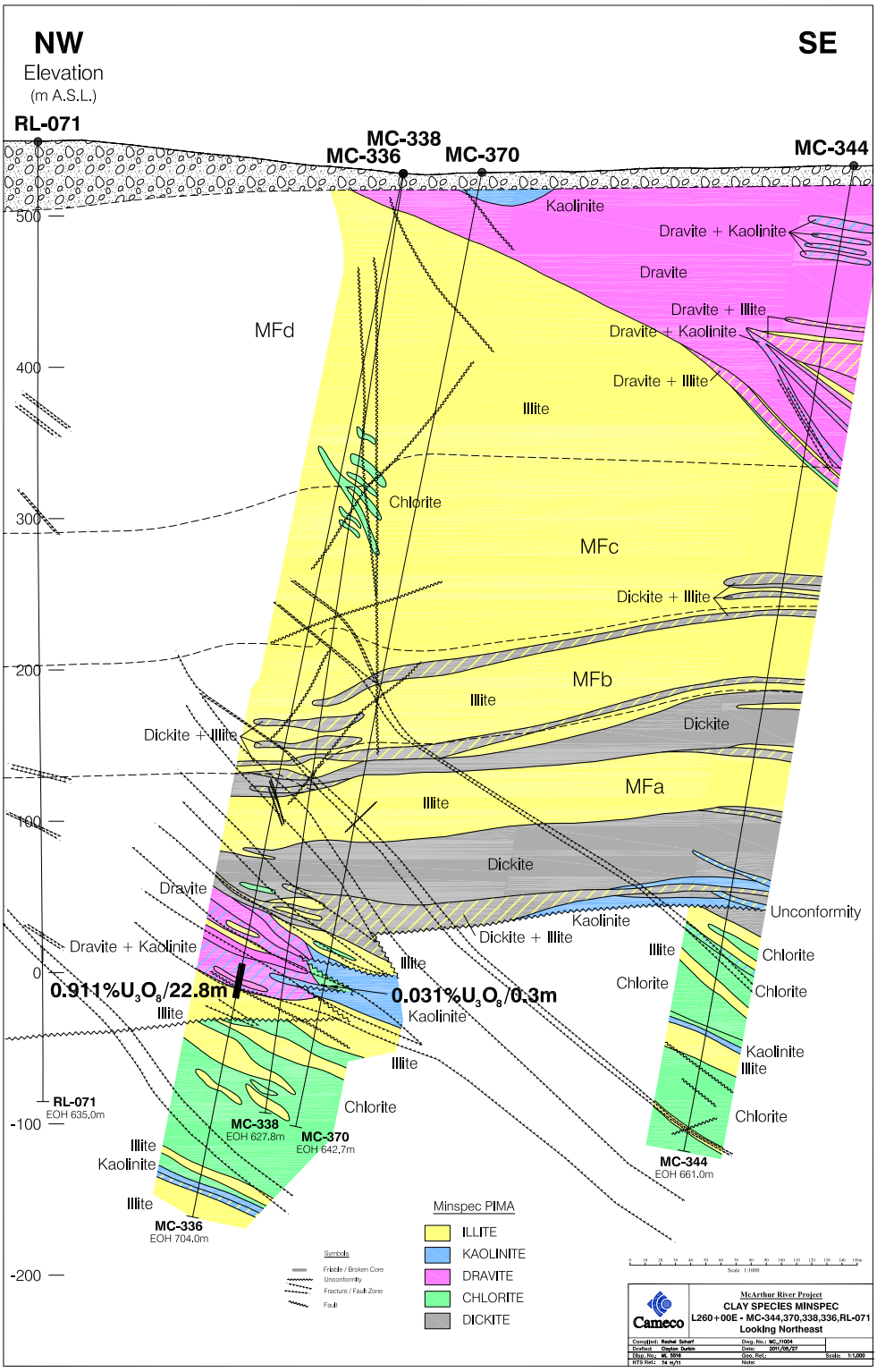

Figure 2.4: Cross-section made using drill-hole data in the McArthur area. It shows the structure of the altered clay in the sandstone and top of the basement (a Cameco Co. plot from CMIC-Footprints project). Note that this section shows the clays identified using SWIR, however the rocks are all completely dominated by quartz in the sandstones.

2.3 Uranium deposition and geological attributes

Uranium deposits in the Athabasca Basin are all classed as unconformity-related deposits, but can be categorized into different types (Jefferson et al., 2007). One of the categorizations, which is based on the location of the uranium deposits, has two types (Figure 2.5). The first type is the fracture-controlled basement ore deposit which occurs below the unconformity in dipping shear zones. The second type is the clay-bounded ore deposit which occurs along and/or above the unconformity. Also, some deposits are considered as a combination of both types.

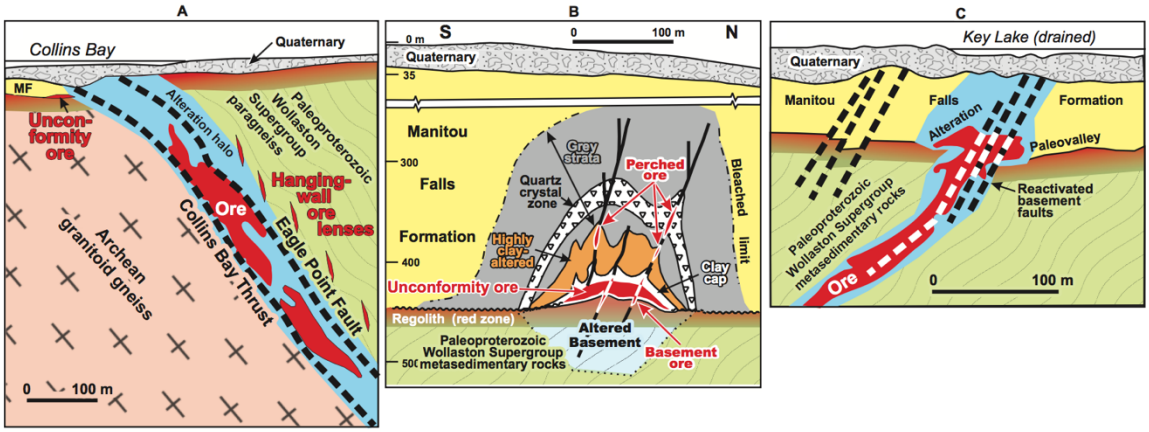

Figure 2.5: A) Basement hosted uranium deposit, B) typical unconformity ore and C) both basement hosted and unconformity type deposit (Tuncer, 2007; Jefferson et al., 2007).

Unconformity-associated uranium deposits can also be categorized, based on the metals which are present with uranium, into monometallic and polymetallic deposits (Figure 2.6; Ruzicka, 1996). Monometallic deposits, which are fracture-controlled basement-hosted deposits, are simple and contain only traces of metals other than uranium and copper. Polymetallic deposits, which are mostly clay-bounded, contain sulphide and arsenide

minerals with significant amounts of Ni, Co, Cu, Pb, Zn and Mo (Jefferson et al., 2007). Unconformity deposits can be either polymetallic or monometallic in mineralogy.

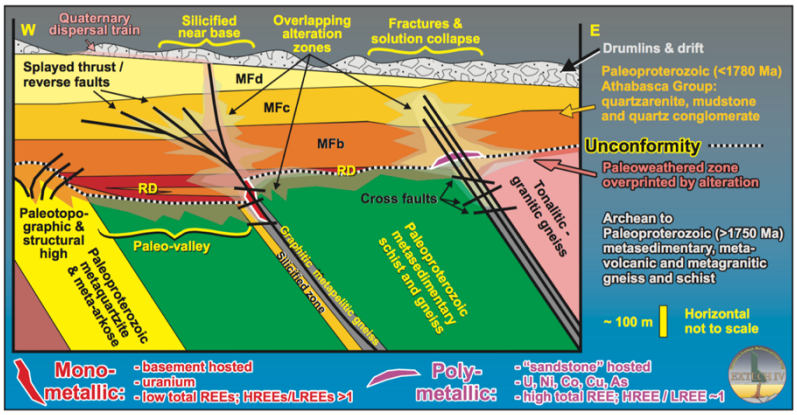

Figure 2.6: Monometallic and polymetallic type uranium deposits (Jefferson et al., 2007).

Another categorization comes from the fluid flow directions. If the fluid flows from the basement to the sandstones, this will generate an egress type uranium deposit (Figure 2.7). In contrast, the ingress type deposit is one in which the fluid flows from sandstones to the basement. Weak alteration occurs in ingress type deposits. Because of the complexity of hydrothermal systems, some deposits such as McArthur River have both ingress and egress types (Jefferson et al., 2007).

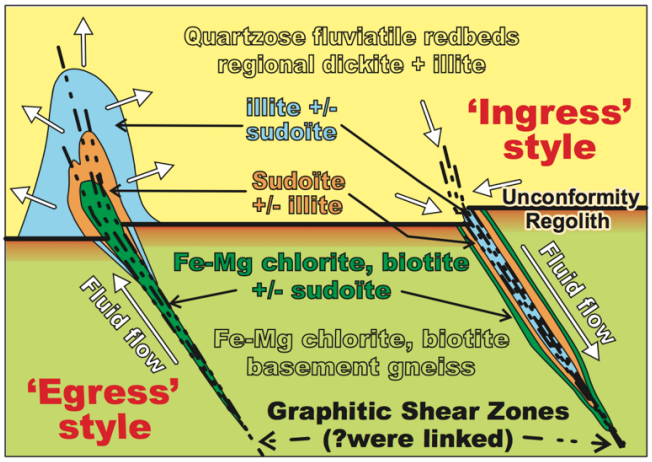

Figure 2.7: Ingress and egress type uranium deposits (Jefferson et al., 2007).

2.4 Quaternary geology

2.4.1 Glaciers

Glaciers are accumulations of large quantities of ice, air, water, and sediments (rock debris) moving downhill under the pull of gravity very slowly, from tens of metres to thousands of metres per year (from 0.01-0.1 m per day for large Continental glaciers to 0.1–2 m per day for Alpine glaciers). They cover one-tenth of the Earth's surface (Jain, 2014). The term "glacial drift" applies to all sediments which have glacial origin. There are two types of glacial drift: till (glacial deposits) and stratified drift (glaciofluvial deposits). Till deposits include till and erratics, and can also form into geomorphological features such as moraines and drumlins. Till is an unsorted and unstratified glacial drift, deposited directly from ice. The grain size in till ranges from clay to boulder. The finer sediments (rock flour) and the larger pieces of sediment (boulders) in till come from abrasion and plucking, respectively. Erratics are large boulders transported by glaciers and left behind when the ice melts. Moraines are concentrated deposits of till, and there are five different types of them: terminal moraine, ground moraines, recessional moraines, lateral moraines, and medial moraine. Drumlins are hills made of till and some partly of bedrock which are molded by the flow of the continental ice sheet. They are usually about 1–2 km long and about 15– 50 m high (Figure 2.8). Glacial melt water and wind can also generate stratified drift deposits, which are sorted and layered sediments such as kettles, kames, eskers, outwash and loess (Figure 2.8). Depressions formed underneath the glacier and filled by water generate small lakes which are called kettles. Kames are low, cone shaped, steep-sided hills. They are

stratified sediments deposited by streams on top of the glacier which are deposited when the glacier melts. Eskers are long sinuous ridges of sediment, with a height of a few to several tens of metres, deposited by streams that flow under a glacier. Outwash deposits are made by the meltwater flowing away from the edge of the glacier. Loess is silt-rich rock flour which is picked up and distributed by wind across wide areas.

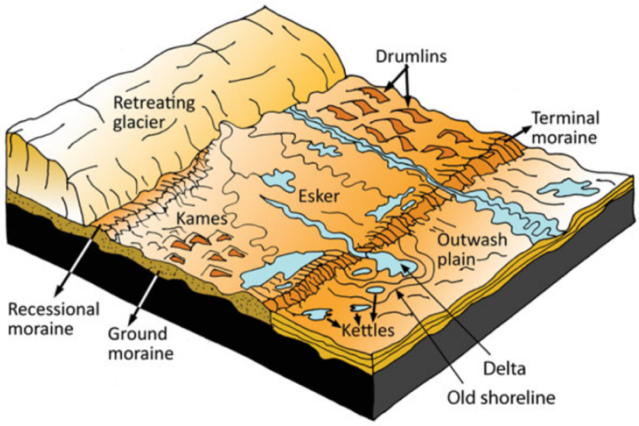

Figure 2.8: Various landforms produced by continental glaciers (Jain, 2014).

2.4.2 Introduction to quaternary geology of the eastern Athabasca Basin

The overburden of the Athabasca Basin is a product of the advance and retreat of the last ice sheet belonging to Late Wisconsinan. Deglaciation of the eastern Athabasca Basin began in the southwest around 9000–8700 BP (before present), and the area was completely ice-free by 8200 BP. The thickness of glacial deposits is variable and ranges from 0 up to 100 m. The area is mostly covered by drumlin, hummocky moraine, esker complexes, and ground moraine. The bedrock surface topography is undulating and variable due to glacial erosion (Campbell, 2007; Campbell and Flory, 1999). Ice-flow direction in the eastern basin has been determined to be southwestward (208°–245°) by glacially streamlined features such as drumlins.

2.4.2.1 Detailed description of the nature of glacial deposits

Till deposits, which form ground and streamlined moraines, are the dominant surface materials in the Athabasca Basin. Other surficial deposits include glaciofluvial and glaciolacustrine sediments, block fields, and eolian and organic deposits, defined below. Drumlins and streamlined features are the most prevalent landforms (Figure 2.9; Sproule, 1939). Figure 2.10 shows the topography map which is dominated by glacial features. Northern and western parts of the eastern Athabasca Basin are covered by outwash plains with sporadic drumlins and esker systems. All the glacial deposits and their nature within various geomorphological features are described in detail below:

Organic deposits: Organic deposits with a thickness of less than 3m, consisting of bogs, are found as surface deposits in depressions close to lakes and rivers.

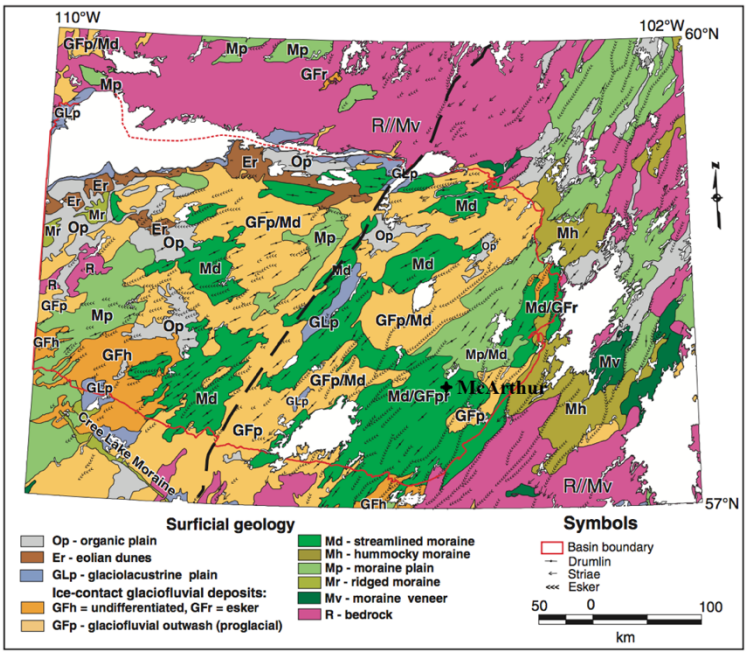

Figure 2.9: Regional surficial geology map of the Athabasca Basin and northern Saskatchewan (modified from 1:1000000 scale maps; Simpson, 1997; Schreiner, 1984a).

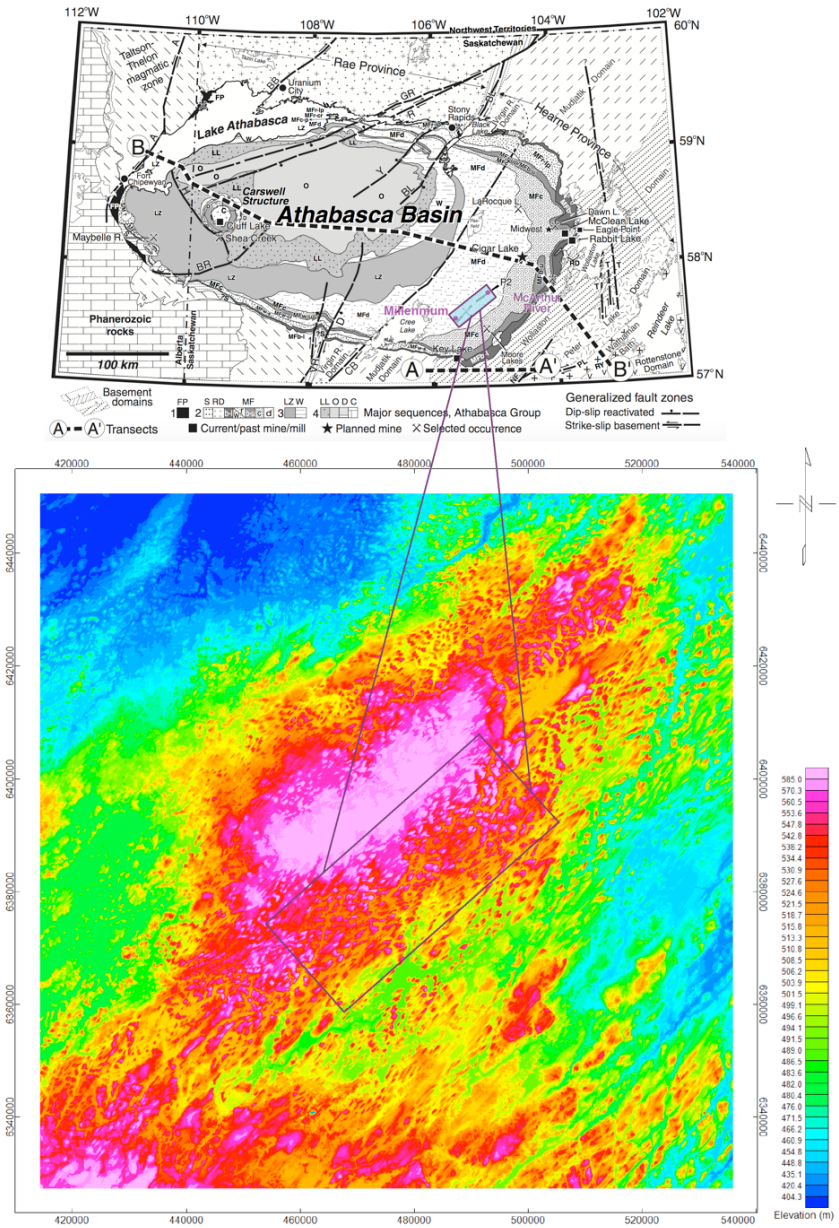

Figure 2.10: Topography of the eastern Athabasca Basin. Rectangular frame shows McArthur-Millennium corridor.

Till: Tills on the Athabasca Basin are mostly composed of sand, silt, clay and gravels. Tills range from very sandy to silty sand (sand ranges from 51% to 95%; Schreiner, 1984a; Campbell and Flory, 1999). Tills with intrabasinal and extrabasinal sources are typically white to pinkish grey and very sandy with less than 15% clasts, and grey to brownish grey

with a silty-sand matrix containing a higher clay component and 35–100% basement clasts, respectively. The extrabasinal materials were derived from the northeast margin of the basin in Nunavut, and have been moved several 100 km from their sources (Campbell, 2007). They comprise pebble- to boulder-size igneous and metamorphic rock and pink feldspar. In general, the thin veneer of till over bedrock is composed mostly of locally derived sandstone (intrabasinal material). When the thickness of till deposits increases, the proportion of extrabasinal detritus increases.

Streamlined deposits: Drumlins in the basin are composed generally of till (Millard, 1988). The core of the large drumlins are predominantly richer in extrabasinal materials. They have been capped by a thin and surficial till unit with a higher sandstone component of intrabasinal materials (Aario and Peuraniemi, 1992). By moving from lee (ice down) to stoss (ice up), the sandstone component in the surface till changes slightly towards the crystalline shield clasts. Some drumlins have a core composed of water-sorted sediments capped by a thin deposit of poorly sorted till (Shaw and Kvill, 1984).

Hummocky moraine: It is formed at the ice margin, and is composed of till that is mostly looser and sandier with a higher proportion of clasts ranging from pebble to boulder which is often sorted by meltwater.

Block fields: They consist of 0.5–2.0 m diameter angular sandstone boulders which are observed in the region.

Glaciofluvial deposits: Sand and gravel in the area are mostly related to esker complexes, ice-walled channels, recessional moraines, and stagnant-ice hummocky moraine. Esker

systems form a dendritic drainage pattern, ranging from tens of metres to several kilometres wide, adjacent to kames, kettles, and/or outwash plains. Ice-walled channels in the area have been eroded through the previously deposited drift, and can be up to 1 km wide (Schreiner, 1983, 1984a).

Glaciolacustrine deposits: Due to the sandy nature of glaciolacustrine sediments in the Basin, this kind of deposit is mostly well sorted, comprising fine- to medium-grained sand and silty sand. They form sand plains, beaches, and spit deposits.

Eolian deposits: Eolian deposits in the eastern Athabasca Basin (less than 5%) have been mostly covered and stabilized by vegetation. Rare dunes and blowouts indicate some eolian activity still occurs. Loess has a thickness up to 20 cm which fills shallow depressions in till surfaces.

2.4.2.2 Quaternary stratigraphy

Based on information gathered from the eastern Athabasca Basin during the 1970s, Geddes (1982) identified three 'till' units. There are also three nonglacial deposits called 'stratified sediments' (Table 2.1). These units are described as follows:

Till 1: Till 1 is the oldest or lowermost till which has been largely eroded by subsequent glaciations. It was largely derived from crystalline shield rocks, and has a fine- to medium-grained, silty sand matrix with variable silt/clay content. Its thickness ranges from less than 1 m to 18 m, and is capped by silt and clay of the 'lower stratified sediments'. It has been deposited by a glacial event that predated the Late Wisconsinan ice advance.

Table 2.1: The regional Quaternary stratigraphic units along the eastern margin of the Athabasca Basin (taken from Geddes, 1982).

Stratigraphic unit	Subunits, materials	Distribution	Associated ice-flow direction
RECENT DEPOSITS	Peat, lacustrine, eolian	Throughout	
UPPER STRATIFIED SEDIMENTS (UPPER DEGLACIAL SEDIMENTS, Geddes (1982))	Sand, gravel; minor silt and clay	Sporadic, throughout Eskerine complexes, outwash plains	
TILL 3 (UPPER TILL, Averill (1977a, b); Geddes (1982))	Ablation till (flow and meltout)	Related to re-advance dominantly west of unconformity Discontinuous Hummocky, drift, thin veneer, small drumlins	190–200°
MIDDLE STRATIFIED SEDIMENTS (MIDDLE DEGLACIALS, Geddes (1982))	Sand, gravel; minor silt and clay	Uncommon; mixed with till 3	
TILL 2 (MIDDLE TILL, Averill (1977a, b); LOWER TILL, Geddes (1982))	Ablation till	Throughout Most common unit Associated with drumlins, fluted and featureless till plains	Drumlins: 210–225° Striae: 205–225°
	Basal till (melt-out and lodgement facies)		
LOWER STRATIFIED SEDIMENTS (LOWER GRAVELS, Geddes (1982))	Clay and silt; sand and gravel	Rare No surface expression	
TILL 1 (LOWER TILL; Averill (1977a, b); OLD DRIFT, Geddes (1982))	Till	Very rare, preserved in bedrock lows	Maybe related to 240°
BEDROCK			

Lower stratified sediments: The ‘lower stratified sediments’, which overlie Till 1 or bedrock, consist of two units: 1) glaciofluvial sand and thin clay layers, and 2) glaciolacustrine silt and clay. The thickest deposits are up to 27 m.

Till 2: Till 2 is the most extensive till deposit in the area, which forms drumlins and ground moraines. It is hard with a texturally mottled sandy and silty-sand matrix (Averill, 1976a). Till 2 contains crystalline shield detritus, and where it overlies the bedrock, it is mostly derived from sandstone. It was deposited by the main Late Wisconsinan ice advance.

Middle stratified sediments: ‘Middle stratified sediments’ is a discontinuous layer of sand and gravel or a thin (<1 m) deposit of silt (Geddes, 1982).

Till 3: Till 3 discontinuously overlies Till 2 with a variable thickness of 0 to 23 m. Hummocky moraine and the smaller-scale drumlins and fluted moraines are mostly composed of Till 3 (Campbell and Flory, 1999). It is loose, sandy, and often bouldery, and often has a higher component of locally derived material than Till 2.

Upper stratified sediments: The 'upper stratified sediments' unit is comprised of ice-contact and proglacial stratified sediments related to deglaciation.

Recent deposits: These include organic deposits, eolian deposits, and modern alluvial and lacustrine sediments.

Recent researches (adapted from Shawn Scott and Martin Ross reports in CMIC-Footprints quarterly Y2Q4 and Y3Q1 reports) on a cross section (exposure) of a drumlin at the McArthur area show that oxidized stratified coarse sands related to the pre-late Wisconsinan are located at the base of the section. The lower till has fewer clasts, higher silt and more distally (basement) derived material. The lower till preserved in the core of drumlins can contain magnetic rocks. Above the lower till, layers of stratified sandy till are located. These layers are covered by a more sandstone rich till. The surface of the area is dominated by local till which is covered by dispersed altered boulders. Also, it has been found that all the tills are very sandy. The lower till has more shield clasts and finer material while the upper till has more sandstone clasts and coarser material.

2.5 Physical properties

Physical properties used in the next chapters are based on published papers and updated values from the CMIC-Footprints project. The CMIC samples were collected on drill core and outcrop samples, and in measurements made in boreholes. Laboratory and in situ measurements were made on these same samples. In the following, these updated values of the physical properties are presented. They are based on the expanded and refined measurements done in the CMIC-Footprints project (collecting the right data and using more expensive downhole multiparameter surveys), and allow the definition of better statistics (i.e. means and standard deviations).

2.5.1 Seismic velocity

In the eastern Athabasca basin, seismic velocity values as well as acoustic properties (density, P-wave seismic velocity V_p and acoustic impedance) increase with increasing depth (Figures 2.11 and 2.12). Hence, the acoustic properties of basement blocks are usually higher than the overlying sandstone, and also the acoustic properties of sandstone are higher than the overlying overburden (glacial deposits). Variations in acoustic properties in the sandstone depend on the degree of silicification. Highly (altered) silicified zones have higher acoustic impedance. Seismic data cannot show the ore-body, mostly due to the small size of the mineralization as well as the resolution of the seismic method. But, the unconformity can be observed due to the change or increase in the velocity associated with this surface. Shi et al. (2014) used a 2D model for the numerical wavefield simulation (for the Millennium area) which is shown in Figure 2.11. In this model, the Athabasca

Group sandstone consists of three subunits: a layer above 300 m whose velocity increases gradually with depth, a thin layer within the sedimentary sequence (300-350m) and the high-velocity Read Formation (350-650m). The seismic velocities of sandstone vary from lower values which can be observed near the top of sandstone to higher values which are near the basement rocks. The velocity contrast along the unconformity within the transition zone between the sandstone and basement rocks has a low contrast of ~500 m/s. Faults and alteration mineralization zones have different seismic velocities from the surrounding rocks. Overburden is not considered in this model as it is assumed to be removed by the static correction.

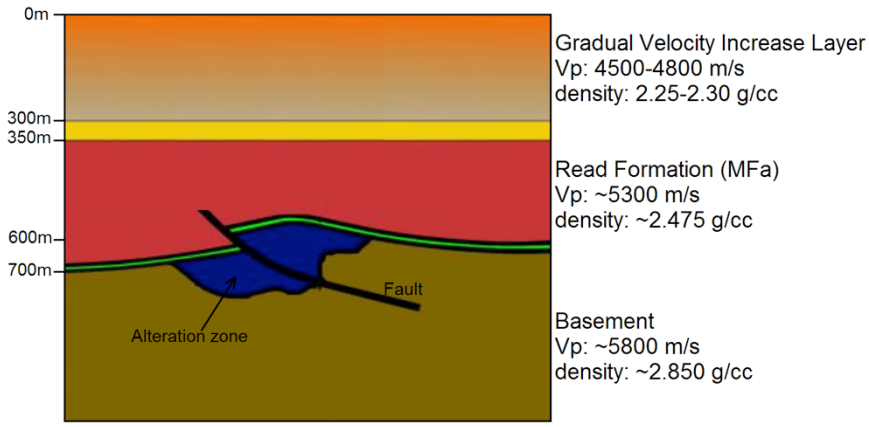

Figure 2.11: Seismic velocity model of the McArthur-Millennium area (Shi et al. 2014; CMIC-Footprints project).

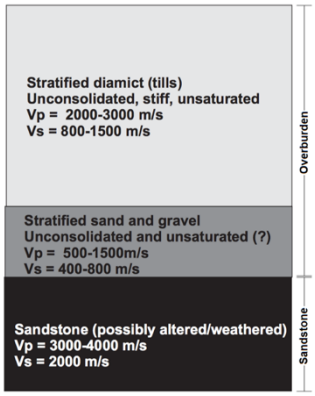

Figure 2.12: Seismic velocities for the overburden and sandstone of the McArthur-Millennium area (adapted from CMIC-Footprints project).

Figure 2.12 shows a conceptual model for the overburden and the top of the sandstone in the Athabasca Basin (from CMIC-Footprints project). It shows that the probability of a blind layer (see 5.2.3) being present in the overburden is high, which could be problematic for the seismic refraction method.

2.5.2 Density

Gravity anomalies result from a difference in density. The density of a rock is dependent on both its mineral composition and porosity. Figures 2.13 to 2.17 show approximate density ranges of some rocks in the Athabasca Basin based on the different sample populations (adapted from CMIC-Footprints project; Thomas and Wood, 2007). However, many old measurements including some logging results show that the in situ values differ than the values from the CMIC-Footprints measurements (Sobczak, 1983; Mwenifumbo et al., 2004).

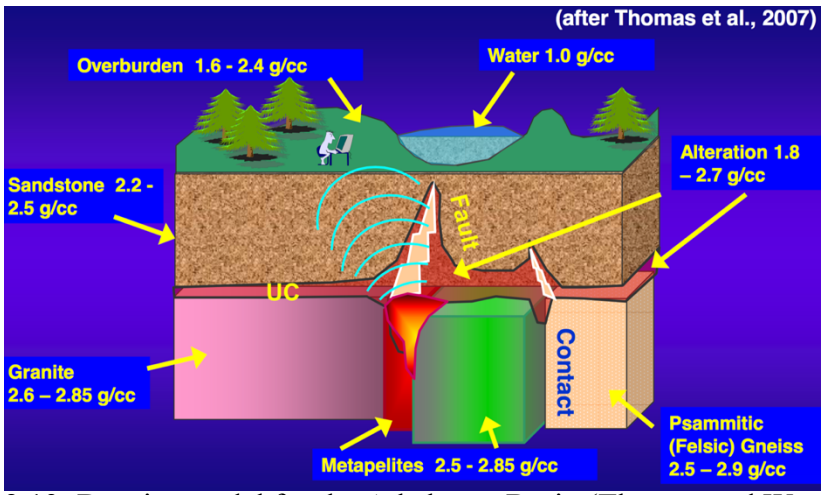

Figure 2.13: Density model for the Athabasca Basin (Thomas and Wood, 2007; adapted from CMIC-Footprints project).

Due to the small number of samples, they (Figures 2.14 to 2.16) only show the measurement of pebbles/boulders in the till, and so are not representative for the till overall. They show that the mean density for the overburden (Quaternary deposits) is around 2.6 g/cc (gram per cube centimeter) which is much higher than what is expected (around 2 g/cc). Recent researches in the CMIC-Footprints project used exposures of the Quaternary stratigraphy to take bulk density measurements at 50 sites within the study area in 2014 and 2015. The heterogeneity of the stratified till causes different densities. But, they confirmed that the average density of overburden in the McArthur-Millennium corridor is around 2 g/cc (adapted from Shawn Scott and Martin Ross reports in CMIC-Footprints quarterly Y3Q3 report).

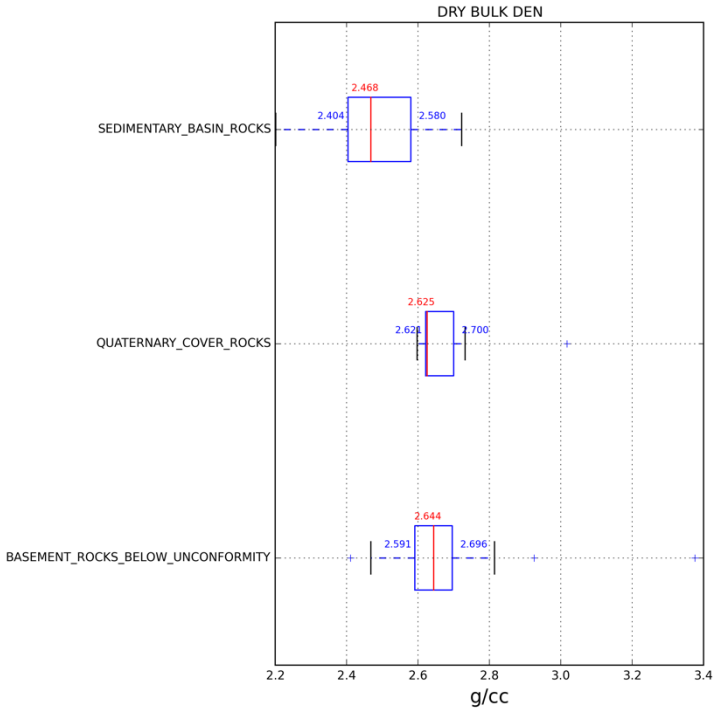

Figure 2.14: Density estimations for the lithology groups of the McArthur-Millennium area (adapted from CMIC-Footprints project). Red and blue numbers (or vertical lines) show median and extreme values, respectively. Blue boxes show the interquartile range.

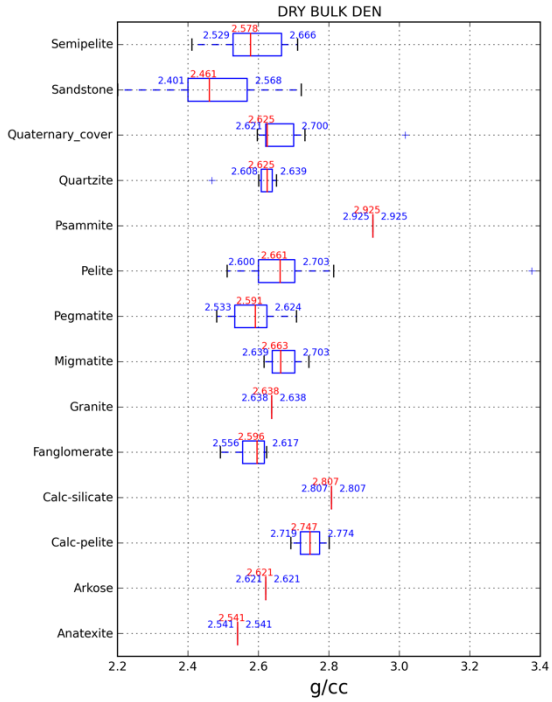

Figure 2.15: Density estimations for the lithologies of the McArthur-Millennium area (adapted from CMIC-Footprints project).

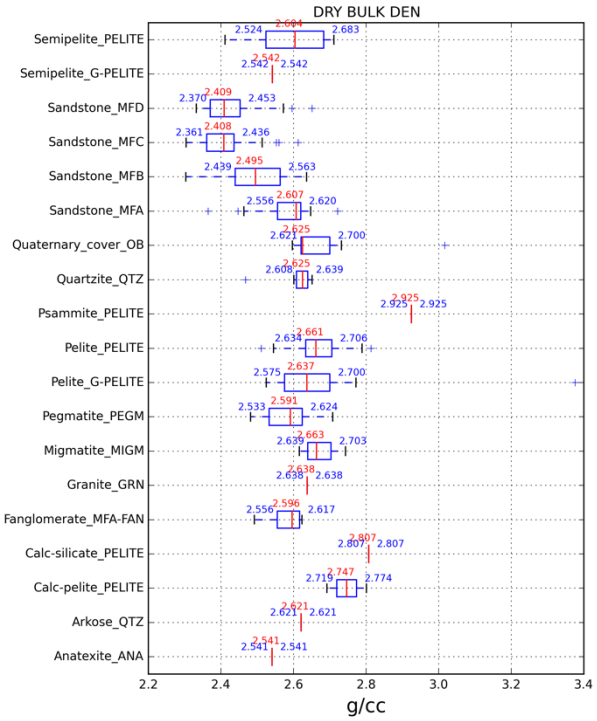

Figure 2.16: Density estimations for the rock-types of the McArthur-Millennium area (adapted from CMIC-Footprints project).

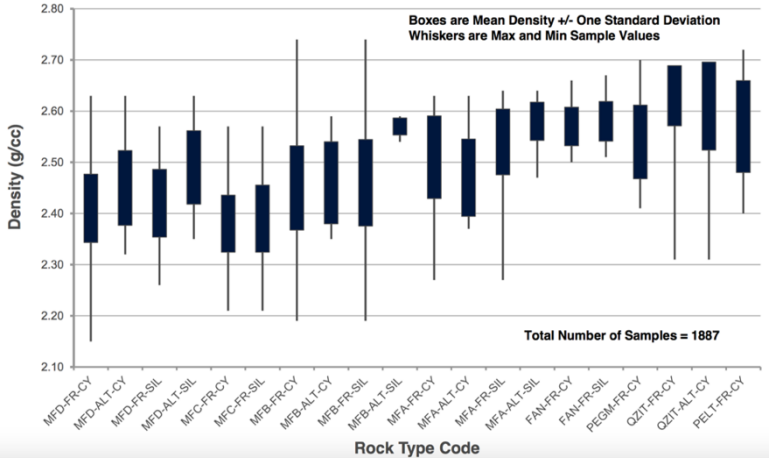

Figure 2.17: Density estimations from drill core from McArthur River/Read Lake (adapted from CMIC-Footprints project). ALT: altered; FR: not altered; CY: clay; SIL: silicification; MFA, MFB, MFC and MFD: sandstone strata, Manito-Falls A, B, C, and D; FAN, PEGM, QZIT and PELT: basement rocks.

Manito-Falls Formations have different ranges of densities especially due to the altered structures (e.g. silicifcation and disilicification; Figures 2.3 and 2.13). Regional sandstone density is in the 2.4-2.5 g/cc range (with an average of 2.43 g/cc), silicified sandstone density is generally more than 2.6 g/cc, while desilicified-altered sandstone density is often around 2.2 g/cc. The average densities for the clay-altered samples are lower than the average densities for the silicified samples for all of the lithologies, except for altered fanglomerate and non-altered quartzite (adapted from CMIC-Footprints project). RD samples shows that there is a decrease in illite, chlorite and dravite and an increase in dickite in the silicified altered samples compared to the clay-altered samples. Also, there is a decrease in chlorite and increase in dickite in the silicified-altered MFb samples compared to the clay-altered MFb samples. There is a decrease in illite and increase in chlorite and dravite in the silicified altered MFc samples compared to the clay altered MFc samples. For MFd, there is a decrease in chlorite and increase in kaolinite and dravite in the silicified-altered samples compared to the clay-altered samples (adapted from CMIC-Footprints

project). Note that the total amount of any of the clay minerals in the sandstones is generally small (no more than a few %), and so there is only a small affect on the total density.

Basement rocks (Figures 1.1 and 2.13) can be categorized into three main groups of density: 1) 2.66–2.67 g/cc including granitoid rocks, pegmatite, psammitic gneiss, and chloritic schist; 2) 2.69–2.71 g/cc including graphitic pelitic schist, quartzo-feldspathic gneiss, albite gneiss, and pelitic and/or psammo-pelitic gneiss; and 3) 2.81–2.95 g/cc including calc-silicate gneiss and metadiorite, metagabbro, and amphibolite (Thomas and Wood, 2007). The mean densities for the non-altered rocks (in both sandstone and basement rocks) are higher than the altered rocks for all of the lithologies, except for quartzite and pelite. However, the non-altered rocks vary in density more than the altered rocks (adapted from CMIC-Footprints project).

2.5.3 Magnetic susceptibility

The magnetic susceptibilities, in SI units, of some rocks and minerals in drill core from the McArthur-Millennium area are given in Figures 2.18 to 2.20. There are not many new measurements for the magnetic susceptibility of the overburden in this area. But, based on the available samples, the variable magnetic susceptibility of the overburden is due to the presence of granite clasts among some glacial deposits especially in the lower layers in drumlins. Different layers of glacial deposits can have different magnetic suscebtibility starting from 0 SI to 1×10^{-2} SI with an average value of 5×10^{-3} SI (adapted from CMIC-Footprints project). Kornik (1987) mentions that since the faulted, fractured or altered rocks have a thicker infilling of magnetic glacial sediments, they can be indirectly detected using

the magnetic method. Also, the sandstone layers (MF members) have very small values, lower than 10^{-5} SI, which are considered to be non-magnetic.

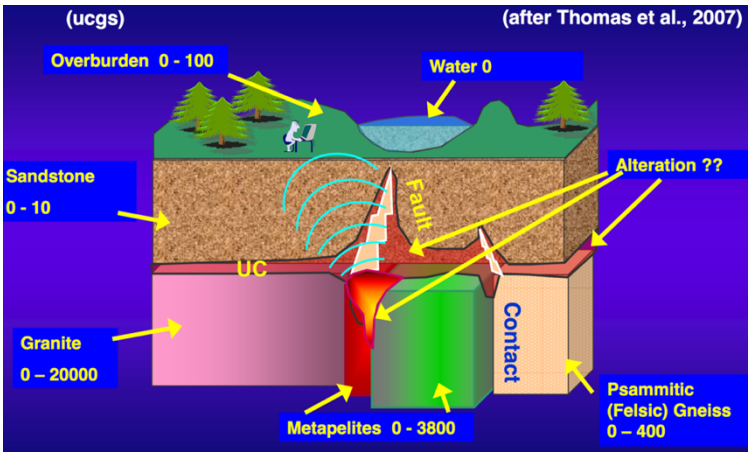

Figure 2.18: Magnetic model for the Athabasca Basin (Thomas and Wood, 2007; adapted from CMIC-Footprints project). Units are in ucgs (= SI × 10^{-6}).

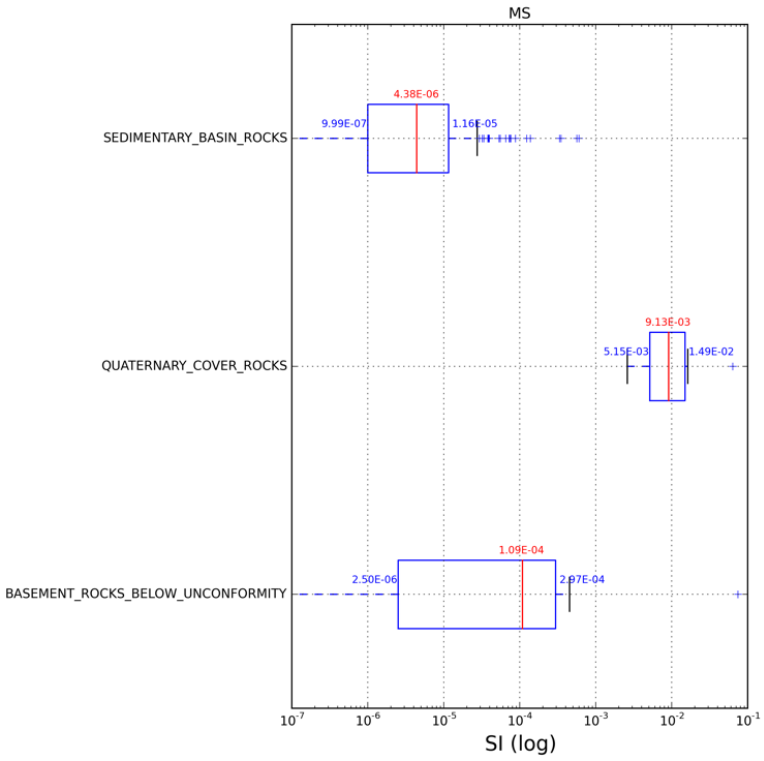

Figure 2.19: Magnetic susceptibility estimations for the lithology groups of the McArthur-Millennium area (adapted from CMIC-Footprints project).

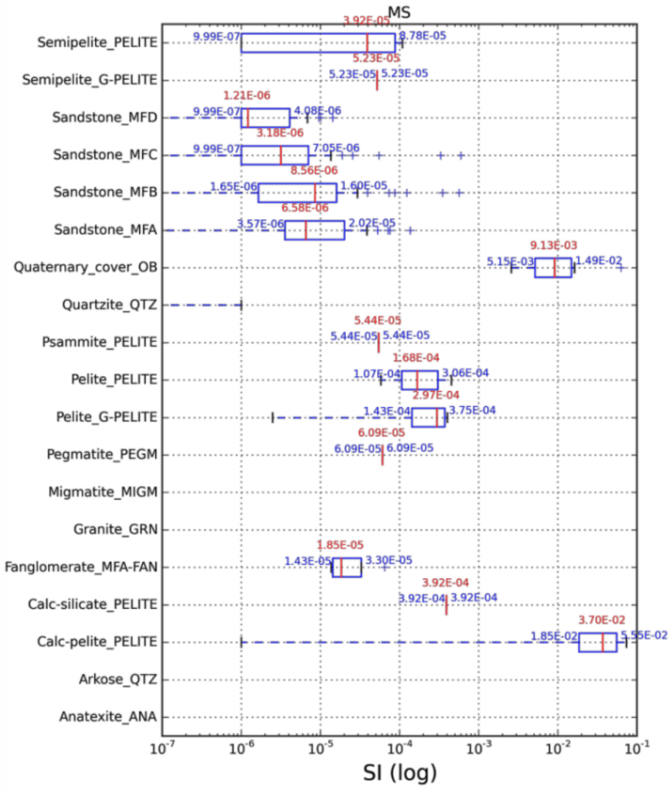

Figure 2.20: Magnetic susceptibility estimations for the rock-types of the McArthur-Millennium area (adapted from CMIC-Footprints project).

Basement blocks have highly variable magnetic susceptibility values. In the McArthur River area, the magnetic susceptibility of rocks in the footwall of the P2 fault is less than the susceptibilities in the hanging-wall (adapted from CMIC-Footprints project; Thomas and Wood, 2007). Magnetic susceptibilities of basement rocks have a wide range with metasedimentary pelitic, psammitic and calc-silicate gneisses (susceptibility μ = 0 to 4 SI $\times$ 10^{-3}) units generally having lowest magnetic susceptibility to granitoid rocks (susceptibility μ = 0 to 20 SI $\times$ 10^{-3}) which have the highest magnetic susceptibility. The magnetic susceptibility of meta-quartzite rocks ranges from 0 to 0.2 SI $\times$ 10^{-3} (Wood and Thomas, 2002).

2.5.4 Resistivity

The resistivity (i.e. reciprocal of conductivity) of some rocks and minerals of the Athabasca Basin are shown in Figures 2.21 to 2.25, based on the different sample populations. The resistivity of the overburden is variable in the Athabasca Basin. Although the resistivity of the surficial sediments was expected to be high based on the laboratory measurements as well as some electromagnetic surveys (Mwenifumbo, 2004; Irvine and Witherly, 2006), there is not a good conductivity contrast between the overburden and the sandstone. The presence of water in the unconsolidated materials of overburden can decrease the resistivity. The borehole log resistivities indicate the resistivity of water saturated rocks. The logs show that the resistivity generally decreases with depth. This might be due to an increase in salinity or of porosity (and therefore water content) with depth. An average of 2000 Ohm-m can be considered for the sandstone resistivity (Figures 2.21 to 2.23). Altered clay in sandstone has a lower resistivity than the host. For the basement blocks (Figures 2.23 to 2.25), the resistivity is highly variable from 10 Ohm-m for graphitic rocks to 80000 Ohm-m for Archean granitoid gneiss (adapted from CMIC-Footprints project).

Silicification in the Read Formation and MFb increases the resistivity. The low resistivity observed in MFc can be due to less intense early hydrothermal silicification or the increase in porosity caused by hydrothermal quartz dissolution. The low resistivity of MFd can be due to the absence of the silisification. The resistivity contrast between silicified and nonsilicified sandstone is significant (McGill et al., 1993; Mwenifumbo et al., 2007).

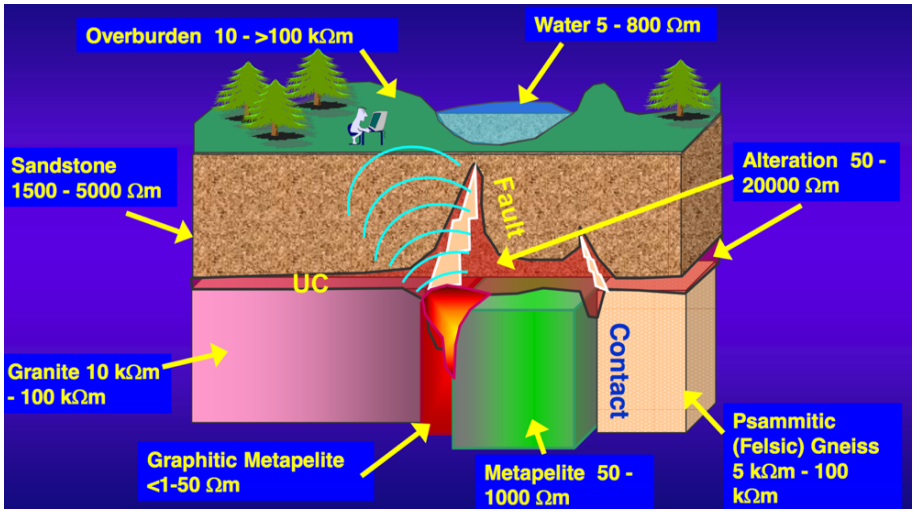

Figure 2.21: Resistivity model for the Athabasca Basin (adapted from CMIC-Footprints project).

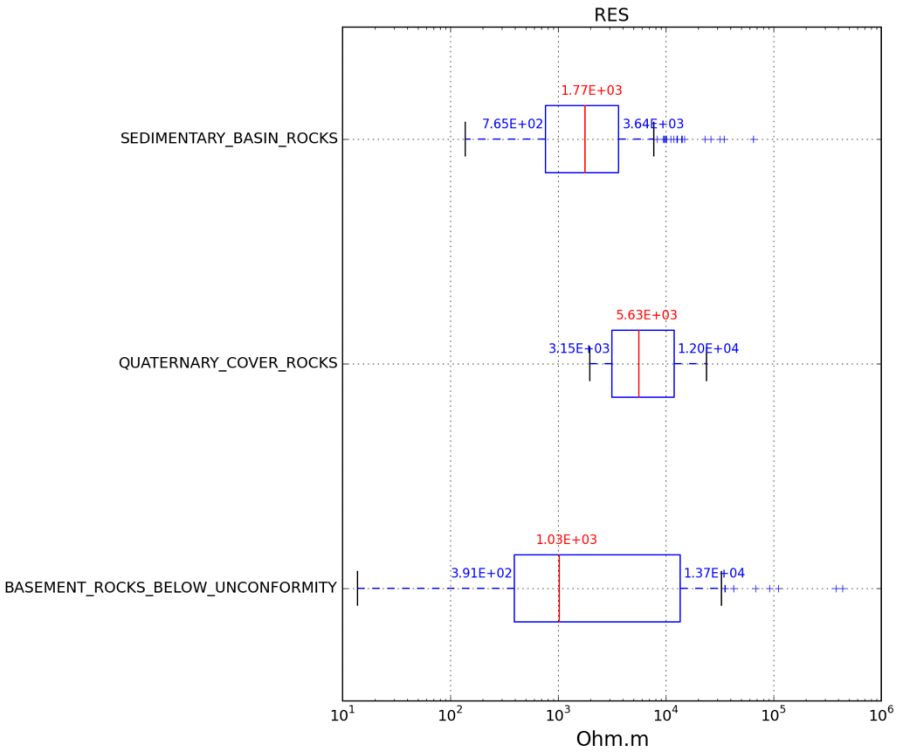

Figure 2.22: Resistivity estimations for the lithology groups of the McArthur-Millennium area (adapted from CMIC-Footprints project).

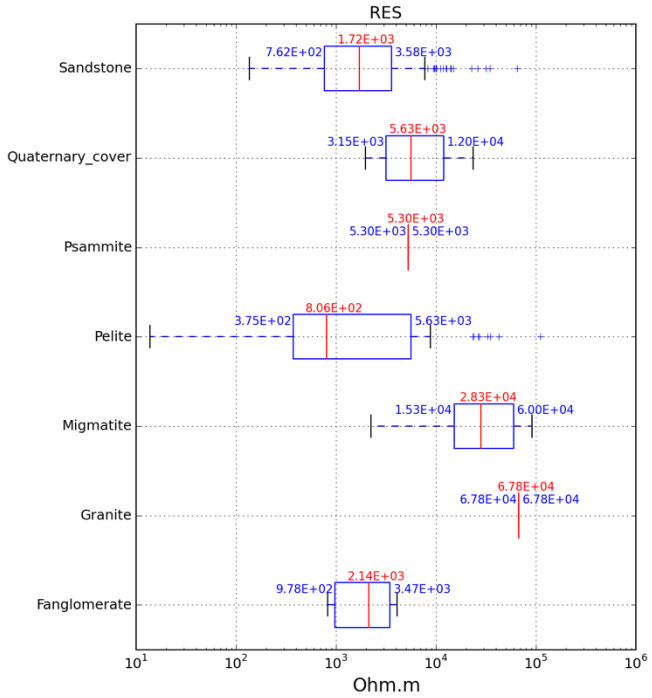

Figure 2.23: Resistivity estimations for the lithologies of the McArthur-Millennium area (adapted from CMIC-Footprints project).

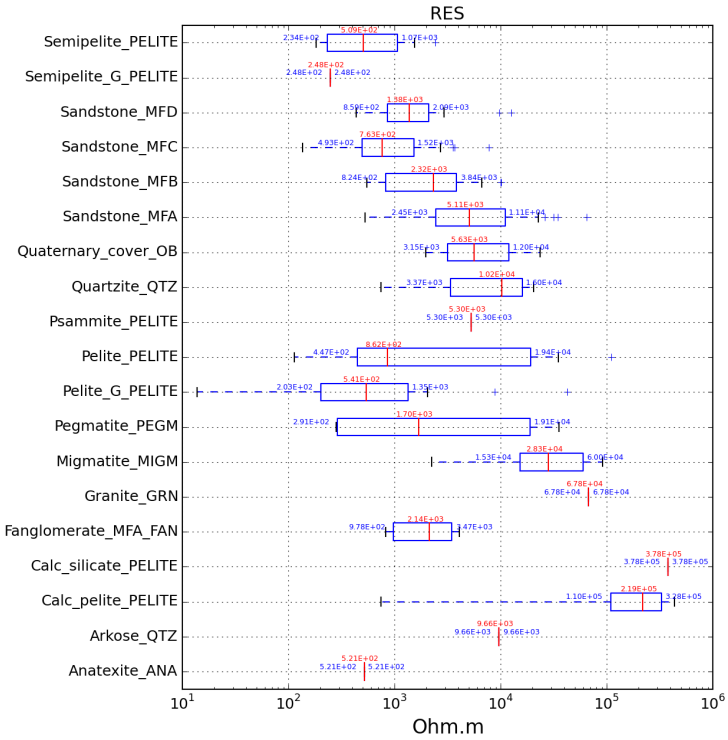

Figure 2.24: Resistivity estimations for the rock-type of the McArthur-Millennium area (adapted from CMIC-Footprints project).

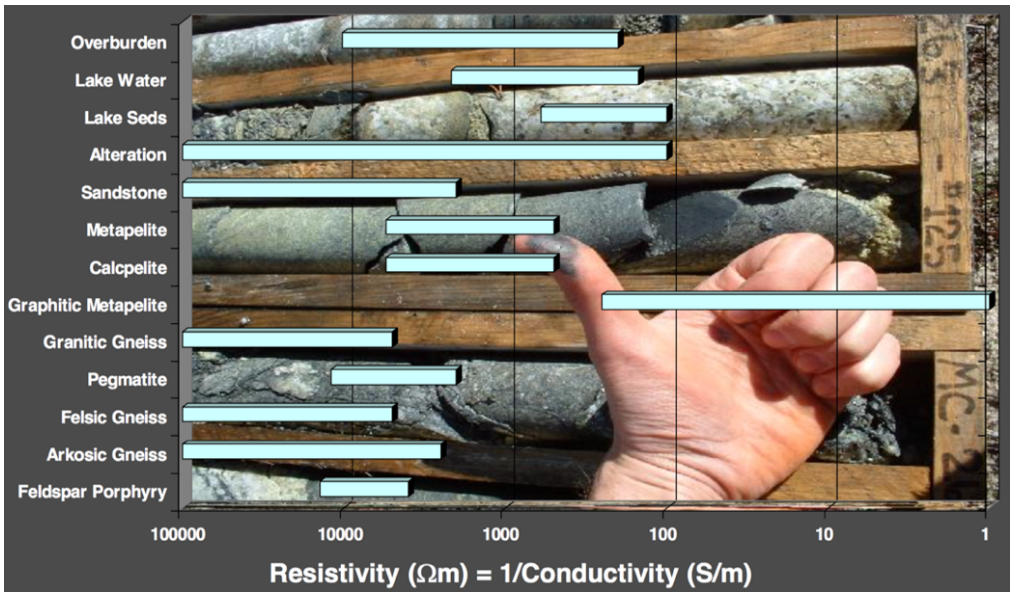

Figure 2.25: Resistivity estimations for the rocks of the Athabasca Basin (adapted from CMIC-Footprints project; U-site workshop 2014).

2.5.5 Geophysical logs

Borehole studies, including measurements of resistivity, density, P-wave velocity and porosity, are used in order to improve the lithological information as well as the physical properties of sandstone and basement rocks (Figure 2.26). They confirm the physical properties obtained from measurements on samples. Geophysical logs from MAC-218, shown in Figures 2.26, demonstrate a change in physical properties at a depth of 300m. Above 300m, the density, seismic velocity (p-wave), and resistivity are low (2.27 g/cc, 4800 m/s, and 2000ohm-m, respectively) and below 300 m they are high (2.48 g/cc, 5670 m/s, and 14000ohm-m, respectively). The increase in values is due to the decrease of porosity in the alteration (silicification) zone. The relatively high gamma-ray activity in MFb and MFa is mostly due to Th and the lesser amount of U (Mwenifumbo et al., 2007).

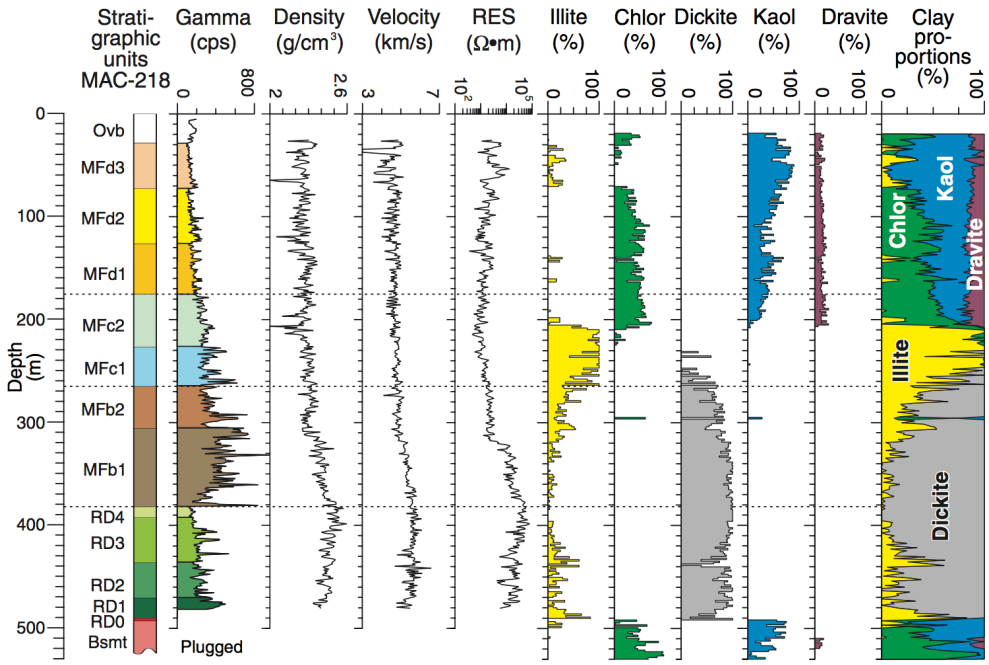

Figure 2.26: Borehole MAC-218 in eastern Athabasca near the McArthur River mine. Geophysical logs including gamma-ray, density, resistivity, seismic velocity and clay minerlogical results are shown while the P2 ore zone is located around 500 m (Chlor = chlorite; Kaol = kaolinite; RES = normal resistivity; stratigraphic codes in ascending order: RD = Read Formation; MFb, MFc, MFd = Bird, Collins, and Dunlop members of Manitou Falls Formation; Ovb = overburden; Mwenifumbo et al., 2007). Note that the clays % are proportion of the clays in the rock. They only make up a small proportion (a few %) of the sandstones.

2.6 Summary

In the eastern Athabasca Basin, most uranium deposits are located in the McArthur-Millennium region where graphitic faults intersect the unconformity between the sandstone and the basement at depth. Uranium deposits are mostly surrounded by alteration zones. Overburden (unconsolidated glacial deposits) which is located on the top of the sandstone comprises drumlin, hummocky moraine, esker complexes, and ground moraine.

Physical properties of the geological structures have a wide range of values which help to detect the approximate location of the uranium mineralization using geophysical methods. These physical properties (such as density, resistivity, magnetic susceptibility and seismic velocity) will be used later in the next chapters for synthetic modellings. Density and seismic velocity of the geological layers increase with increasing depth. There is no specific pattern for the resistivity and magnetic susceptibility of the rocks as they are variable. But, graphitic faults are conductive, and alteration zones can have different density and resistivity from the host rocks. For alteration zones, silicification and desilicification zones are more and less dense than the host rocks, respectively. Blocks in the basement have a better contrast for the resistivity and magnetic susceptibility than the density and seismic velocity. However, the contrast between overburden and sandstone for the resistivity and magnetic susceptibility can be less than the density and seismic velocity in some parts of the area.

Chapter 3

Geophysical Methods: Gravity, Magnetic, Seismic Refraction and Electromagnetic Methods

3.1 Introduction

Geophysical methods measure the response of Earth's features to the physical phenomena such as gravitational and magnetic forces and so on. Because of the differences in the physical properties of the Earth's features, variations in the responses can occur which can be measurable by geophysical instruments. These variations can be also calculated using the physical and mathematical equations. Geophysical methods used in this research, such as magnetic, gravity, seismic refraction and electromagnetic methods, are explained in detail in this chapter.

First, the gravity method will be discussed. Different reductions to the gravity data as well as the definition and the nature of free-air and Bouguer anomalies will be explained. For the magnetic method, in addition to the corrections and processing, the interpretation will be explained. Then, for the seismic refraction method, seismic surveys and the behaviour of the acoustic wave at the interfaces as well as interpretation methods will be discussed. Also, common problems in this method will be mentioned. For the

electromagnetic method, both frequency- and time-domain airborne cases will be considered. And, finally some examples of the previous geophysical studies will be shown.

3.2 Gravity method

The gravity method involves measuring the variation in the Earth's gravitational field due to the changes in the density of the subsurface rocks. The gravity method can be surveyed by either surface or air-borne. After applying the correction methods necessary to take into account all anticipated variations except sub-surface effects, gravity data is ready for interpretation. Forward modelling is one of the main methods for interpretation in which the data will be mathematically synthetized based on some physical or mathematical model with a given set of densities and geometries. The calculated data can be compared with the real data. For the two data sets to be similar (fit each other), the geometries and physical properties in the forward model are adjusted. This process can be done repeatedly to reconstruct a model similar to the real geological structure. Another main and common interpretation method is inversion in which an Earth model can be directly reconstructed from geophysical data.

3.2.1 Accuracy and spatial resolution of gravity method

The gravity field due to the density variation of local mass is very small in comparison with the background field of the Earth (often of the order of 1 part in 10^6 to 10^7; Telford et al, 1976). Gravity on the Earth's surface varies because of the rotation, ellipsoidal shape, internal mass distribution and irregular surface relief (Kearey et al., 2002). Equipotential surfaces (sea-level surface or geoid) are surfaces that connect points of equal gravitational

potantial. The elevation of the points on the land are determined with respect to the equipotential surfaces. The mean value of gravity on the Earth's surface is about 9.8 ms^{-2} (=980665mGal). The c.g.s. unit of gravity is the milligal (1 mgal = 10^{-3} gal = 10^{-3} cm s^{-2}), which is equivalent to 10 gu (gravity unit).

Since the contributions to the total gravity from density variations in the upper crust are very small, gravimeters need to be very sensitive. Gravimeters can measure one part in 100 million of the Earth's gravity field (980 gals or 980,000 milligals) in units of milligals (mGal) or microgals. Some ground measuring systems have a reading resolution of 0.001mGal (www.scintrexltd.com). Today, airborne systems are frequently used in the exploration as they are a fast method for data acquisition and they can measure both gravity and gravity gradiometry (see Appendix D) data. Airborne gravity gradiometers have a better spatial resolution and a higher accuracy than airborne gravimeters (LaFehr and Nabighian, 2012). Modern airborne systems can provide a spatial resolution of around 150 m with an accuracy of 0.1 mGal (www.cgg.com). The station spacing in a ground gravity survey can vary from a few metres in the case of small mineral or geotechnical surveys to several kilometres in regional reconnaissance surveys. A basic rule is to separate stations by no more than half the expected target burial depths. Since the Earth is not a perfect homogeneous sphere, gravity is not constant. Gravity's magnitude depends on the following parameters: latitude, elevation, topography of the surrounding terrain, Earth tides and density variations in the subsurface (Telford et al, 1976). Gravity exploration is based on the last of these parameters the effect of which is less than latitude and elevation effects. Therefore, the effects of these parameters should be removed from observed data to achieve data belonging to the density variations in the subsurface.

3.2.2 Gravity corrections

Before interpretation, one needs to correct for all variations in the Earth's gravitational field which do not result from the subsurface anomalies. This process is called gravity reduction or reduction to the geoid, as sea-level is mostly considered as the datum level (Kearey et al., 2002). The geoid surface, which is based on the mean sea-surface level, is irregular but smoother than the Earth's physical surface. Although the physical Earth has variation from +8,000 m to −418 m, the geoid's variation ranges from −106 to +85 m. For the corrections, the location of the gravimeter should be known precisely. Gravity corrections are as follows (Blakely, 1995):

Drift correction: The instrument's components can change slowly due to the fluctuations in temperature etc. This causes the measurement recorded by the gravimeter to change slowly as well. This problem can be solved by repeating the readings at a base station at recorded times during the day. Drift is assumed to be linear between repeated base readings. The drift correction, determined for each datum at the corresponding times, should be subtracted from the observed values (Blakely, 1995; Kearey et al., 2002; Figure 3.1).

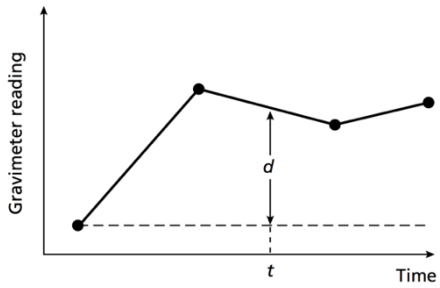

Figure 3.1: A gravimeter drift curve and a drift correction value (d) constructed from repeated readings at a fixed location (Kearey et al., 2002).

Latitude corrections (gf): The gravity decreases from pole to equator because of the centripetal acceleration generated by the Earth's rotation and the difference in equatorial

and polar radii which is about 21 km. The gravity value that would be observed if Earth was a perfect (no geologic or topographic complexities) rotating ellipsoid would be as follows (Blakely, 1995; Kearey et al., 2002):

$$gf = 978031.85\ (1.0 + 0.005278895\ sin^2(lat) + 0.000023462\ sin^4(lat)) \quad \text{mGal} \tag{3.1}$$

where *lat* is latitude [degrees]. For a small scale area, after applying the correction for the most northerly point, which is based on and relative to the absolute gravity in the base station, we can use the following linearized correction for subsequent points (Blakely, 1995):

$$\Delta gl = 0.000812\ sin(2\ lat) \quad \text{mGal/m (N-S)} \tag{3.2}$$

The correction is added to *g* as we move toward the equator.

Free-air correction (FAC): The free-air correction accounts for gravity variations caused by elevation differences in the observation locations (Blakely, 1995; Kearey et al., 2002; Figure 3.2a),

$$FAC = 0.3086\ h \quad \text{mGal} \tag{3.3}$$

where *h* is the elevation [metres] of each gravity station above the datum (typically sea level). The FAC is positive for an observation point above datum to correct for the decrease in gravity with elevation. In airborne surveys, *h* is the elevation of the observation point (height of the aircraft) above the datum.

Bouguer correction (BC): The Bouguer correction attempts to remove the gravitational

effect of the rock present between the observation point and datum by approximating the rock layer beneath the observation point by an infinite horizontal slab with a thickness equal to the elevation of the observation above datum (Blakely, 1995; Kearey et al., 2002; Figure 3.2b).

$$\mathrm{BC} = 2\pi G\rho h \approx 0.04192\,\rho h \quad \text{mGal} \tag{3.4}$$

where G is the Gravitational constant, ρ is the average density of the underlying rocks in g/cc (the usual value is 2.67 g/cc) and h is the elevation in metres. On land the Bouguer correction must be subtracted, and for sea surface observations must be added (to account for the lack of rock between sea surface and sea bed). For the sea water, the correction can be done by considering the replacement of the water layer (with a density of ρ_w=1.023g/cc) by a specified rock (with a usual density of ρ_s=2.67g/cc). Therefore, h is the water depth and $\rho = \rho_s - \rho_w$. In airborne surveys, h is the height (thickness) of the ground (directly beneath the observation) above the datum.

Terrain correction (TC): The Bouguer correction which is based on a horizontal slab is only an approximation as the topography has an effect on the gravity data as well. The terrain correction is based on the topographic effect in the vicinity of the gravity station. This correction is always positive in ground surveys regardless of whether the local topography consists of a mountain or a valley (Blakely, 1995; Kearey et al., 2002; Figure 3.2c). But, in airborne surveys the terrain correction is positive for heights above the surface height directly beneath the airborne measurement and vice versa (Hinze et al., 2013). In this research, a complete Bouguer correction based on the forward modelling with an

accurate representation of topography will be done (Chapter 5).

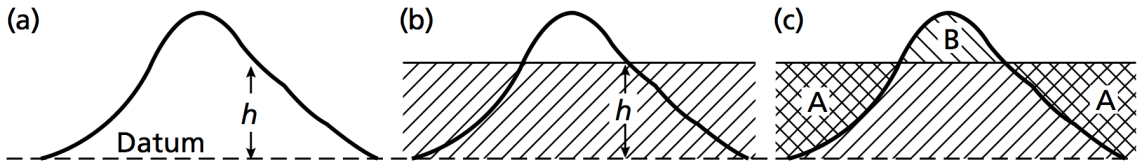

Figure 3.2: (a) The free-air correction (b) The Bouguer correction (c) The terrain correction (Kearey et al., 2002).

Tidal correction: Gravity in a fixed location changes with time because of the periodic variation in the gravitational effects of the Sun and Moon, and correction must be made for this variation which is predictable and quantifiable. The tidal effect never exceeds 0.3mGal (Blakely, 1995; Kearey et al., 2002).

Eötvös correction (EC): The Eötvös correction is applied to gravity data taken on a moving vehicle such as a ship or a plane. The motion of the vehicle generates a centrifugal acceleration associated with the movement of the vehicle over the Earth's surface and relative to the Earth's axis of rotation. Therefore, the readings are lower when the vehicle moves eastwards, and higher when it moves westward (Blakely, 1995; Kearey et al., 2002).

$$EC = 7.503\, V \sin(a) \cos(f) + 0.004154\, V^2 \quad \text{mGal} \tag{3.5}$$

where V is the speed of the vehicle in knots, a is the heading and f is the latitude of the observation.

3.2.3 Gravity anomalies

The definition of gravity free-air (FAA) and Bouguer (BA) anomalies are defined below:

Free-air and Bouguer anomalies: The free-air anomaly (FAA) and Bouguer anomaly (BA) are defined by (Kearey et al., 2002):

$$FAA=gobs-gf+FAC(\pm EC) \tag{3.6}$$

$$BA=gobs-gf+FAC\pm BC+TC(\pm EC) \tag{3.7}$$

The interpretation of gravity data on land is mostly based on the Bouguer anomaly. In marine surveys, the Bouguer anomaly is not appropriate for deeper water surveys but can be calculated for inshore and shallow water areas. Thus, the free-air anomaly is frequently used for interpretation in deep water surveys.

In general, the observed gravity is composed of various components as follows (Blakley, 1995):

observed gravity = [attraction of the reference ellipsoid]
+ [effect of elevation above sea level (free-air)]
+ [effect of "normal" mass above sea level (Bouguer and terrain)]
+ [time-dependent variations (tidal)]
+ [effect of moving platform (Eötvös)]
+ [effect of masses that support topographic loads (isostatic)]
+ [effect of crust and upper mantle density variations ("geology")].

Blakely (1995) illustrated the various contributions to observed gravity in Figures 3.3 to 3.7. Figure 3.3 shows the variations in density in a cross section as well as the gravity data along a west-east profile which is observed at the topographic surface. The crust and mantle have densities of 2.67 and 3.07 g/cc, respectively. The mountain is isostatically compensated by a crustal root. The aim is to isolate the square-shaped anomaly with a high density of 2.97 g/cc in the upper crust.

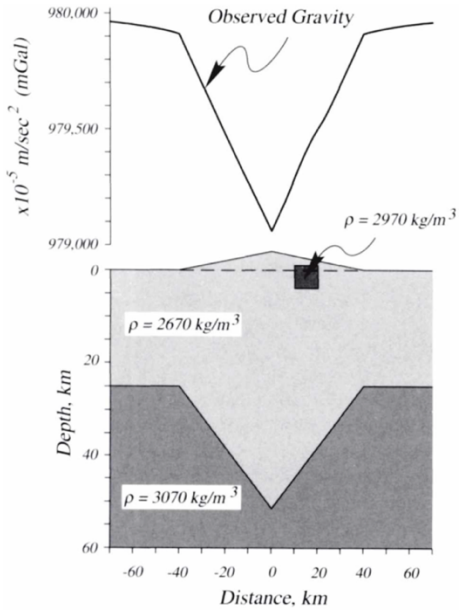

Figure 3.3: Crustal cross section and observed gravity (vertical exaggeration 2; Blakely, 1995).

Theoretical gravity, which is the normal gravitational attraction of a mathematical model representing a physically homogeneous-smoothed Earth (Earth ellipsoid), can be theoretically calculated and then subtracted from gravity data. The remainder represents departures of the Earth's density from the homogeneous ellipsoid which includes the effects of altitude, tides, and various other factors. In this example, 0 m elevation is considered as the datum (reference ellipsoid), and a density of 2.67 g/cc is considered for the homogeneous-smoothed Earth (Figure 3.4; Blakley, 1995).

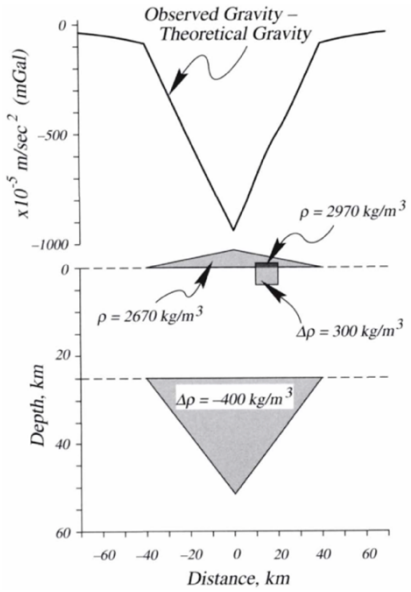

Figure 3.4: Crustal cross section and gravity data after subtraction the theoretical gravity (Blakely, 1995).

Tidal and Eötvös corrections need to be applied as well. The large negative anomaly in Figure 3.4 is due to the changes (increasing) in distance between the elevation of gravity meter and the center of the Earth (reference ellipsoid) as the profile rises over the topographic edifice. This large negative anomaly can be eliminated by the free-air correction (Figure 3.5; Blakely, 1995). It can be seen that the free-air correction has not accounted for the additional mass represented by the topographic edifice as well as the crustal root (which produces a long-wavelength, relatively low-amplitude, negative component in the free-air anomaly). But, the free-air correction adjusts measured gravity to what would have been measured at a reference (ellipsoid) level. This reference level is commonly taken as the mean sea level. Note that the concept of the free-air correction as 'moving' the observation location to the reference level is correct only if there is no other effect such as the contribution due to a crustal density anomaly. For this case, it is important to not move the observation location but keep it where it is, so that the contribution from the density anomaly can be correctly evaluated.

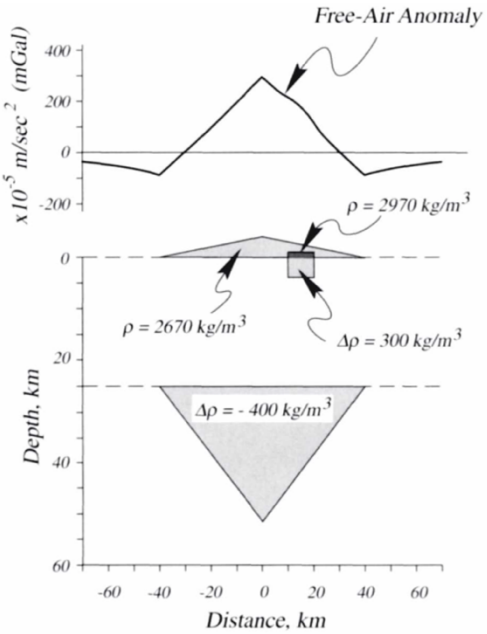

Figure 3.5: Crustal cross section and gravity data after the free-air correction (Blakely, 1995).

The gravity signature of the additional mass that exists between the level of observation and datum (here sea level) can be removed from the data using the Bouguer correction. Here, the additional mass has a density of 2.67 g/cc (Figure 3.5). In addition to the Bouguer correction, the terrain correction is essential in order to remove the effect of the topography on the data. In Figure 3.6, the dashed line shows the data after Bouguer correction, and the solid line shows the data after both Bouguer and terrain corrections (Blakely, 1995).

Although the Bouguer correction has accounted for the direct effects of the topographic edifice, it has not accounted for the low-density root that isostatically supports the topography. The extra mass of large topographic features is generally compensated at depth by mass deficiencies (Figure 3.6), whereas large topographic depressions are matched at depth by mass excesses. This is called isostatic compensation. This can be removed from gravity data using a digital terrain model, in which first we need to calculate the shape of

the crust-mantle interface consistent with the Airy model for isostatic compensation, and second calculate at each observation point the gravitational effect of the volume (Blakely, 1995).

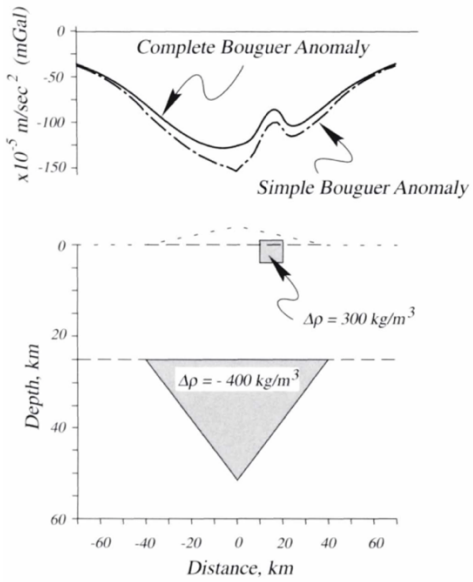

Figure 3.6: Crustal cross section and gravity data after the Bouguer correction (dashed line) and both Bouguer and terrain corrections (solid line; Blakely, 1995).

According to the Airy's hypothesis of isotacy, the mountain range can be thought of as a block of lithosphere (crust) floating in the asthenosphere (mantle). Mountains have roots, while ocean basins have anti-roots (Figure 3.7). The depth below sea level of the compensating root (d_m) can be calculated by (Blakely, 1995):

$$d_m = h\frac{\rho_t}{\rho_m - \rho_c} + d_s \tag{3.8}$$

where ρ_c is crustal density, ρ_m is mantle density, ρ_t is the average density of rocks that make up the terrain, d_s is the depth of compensation at shorelines, and h is elevation of the observation point above sea level. Isostatic residual anomaly can be obtained by subtraction the isostatic regional anomaly from the data (Figure 3.8). The isostatic regional is negative

over continents and positive over oceans (Blakely, 1995).

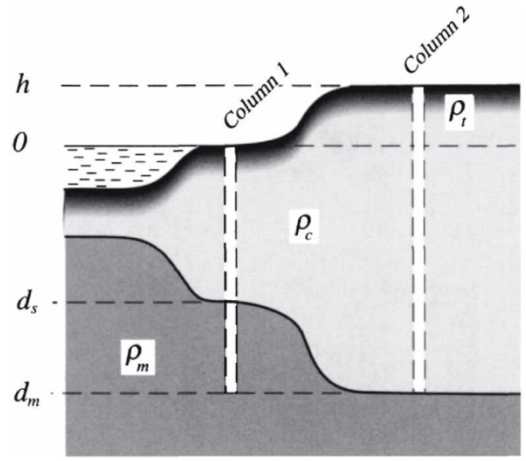

Figure 3.7: Airy model of isostatic compensation (Blakely, 1995).

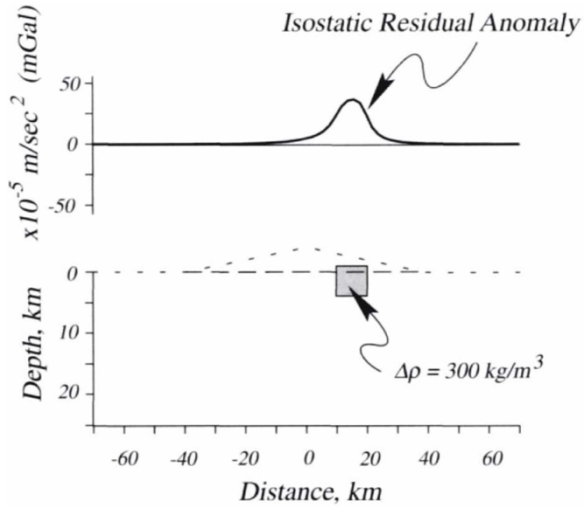

Figure 3.8: Isostatic residual gravity profile over crustal cross section (Blakely, 1995).

Residual anomalies: Bouguer anomaly fields (shorter wavelength) are often affected and covered by regional anomaly fields (longer wavelength; Figure 3.9). The removal of the regional field, to isolate the residual anomalies, is performed by analytical methods such as trend surface analysis and low-pass filtering. Upward continuation is employed in gravity interpretation to determine the form of regional gravity variation over a survey area, since the regional field is assumed to originate from deep structures (Kearey et al., 2002).

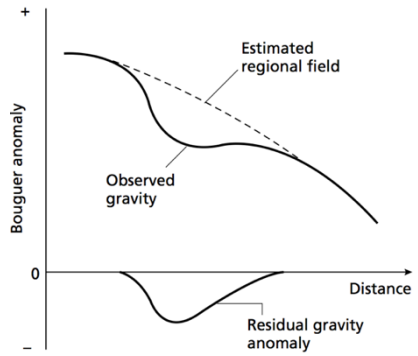

Figure 3.9: Regional and residual gravity anomalies from the observed Bouguer anomaly (Kearey et al., 2002).

3.2.4 Filtering and spectral analysis of gravity data

Since there is a relationship between the wavenumbers/wavelengths of a gravity anomaly and the size, shape, and depth of the causative body, Fourier-transform techniques (such as frequency filtering and spectral analysis) can be used for interpreting gravity data. We can apply filters to enhance some anomaly characteristics at the expense of others. I tested some of these filters such as the low-pass, high-pass, band-pass and the vertical derivative as well as spectral analysis such as 2D power spectrum and radially averaged power spectrum on both synthetic and real data (see Appendix F) but they did not work well enough for the overburden stripping as the wavelength of the overburden signature has a wide range similar to the alteration signature. Note that these methods can be achieved by using the Fourier-transform methodology in which the data must be transformed from the space domain to the wavenumber domain. The low-pass and high-pass filters are designed to reduce the high-wavenumber and the low-wavenumber portions of the spectrum, respectively. Although the vertical derivative is not an anomaly-separation technique, it is used to find the location of possible geologic targets of interest. Spectral analysis can separate sources and represent the depth to the source in the wavenumber domain (under

certain assumptions and simplifications; see Appendix F for more details).

3.3 Magnetic method

The magnetic method investigates subsurface features based on their magnetic properties. Although most rocks are non-magnetic, a few types contain sufficient magnetic minerals that they can contribute to the measureable magnetic field. When a magnetic rock is placed in the Earth's magnetic field, it generates an induced magnetic field with these variations being considered as a magnetic anomaly. The possibility of remanent magnetization can also contribute to a magnetic anomaly. Magnetic surveying is common, and an initial method in many exploration situations. In exploration applications, the magnetic field is surveyed by surface, airborne, marine and borehole measurements.

3.3.1 Magnetization and geomagnetic field

The SI unit of magnetic field strength (in the geomagnetic exploration field) is *tesla* (T). *nanotesla,* (nT) is used commonly in exploration. 1nT is numerically equivalent to 1 *gamma* (*g*) in c.g.s. units. Also, 1nT is equivalent to 10^{-5} *gauss* (*G*). In a vacuum, the magnetic field strength *B* and magnetizing field *H* (with unit *A* m^{-1}) inside a material are related by $B = \mu_0 H$ as

$$B = \mu_0 H + \mu_0 kH = (1 + k)\mu_0 H \tag{3.9}$$

where k is the magnetic susceptibility of the material indicating the response of the materials to an applied field. Susceptibility is dimensionless in the SI and c.g.s. systems (SI susceptibility value = $4\pi \times$ c.g.s susceptibility value). The magnetic induction *B* is the total

field including the effect of magnetization. Susceptibility is useful for induced magnetization when magnetization is proportional to the applied field (Blakely, 1995). Earth's materials have a wide a range of magnetic susceptibility. Section 2.5.3 shows the range of susceptibilities for the Athabasca Basin.

The geomagnetic field mostly originates from the Earth's core. It is believed that the flow of liquid iron in the outer core, resulting from the Earth's spin, generates electric currents, which in turn produce magnetic fields. Charged metals passing through these fields go on to create electric currents of their own, and so the cycle continues. This self-sustaining loop is known as the geodynamo (Fowler, 2005).

Declination (*D*) is the angle on the horizontal plane between magnetic north and true north), inclination (*I*) is the angle at which the magnetic field lines intersect the Earth's surface) and the magnitude of the total field vector (*B*) are used to represent the magnetic field (Figure 3.10). The magnetic intensity of the Earth's magnetic field varies with latitude from around 25,000 nT at the magnetic equator to 70,000 nT at the magnetic poles (Kearey et al., 2002). Also, due to fields with an external origin, the geomagnetic field varies on a daily basis to produce diurnal variations (less than 50 nT).

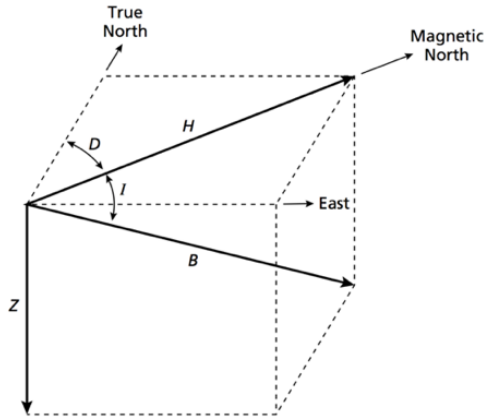

Figure 3.10: Geomagnetic elements (Kearey et al., 2002).

3.3.2 Magnetic corrections, processing and interpretation

The International Geomagnetic Reference Field (IGRF) is a standard mathematical description of the Earth's main magnetic field and its secular variation. Subtracting the IGRF value from the observed data, which is called "geomagnetic correction", removes the large fields believed to be associated with currents in the outer core. In magnetic processing, removing the effects of diurnal variation from the observed data is called "diurnal variation correction". Some days the amplitude of diurnal variations is not regular, up to 1000nT, which are known as magnetic storms. Magnetic surveying should be discontinued during such days. After applying diurnal and geomagnetic corrections, the remaining magnetic field variations, called residual data or magnetic anomaly are caused by regional, remanent and anomaly variations. Regional variations can be removed from data, and remanent variation mostly has a small value and could be ignored as they are not typically as common as induced magnetization. Anomaly variations are referred to as magnetic anomalies (Telford et al., 1976; Kearey et al., 2002),

$$F = F_{IGRF} + F_{Anomaly} + F_{Remanent} + F_{Regional} \tag{3.10}$$

There are many methods for the processing of magnetic data. Two of them which are used in this thesis are "upward and downward continuations". They are used to emphasize the effects of deep or shallow structures (Telford et al., 1976; Reid et al. 1990).

The interpretation of magnetic data is similar to that of gravity data. But, there are a few differences between them. Although, the gravity anomaly of a body is positive or negative

(depending on more or less dense in comparison with its surroundings), the magnetic anomaly of a body contains generally both positive and negative elements which arise from the dipolar nature of magnetism (Figure 3.11). Also, the different direction of magnetization in bodies with identical shape can cause different magnetic anomalies. Nowadays, inversion is considered as the main method for the interpretation of magnetic data.

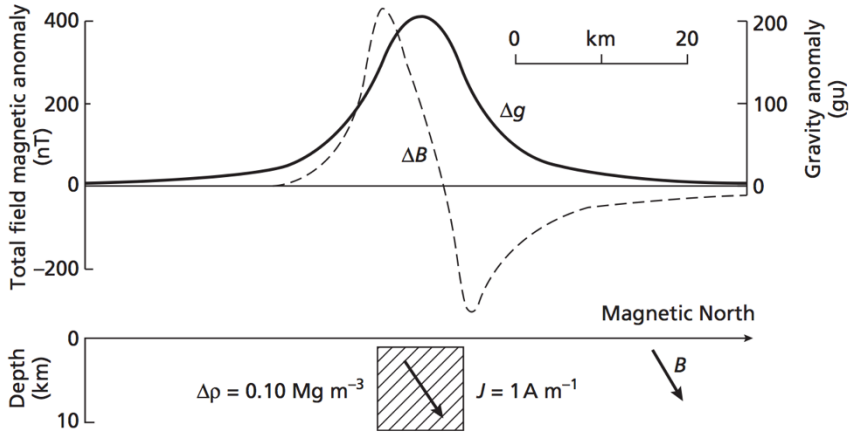

Figure 3.11: Gravity *(*Δ*g*) and magnetic *(*Δ*B*) anomalies over the same two-dimensional body. The positive and negative values in the magnetic data are due to the dipolar nature of magnetism (Kearey et al., 2002).

3.4 Seismic refraction method

Seismic methods are based on the laws of elastic wave propagation in the ground. Using the travel times between the source and the receiver, we can determine the depth of different geological boundaries and the elastic properties of rocks based on the difference in the seismic velocity and acoustic impedance of structures and materials. Seismic exploration is divided into refraction and reflection surveys (Telford et al. 1976; Sjörgen, 1984; Reynolds, 1997). The seismic refraction method is based on the measurement of the travel

time of refracted waves. One of the main applications of seismic refraction is for determining depth to bedrock. Seismic waves refract/bend by velocity gradient and velocity contrast across interfaces. Since velocity generally increases with depth, seismic energy is refracted back to the surface eventually. This can tell us about vertical and lateral variation in velocity, particularly sub-horizontal interfaces where the lower layer has a higher velocity like the base of the overburden (Figure 3.12; Redpath, 1973; Okwueze; 1988; Lankston, 1990).

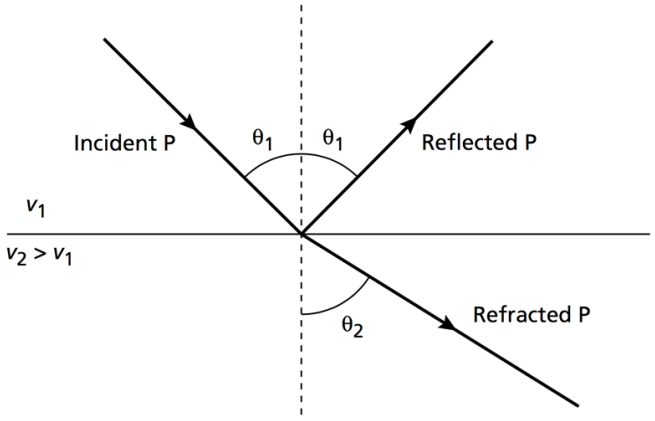

Figure 3.12: Reflected and refracted P-wave rays at an interface between two layers of differing seismic velocity (Kearey et al., 2002).

There are two groups of seismic waves, “body waves” (P and S) and “surface waves” (Love and Rayleigh). Due to the type of the source as well as the surface wave effect, body waves can have a higher frequency and velocity than surface waves. The P (or compressional) wave is mostly used for seismic exploration which is the fastest and moves particles in the direction of wave propagation (Cerveny and Ravindra, 1971; Kearey et al., 2002). In the seismic method, “Seismic rays” are everywhere perpendicular to wavefronts. Seismic energy returns to the surface by the “head wave” (Figure 3.13). In the refraction method, the critically refracted ray travels along the interface at the higher velocity v_2

(underlying layer). The wave propagation is based on Huygen's principle. The critical angle (θ_c) is defined as the angle of the incident ray when the angle of refraction is 90°.

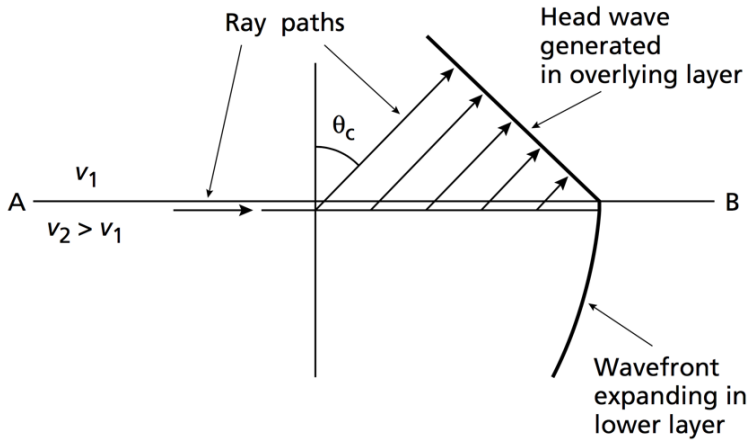

Figure 3.13: Generation of a head wave (Kearey et al., 2002).

3.4.1 Practicalities of seismic refraction surveying

Seismic sources can be categorized into two main groups, explosive sources and non-explosive sources. Vibroseis, shotguns, rifles, weight drops and hammers are a few examples of non-explosive land sources. Weight drops range from dropping a weight of several tonnes to a sledgehammer. They can be fast and efficient especially for defining the base of the overburden using the seismic refraction method. Geophones are devices to detect seismic motions on land. Vertical movements of P-waves and horizontal movement of S-waves can be detected (Telford et al. 1976; Sheriff and Geldart, 1995; Reynolds, 1997; Kearey et al., 2002).

Seismic refraction is generally applicable only where the seismic velocities of layers increase with depth. It can be applied in a wide range from engineering site investigation surveys (Redpath, 1973; Lim and Jones, 1989) to the study of the structure of the crust or

the lithosphere (Bamford et al., 1978; Stoffa and Buhl, 1979; Wright et al., 1990). Refraction profiles should be about five times bigger than the depth of investigation (Telford et al. 1976; Kearey et al., 2002). In order to better understand the seismic refraction method especially for determining the base of the overburden, consider a simple geological section as shown in Figure 3.14c ($v_2 > v_1$). There are three types of ray paths. The direct ray which travels through the top layer (v_1) from the source to the receiver along a straight line. The reflected ray, travelling at the speed of the top layer (v_1), is reflected at the interface and travels back through the top layer to the detector. The refracted ray goes down to the interface at the critical angle and velocity v_1, moves along the interface at the higher velocity v_2, and back up through the upper layer via the headwave at v_1.

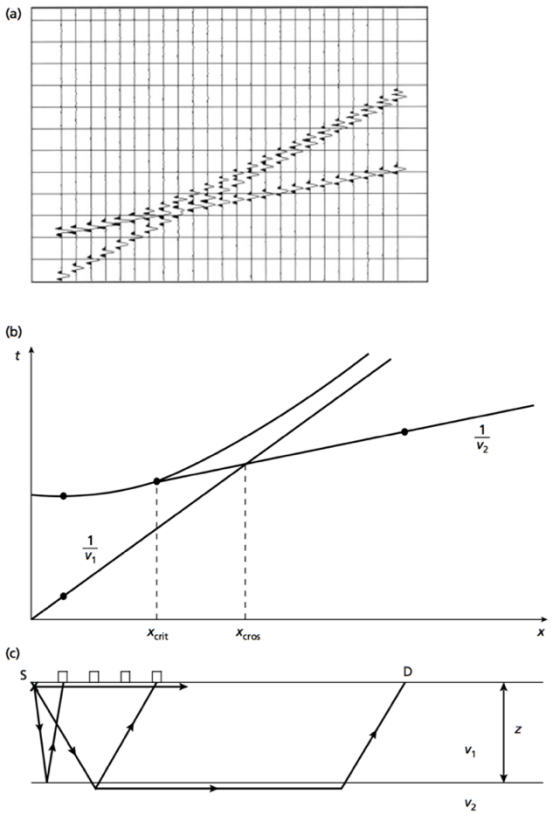

Figure 3.14: Top: Seismogram of traces along the Earth's surface as a function of time. Middle: Travel-time curves for direct, reflected and refracted rays. Bottom: Direct, reflected and refracted ray paths from a source to a receiver (Kearey et al., 2002).

According to Figure 3.14b&a, before the crossover distance x_{cros}, the first arrival is a direct ray. Beyond this offset distance the first arrival is always a refracted ray. At the critical distance x_{crit}, the travel times of reflected rays and refracted rays coincide. The reflection from an interface at angles near the critical angle often leads to strong wide-angle reflections. These wide-angle reflections can be used for indicating the presence of a low-velocity layer which would not be revealed by refracted arrivals alone.

Figure 3.15 illustrates progressive positions of the wavefront for the first-arrival as well as the direct and refracted ray paths for a two-layer case with horizontal interface. The travel-time equation for the refracted wave is given by:

$$t = \frac{x}{v_2} + \frac{2z(v_2^2+v_1^2)^{1/2}}{v_1 v_2} = \frac{x}{v_2} + t_i \tag{3.11}$$

where t_i is the intercept on the time axis of a travel-time plot and the straight line has a slope of $1/v_2$ (Figure 3.16). v_1 and v_2 can be obtained from the reciprocal of the gradient of travel-time plots, and the depth, z, can be determined from the intercept time t_i.

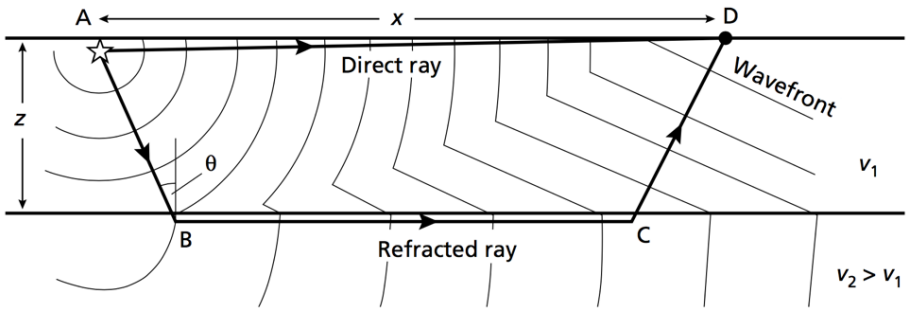

Figure 3.15: Positions of the wavefronts for direct and refracted waves and the headwaves (Kearey et al., 2002).

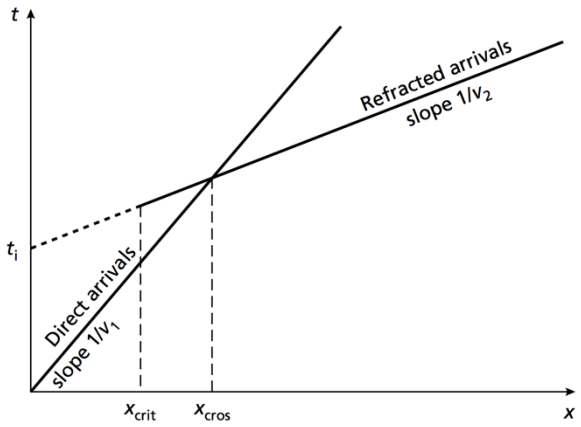

Figure 3.16: Travel-time curves for the direct and refracted waves from a two-layer model (Kearey et al., 2002).

3.4.2 Interpretation of seismic refraction data

In the refraction method, hidden layers produce head waves but no first arrivals may result (Figure 3.17a) as a consequence of the thinness of the layer, or from the closeness of its velocity to the overlying layer. A blind layer results from a low-velocity layer (Figure 3.17b; for example, a peat layer in muds and sands above bedrock) in which rays cannot be critically refracted. This leads to an overestimation of the depth to underlying interfaces (Domzalski, 1959; Kearey et al., 2002).

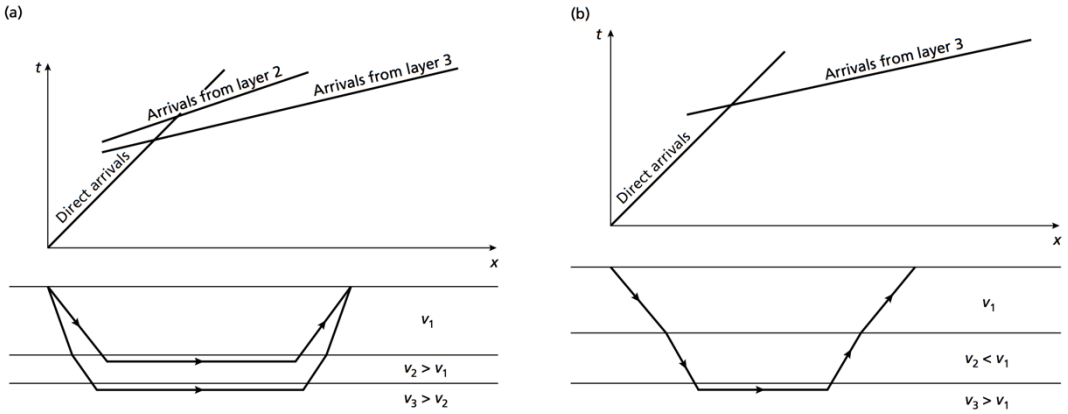

Figure 3.17: Left: hidden layer. Right: blind layer (Kearey et al., 2002).

Figure 3.18 shows the traveltime–distance graphs for a few models. The data in Figure 3.18 illustrate two points: 1- "Parallelism" in which travel time graphs from the same interface, recorded in the same direction with different source locations, are parallel, meaning if the branches are not parallel, then the two arrivals at the relevant detectors did not come from the same layer; 2- "Reciprocal time (T_{Recip})" in which the time to travel between two points is the same regardless of the direction of travel of the waves. Surface topography, subsurface irregularities, and inhomogeneties within layers have effects on the traveltime-distance curve (Figure 3.19; Hauck and Kneisel, 2008).

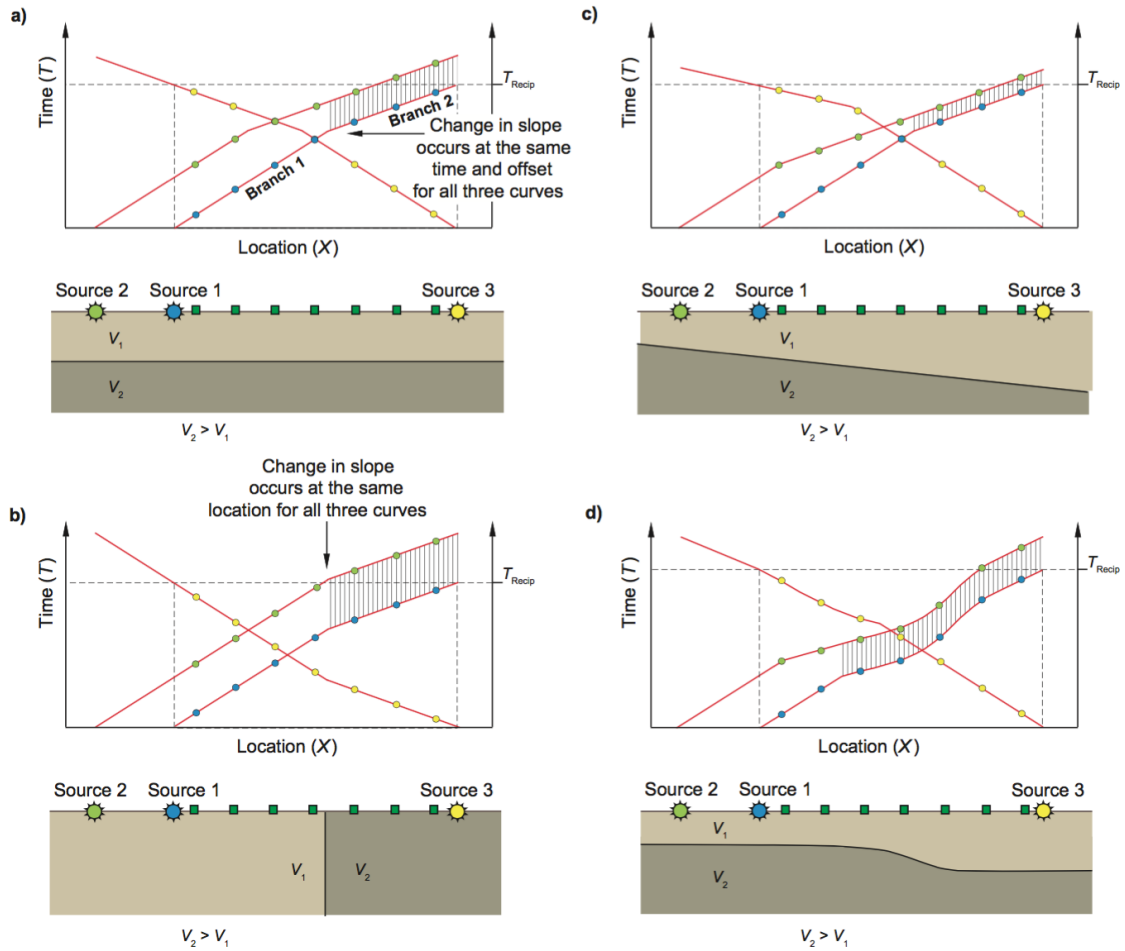

Figure 3.18: Time–distance (T–X) graphs produced by various subsurface velocity distributions. The vertical hatching indicates the locations where the T–X graphs for sources 1 and 2 are parallel. T_{Recip}: reciprocal time (modified after Reynolds, 1997).

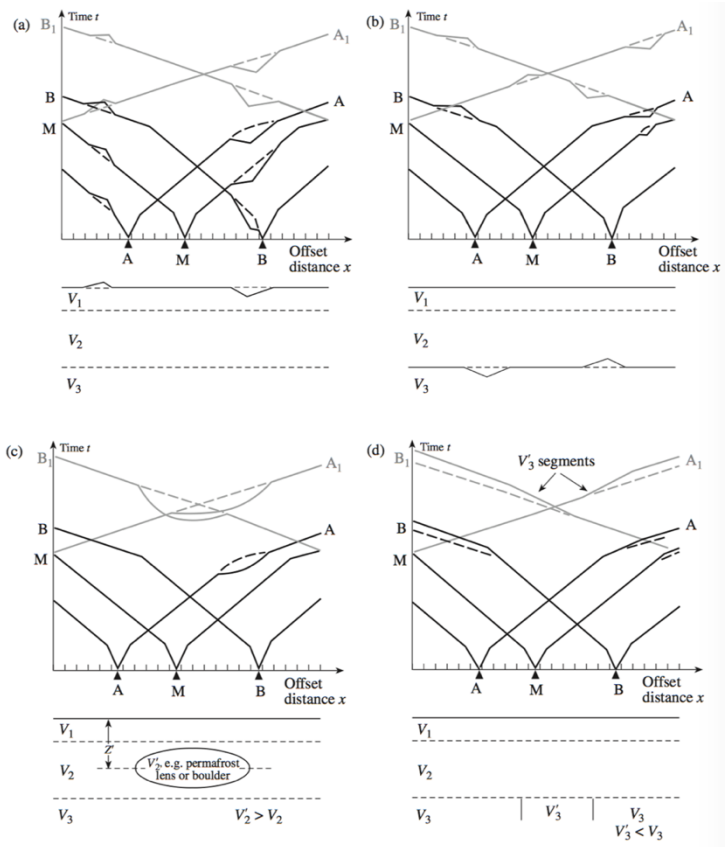

Figure 3.19: Examples of traveltime anomalies and their causes: the effect of the topography of Earth-air interface (a), the effect of the topography of refractor (b), the effect of a high-velocity mass within a layer (c) and the effect of the vertical low-velocity block in lower layers (d). Solid lines indicate traveltimes and dashed lines indicate regular traveltimes (Hauck and Kneisel, 2008).

There are several methods to determine subsurface structure from travel times such as (conventional) the reciprocal method (CRM) (or plus–minus method) and the generalized reciprocal method (GRM; Palmer, 1980; Palmer, 1981). Nowadays, inversion can be considered as one of the main approaches for interpretation (Zhang and Toksoz, 1998; Lelièvre et al., 2012).

3.5 Electromagnetic method

Electromagnetic (EM) geophysical methods can detect conductive structures in the ground. In the controlled source EM (CSEM) method, sources and receivers are loops of wires. The CSEM method can be categorized into those with frequency-domain (FDEM) and time-domain (TDEM) electromagnetic methods. They can also be categorized by the nature of their sources (bipoles, small loops, large loops) and receivers (small and large coils, magnetometers, etc). They can also be classified by the manner in which the sources and receivers are carried, airborne, marine, ground, borehole (Swift, 1988).

3.5.1 Frequency-domain EM (FDEM)

In FDEM, a time-varying electric current flows through a transmitter coil (Figure 3.20). This current is varying sinusoidally with time at a particular frequency or set of frequencies (i.e., a very particular variation with time that's characteristic of the FDEM method). The current in the transmitter coil generates a magnetic field which penetrates the Earth. Time variations of the primary magnetic field induce an electromotive force (emf) within the ground. The emf generates eddy currents in any conductor within the Earth, which then generate a secondary magnetic field. The sum of the primary and secondary fields in the receiver can have a phase and amplitude that is different from the primary field. The secondary magnetic field due to the eddy currents in the ground comprises components both in-phase and out-of-phase with the primary magnetic field because of the conductivity distribution in the subsurface.

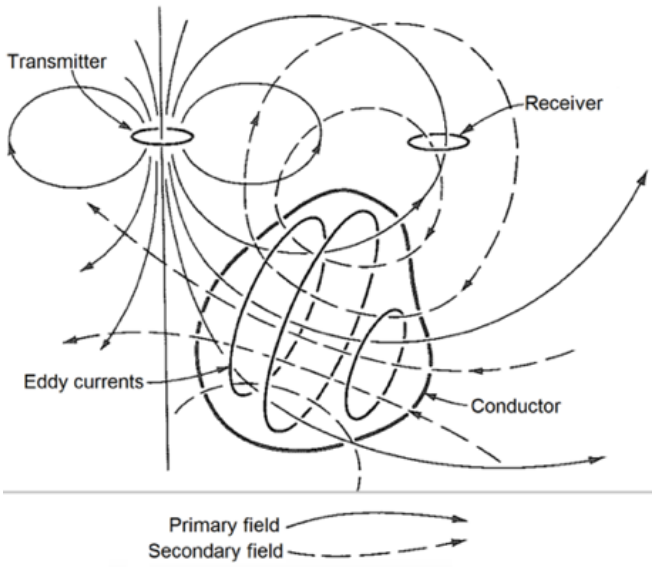

Figure 3.20: General principle of FDEM method (Grant and West, 1965).

In this research for FDEM, a helicopter-borne method (DIGHEM; Fraser, 1986; Cain, 2000) is applied for overburden stripping (Figure 3.21). There is no real DIGHEM data-set available in the uranium project, but the method will nevertheless be investigated as a possible means for overburden stripping (see Appendix E for the real DIGHEM data from the Canadian Malartic project). DIGHEM typically uses five frequencies from 880 Hz to 55840 Hz with two coil configurations: coaxial (horizontal dipole; 5848 Hz and 1082 Hz) coil pairs and coplanar (vertical dipole; 880 Hz, 7213 Hz and 55840 Hz) coil pairs (Figure 3.22). Coil separation (between receiver and transmitter) is 8 m except for 55840 Hz which is 6.3 m. Receiver and transmitter coils have a diameter of about half a metre. DIGHEM is suited to mapping the top 150 m or so of the subsurface which makes it a good method for overburden stripping (Holladay and Lo, 1997; Hodges, 1999).

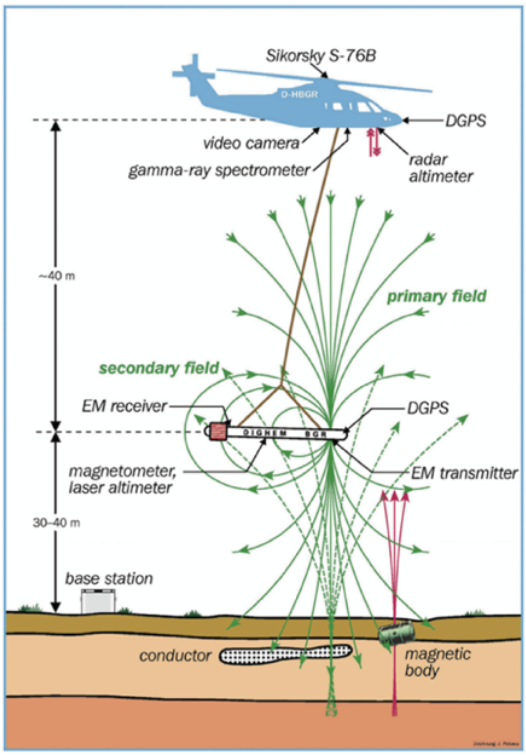

Figure 3.21: DIGHEM helicopter-borne geophysical system (from BGR website).

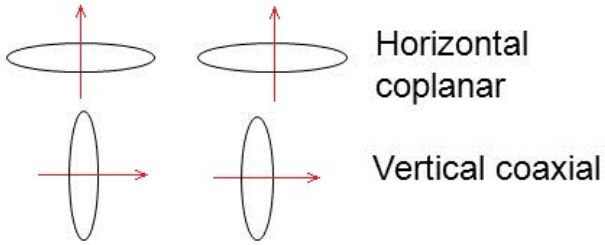

Figure 3.22: Loop configurations for DIGHEM.

3.5.2 Time-domain EM (TDEM)

Smaller secondary fields can be measured if the transmitters are larger (i.e. bigger loop) and carry more current and hence have a larger transmitter moment and deeper penetration into the subsurface. This can be done by the time-domain electromagnetic surveying (TDEM) method (sometimes called pulsed or transient-field EM; Figure 3.23) which measures the secondary field in the off time that allows for measuring much smaller

secondary fields. The investigation depth for TDEM is more than for FDEM. In this method the primary field is not continuous but is a series of pulses which are separated by off-time intervals. During these intervals, when the primary field is absent, the small secondary field is generally measured. The eddy currents decay in the subsurface conductor during these intervals. Measurement of the amplitude and the rate of decay of the eddy currents can provide the information on the location and conductivity of anomalies. The observations can be values of voltage (i.e., dB/dt) or magnetic field (Nabighian and Macnae, 1991).

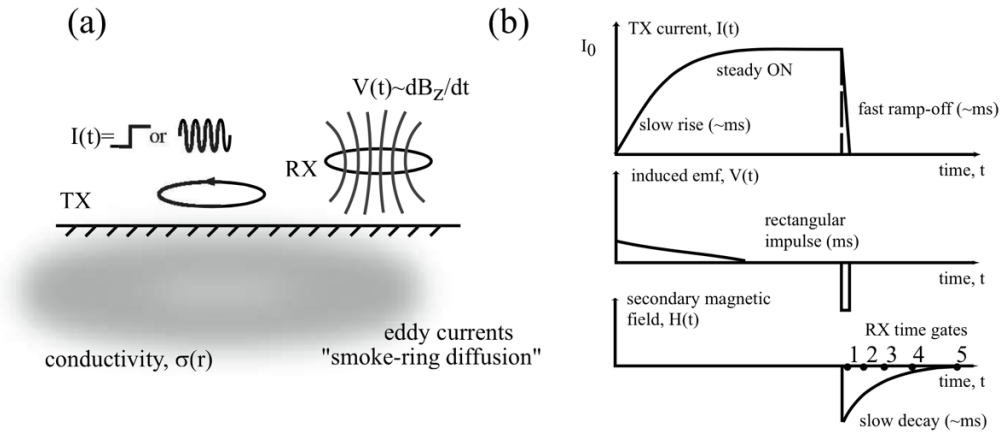

Figure 3.23: General principle of TDEM method (Everett and Meju, 2005).

In this research, for TDEM a helicopter-borne method (VTEM) is considered (Figure 3.24; Witherly et al., 2004; Witherly and Irvine, 2006). The standard VTEM system has a 13 m radius (vertical axis) with a 4 turn transmitter coil which can produce over 500,000 Am^2 of dipole-moment. The recent high power VTEM™35 system has a 17.5 m radius loop and 1,000,000 Am^2 dipole-moment that has increased the depth penetration (adapted from geotech.ca). The VTEM system measures a voltage that is proportional to the time derivative of the vertical magnetic field (dBz⁄dt) in 44 off-time channels.

Early time TDEM data can be suitable for shallow investigations in addition to the use of late time for deeper exploration (Legault et al., 2011). Early-time measurements in VTEM (early-channel closer to the transmitter current turn-off) from 20μs after the current turn-off (versus ~100μs for standard VTEM) led to improvements in the investigation of shallow structures. Thus, early-time VTEM could be a method for overburden stripping if there is a good conductivity contrast.

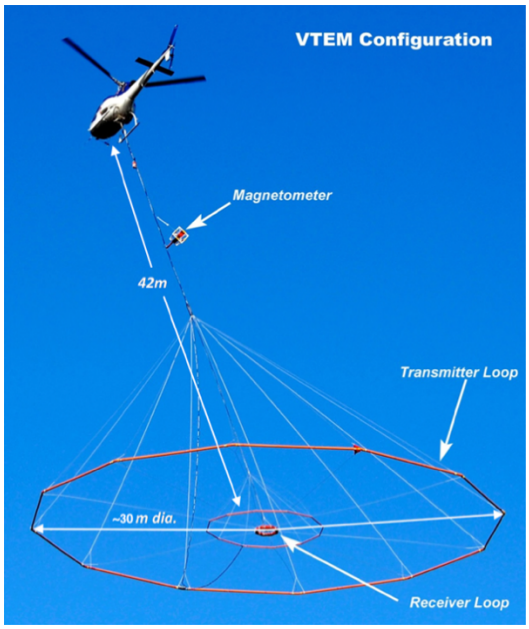

Figure 3.24: System for VTEM method (Geotech Ltd., 2013).

3.5.3 Resolution and sensitivity of airborne EM methods

In the EM method, increasing the frequency range increases the range of resistivities that can be distinguished. Since FDEM systems are broad-banded with a frequency range from ~300 Hz to ~150 kHz, their sensitivity can cover a range of magnitude in resistivity between 0.1 and 50,000 Ohm-m (Hodges, 2013; Legault, 2015). Some modern FDEM ground surveying tools are extremely sensitive and accurate, capable of detecting variations in

conductivity of as little as 3%. Modern TDEM systems have an expanded frequency bandwidth from ~25 Hz to >100 kHz. Since they measure the off-time EM response, they are less sensitive in high resistivity range in comparison with the FDEM method (Macnae, 2007). Also, TDEM systems use a lower frequency range that help them to resolve higher conductivities (up to 1000 S/m; Macnae, 2010). The higher frequencies in the FDEM method give a reduced depth of penetration compared to TDEM systems; however, since the FDEM method measures relatively small secondary fields in the presence of large primary fields, accurate measurements need instruments to be less powerful and smaller size which subsequently limits their depth of investigation (Hodges, 2013). For example, the transmitter dipole-moment for FDEM systems is usually less than 300 Am^2, whereas TDEM systems are usually in a range of 0.1-2 million Am^2 (Macnae, 2007), which means 100-1000x more powerful. Therefore, airborne TDEM systems have more powerful transmitters which means they are able them to penetrate more deeply than airborne FDEM systems (Allard, 2007). Airborne FDEM can be used when targets are poorly conductive, host rocks are resistive (>10000 Ohm-m) and near-surface (<50 m) resolution is important (Holladay and Lo, 1997; Hodges, 2013). In contrast, airborne TDEM is optimally used in cases of thick and conductive cover for mapping deeply buried (>150 m) geology, and for discriminating more highly conductive (>10 S/m) targets (Nabighian and Macnae, 2005; Macnae, 2007; Legault, 2015).

3.6 Previous geophysical studies for mineral exploration in the Athabasca Basin

Exploration for uranium using geophysical methods can be classified into direct and indirect methods. Direct methods can directly detect the zone of uranium mineralization, such as gamma-ray spectrometry (GRS) that is used for defining areas with radioactive minerals such as K, U and Th. The problem is that the direct methods are only effective for shallow deposits. Indirect methods look for structures which host the uranium deposits, for example, the gravity method can potentially detect the alteration zones. Electromagnetic (EM) methods can locate graphitic faults. Seismic methods can image the unconformity and the basement faults. Magnetic data can delineate basement structures associated with faults.

Regional airborne geophysical methods (such as airborne GRS, airborne EM, aeromagnetic and airborne gravity surveys) are initial and reconnaissance methods used in order to define areas of potential uranium mineralization. Then, ground geophysical surveys, such as electrical and EM, gravity, magnetic, seismic and radiometry, are used in order to explore for the mineralization zones with greater accuracy.

3.6.1 Airborne GRS

The GRS method is a geophysical technique used to estimate concentrations of the radioelements potassium, uranium and thorium by measuring the energy of gamma-rays which the radioactive isotopes of these elements emit during radioactive decay. Airborne

radiometric data cover the entire Athabasca Basin. These data reveal the presence of radioactive minerals in the upper few centimetres of the subsurface (Milsom, 1989). Note that most near-surface material has been transported by glaciation (Campbell et al., 2002). The regional radiometry data are shown in Figure 3.25. It can be seen that these maps do not show a good correlation with the location of uranium deposits located at the eastern part of the Basin. Thus, this method is mostly used as a reconnaissance exploration.

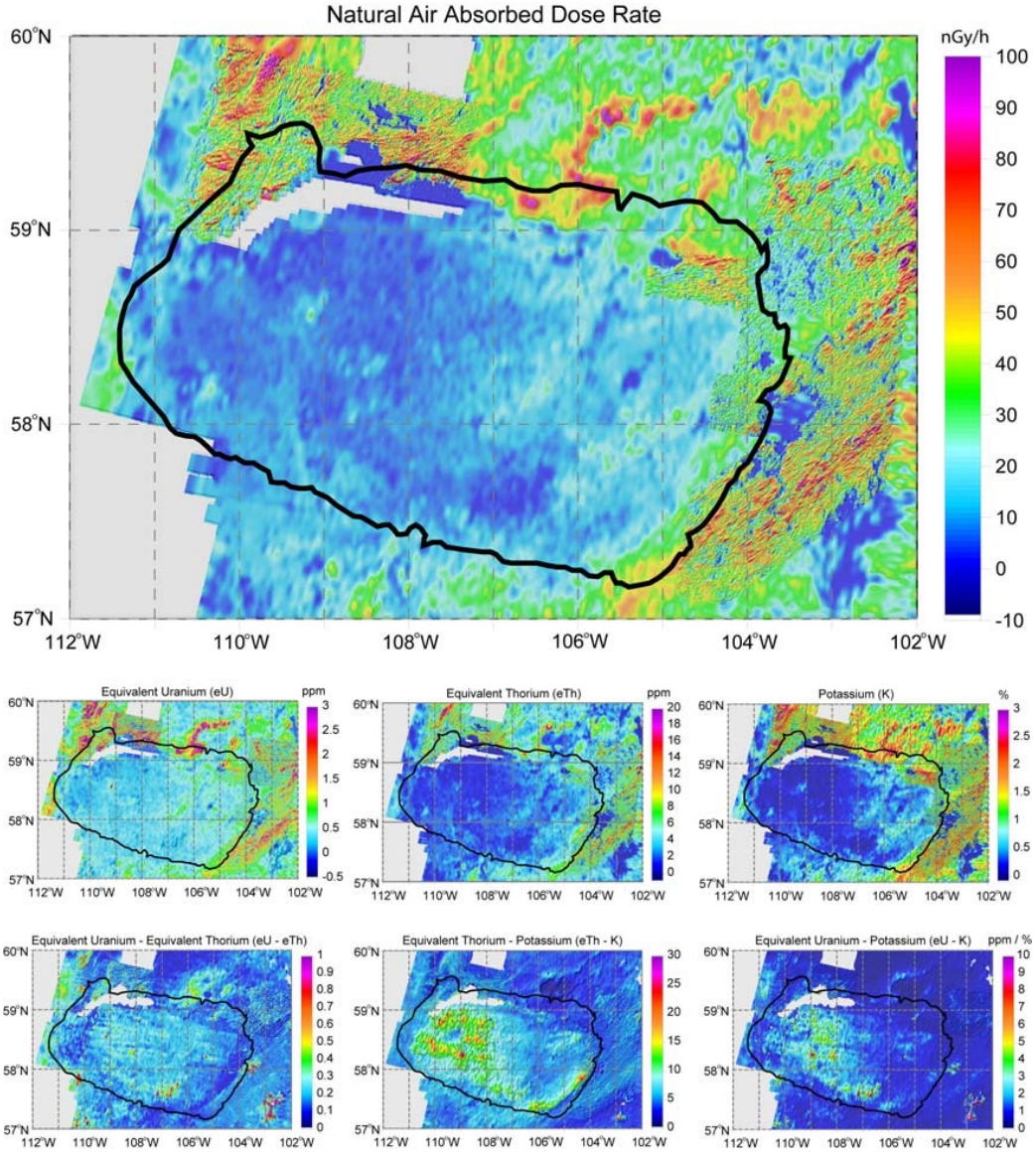

Figure 3.25: Regional radiometry data from the Athabasca Basin. Black line shows the limit of the Basin (Tuncer, 2007).

3.6.2 Seismic imaging

As mentioned before (Section 2.5.1), seismic (reflection) data cannot distinguish between different members of the Manitou Falls formation nor the signature of the uranium ore-body itself, but the unconformity and fault zones are well imaged (Juhojuntti et al., 2012). In Figure 3.26, the reflections are weak or non-existant in the vicinity of the ore-body and are interpreted as a hydrothermal alteration zone. In the 3D raw reflection seismic survey data of Millennium area, there are significant time delays in the unconformity reflections due to variable overburden. Accurate refraction static corrections are essential to correct for these effects. This refraction data can be obtained by picking the first arrivals from the seismic reflection data, and can be used to determine the thickness of the overburden as well. There is no seismic refraction survey in the McArthur-Millennium area. Also, seismic data can map the depth of the basement and other regional features such as the Moho (White et al., 2007). Note that the seismic sections need constraints from drilling to relate them to the geological structures.

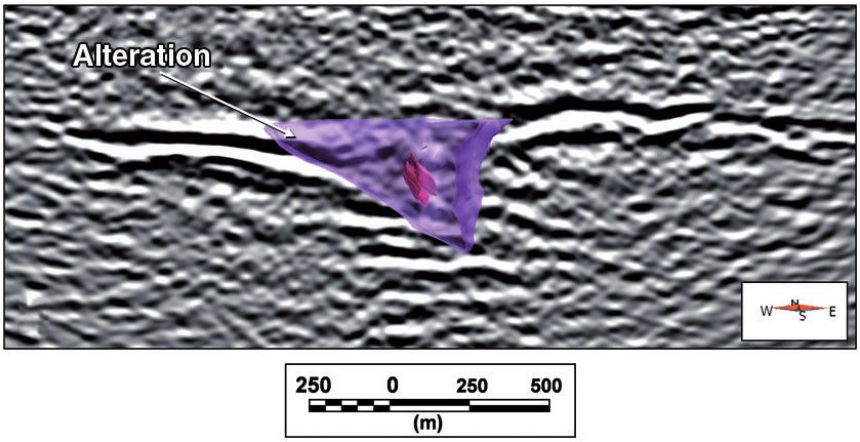

Figure 3.26: Vertical depth section of Millennium site showing the unconformity surface and the alteration zone in the vicinity of the orebody; seismic image in the background (Juhojuotti et al., 2012).

3.6.3 Magnetic studies

Regional aeromagnetic coverage delineates the basement structures such as fault systems and alteration features (Matthews et al., 1997). Most of the uranium deposits are located in the magnetic low trends (blue colors) in the eastern Athabasca Basin, which is coincident with the boundary of the Mudjatik and Wollaston domains (Figure 3.27).

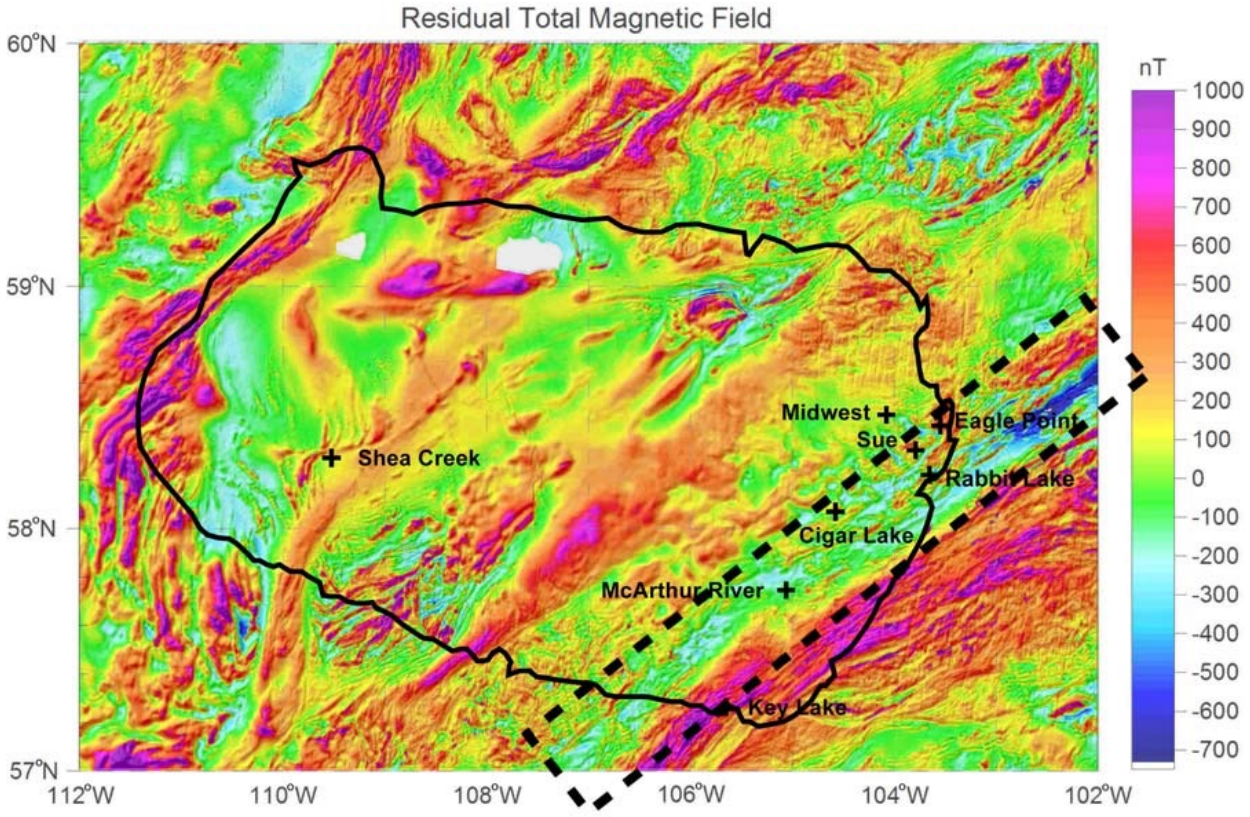

Figure 3.27: Total residual magnetic field in the Athabasca Basin. Dashed line shows one of the magnetic low trends interpreted as the Wollaston Domain–Mudjatik Domain transition zone (Matthews et al., 1997)

Thomas and McHardy (2007) mention that the magnetic lows near the McArthur River deposit are associated with pelitic - psammopelitic gneiss and lesser quartzite, intermediate levels with psammatic gneiss and highs with granitoid units. Although the magnetic low

can often determine structures related to the uranium deposits, it is not able to directly detect the uranium deposit or locate graphitic faults. Thomas and Wood (2007) modelled a 2D magnetic susceptibility structure along a profile (B-B') close to the McArthur area using magnetic data (Figures 3.28 and 3.29). For the forward modelling, they used seismic reflection images to shape the blocks in the basement. To fit the data, the appropriate magnetic susceptibilities are given to these blocks using drill-hole data. Overburden and sandstone are considered as non-magnetic in this modelling. Figure 3.29 shows that different blocks in the basement such as granitoid rocks, psammitic gneiss and pelitic gneiss have a wide range of magnetic susceptibility from 0.1×10^{-3} SI (for pelitic gneiss) to 23×10^{-3} SI (for high-susceptibility granitoid rocks)

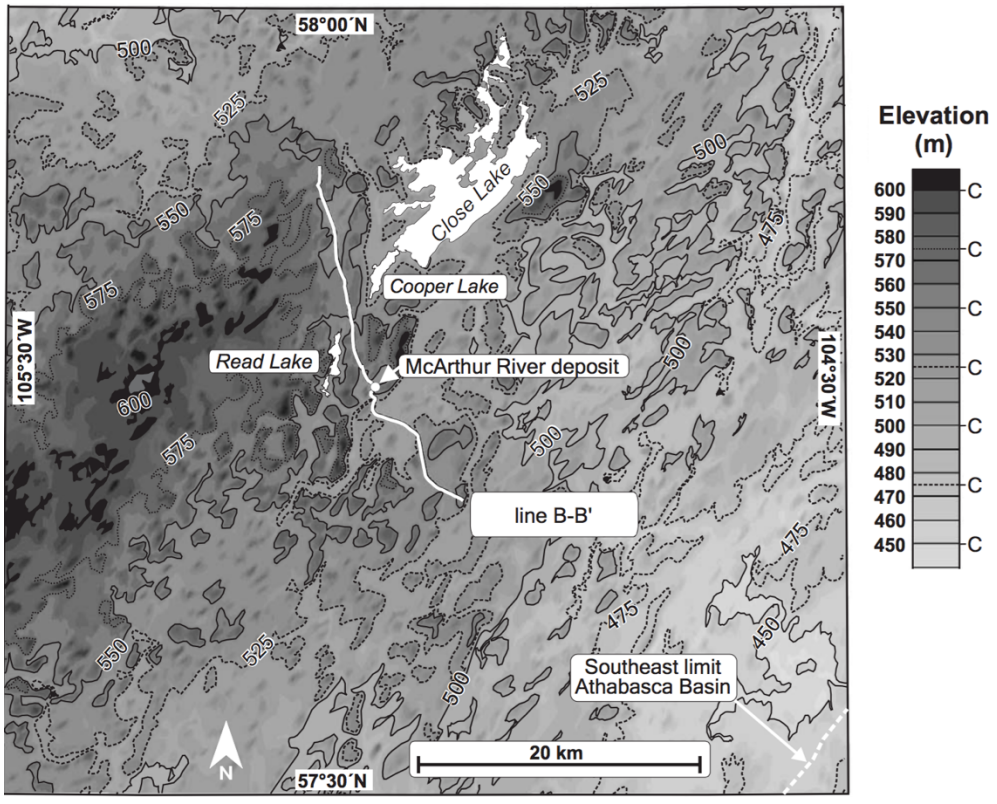

Figure 3.28: Topography map of region around the survey line B-B' (Thomas and Wood, 2007).

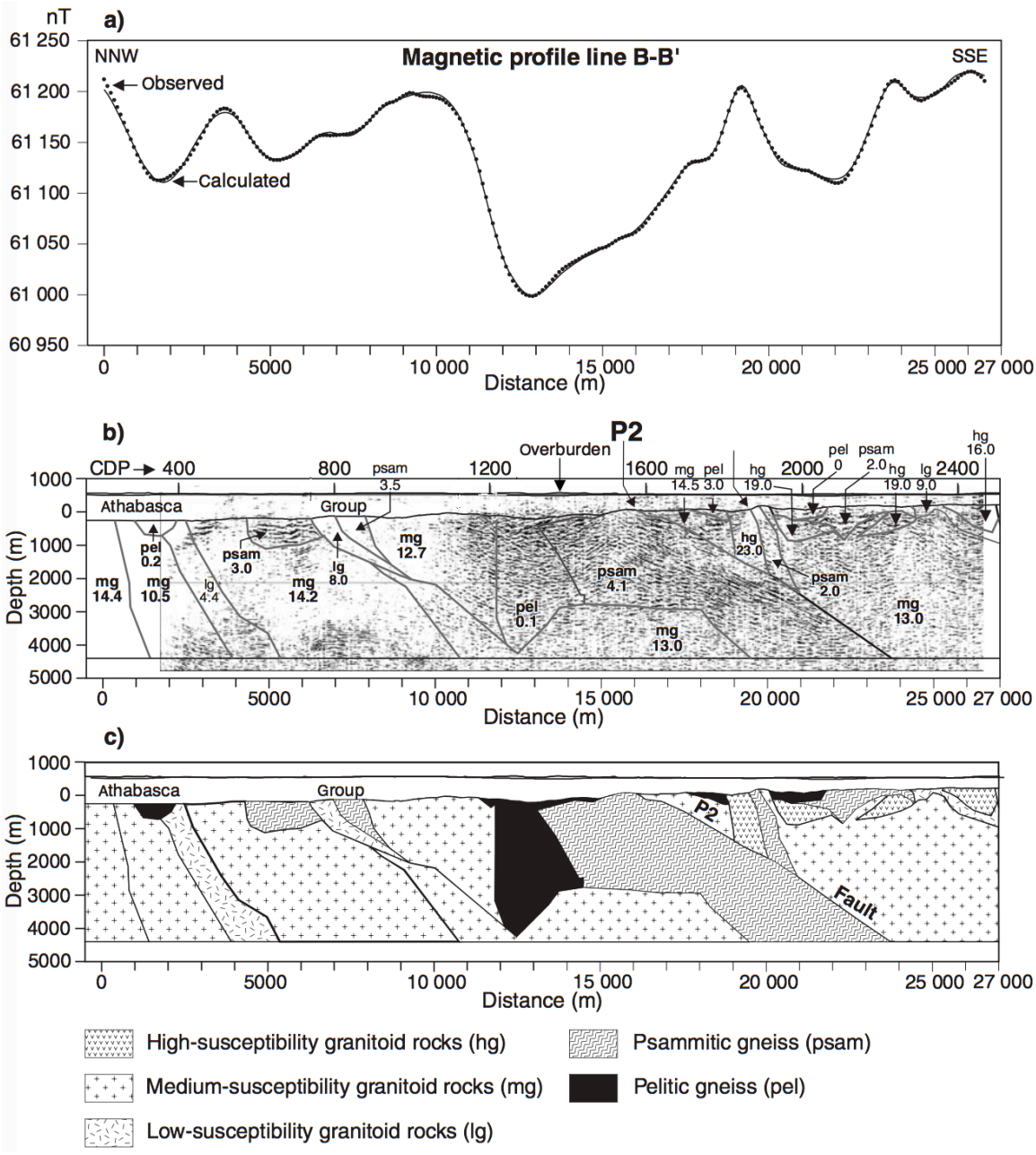

Figure 3.29: Geological section interpreted from a) magnetic profile along B-B'. b) Section illustrating boundaries of interpreted geological units and seismic reflection image. Magnetic susceptibilities ($\times 10^{-3}$ SI) of units are indicated; P2 is location of P2 fault. c) Patterned geological section. High-, medium-, and low-susceptibility granitoid rocks show arbitrary subdivision of interpreted granitoid units based on relative magnetic susceptibility (Thomas and Wood, 2007).

There has not been a detailed, comprehensive study of the overburden signature in the magnetic data in the McArthur-Millennium area, but similar research has been done for another area in Canada, namely, Quaternary glacial paleo-channels infilled by fluvial sediment in the Western Canadian Sedimentary Basin (WCSB). The resulting data indicates that the unconsolidated sediments have higher susceptibility values ($0.2 - 0.8 \times 10^{-3}$ SI) than the underlying bedrock ($0.05 - 0.4 \times 10^{-3}$ SI). The high susceptibility value of tills results from Canadian Shield-derived igneous and metamorphic rock materials. An aeromagnetic survey was done using the HELI-TRIAX system with a sensor height of 30 m and a flight line spacing of 50 m. After data processing, it can be seen that several magnetic anomalies with a pattern of drainage are clearly imaged (Figure 3.30; Davies et al., 2004).

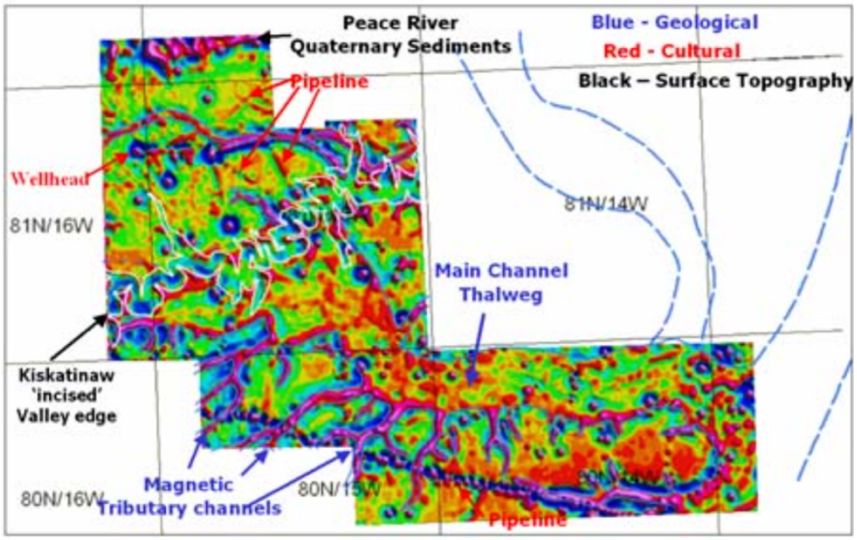

Figure 3.30: Residual HELI-TRIAX total magnetic intensity with interpretation (Davies et al., 2004).

3.6.4 Gravity exploration

Regional gravity data have been used to map the basement structures in the Athabasca

Basin with average data spacing ranging from 5 to 10 km (Figure 3.31). An average overburden density of 2.1 g/cc was used for the Bouguer correction (see Section 3.2.3; Matthews et al. 1997). The Bouguer anomaly is dominated by variations in the basement densities. The high values are associated with granulite facies metamorphic rocks and metamorphic terranes. The low values are often correlated with amphibolite facies terranes, in part retrograde granulites (Matthews et al., 1997).

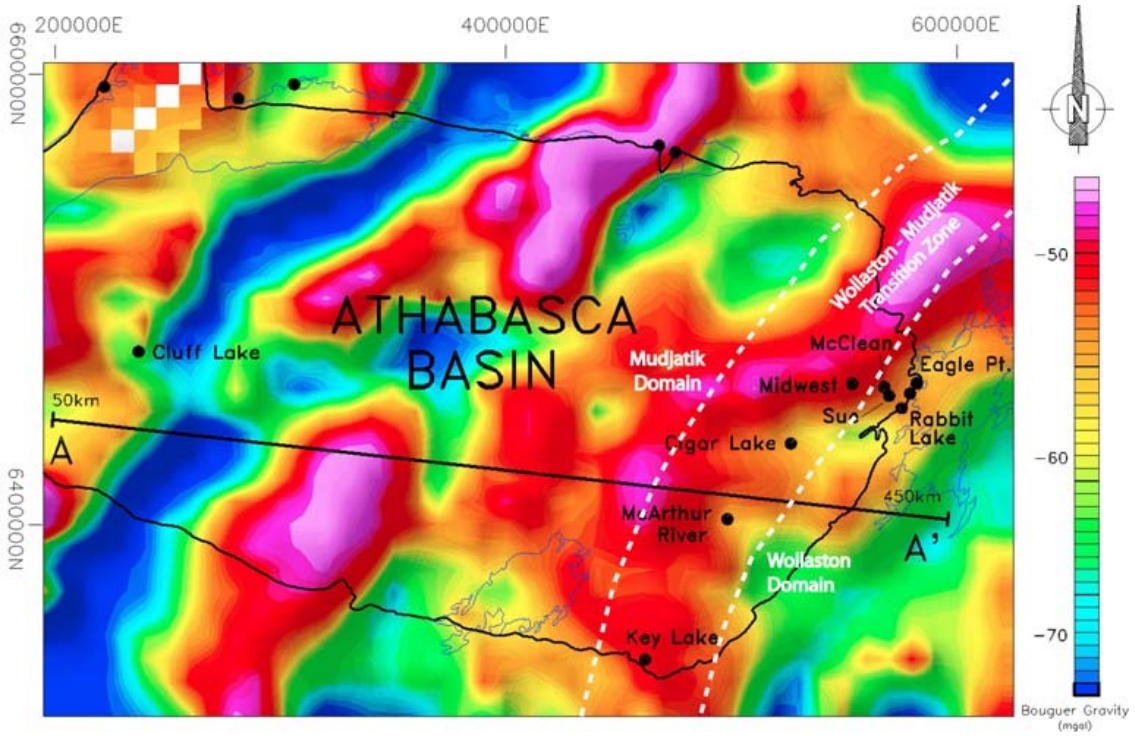

Figure 3.31: Corrected Bouguer gravity anomaly map for the Athabasca Basin. Black line shows the limit of Athabasca Basin (Matthews et al., 1997).

A high resolution ground gravity data-set was modelled along a profile (B-B'; Figure 3.28) by Wood and Thomas (2002) using forward modelling (Figure 3.32). The Bouguer anomaly was computed with a density of 2 g/cc. The Bouguer anomaly data show a variation of less than 3 mGal along the profile. Short wavelengths of less than 500 m and intermediate wavelengths (500–1800 m) are associated with the overburden and alteration

zones, respectively. Zones of alteration are anticipated to give gravity lows in the range 0.4 – 1 mGal. Desilicification decreases the density and gives a small negative Bouguer anomaly, whereas silicification increases the density and gives a small positive Bouguer anomaly (see Section 2.5.2). Sandstone, silicification and desilicification have a density of 2.42 g/cc, 2.47 g/cc and 2.39 g/cc, respectively. Long wavelength components (>2500 m) in the range 0.5 - 1 mGal are due to the deeper structures such as variations in the basement densities. The density of different blocks in the basement has a range from 2.65 g/cc (for quartzite) to 2.77 g/cc (for pelitic gneiss).

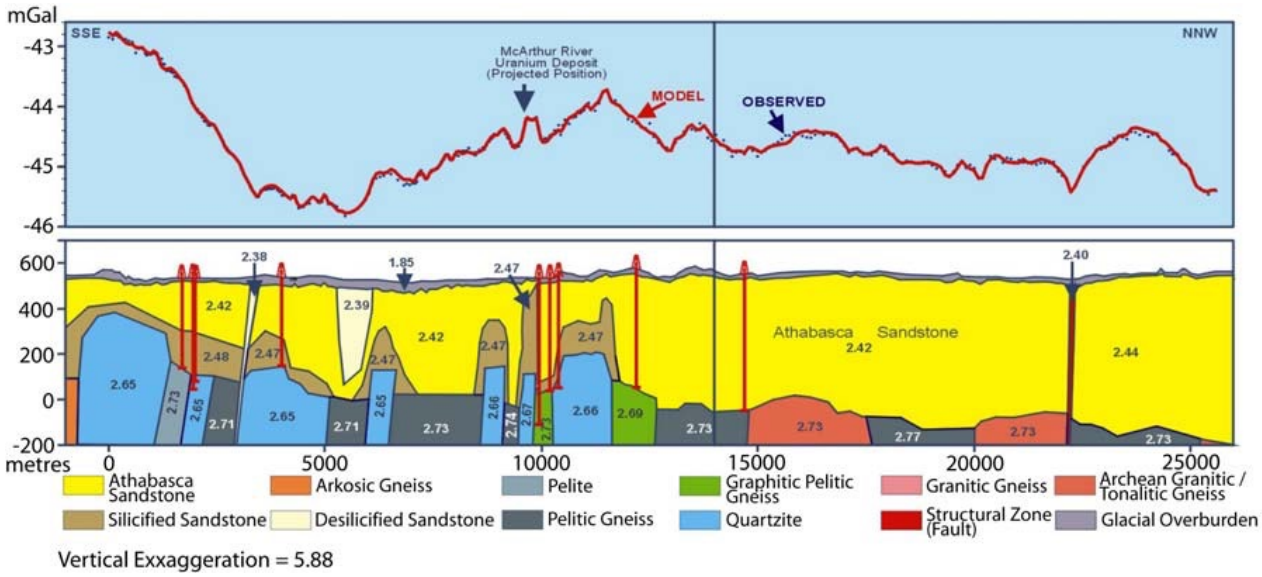

Figure 3.32: Observed and modelled gravity profiles along the high-resolution gravity profile (the same profile shown in Figure 3.28) at McArthur area (Wood and Thomas, 2002). Densities (g/cc) of modelled geological units are indicated. Note that the direction of the profile is flipped between the figures. If 3.29 and 3.33 show B-B', then Fig 3.32 shows B'-B.

A modelling using seismic constraints (Figure 3.33) was done on another high resolution ground gravity data-set by Thomas and Wood (2007) along the profile B-B' shown in Figure 3.28. Modelling was started by assigning densities to all blocks shown in Figure

3.29. Psammitic gneiss and granitoid pelitic gneiss units were assigned densities of 2.67 g/cc, 2.67 g/cc and 2.71 g/cc, respectively. Also, densities of 2.46 g/cc, 2.48 g/cc, 2.52 g/cc, and 2.60 g/cc were assigned to the MFd, MFc, MFb, and RD members, respectively. In the next step, the inversion was applied to seek the best match between the observed and modelled profiles. As shown in Figure 3.33, the inverted densities for granitoid units varies within the range 2.634–2.682 g/cc, which is compatible with values for Archean and Proterozoic granitoid rocks. Also, inverted densities for psammitic gneiss and pelitic gneiss units range from 2.640 g/cc to 2.689 g/cc and from 2.674 g/cc to 2.875 g/cc, respectively. There is a good match between calculated densities and drill-hole data.

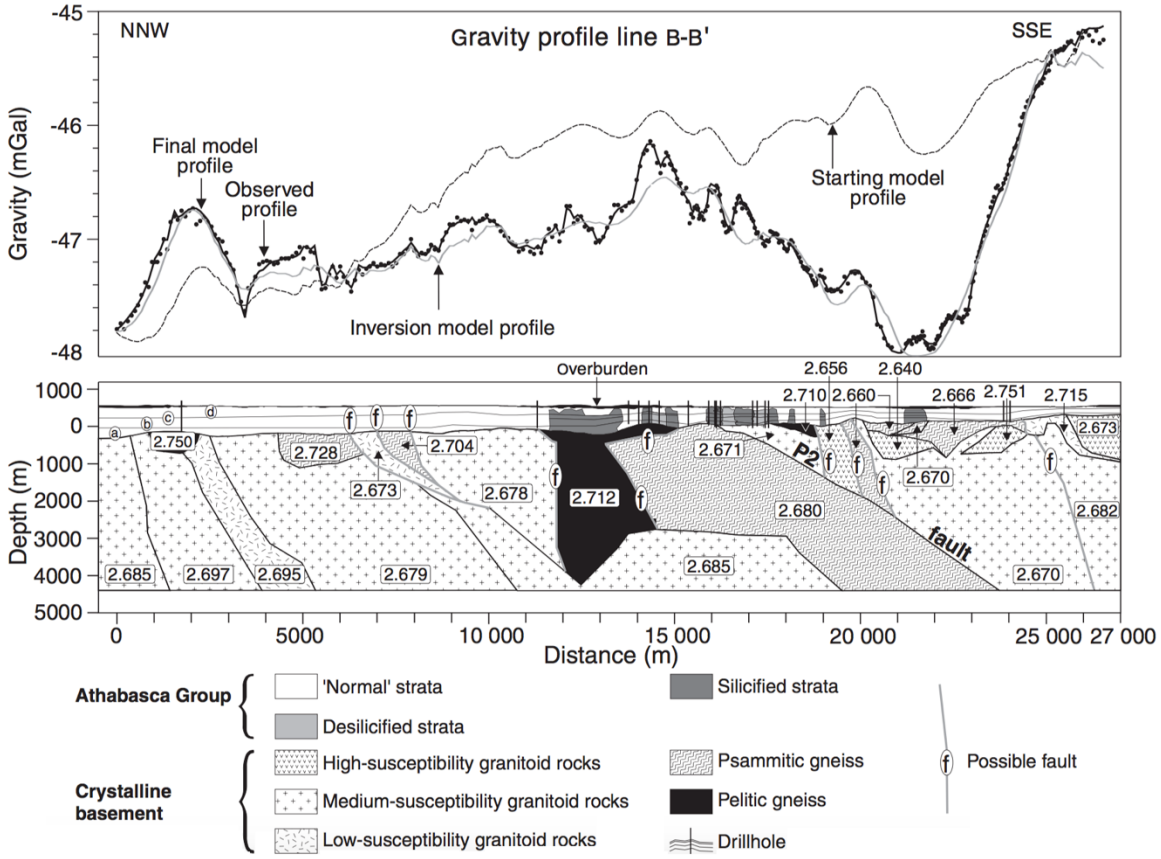

Figure 3.33: Gravity model along profile B-B' shown in Figure 3.28 obtained using inversion by considering the basement subdivisions which are based on the magnetic model shown in Figure 3.29. Densities (g/cc) of units are indicated by numbers in boxes (Thomas and Wood, 2007).

3.6.5 Electromagnetic studies

As mentioned before, uranium deposits are often found in the vicinity of graphite in the Athabasca Basin (Jefferson et al., 2007). Graphite is considered as an electrical conductor which can easily be detected using EM methods. Figure 3.34 shows a smooth model 1D inversion of ground EM data (the in-loop data from Step Loop) in the Athabasca Basin (but not McArthur area; Powell et al., 2006). The unconformity is well resolved at a depth of 175 m. A large conductive body (< 200 Ohm-m) with hints of a steeply dipping fault represents the lower Wollaston Group which contain the graphitic conductors.

Figure 3.35 shows a vertical section of electrical resistivity in the Athabasca Basin (but not McArthur area) determined from airborne time-domain MEGATEM data (Irvine and Witherly, 2006). The sandstone and the basement are associated with high values of electrical resistivity. Silicified zones and desilicified zones have relatively high resistivities (due to the silica content in pore spaces) and low resistivities (due to the clay content in the pore space), respectively. The overburden has mostly low resistivity in the Athabasca Basin, because of the deposit compositions and/or the presence of penetrated water and lake waters. In some regions in the Athabasca Basin, therefore, the overburden can be investigated using EM methods. In Figure 3.34, the overburden can be seen as a narrow conductive shallow layer along the vertical section represented by green color.

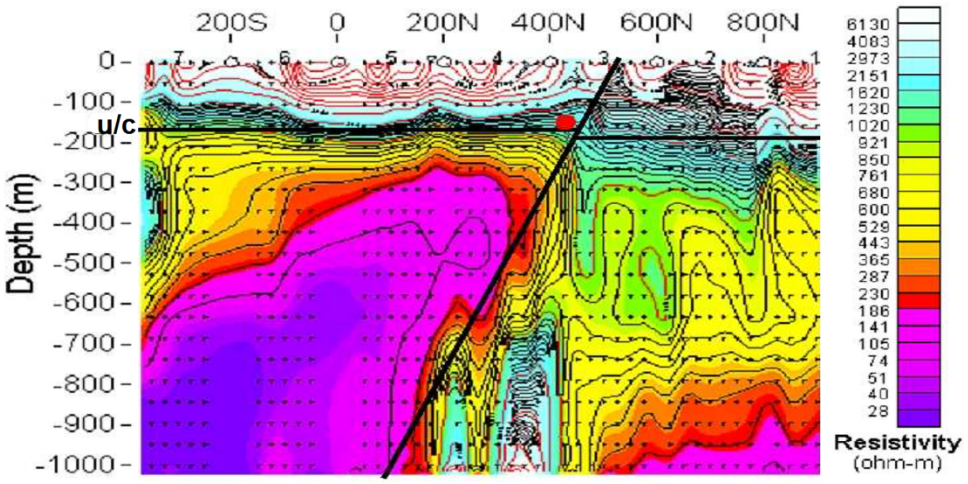

Figure 3.34: Resistivity model of the 1D inversion of ground (Step Loop) EM data in the Athabasca Basin. The location of mineralization is shown in a red circle (Powell et al., 2006).

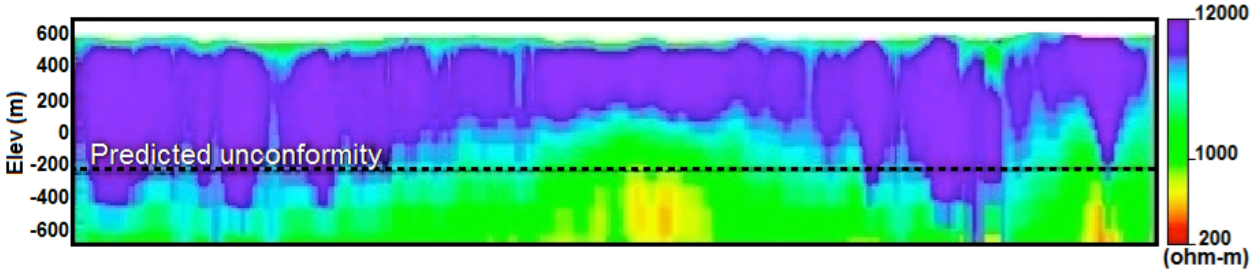

Figure 3.35: Resistivity depth section along a profile in the Athabasca Basin (Irvine and Witherly, 2006).

3.7 Conclusions

Geophysical methods can help to reveal the subsurface structures. A few of them such as gravity, magnetic, seismic refraction and electromagnetic methods are explained in this chapter. These methods are used in this research for the overburden stripping. Gravity method is the response of density of geological structures. But, before any interpretation the reduction should be done on the data. The corrected data can end up in two types of data: free-air data or Bouguer data. Magnetic method is the response of magnetic

susceptibility of geological structures. Geomagnetic correction, which is subtracting the IGRF's value, as well as diurnal variation correction, which is subtracting the diurnal variations, should be applied on the magnetic data before the interpretation.

The seismic refraction method measures the travel time of refracted waves in order to determine the depth of different geological boundaries and the type of rocks. This method works as the seismic velocity of the geological structures is increasing as the depth increases. There are several methods for the interpretation of seismic data such as (conventional) reciprocal method (CRM; or plus–minus method), generalized reciprocal method (GRM) and the inversion method which is used in this thesis. EM method includes the response of the conductive structures in the ground. In the controlled source EM (CSEM) method, time varying magnetic fields in the subsurface generate electromotive force (emf), which drives eddy current in conductive bodies. The currents generate a secondary magnetic field which can be detected by receivers. The CSEM method is divided into frequency domain (FDEM) and time domain (TDEM) methods.

Many geophysical works were done in the Athabasca Basin, especially in the McArthur-Millennium corridor. Airborne and ground gravity, magnetic and electromagnetic data were obtained over the corridor, and the processing and interpretation were made to find the location of the uranium deposits. Seismic data were helpful as well. But there hasn't really been a successful stripping of the overburden effect yet, certainly not on the scale of the McArthur-Millennium corridor.

Chapter 4

Forward Modelling and Inverse Theory

4.1 Introduction

Forward modelling, which is a mathematical process, is applied for different geophysical methods to synthetize the data from the model parameters. Also, in this research the inversion method will be applied on both synthetic and real data to reconstruct the geological structures from different observed data such as seismic refraction, gravity, magnetic and electromagnetic data. Therefore, the basic concept of the inverse theory will be introduced in this chapter as it is a mathematical process of estimating the values of model parameters from a set of observed data (see Appendix C for a simple example of linear gravity inversion). In this research, the latest modelling and inversion methods and codes are used. Hence, conclusions from all the synthetic modelling studies could well be different (more successful) from what people might expect using old methods.

In this chapter, the theory of the forward modelling of gravity, magnetic, first-arrival seismic traveltime and electromagnetic methods will be explained. The methods used for gravity and magnetics are based on analytical solutions while the methods for first-arrival seismic traveltime and electromagnetics are based on the numerical methods (finite

difference and finite element). Subsequently, the minimum-structure approach for inversion, which is the approach used in this thesis, will be discussed.

4.2 Gravity and magnetic forward modelling

In this research, 2D and 3D gravity and magnetic data were synthesized using the forward modelling code of Lelièvre et al. (2011). The analytical expressions used for the forward modelling on unstructured tetrahedral meshes is based on using a method presented by Okabe (1979). Okabe develops the analytical expressions for the derivatives of the gravitational potential in an arbitrary direction due to a polyhedral body composed of polygonal facets using the divergence theory. Gravity and magnetic fields are calculated in a similar manner in the forward modelling codes. Also, the magnetic potential due to a magnetized body can be directly derived from the first derivative of the gravitational potential in a given direction (Okabe, 1979). Here, I will simply and initially describe this method for a 2D case on a triangular mesh (see Appendix B for Fortran code). And then the theory (and the code) will be briefly expanded for a 3D case.

Okabe (1979) applies the divergence theorem for 2-D polygonal and 3-D polyhedral bodies to gravity potential fields. He develops analytical expressions for gravity anomalies due to a homogeneous polyhedral body composed of polygonal facets. For a 2D case, in the 2D basic Cartesian system, (p_0,q_0) and (p,q) are considered as observation points and vertices points, respectively.

$z = p - p_0$ and $x = q - q_0$ (4.1)

In two dimensions, with due attention to Figure 4.1 for the i*th* edge in a coordinate rotation case we have

$$\begin{bmatrix} X \\ Z \end{bmatrix} = \begin{bmatrix} cos\psi & sin\psi \\ -sin\psi & cos\psi \end{bmatrix} \begin{bmatrix} x \\ z \end{bmatrix} \quad (4.2)$$

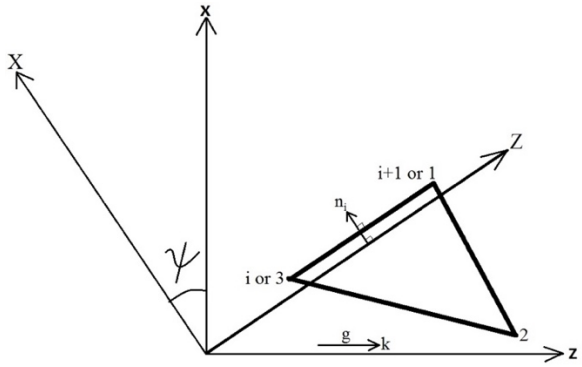

Figure 4.1: The edge rotation of the Cartesian system for calculating the *k*th component of the gravity due to a uniform triangular prism.

Finally, we have the forward modelling equation as

$$U_k = \rho\, G \sum_i \boldsymbol{k}^T \boldsymbol{n}_i \boldsymbol{I}_i \quad (4.3)$$

where

$$\boldsymbol{n}_i = \begin{bmatrix} -sin\psi \\ cos\psi \end{bmatrix} \quad (4.4)$$

is the direction vector specifying the outward normal on the i*th* edge. Note that U_k is the first derivative of the potential in *k*-direction, and the magnetic potential is similar but set ρG=1. In the gravity case, $\boldsymbol{k}$ and $\boldsymbol{I}$ are the given direction of measurement. In the magnetic case, $\boldsymbol{k}$ is the magnetic intensity vector for the potential or given direction for the field, and

$\boldsymbol{I}$ is the magnetic intensity vector for the field. Supposing that the vertices of the triangle are numbered clockwise, and the i*th* edge has two vertices i and i+1 (for the last edge, vertex i+1 corresponds to vertex 1), then we have

$$\boldsymbol{I}_i = [Z\ ln(Z^2 + X^2) + 2Xtan^{-1}\left(\frac{Z}{X}\right) - 2Z]_{Z_i}^{Z_{i+1}} \tag{4.5}$$

where the direction vector $\boldsymbol{k}^T$ (T means transverse) is

$$\boldsymbol{k}^T = (k_z, k_x) = [\cos(z,k)\,, \cos(x,k)] = [1 \quad 0] \tag{4.6}$$

and

$$cos\psi = \frac{z_{i+1} - z_i}{\sqrt{(z_{i+1}+z_i)^2 + (x_{i+1}+x_1)^2}} \tag{4.7}$$

and

$$sin\psi = \frac{x_{i+1} - x_i}{\sqrt{(z_{i+1}+z_i)^2 + (x_{i+1}+x_1)^2}} \tag{4.8}$$

We should also consider the following conditions in solving the forward equation: 1) If the first term of I_i, $Z^2 + X^2$ converges to zero, then the whole first term is equal to zero. 2) If $x = 0$, the second term of I_i is equal to zero.

In three dimensions, with due attention to Figure 4.2, it is necessary to first rotate the x- and y-axes around the z-axis until the rotated x-direction is coincident with the projected direction of the outward normal onto the x-y plane. And then we rotate the z- and x- axes around the Y-axis until the rotated z-direction is coincident with the direction of the

outward normal. By these rotations we obtain the target system (X, Y, Z) which can be written as (Okabe, 1979):

$$\begin{bmatrix} X \\ Y \\ Z \end{bmatrix} = \begin{bmatrix} cos\phi & 0 & -sin\phi \\ 0 & 1 & 0 \\ sin\phi & 0 & cos\phi \end{bmatrix} \begin{bmatrix} cos\theta & sin\theta & 0 \\ -sin\theta & cos\theta & 0 \\ 0 & 0 & 1 \end{bmatrix} \begin{bmatrix} x \\ y \\ z \end{bmatrix} \tag{4.9}$$

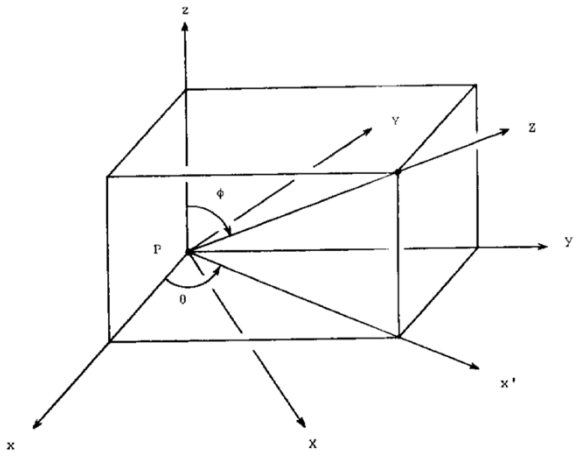

Figure 4.2: The surface rotation of the Cartesian system (Okabe, 1979).

where $0 \leq \theta < 2\pi$ and $0 \leq \phi \leq \pi$. Hence, the forward modelling equation can be written

$$U_k = \rho\, G \sum_i \sum_j \boldsymbol{k}^T \boldsymbol{n}_i \boldsymbol{J}_j(i) \tag{4.10}$$

where

$$\boldsymbol{n}_i = \begin{bmatrix} sin\phi\, cos\theta \\ sin\phi\, sin\theta \\ cos\phi \end{bmatrix} \tag{4.11}$$

is the direction vector specifying the outward normal on the i*th* facet. Supposing that the j*th* edge of the polygon has vertices *j* and *j*+1 (for the last edge, vertex *j*+1 corresponds to vertex 1), then we have (see, Okabe, 1979, for more information):

$$\boldsymbol{J}_j(i) = \Bigg\{ (X\,sin\psi - Y\,cos\psi)\ln[X\,cos\psi + Y\,sin\psi + (X^2+Y^2+Z^2)^{\frac{1}{2}}] - 2Z\,tan^{-1}\frac{(1+sin\psi)\left[Y+(X^2+Y^2+Z^2)^{\frac{1}{2}}\right]+X\,cos\psi}{Z\,cos\psi}\Bigg\}_{(X_j,Y_j)}^{(X_{j+1},Y_{j+1})} \tag{4.12}$$

Note that these equations for a 3D case can give the solution for the magnetic potential by assuming ρG=1 and regarding the direction vector $\boldsymbol{k}$ as the magnetic intensity vector for the potential or given direction for the field. The gravity and magnetic fields can be derived from the same expressions. The contributions from all the cells in the model (each contribution computed using the appropriate formula above) are added up (superposition) to get the gravity or magnetic datum for the whole density or susceptibility model.

4.3 Modelling of first-arrival seismic traveltimes

The forward problem for the first-arrival seismic traveltimes is solved using the Fast Marching Method (FMM; Lelièvre et al., 2011). FMM is a numerical method which is used for propagating first-arrival seismic wavefronts through a velocity distribution. In this method, each cell in the mesh is first assigned a constant slowness value. The solution starts by initializing the traveltimes at near-source nodes. This can be done by defining a radius from the source and calculating the traveltime at nodes within that radius (by assuming uniform slowness within this radius) by multiplication of the slowness by the distance from each node to the source (Lelièvre et al., 2011).

Figure 4.3 shows the FMM solution on a rectilinear grid after the initialization stage. In this grid, nodes can be categorized into “upwind” or “downwind” nodes. Upwind nodes have firm traveltime values that can not be changed at later stages in the FMM solution. The downwind nodes can also be categorized into “close” nodes which are connected to upwind nodes at which the traveltimes are calculated based on the traveltimes at their neighbouring upwind nodes, and “far” nodes which are not immediately connected to upwind nodes. For a close node, there can be several calculations due to the adjacent nodes. Actually, the FMM calculates first arrivals so the actual traveltime taken by a node is the minimum of all those calculated traveltimes coming from the local adjacent nodes. Thus, the close node with the smallest traveltime is chosen as an upwind node. Afterwards, the far nodes which are now connected to the new upwind node will be considered as the close nodes. The solution goes forward until all nodes have been visited, and have been considered as the upwind nodes (Lelièvre et al., 2011).

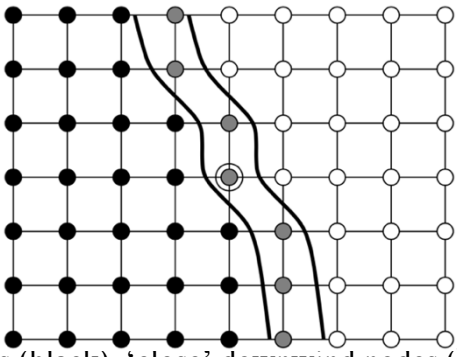

Figure 4.3: Upwind nodes (black), ‘close’ downwind nodes (grey) and ‘far’ downwind nodes (white) in a section of a rectilinear 2D grid through which an FMM solution is progressing. Thin connecting lines indicating the grid cells. Two parallel thick lines show the sides of a narrow band of ‘close’ nodes (Lelièvre et al., 2011).

The mathematical equations for the FMM method for a 2D mesh made up of triangular cells can be described using Figure 4.4. Suppose that the traveltimes at nodes A and B (t_A and t_B) are calculated at previous stages in the FMM solution. Thus, the traveltime at node

C (t_C) corresponding to a wave transmitted through the cell can be calculated using (Lelièvre et al., 2011)

$$t_C = t_A + u\xi_0 + wc^{-1}\rho_0 \tag{4.13}$$

with

$$w^2 = s^2c^2 - u^2 \tag{4.14}$$

where $u = t_B - t_A$, c is the length of line AB, s is the homogeneous slowness of the triangular cell, ξ_0 is the normalized projection of node C onto line AB, and ρ_0 is the length of the normal from node C to the point at ξ_0. However, traveltime t_C could also be due to a head wave travelling along side AC or BC. Therefore, in general we have

$$t_C = \min\left(t_A + u\xi_0 + wc^{-1}\rho_0 \ , \ t_A + sb \ , \ t_B + sa\right) \tag{4.15}$$

where a is the length of line BC, and b is the length of line AC.

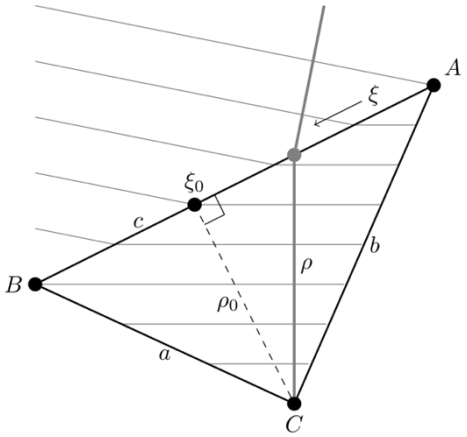

Figure 4.4: A geometrical scheme for the traveltime calculating procedure in a triangular cell that lies between three nodes A, B and C. A traversing ray hitting node C is drawn as a thick grey line perpendicular to the (linear) wavefronts which are drawn as thin grey lines (Lelièvre et al., 2011).

4.4 Electromagnetic modelling

Maxwell's equations are the fundamental equations of electromagnetic theory. For a conductive medium, they can be expressed as:

$$\boldsymbol{\nabla} \times \boldsymbol{E} = -\frac{\partial \boldsymbol{B}}{\partial t} \qquad \text{Faraday's law} \tag{4.16}$$

$$\boldsymbol{\nabla} \times \boldsymbol{H} = \boldsymbol{J} - \frac{\partial \boldsymbol{D}}{\partial t} \qquad \text{Ampère's law} \tag{4.17}$$

$$\boldsymbol{\nabla}.\boldsymbol{B} = 0 \qquad \text{Gauss's law} \tag{4.18}$$

$$\boldsymbol{\nabla}.\boldsymbol{D} = q \qquad \text{Coulomb's law} \tag{4.19}$$

where $\boldsymbol{E}$ [V/m] is the electric field intensity, $\boldsymbol{B}$ [Wb/m^2] is the magnetic induction, $\boldsymbol{H}$ [A/m] is the magnetic field intensity, $\boldsymbol{J}$ [A/m^2] is the current density, $\boldsymbol{D}$ [C/m^2] is the electric displacement, and q [C/m^3] is the electric charge density. Faraday's law describes the generation of the electric field by a time-varying magnetic field. Ampere's law describes that the conduction and displacement currents are sources of the magnetic field. Coulomb's law states that $\boldsymbol{D}$ is produced by electric charge q, and can be monopolar in nature. Gauss's law states that the magnetic flux through any closed surface is zero, and $\boldsymbol{B}$ cannot be a monopole, and must be dipolar in nature (Fitterman and Labson, 2005).

For an isotropic medium, $\boldsymbol{E}$ and $\boldsymbol{H}$ are related to $\boldsymbol{D}$ and $\boldsymbol{B}$, and $\boldsymbol{J}$ and $\boldsymbol{E}$ are linked through the following constitutive equations

$$\boldsymbol{B} = \mu \boldsymbol{H}, \quad \boldsymbol{D} = \epsilon \boldsymbol{E} \quad \text{and} \quad \boldsymbol{J} = \sigma \boldsymbol{E} \tag{4.20}$$

where μ [H/m] is the magnetic permeability, ϵ [F/m] is the electric permittivity, and σ [S/m] is the electrical conductivity which is the main physical property in the EM method. In the Earth, μ, ϵ and σ are spatially variable, and describe the physical properties of the materials. Magnetic permeability and electric permittivity are

$$\mu = \mu_r \mu_0 \quad \text{and} \quad \epsilon = \epsilon_r \epsilon_0 \tag{4.21}$$

where $\mu_0 = 4\pi \times 10^{-7}\text{H/m}$ is the magnetic permittivity of vacuum, and $\epsilon_0 = 8.85 \times 10^{-12}\text{F/m}$ is the dielectric permittivity of vacuum. μ_r and ϵ_r are dimensionless multipliers. Relative permeability μ_r is the ratio of permeability of material to that of a vacuum. Relative permittivity ϵ_r (also called dielectric constant) is the ratio of permittivity of material to that of a vacuum. In the simple isotropic case, they are constant, but in anisotropic cases they are tensors. If the material is magnetically or electrically polarizable, they can be frequency or time dependent.

The Fourier transform pair between time and frequency are as follows (Ward and Hohmann, 1988)

$$F(\omega) = \int_{-\infty}^{+\infty} f(t) e^{-i\omega t} dt \qquad \text{(time-domain to frequency-domain)} \tag{4.22}$$

$$f(t) = \frac{1}{2\pi} \int_{-\infty}^{+\infty} F(\omega) e^{i\omega t} d\omega \qquad \text{(frequency-domain to time-domain)} \tag{4.23}$$

where i^2=-1 and ω is the angular frequency. Faraday's and Ampère's laws can be transformed from the time-domain to the frequency-domain using the Fourier transform as

$$\boldsymbol{\nabla} \times \boldsymbol{E} = -i\omega \boldsymbol{B} \tag{4.24}$$

$$\boldsymbol{\nabla} \times \boldsymbol{H} = \boldsymbol{J} + i\omega \boldsymbol{D} \tag{4.25}$$

By taking the curl of the Faraday's and Ampere's laws we have "wave equations" which in the time-domain are given by

$$\boldsymbol{\nabla} \times \boldsymbol{\nabla} \times \boldsymbol{E} + \mu \boldsymbol{\nabla} \times \frac{\partial}{\partial t} \boldsymbol{H} = 0 \tag{4.26}$$

$$\boldsymbol{\nabla} \times \boldsymbol{\nabla} \times \boldsymbol{H} - \epsilon \boldsymbol{\nabla} \times \frac{\partial}{\partial t} \boldsymbol{E} = \sigma \nabla \times \boldsymbol{E} \tag{4.27}$$

Using the vector identity

$$\boldsymbol{\nabla} \times \boldsymbol{\nabla} \times \boldsymbol{T} = \boldsymbol{\nabla}(\boldsymbol{\nabla}.\boldsymbol{T}) - \boldsymbol{\nabla}^2 \boldsymbol{T} \tag{4.28}$$

where $\boldsymbol{T}$ is a vector, and considering that in a homogeneous charge free medium $\nabla.\mathrm{H} = 0$ and $\nabla.\mathrm{E} = 0$, the wave equations (in time-domain) will be as

$$\boldsymbol{\nabla}^2 \boldsymbol{E} - \mu\epsilon \frac{\partial^2 \boldsymbol{E}}{\partial^2 t} - \mu\sigma \frac{\partial \boldsymbol{E}}{\partial t} = 0 \tag{4.29}$$

$$\boldsymbol{\nabla}^2 \boldsymbol{H} - \mu\epsilon \frac{\partial^2 \boldsymbol{H}}{\partial^2 t} - \mu\sigma \frac{\partial \boldsymbol{H}}{\partial t} = 0 \tag{4.30}$$

These wave equations can be written in the frequency-domain as

$$\boldsymbol{\nabla}^2 \boldsymbol{E} + (\mu\epsilon\omega^2 - i\mu\sigma\omega)\boldsymbol{E} = 0 \tag{4.31}$$

$$\boldsymbol{\nabla}^2 \boldsymbol{H} + (\mu\epsilon\omega^2 - i\mu\sigma\omega)\boldsymbol{H} = 0 \tag{4.32}$$

These two equations are also known as Helmholtz equations for $\boldsymbol{E}$ and $\boldsymbol{H}$ fields. For common values of μ, ϵ and σ of Earth materials, and for frequencies smaller than 10^5 Hz (which is common in EM geophysical surveys except GPR), it can be seen that the displacement current term ($\mu\epsilon\omega^2$) is much smaller than the conduction current term ($\mu\sigma\omega$). Therefore, displacement currents can be neglected. This assumption is called the "quasi-static approximation" in which the primary magnetic field in free space generated by a source loop of alternating current is in-phase with current; and the primary electric field is in quadrature with current, being generated by the time derivative of the magnetic field (West and Macnae, 1991). Therefore, wave equations can be transformed into

$$\boldsymbol{\nabla}^2\boldsymbol{E} - \mu\sigma\frac{\partial \boldsymbol{E}}{\partial t} = 0 \tag{4.33}$$

$$\boldsymbol{\nabla}^2\boldsymbol{H} - \mu\sigma\frac{\partial \boldsymbol{H}}{\partial t} = 0 \tag{4.34}$$

and

$$\boldsymbol{\nabla}^2\boldsymbol{E} - i\mu\sigma\omega\,\boldsymbol{E} = 0 \tag{4.35}$$

$$\boldsymbol{\nabla}^2\boldsymbol{H} - i\mu\sigma\omega\,\boldsymbol{H} = 0 \tag{4.36}$$

These equations are "diffusion equations" in homogeneous media. It is common to define

$$k = \sqrt{-i\mu\sigma\omega} \tag{4.37}$$

where k [1/m] is "wavenumber". Actually, the propagation of the electromagnetic signals

in the Earth is diffusive. When the time-varying magnetic field penetrates into the ground, it induces a time varying electric current. While this electric current flows, energy is converted to heat which cannot be converted back into electric or magnetic fields. Thus, the amplitudes of the EM fields in a medium generally decrease by a factor of 1/*e* over the distance δ which is known as the "skin depth" given by (West and Macnae, 1991)

$$\delta = \sqrt{\frac{2}{\omega\mu\sigma}} \approx \frac{500}{\sqrt{\sigma f}} \tag{4.38}$$

It can be seen that by increasing frequency and/or conductivity, the skin depth decreases. Therefore, a low conductivity or a low frequency is necessary for the deep imaging. Note that the skin depth formula given above is only truly applicable to plane waves. For a localized source, there is the additional geometric decay with distance from the source.

All the equations presented so far are based on the "direct EM-field formulation". In order to solve the electromagnetic problems more effectively, we can use the "potential method" in which a vector potential is used from which E and H can both be derived (Grant and West, 1965). The benefit is that the linear system of equations we end up having to solve is not as ill-conditioned. The problem can be formulated in terms of magnetic vector potential ($\boldsymbol{A}$) and electric scalar potential (ϕ) rather than electric ($\boldsymbol{E}$) and magnetic ($\boldsymbol{H}$) fields. As a result of the Gauss's law and the Helmholtz equation, $\boldsymbol{B}$ can be considered as the curl of a vector potential $\boldsymbol{A}$. Thus, magnetic induction can be written as

$$\boldsymbol{B} = \boldsymbol{\nabla} \times \boldsymbol{A} \tag{4.39}$$

Thus, by substituting this into Equation 4.16 in frequency-domain, we have

$$\boldsymbol{\nabla} \times (\boldsymbol{E} + i\omega \boldsymbol{A}) = 0 \tag{4.40}$$

It can be seen that the curl of the vector ($\boldsymbol{E} + i\omega \boldsymbol{A}$) is equal to zero. If the curl of a vector is zero, the vector must be zero or equal to the gradient of a scalar function, as curl of a gradient of anything is zero. Since, the curl of a vector is equal to the negative gradient of a scalar potential ($-\boldsymbol{\nabla}\phi$), we have

$$\boldsymbol{E} = -i\omega \boldsymbol{A} - \boldsymbol{\nabla}\phi \tag{4.41}$$

The scalar and vector potentials are not unique, because any function whose curl is zero can be added to $\boldsymbol{A}$ without changing the value of $\boldsymbol{B}$. To keep the electric field unique, ϕ should be changed accordingly. These changes in the scalar and vector potentials are called "gauge transformations" (Griffiths, 1999). This freedom of choosing the values of the potentials can be exploited to adjust the divergence of $\boldsymbol{A}$ (i.e., gauge fixing). The simplest choice is a vanishing divergence:

$$\boldsymbol{\nabla}.\boldsymbol{A} = 0 \tag{4.42}$$

which is called the "Coulomb gauge" (Griffiths, 1999; Jahandari, 2015).

For controlled source EM (CSEM), the source can be incorporated using a current density. Thus, if we consider the current density of EM source ($\boldsymbol{J}^s$), Faraday's and Ampère's laws in the frequency domain can be rewritten as

$$\boldsymbol{\nabla} \times \boldsymbol{E} = -i\omega \boldsymbol{B} \tag{4.43}$$

$$\boldsymbol{\nabla} \times \boldsymbol{H} = \boldsymbol{J^s} + \sigma \boldsymbol{E} \tag{4.44}$$

Thus, the E-field Helmholtz equation will be as

$$\boldsymbol{\nabla} \times \boldsymbol{\nabla} \times \boldsymbol{E} + i\mu_0 \sigma \omega \boldsymbol{E} = -i\mu_0 \omega \boldsymbol{J^s} \tag{4.45}$$

Replacing $\boldsymbol{E}$ in Equation 4.41 into the E-field Helmholtz equation we have

$$\boldsymbol{\nabla} \times \boldsymbol{\nabla} \times \boldsymbol{A} + i\mu_0 \sigma \omega \boldsymbol{A} + \mu_0 \sigma \boldsymbol{\nabla} \phi = \mu_0 \boldsymbol{J^s} \tag{4.46}$$

Using Ohm's law ($\boldsymbol{J} = \sigma \boldsymbol{E}$) and substituting Equation 4.41 into the following equation (conservation of charge)

$$\boldsymbol{\nabla}. \sigma \boldsymbol{E} = -\boldsymbol{\nabla}. \boldsymbol{J^s} \tag{4.47}$$

gives

$$i\omega \boldsymbol{\nabla}. \sigma \boldsymbol{A} + \boldsymbol{\nabla}. \sigma \boldsymbol{\nabla} \phi = \boldsymbol{\nabla}. \boldsymbol{J^s} \tag{4.48}$$

This equation and Equation 4.47 constitute a system of equations. In order to solve this system, homogeneous Dirichlet boundary conditions on $\boldsymbol{A}$ and ϕ are imposed by introducing a region Ω for the whole domain of the physical EM problem with Λ as its outer boundary. The boundary conditions are as follows

$$(\boldsymbol{n} \times \boldsymbol{A})_\Lambda = 0 \tag{4.49}$$

and

$$\phi_{\Lambda} = 0 \tag{4.50}$$

where $\boldsymbol{n}$ is the normal vector for the boundary surfaces of the domain. This means that if the EM sources are located inside the numerical domain (as in the CSEM methods) and they are far enough away from the boundaries of the domain, then the EM fields vanish on the boundaries due to the attenuation. Thus, EM fields can be considered to be zero on the boundary surfaces of the numerical domain.

The geophysical EM problem needs boundary value problem at the interfaces of the media with different EM properties as well. It also needs conditions to be satisfied on the interfaces between media with different EM properties. These interface conditions for the EM potentials can be derived by integrating Maxwell's equations in terms of the scalar and vector potentials (ϕ and $\boldsymbol{A}$) over infinitesimal Gaussian pill-boxes (Griffiths, 1999; Jahandari, 2015):

$$\boldsymbol{A}_{t1} = \boldsymbol{A}_{t2} \tag{4.51}$$

This boundary condition shows that the tangential components of the vector potential ($\boldsymbol{A}_t$) are continuous across interfaces between two media 1 and 2, so is the normal component if one is using the Coulomb gauge (i.e., to satisfy $\boldsymbol{\nabla}.\boldsymbol{A} = 0$ right on the interface).

Finally, the system of equations can be solved and discretized using numerical methods such as finite-difference approaches (Weiss, 2010), finite-volume approaches (Madsen and Ziolkowski, 1990; Jahandari and Farquharson, 2014), and finite-element approaches (Jin,

2002; Börner, 2010). In this research, the code of Ansari and Farquharson (2014) is used, which is based on the finite-element method in the frequency domain. The finite-element discretization in this research is based on the Galerkin method of weighted residuals in which a residual function is formed which gives the error (***R***) between the true solution and the approximate solution. The residual is weighted by the same basis functions (***N***) that are used for approximating the unknowns (Jahandari et al., 2017). Then, the weighted residual over the whole domain is set to zero, which then enables the approximate solution to be found. The weighted vector and scalar residuals can be written as

$$\boldsymbol{R} = \boldsymbol{N}.(\boldsymbol{\nabla} \times \boldsymbol{\nabla} \times \widetilde{\boldsymbol{A}} + i\mu_0\sigma\omega\widetilde{\boldsymbol{A}} + \mu_0\sigma\boldsymbol{\nabla}\tilde{\phi} - \mu_0\boldsymbol{J^s}) \tag{4.52}$$

$$R = N(i\omega\boldsymbol{\nabla}.\sigma\widetilde{\boldsymbol{A}} + \boldsymbol{\nabla}.\sigma\boldsymbol{\nabla}\tilde{\phi} - \boldsymbol{\nabla}.\boldsymbol{J^s}) \tag{4.53}$$

where $\widetilde{\boldsymbol{A}}$ and $\tilde{\phi}$ are approximate vector and scalar potentials, respectively. Inside each tetrahedral element these approximated potentials can be defined as (Ansari and Farquharson, 2014)

$$\widetilde{\boldsymbol{A}} = \sum_{u=1}^{6} \boldsymbol{N}_u \tilde{A}_u \tag{4.54}$$

$$\tilde{\phi} = \sum_{u=1}^{4} N_u \tilde{\phi}_u \tag{4.55}$$

where $\boldsymbol{N}_u$ and $\tilde{A}_u$ are vector basis functions and approximate vector potentials corresponding to the edges, respectively, and N_u and $\tilde{\phi}_u$ are scalar basis functions and scalar potentials corresponding to the nodes, respectively. Integrating the weighted residuals over the entire numerical domain Ω and equating to zero gives

$$\sum_{q=1}^{\bar{m}} \widetilde{A}_q \int_\Omega (\boldsymbol{\nabla} \times \boldsymbol{N}_m).\left(\boldsymbol{\nabla} \times \boldsymbol{N}_q\right) d\Omega + i\omega\mu_0 \sum_{q=1}^{\bar{m}} \widetilde{A}_q \int_\Omega \sigma \boldsymbol{N}_m.\boldsymbol{N}_q d\Omega +$$

$$\mu_0 \sum_{k=1}^{\bar{n}} \widetilde{\phi}_k \int_\Omega \sigma \boldsymbol{N}_m.\nabla N_k d\Omega = \mu_0 \int_\Omega \boldsymbol{N}_m.\boldsymbol{J}_P d\Omega \tag{4.56}$$

$$i\omega \sum_{q=1}^{\bar{m}} \widetilde{A}_q \int_\Omega \nabla N_n.\left(\sigma \boldsymbol{N}_q\right) d\Omega + \sum_{k=1}^{\bar{n}} \widetilde{\phi}_k \int_\Omega \nabla N_n.(\sigma \nabla N_k) d\Omega = -\int_\Omega N_n \nabla.\boldsymbol{J}_P d\Omega \tag{4.57}$$

where $\bar{m}$ and $\bar{n}$ are the numbers of edges and nodes in the mesh, respectively, $m = 1, \ldots, \bar{m}$ and $n = 1, \ldots, \bar{n}$. These two equations are solved for the coefficients $\tilde{A}_q$ of the approximate vector potential and the coefficients $\tilde{\phi}_k$ of the approximate scalar potential. When the system has been solved for the real and imaginary parts of the vector and scalar potentials, the electric field can be obtained using Equation 4.41. Also, the magnetic field can be calculated by taking the curl of the vector potential and using the edge-element basis functions as

$$\boldsymbol{H} = \frac{1}{\mu_0} \sum_{q=1}^{\bar{m}} \tilde{A}_q \boldsymbol{\nabla} \times \boldsymbol{N}_q \tag{4.58}$$

4.5 Inverse theory

The inversion approach used in this research is that of the code of Lelièvre et al. (2012). This uses the minimum-structure approach in which an objective function is minimized using a Gauss-Newton method. It should be noted that inversion problems are not typically well-posed problems. This means that they do not usually satisfy the three conditions 1-existence, 2-uniqueness and 3-stability of a solution. In these cases, regularization helps to solve the inversion problem. For a single dataset, the typical objective function can be written as

$$\boldsymbol{\Phi} = \phi_d + \beta\phi_m \tag{4.59}$$

where β is the trade-off parameter which controls the relative contributions of the data misfit term (ϕ_d) and the regularization (or model) term (ϕ_m). The data misfit term controls the fit to the data, and the regularization term controls the amount and type of structure in the recovered model (Lelièvre and Oldenburg, 2009). The data misfit and regularization terms have the general forms

$$\phi_d = \phi_d(\boldsymbol{u}) \tag{4.60}$$

$$\phi_m = \sum_k \alpha_k \phi_k(\boldsymbol{v}_k) \tag{4.61}$$

where $\alpha_k$is a constant value, and

$$\boldsymbol{u} = \mathbf{W}_d(\boldsymbol{d}^{obs} - \boldsymbol{d}^{prd}) \tag{4.62}$$

$$\boldsymbol{v}_k = \mathbf{W}_k\left(\boldsymbol{m} - \boldsymbol{m}_k^{ref}\right) \tag{4.63}$$

where $\boldsymbol{d}^{obs}$ is the vector of observed data, $\boldsymbol{d}^{prd}$ is the vector of data calculated for the vector, **m**, of model parameters, and the data-weighting matrix, $\mathbf{W}_d$, is a diagonal matrix whose elements are the reciprocals of the estimates of the standard deviations of the noise in the observations (Farquharson, 2008). The data misfit, ϕ_d, can be written as

$$\phi_d = \sum_{i=1}^{N} \left(\frac{d_i^{prd} - d_i^{obs}}{\sigma_i}\right)^2 \tag{4.64}$$

where N is the number of measured data, and σ_i are the estimated uncertainties. In the code of Lelièvre et al. (2012), if the uncertainty value is unknown, it will be considered to be 5% of the datum. Also, ϕ_m can be written as

$$\phi_m = \alpha_s \phi_s(\boldsymbol{W}_s(\boldsymbol{m} - \boldsymbol{m}^{ref})) + \alpha_t \phi_t(\boldsymbol{W}_t \boldsymbol{m}) \tag{4.65}$$

where $\boldsymbol{W}_s$ contains cell volume information, $\boldsymbol{W}_t$ calculates model differences between adjacent grid cells (weighted by cell volumes), and α_s and α_t are constant values during the inversion which are used to adjust the relative amount of structure recovered in the physical property models. Thus, the objective function can be written as (Farquharson and Oldenburg, 1998)

$$\boldsymbol{\Phi} = \phi_d(\mathbf{W}_d(\boldsymbol{d}^{obs} - \boldsymbol{d}^{prd})) + \beta[\alpha_s \phi_s(\boldsymbol{W}_s(\boldsymbol{m} - \boldsymbol{m}^{ref})) + \alpha_t \phi_t(\boldsymbol{W}_t \boldsymbol{m})] \tag{4.66}$$

To solve the inverse problem, we minimize $\boldsymbol{\Phi}$ by differentiating with respect to the model parameters, $\boldsymbol{m}$, and equating the resulting derivatives to zero.

In a general form, ϕ_d and ϕ_m can be written as

$$\phi(\boldsymbol{x}) = \sum_j \gamma(x_j) \tag{4.67}$$

The measure proposed by Ekblom (1973, 1987), used in this research, is a modified version of the l_p norm:

$$\gamma(x) = (x^2 + \varepsilon^2)^{p/2} \tag{4.68}$$

where ε is a very small positive number, and p is the order of norm (e.g. p=1 and p=2 for

L1-norm and L2-norm, respectively). The final linear system of inversion equations obtained by minimizing the objective function $\boldsymbol{\Phi}$ is

$$[\beta\alpha_s \boldsymbol{W}_s^T \boldsymbol{R}_s \boldsymbol{W}_s + \beta\alpha_t \boldsymbol{W}_t^T \boldsymbol{R}_t \boldsymbol{W}_t + \boldsymbol{G}^T \boldsymbol{W}_d^T \boldsymbol{R}_d \boldsymbol{W}_d \boldsymbol{G}]\boldsymbol{m} = \boldsymbol{G}^T \boldsymbol{W}_d^T \boldsymbol{R}_d \boldsymbol{W}_d \boldsymbol{d}^{obs} + \beta\alpha_s \boldsymbol{W}_s^T \boldsymbol{R}_s \boldsymbol{W}_s \boldsymbol{m}^{ref} \quad (4.69)$$

where $\boldsymbol{G}$ is a kernel or Jacobian matrix for the general non-linear case that contains all the physics of this problem, and T indicates the transpose of a matrix. Since $\boldsymbol{R}_s$, $\boldsymbol{R}_t$ and $\boldsymbol{R}_d$ are diagonal matrices depending on the model $\boldsymbol{m}$, this equation is non-linear. This problem can be solved with an iterative procedure:

$$\boldsymbol{m}^{k+1} = \boldsymbol{M}_k^{-1} \boldsymbol{y}^k \quad (4.70)$$

where

$$\boldsymbol{M}_k = \left[\beta\alpha_s \boldsymbol{W}_s^T \boldsymbol{R}_s^k \boldsymbol{W}_s + \beta\alpha_t \boldsymbol{W}_t^T \boldsymbol{R}_t^k \boldsymbol{W}_t + \boldsymbol{G}^T \boldsymbol{W}_d^T \boldsymbol{R}_d^k \boldsymbol{W}_d \boldsymbol{G}\right] \quad (4.71)$$

and

$$\boldsymbol{y}^k = \boldsymbol{G}^T \boldsymbol{W}_d^T \boldsymbol{R}_d^k \boldsymbol{W}_d \boldsymbol{d}^{obs} + \beta\alpha_s \boldsymbol{W}_s^T \boldsymbol{R}_s^k \boldsymbol{W}_s \boldsymbol{m}^{ref} \quad (4.72)$$

where k is the iteration number and $\boldsymbol{R}_d^k = \boldsymbol{R}_d(\boldsymbol{m}^k)$, etc. At the first iteration, for the starting model, $\boldsymbol{R}_s = \boldsymbol{R}_t = \boldsymbol{R}_d = \boldsymbol{I}$ where $\boldsymbol{I}$ is the identity matrix. These matrices will be computed at each iteration in order to solve the inversion equation to obtain a new model. The iterations are terminated when the model no longer changes by a significant amount.

The iteration procedure of the inversion code (Lelièvre et al., 2012) will terminate when

"*omega (ω)*" reaches 1. This means that a good fit between the observed and calculated data is obtained (Carter-McAuslan et al., 2013). Therefore, the normalized data residuals should ideally reach zero on average (or close to zero and between -1 and 1).

$$\text{Normalized Data Residual} = \frac{d_i^{cal} - d_i^{obs}}{\sigma_i} \tag{4.73}$$

where d_i^{cal} is the *i*th datum calculated by the model constructed by the inversion, d_i^{obs} is the *i*th datum from the (observed) dataset that was provided for the inversion, and σ_i is the uncertainty on the *i*th datum.

The fitting can be controlled by changing the value of "*chifact*". "*chifact*" and "$omega$" (ω) are

$$chifact = \frac{target\ misfit\ (\phi_d^*)}{number\ of\ data\ (N)} \tag{4.74}$$

$$omega\ (\omega) = \frac{data\ misfit\ (\phi_d)}{target\ misfit\ (\phi_d^*)} \tag{4.75}$$

The use of *chifact* to yield the optimal model is based upon the assumption that noise and error on the data are random and have a Gaussian distribution. Thus, if uncertainties are well chosen, the appropriate target misfit will have a value of *N* (number of data) and hence a *chifact* of 1. For noisy data, if we know the standard deviations of the noise in each measurement we should be able to get to a target misfit of N (*chifact* of 1). If we do not know the standard deviations of the noise for each data value, we can guess them. If our guessed standard deviations are too small, then we will probably need to aim for a target

misfit that is larger than *N*, and if our guessed standard deviations are too big, we should really end up with a misfit lower than *N*. Therefore, for noisy data the target misfit may have to be larger than *N*, thus *chifact* would be specified as more than 1. And, for clean data, *chifact* can be set less than 1.

Therefore, the code inverts by searching and finding a value for the trade-off parameter β that provides a misfit value close to the number of data (target misfit, and $\omega = 1$). A typical procedure is that the value of β reduces slowly from one iteration to the next from an initially large value. By decreasing values of β, a model can be obtained that fits the data better but that contains more structure. However, a very low value of β can fit noise in the data which leads to spurious structures in the model (Lelièvre et al., 2012). In the code of Lelièvre et al. (2012), β can be controlled and reduced using

$$\beta^{(k+1)} = \frac{\beta^{(k)}}{\nu_\beta} = \frac{\beta^{(k)}}{1+\tau_\beta|\omega-1|} \tag{4.76}$$

where $\tau_\beta = 1$, and $\nu_\beta \in [1+\epsilon, 2]$ with ϵ some small value (i.e. here 0.05). The value of ν_β should lie on $[1+\epsilon, 2]$ so that the adjustment of β is neither too large nor too small from one iteration to the next. During the inversion process, various parts of the objective function such as data misfit term (ϕ_d), model term (ϕ_m), and the objective function itself ($\mathbf{\Phi}$) and trade-off parameter (β) change at each iteration. Ideally, their values decrease during the inversion process except the value of the model term which increases.

4.5.1 Joint inversion

Independent single-property inversion can often encounter difficulties when the geology is complicated. Inverting a data-set jointly with another complementary data-set can solve and improve the construction of a single Earth model. This process is called joint inversion. With two data-sets in the joint inversion, the objective function can be written as (Lelièvre et al., 2012)

$$\boldsymbol{\Phi}(\boldsymbol{m}_1, \boldsymbol{m}_2) = \lambda_1 \phi_{d1}(\boldsymbol{m}_1) + \lambda_2 \phi_{d2}(\boldsymbol{m}_2) + \alpha_1 \phi_{m1}(\boldsymbol{m}_1) + \alpha_2 \phi_{m2}(\boldsymbol{m}_2) + \Phi_j(\boldsymbol{m}_1, \boldsymbol{m}_2)$$

$$= \lambda(\phi_{d1}(\boldsymbol{m}_1) + \gamma \phi_{d2}(\boldsymbol{m}_2)) + \alpha_1 \phi_{m1}(\boldsymbol{m}_1) + \alpha_2 \phi_{m2}(\boldsymbol{m}_2) + \Phi_j(\boldsymbol{m}_1, \boldsymbol{m}_2) \qquad (4.77)$$

where the two ϕ_d and two ϕ_m terms are the data misfit and regularization terms for each of the two data sets $\boldsymbol{d}_1$ and $\boldsymbol{d}_2$ and models $\boldsymbol{m}_1$ and $\boldsymbol{m}_2$, respectively. And, α_1 and α_2 are constant parameters for adjusting the relative amount of structure constructed in the models. By increasing one of them, the influence of the related data-set on the constructed models will be more than the other. Lelièvre et al. (2012) position the trade-off parameters $\lambda_1 (= \lambda)$ and $\lambda_2 (= \lambda\gamma)$ in front of the data misfit terms (instead of regularization terms). In order to avoid confusion, λ is used instead of β as the symbol for the tradeoff parameters when multiplying the data misfit terms. The coupling term, Φ_j, is a quantity that gets larger the more unlike the models are and is hence a measure of the dissimilarity between the two models:

$$\Phi_j = \sum_i \rho_i \Psi_i(\boldsymbol{m}_1, \boldsymbol{m}_2) \qquad (4.78)$$

where ρ_i is the coupling factor, and Ψ_i is a joint coupling measure which is defined below.

The iteration procedure of the joint inversion code of Lelièvre et al. (2012) will terminate when an average "ω" reaches unity, where

$$\omega = \frac{(\omega_1+\omega_2)}{2} = \frac{(\frac{\phi_{d1}}{\phi^*_{d1}}+\frac{\phi_{d2}}{\phi^*_{d2}})}{2} \tag{4.79}$$

The joint inversion algorithm searches for the appropriate values of parameters λ and γ to have both misfits equal their respective targets. The approach is to set γ to some value (initially equal to 1) and then search for the value of λ that best yields the target misfits. Then γ can be adjusted as misfits move toward their targets. The value of λ can be calculated using

$$\lambda^{(k+1)} = \lambda^{(k)}\, \nu_\lambda = \lambda^{(k)}\, (1 + \tau_\lambda |\frac{\omega_1+\omega_2}{2} - 1|) \tag{4.80}$$

where $\tau_\lambda = 1$, and $\nu_\lambda \in [1+\epsilon, 2]$. In this case, the value of ν_λ multiplies the value of λ such that it slowly increases. After adjusting λ, we can adjust γ using

$$\gamma^{(k+1)} = \gamma^{(k)}\, \nu_\gamma = \gamma^{(k)}\, (1 + \tau_\gamma(|\omega_1 - 1| + |\omega_2 - 1|)) \tag{4.81}$$

where $\tau_\gamma = 2$, and $\nu_\gamma \in [1+\epsilon, 2]$. The process of adjusting λ and γ values will go on at each iteration until the misfits reach to their targets, and "ω" reaches 1.

Since there are several possible measures for the joint coupling measure (Ψ_i), there are different types of possible coupling. In this research, the fuzzy c-mean clustering method and the correlation method have been used. In the fuzzy c-mean method, a relationship between the physical properties can be specified that lies in discrete clusters (Paasche and

Tronicke, 2007):

$$\Psi(\boldsymbol{r},\boldsymbol{s}) = \sum_{i=1}^{C}\sum_{k=1}^{M} w_{ik}^{f} z_{ik}^{2} = \sum_{i=1}^{C}\sum_{k=1}^{M} w_{ik}^{f}((r_k - u_i)^2 + (s_k - v_i)^2) \tag{4.82}$$

where C is the number of clusters, M is the number of cells, and f is typically set to a value of 2. The term w_{ik} relates the model parameter set (physical property values) for the kth cell to the ith cluster (Lelièvre et al., 2012). Vectors **r** and **s** are two inversion models (e.g. density and slowness models) on a grid containing M cells, and (u_i, v_i) defines the ith cluster location in physical property space. This method can be used where there is not a strict linear relationship between the physical properties, and therefore a statistical relationship between the two physical properties can be used. Thus, the physical properties of geological structures should be used as initial/input information in the inversion code. Also, the coupling factor (ρ) needs to be provided to the code. If ρ is set too low, there won't be enough similarity imposed between the two models. By increasing the ρ value and imposing a greater degree of similarity the model begins to improve (although this can make the inverse problem harder to solve).

In the correlation method for joint inversion a statistical relationship between the two physical properties is used. In this method a correlation measure from statistics is used, which measures the degree of the implicit linear relationship between two sets of values. It does not require any knowledge of the range of the physical properties. The correlation measure is

$$\Psi(\boldsymbol{r},\boldsymbol{s}) = \left(\frac{\sum_{i=1}^{M}(r_i-\mu_r)(s_i-\mu_s)}{M\sigma_r\sigma_s} \pm 1\right)^2 \tag{4.83}$$

where M is the number of cells in the model, r_i and s_i are the two physical properties (e.g. density and slowness) of the ith cell, σ_r and σ_s are the standard deviations, and μ_r and μ_r are the means of the physical property distributions. The positive or negative linear correlation between the physical properties can be defined by choosing the negative or positive sign in the equation. Both fuzzy c-mean and correlation methods are considered as "compositional" approaches, because their coupling defines a relationship between the physical properties involved.

4.5.2 Depth/distance weighting

Note that magnetic and gravity data have no inherent depth resolution (Li and Oldenburg, 1998). Therefore, using a typical minimum-structure inversion method the values close to the observation points will be varied the most, as these locations have the strongest sensitivity via the Jacobian matrix. To deal with this, the objective function (the model norm part) includes a term to overcome the natural decay of the field (which is $1/r^2$ for the gravity and $1/r^3$ for the magnetic method, where r is distance between causative feature and sensor). Lelièvre et al. (2012) considered a "depth weighting" for a cell as

$$(z - w_z)^{-w_p} \tag{4.84}$$

where z is the depth of the cell centroid, w_z is the average survey height in the input coordinate system, and w_p is a constant. For surface data, the sensitivity (effect of a feature on a measurement) decays in the depth direction so a weighting which overcomes the decay in the vertical direction is appropriate, so long as the elevation of measurements is properly

accounted for. Lelièvre et al. (2012) considered a "sensitivity weighting" for the *j*th cell as (Li and Oldenburg, 2000b)

$$W_j = \sum_{i=1}^{N} \left(\left| \frac{g_{ij}}{v_j} \right|^{w_n} \right)^{(w_b/w_n)} \tag{4.85}$$

where N is the number of data, g is a column of the sensitivity matrix, v is the cell volume, and w_n and w_b are constants. Sometimes a weighting function that varies in three dimensions is needed (e.g. for data sets that contain borehole measurements). Therefore, a generalized version of depth weighting called "distance weighting" is used which accounts for the distance between each model cell and measurement. Lelièvre et al. (2012) considered the "distance weighting" for the *j*th cell as (Li and Oldenburg, 2000b)

$$W_j = \sum_{i=1}^{N} \left(|r_{ij} + w_z|^{(-w_p \times w_n)} \right)^{(w_b/w_n)} \tag{4.86}$$

where r is the distance between cell centroids and observation points. For the distance weighting, w_z should be a small value, such as half the smallest cell dimension.

4.5.3 Constraints via reference model and bounds

In this thesis, triangular cells (for 2D) and tetrahedral cells (for 3D) are used for all inversion meshes (as well as modelling meshes). The advantage of these meshes, in comparison with rectangular and rectangular cube meshes, is the ability of modelling an accurate topography. Also, the constrained inversion method used in this thesis is based on the two methods: 1- constraining by being close to the reference model, 2- constraining via upper and lower bounds. In the first constraining method, there are two "reference" and

"weight" models which use the same mesh as the model being constructed. Each number in the "reference" model represents a physical property value, and each number in the "weight" model is a weight given to the equivalent physical property value in the "reference" model. By increasing the weight of a cell, the initial physical property considered in the "reference" model for the cell will change less during the inversion process. For the second constraining method, called Gradient-Projection-Reduced-Newton method (Vogel, 2002; Lelièvre, 2003), the basic idea is that at any given point in the minimization there are some solution parameters on the bounds (referred to as "active") and others between bounds (referred to as "inactive"). A Newton step is performed with the inactive parameters but "project" the step. So we will have

$$\boldsymbol{m}(k+1) = \boldsymbol{m}(k) + \alpha\delta\boldsymbol{m} \tag{4.87}$$

where $\boldsymbol{m}(k)$ is the inactive part of the current model, $\boldsymbol{m}(k+1)$ is the inactive part of the model after the step, $\delta\boldsymbol{m}$ is the step direction for the inactive part of the model, and α is the step length. Then a value of α is sought that reduces the objective function, but the projection means that every time a value of α is tried, the candidate $\boldsymbol{m}(k+1)$ onto the bounds should be projected, which basically means that if any parameters move past their bounds then they will be set to their bounds. For a quadratic minimization problem, $\alpha = 1$ but when the projected step is done it should be tried harder. After doing that, then the active and inactive sets will be recalculated and a projected gradient step will be done, which is a gradient step with only the active set. This step allows the active parameters (those on the bounds) to jump off of the bounds if needed. Those two steps will be

alternated. In this constraining method, the physical property of each cell can be controlled by upper and lower bounds. A wider range of the bounds gives more freedom to the inversion code to assign an appropriate value. When the physical property of a cell is known (e.g. from borehole data), the range of the bounds can be as narrow as having both bounds share the same value.

4.5.4 Heating schedules

In the code of Lelièvre et al. (2012), inversions start from an initial model which can be a model with uniform values of physical properties. Since the minimum structure method (the method used in the inversion) is not dependent on the initial model, the assigned values can be zero except for the seismic method for which the values should be more than zero. For the joint inversion there are two initial models/values for one mesh. And, for each of the two data-types we need to consider specific values for the *chifact* and trade-off parameter (β). In the code of Lelièvre et al. (2012), the process of joint inversion (i.e., how the trade-off parameter(s) is varied during an inversion) can be run in different ways: heating joint inversion without pre-heating (JwP) and heating joint inversion after pre-heating (JaP). In the "JwP", the joint inversion directly starts by considering the coupling factor, thus the inversion will converge when both *omega* values of the two data-sets as well as the total *omega* value (related to the all data misfit terms in the objective function) reach to 1. The coupling factor can be heated in different stages in which each stage is a separate and complete process of joint inversion. The number of stages can be defined by the user. During these stages, the coupling factor starts from a smaller value than the

assigned value, and in each stage the value of the coupling factor will increase until it reaches the assigned value in the final stage. The models and trade-off parameters obtained in each stage will be used as initial models and initial trade-off parameters in the next stage. In the “JaP”, the objective function is first minimized without any joint coupling (which is called "stage 0"), followed by heating in the joint coupling measure over one/several stage(s).

4.5.5 1D EM inversions

In the codes EM1DFM (Farquharson and Oldenburg, 2000) and EM1DTM (Farquharson and Oldenburg, 2006), which are 1D modelling and inversion codes for electromagnetic frequency- and time-domain data, the general concept of the objective function is the same as mentioned before (see equation 4.59; Farquharson and Oldenburg, 2004). Also for the 1D case, rather than the (triangular or tetrahedral) mesh we have layers. Since the inverse problem is nonlinear, it is solved using an iterative procedure. In the misfit ϕ_d and at the nth iteration, the forward-modelled data $\mathbf{d}^n$ are those for the model that is sought at this iteration. They are approximated by:

$$\mathbf{d}^n = \mathbf{d}^{n-1} + \mathbf{J}^{\sigma,n-1}\delta\mathbf{m}^{\sigma} \tag{4.88}$$

where $\delta\mathbf{m}^{\sigma} = \delta\mathbf{m}^{\sigma,n} - \delta\mathbf{m}^{\sigma,n-1}$and $\mathbf{J}^{\sigma,n-1}$ is the Jacobian matrix given by the equation 4.89 and evaluated for the model from the previous iteration. At the nth iteration, the problem to be solved is that of finding the change, $\delta\mathbf{m}^{\sigma}$, to the model which minimizes the objective function $\mathbf{\Phi}^n$.

$$\mathbf{J}_{ij}^{\sigma} = \frac{\partial \mathbf{d}_i}{\partial log \sigma_j} \tag{4.89}$$

$\mathbf{d}_i$ is the *i*th observation, and σ_j is the conductivity of the *j*th layer. There are different methods to find the appropriate value for the trade-off parameter, but I have used the generalized cross-validation (GCV; Haber, 1997; Haber and Oldenburg, 2000; Farquharson and Oldenburg, 2004) method in which the trade-off parameter is automatically chosen using the GCV criterion. As a conceptual description, the GCV method is based on inverting all but the first observation using a trial value of β, and then computing the individual misfit between the first observation and the first forward-modelled datum for the model produced by the inversion (for linear problems). This can be repeated leaving out all the other observations in turn using the same value of β. The best value of β can then be defined as the one which gives the smallest sum of all the individual misfits. The GCV function for the *n*th iteration is given by:

$$GCV(\beta) = \frac{\|\boldsymbol{W}_d(d^{obs} - d^{n-1}) - \boldsymbol{W}_d \boldsymbol{G}^{\boldsymbol{n-1}} \boldsymbol{M}^{-1}(\boldsymbol{G}^{n-1T} \boldsymbol{W}_d^T \boldsymbol{W}_d (d^{obs} - d^{n-1}) + \beta \sum_{i=1}^{2} \boldsymbol{W}_i^T \boldsymbol{W}_i (\boldsymbol{m}_i^{ref} - \boldsymbol{m}^{n-1}))\|^2}{[trace(\boldsymbol{I} - \boldsymbol{W}_d \boldsymbol{G}^{n-1} \boldsymbol{M}^{-1} \boldsymbol{G}^{n-1T} \boldsymbol{G}_d^T)]^2} \tag{4.90}$$

where

$$\boldsymbol{M}(\beta) = \boldsymbol{G}^{n-1T} \boldsymbol{W}_d^T \boldsymbol{W}_d \boldsymbol{G}^{n-1} + \beta \sum_{i=1}^{2} \boldsymbol{W}_i^T \boldsymbol{W}_i \tag{4.91}$$

If β^* is the value of the trade-off parameter that minimizes GCV function at the *n*th iteration, the actual value of β used to compute the new model is given by:

$$\beta^n = \max(\beta^*, bfac \times \beta^{n-1}) \tag{4.92}$$

where the user-supplied factor *bfac* is such that 0.01 < *bfac* < 0.5. Also, the codes are considered to have converged when both of the following equations are satisfied (Gill et al., 1981).

$$\boldsymbol{\Phi^{n-1} - \Phi^{n}} < \vartheta(1 + \boldsymbol{\Phi}^{n}) \tag{4.93}$$

$$\| \boldsymbol{m}^{n-1} - \boldsymbol{m}^{n} \| < \sqrt{\vartheta}(1 + \| \boldsymbol{m}^{n} \|) \tag{4.94}$$

where ϑ is a user-specified parameter with a default value of 0.01.

4.5.6 Meshes

In this research, "Triangle" (Shewchuk, 1996) and "Tetgen" (Si, 2015) codes are used to generate 2D triangular and 3D tethrahedral meshes, respectively. Many codes are used in order to do format conversion, data processing and model processing as well (see appendix A; Lelièvre and Farquharson, 2015). Models and results are mostly shown using Paraview software (www.paraview.org). Data are plotted using the Generic Mapping Tools (GMT; Wessel and Smith, 1991). For the modelling and inversions, the meshes larger than 50,000 cells use a computing environment which has a 600-core, 14-GPU hybrid CPU/GPU computer cluster with up to 64 GB of RAM. And, the meshes smaller than the 50,000 cells use a computing environment which has a 4-core CPU with up to 32 GB of RAM.

4.6 Summary

Forward modelling is a mathematical solution to calculated data from the model parameters while inversion is a mathematical process of estimating the model parameters from the

observed data. Therefore, the forward modelling can be a part of the inversion process. For the forward modelling, the gravity and magnetic methods can be solved easily using the analytical solution but the seismic and electromagnetic methods should be solved by the numerical methods such as finite difference and finite element methods.

There are many inversion methods. In this research, we use the minimum structure approach in which an objective function is minimized using a Gauss-Newton method. Due to the complicated geology, joint and constrained inversions can also help to improve the results. Joint inversion can be defined as inverting a data-set jointly with another complementary data-set. Also, the constrained inversion method can be based on the two methods: 1- constraining by being close to the reference model; 2- constraining via upper and lower bounds. Inversion methods (particularly the joint and constrained) that are going to be investigated as the main tool in this thesis as means to "strip" the overburden contribution.

Chapter 5

Gravity Forward Modelling of the Athabasca Basin

5.1 Introduction

As mentioned before, using the forward modelling we will be able to synthesize the data in order to compare with real data to investigate the subsurface. The gravity data involves the variations in the density of geophysical structures. Therefore, forward modelling of gravity data can give us a better understanding of relationship between the gravity data and variations in density.

Synthesizing the gravity response of different components of the geology in the McArthur-Millennium corridor, and as a result assessing the size and character of the various responses, will be done in this chapter. This includes the "target" responses, i.e., alteration zones in the sandstones, as well as all the other non-target responses/signals including from the overburden/glacial sediments and basement.

In this chapter, two synthetic models will be built up component by component, with the gravity contribution being assessed component by component in order to investigate the free-air and Bouguer anomalies of the McArthur-Millennium region. Realistic models were built taking into account everything that is known (such as topography as well as location of structures from boreholes) and structures that are estimated or speculated (such as base of overburden and unconformity) as wells as allowing an assessment to be made of the various contributions to gravity data. The data-sets generated here will be used to test inversion procedures for overburden stripping in subsequent chapters.

5.2 3D gravity forward modelling of an anomaly

The size, depth and density of heterogeneities have the strongest effects on gravity data, whereas the shape has less effect. As a first example of 3D modelling, gravity data were synthesized using the forward modelling code of Lelièvre et al. (2011) for one irregular-shaped anomaly and one cylinder-shaped anomaly (Figure 5.1).

In Figure 5.2, it can be seen that the gravity response due to the cylinder with a diameter of 300 m (shown by grey color in Figures 5.1 and 5.2) is similar to that due to the irregular, more realistic, density anomaly (red color) at the same depth and of the same density (2.47 g/cc). The centre of cylinder is located at depth 400 m (from the observation points). There is no topography in this modelling as all stations along the profile have the same elevation. This comparison is done only to show that the shape of anomaly has less effect on the gravity data as in this thesis I have used both cylinder- and irregular-shaped anomalies.

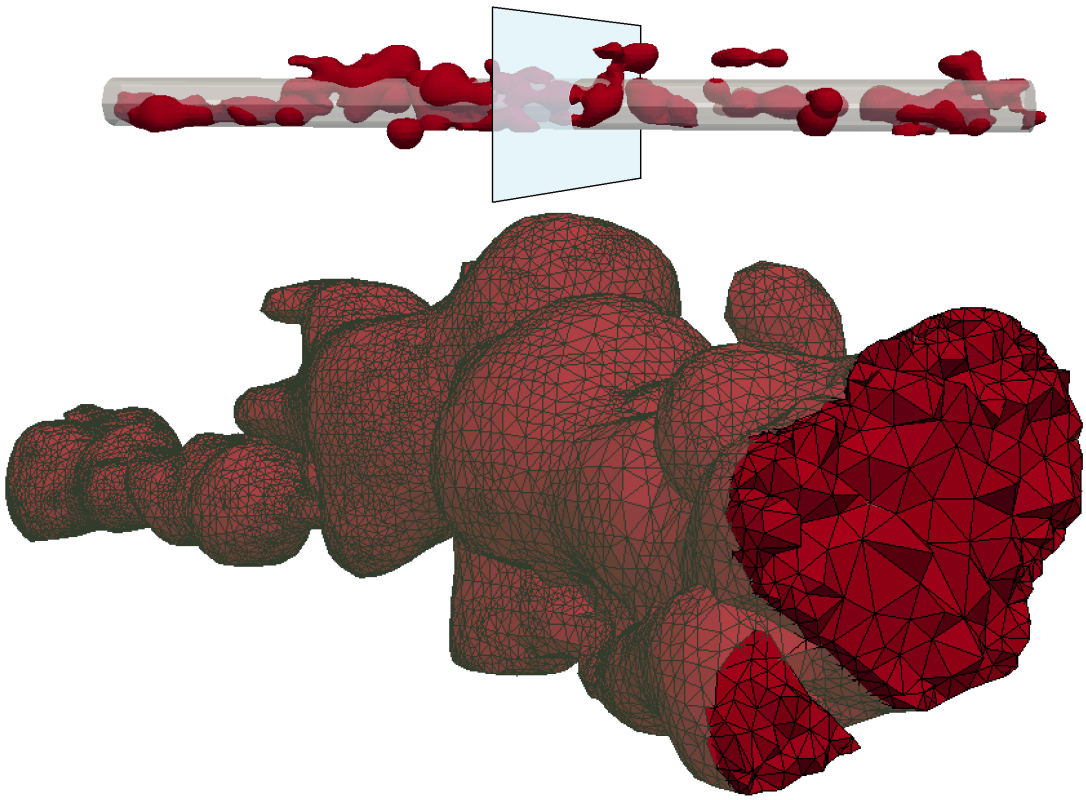

Figure 5.1: Top: models (irregular & cylinder) viewed from side, and the plane of cross-section. Bottom: cross-section of 3D tetrahedral mesh of irregular body.

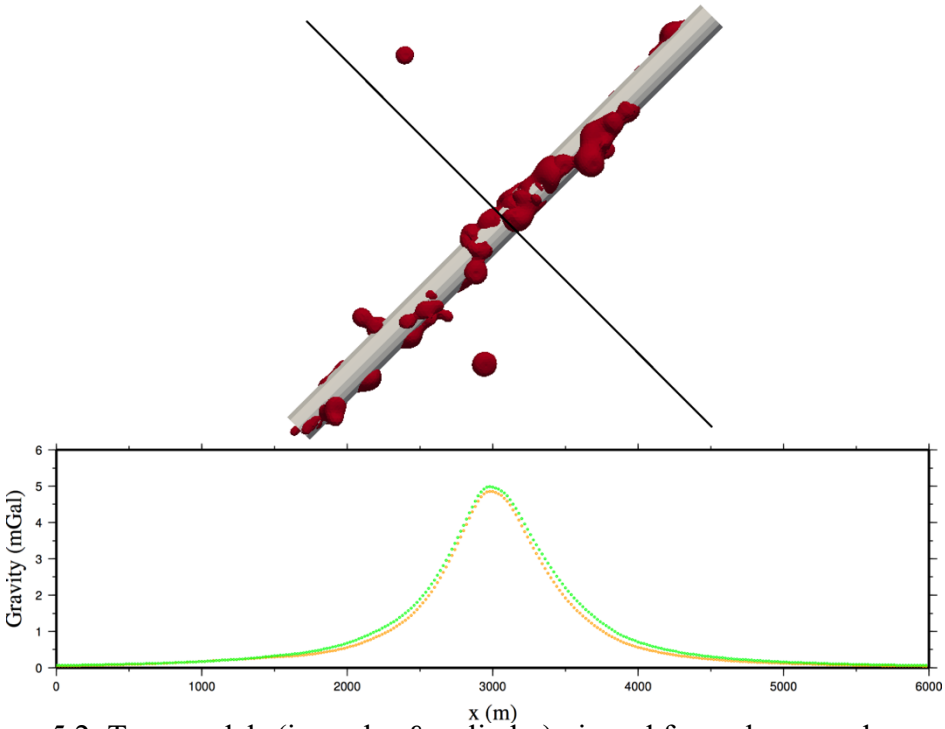

Figure 5.2: Top: models (irregular & cylinder) viewed from above, and a survey line (black line) of length 6 km. Bottom: gravity data over the cylinder (green) and irregular density anomaly (orange). Density contrast for both models is 2.47g/cc.

Here, in order to make the irregular anomaly I used the isosurfaces of SWIR data collected on core extracted from drill-holes (modified by GOCAD software; www.pdgm.com). The SWIR 3D shells represent an isotropic estimate of the 3D distribution of alteration minerals (altered clays such as illite, drivite, kaolinite, dickite and chlorite). They are a function of drilling distribution so require knowledge of the drill-hole locations. The shells are generated based on cut off percentage values, which means all data inside the threshold will be equal or higher than a specified percent value. For example, dravite_65 captures all data points having a value of 65% or higher in Dravite content. SWIR data is considered to be the best direct representation of the clay alteration halos. Note that the "alteration zone" is actually weak, with only a small amount of clay typically around 1% being present. Thus, 65% dravite in clays, might mean 0.65% dravite and 0.35% by volume of another clay in 99% quartz (see Section 2.2).

5.3 Modelling of free-air and Bouguer anomalies (McArthur area #1)

For geological models, gravity data computed directly using the code of Lelièvre et al. (2011) are equivalent to the free-air anomaly data. In these modelling, a datum (mostly sea level) is considered as the "reference ellipsoid". The layers (or structures) above the reference ellipsoid have real densities while the layers (or structures) below the reference ellipsoid have relative density (see Chapter 3.2.3).

relative density = (real density of the structure) – (reference density)

Reference density for below the reference level usually equals to 2.67 g/cc (the average

density of the Earth's crust). The Bouguer anomaly is calculated after applying the Bouguer correction on the free-air anomaly (see Section 3.2.3). Two main scenarios (#1 and #2) are considered in this chapter in order to investigate the free-air and Bouguer anomalies in the McArthur area based on Wood and Thomas (2002; see Figure 3.32) and Thomas and Wood (2007; see Figure 3.33), respectively. The structure of the basement is the main difference between these two models. These models were generated before the basement model in the CMIC model was completed (see Section 8.4 and Figure 8.17). The McArthur area is chosen for modelling because of the previous studies of geology, geophysics and physical properties for this area, as it can be seen from the two papers mentioned above.

For the scenario #1, gravity data (free-air and Bouguer anomalies) were computed for 3D models for the McArthur area based on Wood and Thomas (2002; Figure 5.3). Models varied from simple to complicated in order to investigate and better understand the different contributions to gravity data. The complicated model (which is the last one; Model 8 in Table 5.1) tried to be similar to the model shown in Figure 5.3 in densities, the basement structure and the thickness of the model. But the interfaces (topography, top of sandstone and unconformity) are modified using the available borehole and elevation data from the CMIC-Footprints project. In this scenario (#1), densities of 1.85 g/cc, 2.42 g/cc, 2.47 g/cc are considered for the overburden, sandstone and alteration zone, respectively. For the blocks in the basement different densities ranging from 2.66 g/cc to 2.74 g/cc are used.

In the following, each model is similar to the previous model, but with a small difference. Table 5.1 briefly demonstrates some of the characteristics of the models. The images of the 3D models in this section show the central 5 by 5 km. The actual 3D models

used for the computations had a size of 500 by 500 km in order to avoid any effect of the edges on the gravity data. The primary effect of the padded region is to shift the data by a constant value. The requirement for such a big model, for which the edges no longer affect the computed data, is because we want to have the option of modelling for real densities, not just anomalous densities for which large parts of the model could be zero.

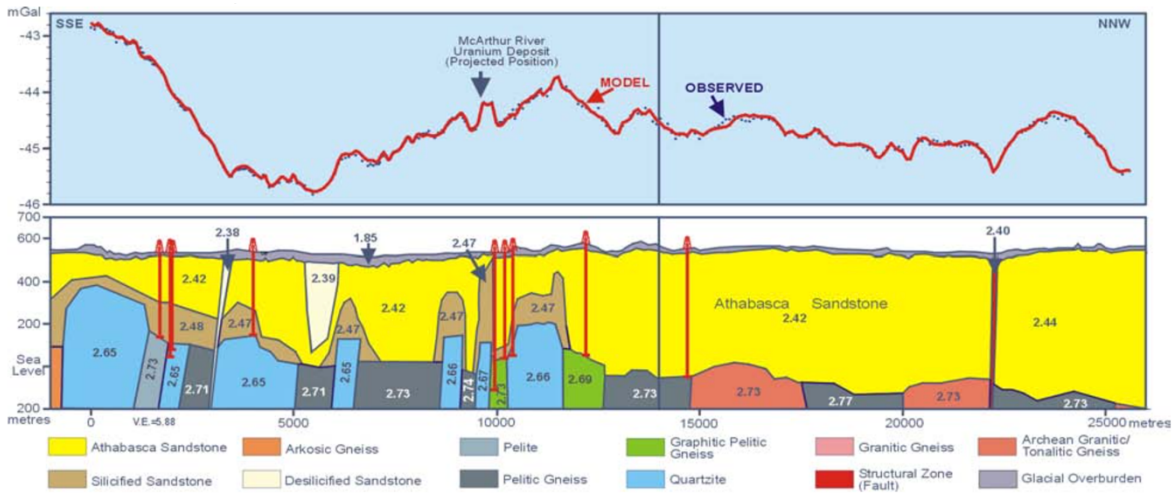

Figure 5.3: Density model made for gravity data along a profile crossing the McArthur area in the Athabasca Basin (Wood and Thomas, 2002).

Table 5.1: Characteristics of the models.

	Number of layers	Topography	Interface(s)	Datum in BC	Reference ellipsoid	Thickness of model	Anomaly
Model 1	2	flat	flat	at 0m	at 0m	950m	-
Model 2	2	real	flat	at 0m	at 0m	~1000m	-
Model 3	2	real	flat	at 500m	at 500m	~1000m	-
Model 4	2	real	flat	at 500m	at 500m	~1000m	cylinder
Model 5	2	real	real	at 500m	at 500m	~1000m	cylinder
Model 6A	3	real	flat	at 500m & 0m	at 0m	~1000m	cylinder
Model 6B	3	real	flat	at 500m & 0m	at 500m	~1000m	cylinder
Model 6C	3	real	flat	at 500m & 0m	at 500m	~1000m	cylinder
Model 7	3	real	flat	at 500m	at 500m	~5000m	cylinder
Model 8A	3	real	real	at 0m & upper real interface	upper real interface	~5000m	irregular (small)
Model 8B	3	real	real	upper real interface	upper real interface	~5000m	irregular(big)

The effect of the edge can be seen in Table 5.2, in which three models are tested with sizes 20×20 km, 100×100 km and 500×500 km. All models are made of a simple block (layer) with a density of 2 g/cc. The observation point is located at the centre of the model on the surface (0 m elevation). Gravity data are calculated for these three models, and then the Bouguer correction is applied on the data. For the Bouguer correction a density of 2 g/cc is considered, thus it is expected that the Bouguer anomaly (= gravity data – Bouguer correction) will be equal to zero (see Section 3.2.3). Table 5.2 shows that by (laterally) increasing the size of the model, the Bouguer anomalies are getting close to zero. It also shows the effect of the thickness of layer (10 m and 100 m) on the gravity data and the Bouguer anomaly. It's not so much that the Bouguer anomaly calculated for the slab is zero (it's closer to zero for the smaller slabs). It's that the computed gravity value asymptotes to a constant value as the width of the slab gets larger. The thickness of the slab should just cause a constant shift from one thickness to another. According to these results, in this research a size of 500×500 km is used for the all modelling. Note that in the gravity forward modelling (like magnetic method and unlike electromagnetic method; see Chapter 4) the quality of mesh (here tetrahedral cells), number and size of the cells have no effect on the results (data).

Table 5.2: Edge effect on synthetic gravity data.

	Thickness of 10m			*Thickness of 100m*		
	20×20km	100×100km	500×500km	20×20km	100×100km	500×500km
Gravity data (*mGal*)	0.83828321	0.838585234	0.838645639	8.348855191	8.379056809	8.385097282
Bouguer anomaly (mGal)	-0.00011679	0.000185234	0.000245639	-0.035144809	-0.004943191	0.001097282

Model 1: Gravity data (free-air and Bouguer) were first computed for a simple model (Figure 5.4) which has two horizontal layers and a total thickness of 950 m (elevation from -400 m to 550 m). The measurement locations are located on the ground surface (at the elevation of 550 m). The interface between the two layers is located at an elevation of 0 m. Gravity data were computed at 20 m intervals along a 6 km line across the model.

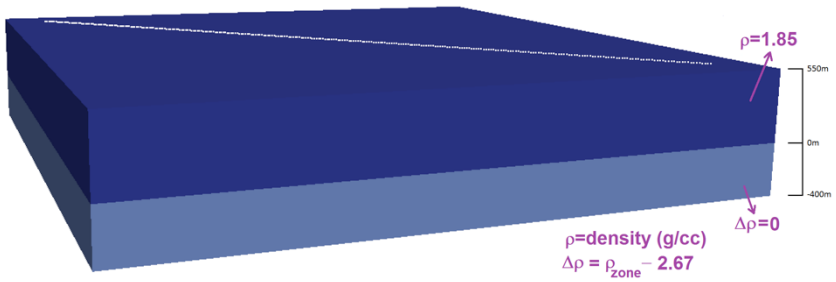

Figure 5.4: Model 1; 3D structure (5×5×1 km) for the simple model with two layers. White line on the surface is the survey line of a length of 6 km.

In this model, I consider the one elevation as the datum for the "reference ellipsoid". Therefore, since in Model 1 the sea level (0m) is considered as the reference ellipsoid, the upper layer (i.e., overburden) has a real density of 1.85 g/cc whereas the lower layer (i.e., crust) has a relative density of 0 g/cc. This would correspond to the real density of the lower layer being 2.67 g/cc.

As mentioned before, the Bouguer correction (BC) removes the gravitational effect of the rock present between the observation point and the datum, and does so by approximating the rock layer beneath the observation point by an infinite horizontal slab with a thickness equal to the elevation of the observation above the datum (see Section 3.2.3). For the BC for Model 1, I consider the datum to be 0m elevation with ρ=1.85 g/cc. As expected, the free-air anomaly is a constant value for all stations (see Figure 5.5). Thus, after the BC the value of Bouguer anomaly is 0 mGal for all the stations.

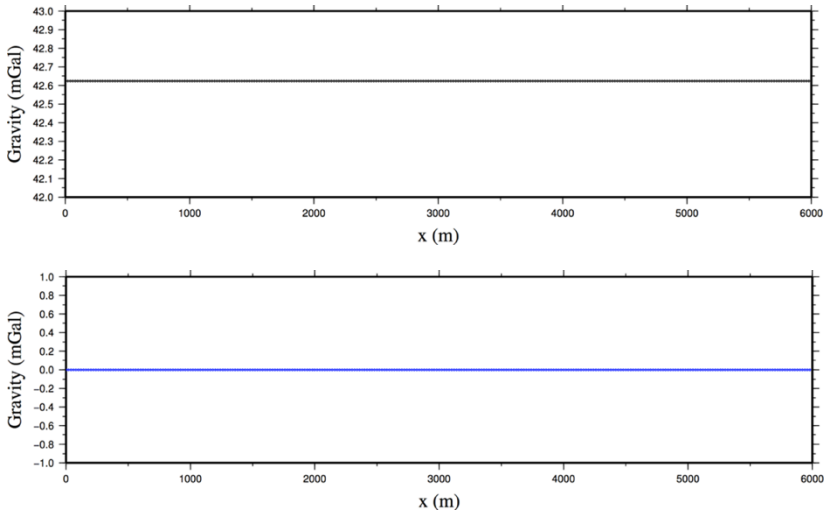

Figure 5.5: Top: free-air anomaly over Model 1 (black dots). Bottom: Bouguer anomaly over Model 1 (blue dots). For the Bouguer correction, the datum is at 0 m and ρ=1.85 g/cc.

Model 2: Model 2 (Figure 5.6) is similar to Model 1, but with real topography (from the McArthur area). The topography is made of digital elevation model (DEM) available in the geological database of the Geological Survey of Canada (GeoBase) which covers the eastern Athabasca Basin with a lateral resolution up to around 10 m. The measurement locations are still on the ground surface (all stations in the modelling in this chapter are located on the ground surface). Figure 5.7 shows the corresponding free-air and Bouguer anomalies. Both anomalies are correlated with the topography (free-air anomaly is very correlated). It can be seen that the Bouguer anomaly still has a non-zero value, whereas it should be 0 mGal (if all the mass above the reference level up to the topography were truly taken into account). This is due to the terrain effect. Including a real topography with digital resolution of around 20 m increases the size of the tetrahedral mesh to around 280,000 cells.

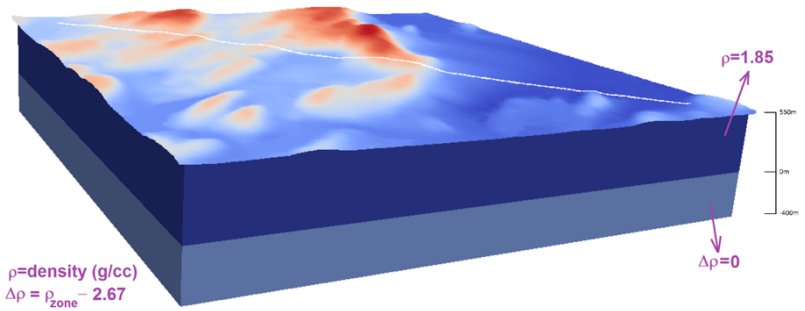

Figure 5.6: Model 2; Topography is real (McArthur area; see Figure 1.1). White line is the survey line on the topography.

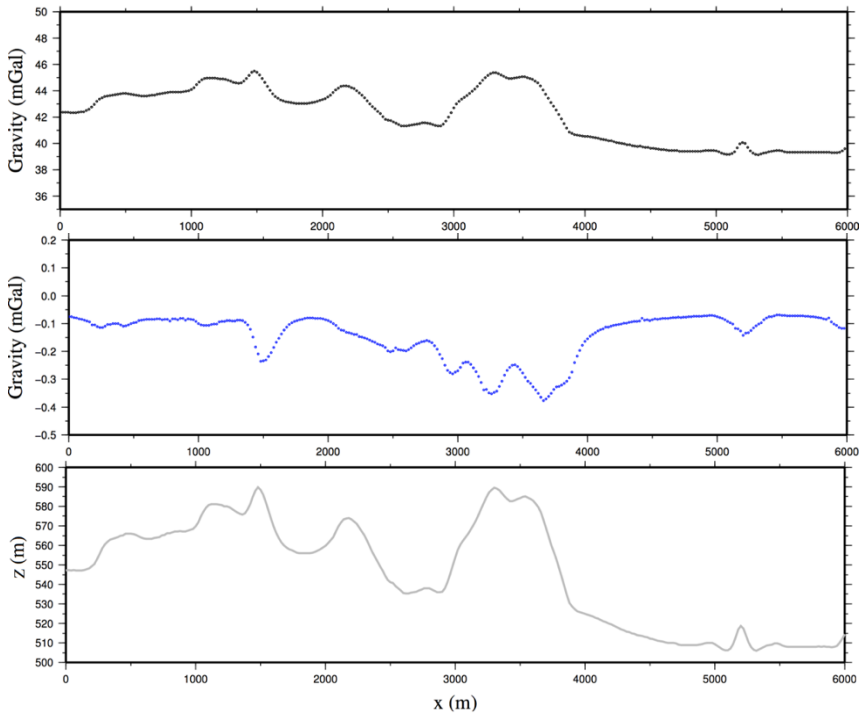

Figure 5.7: Top: free-air anomaly over Model 2 (black dots). Middle: Bouguer anomaly over Model 2 (blue dots). For the Bouguer correction, the datum is at 0 m and ρ=1.85 g/cc. Bottom: topography along the survey line.

Model 3: Model 3 is similar to Model 2, but the thickness of the upper layer has been reduced. The interface between the two layers has been moved from 0 m elevation to 500 m as the base of the overburden in the McArthur area is located around 500 m. Both the reference ellipsoid and the datum for the BC are now considered to be at 500 m (Figure 5.8). It can be seen that the data after BC still have values similar to those for Model 2

(Figure 5.9). These values, ranging from 0.5 to 0.35 mGal, are due to the terrain effect. This range is consistent with the results of Wood and Thomas (2002). The terrain correction (TC) takes into account the terrain and topographic effect in the vicinity of a gravity measurement. The residual data in the lower panel in Figure 5.9 are used as the TC for all subsequent examples.

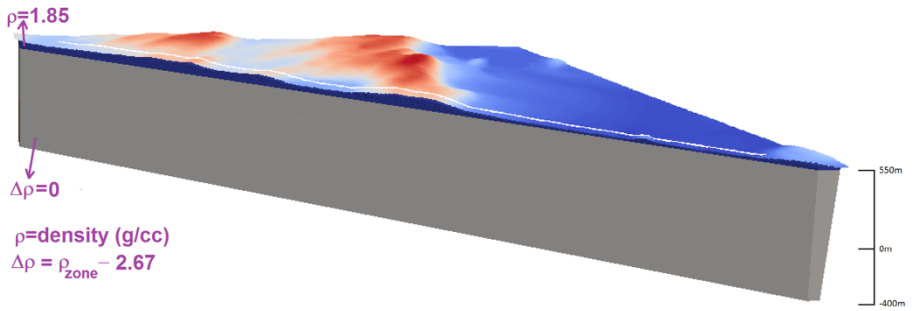

Figure 5.8: Model 3; A cross-section along the survey line. Interface between two layers is located at 500 m elevation. White line is the survey line on the topography.

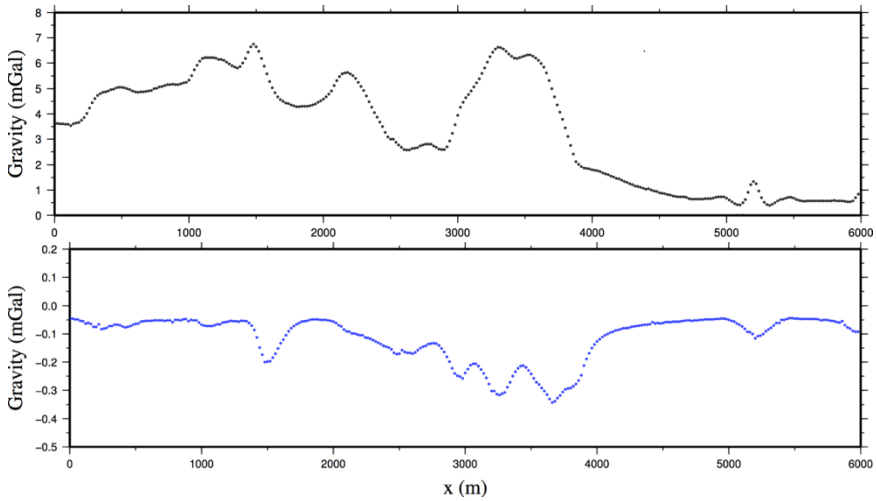

Figure 5.9: Top: free-air anomaly over Model 3 (black dots). Bottom: Bouguer anomaly over Model 3 (blue dots). For the Bouguer correction, the datum is at 500 m and ρ=1.85 g/cc.

Model 4: Model 4 is similar to Model 3, but for this model I add a cylinder (perpendicular to the profile; which could be the alteration zone) with a diameter of 300 m (from an elevation of 0 m to 300 m). It has a density of 2.47 g/cc, but since the reference ellipsoid is

at 500 m, it has a relative density of -0.2 g/cc (relative to 2.67 g/cc; see Figures 5.10 and 5.11). It can be seen that, as expected, the Bouguer anomaly (after BC+TC) is similar to the gravity signature of the cylinder anomaly.

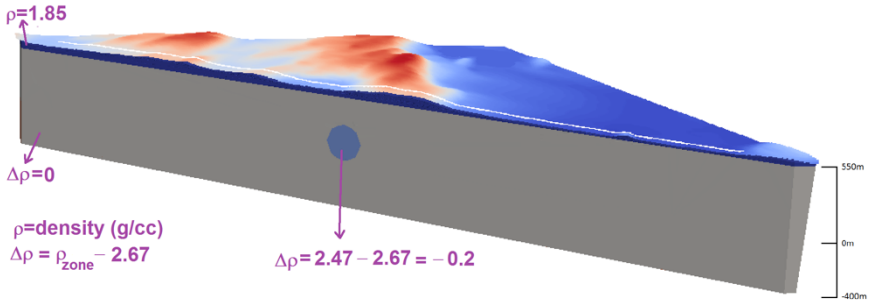

Figure 5.10: Model 4; cross-section of two layers plus a cylinder anomaly.

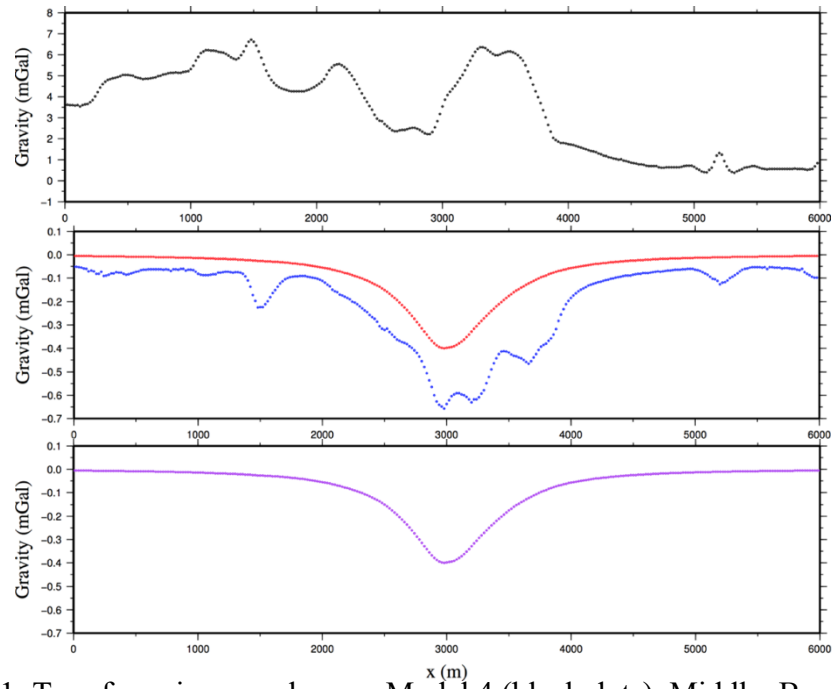

Figure 5.11: Top: free-air anomaly over Model 4 (black dots). Middle: Bouguer anomaly over Model 4 after BC (blue dots) and after BC+TC (red dots). For the Bouguer correction, the datum is at 500 m and ρ=1.85 g/cc. Bottom: gravity signature of cylinder anomaly (Δρ=-0.2 g/cc).

Model 5: Model 5 (Figure 5.12) is similar to Model 4, but with a rugged interface between the two layers (based on McArthur drill-hole data; see Figure 2.2). The wide spacing

between some of the drill holes and an assumed linear variation between these holes makes the rugged interface look peicewise linear. For the BC, I still consider a plane interface at an elevation of 500 m as the datum. As can be seen from Figure 5.13 the Bouguer anomaly along the profile has a shape that mimics the topography of the interface between the two layers under the survey line. There is no obvious indication of the cylinder in the Bouguer anomaly.

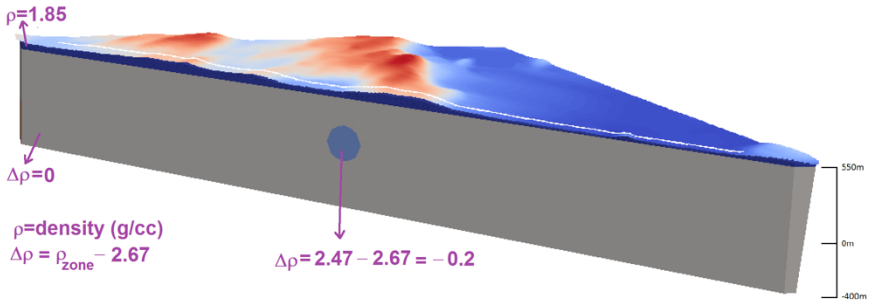

Figure 5.12: Model 5; cross-section of two layers with a rugged interface.

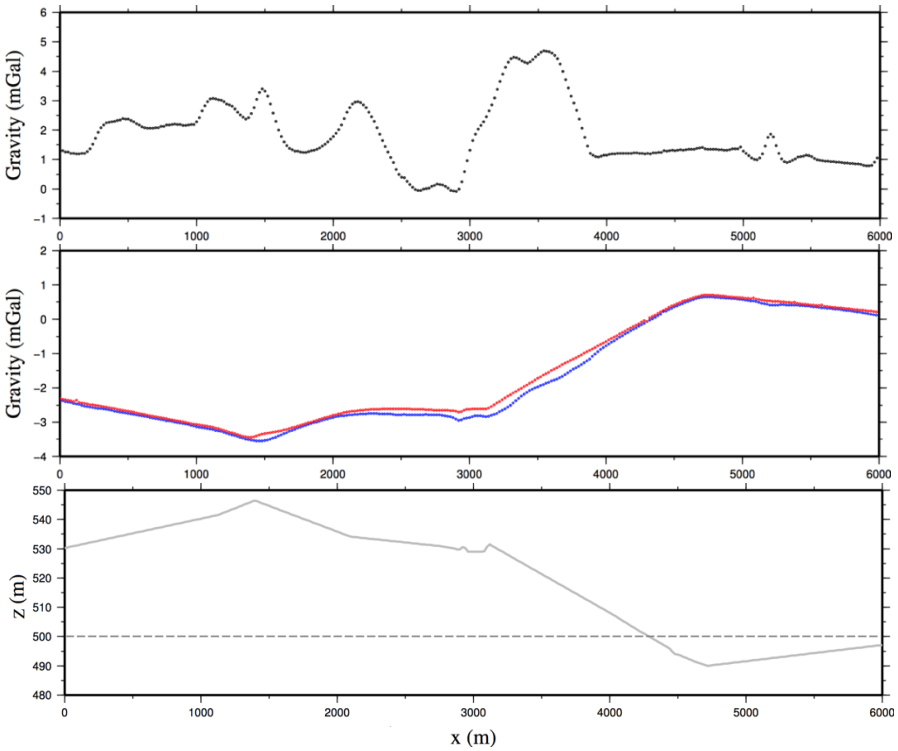

Figure 5.13: Top: free-air anomaly over Model 5 (black dots). Middle: Bouguer anomaly over Model 5 after BC (blue dots) and after BC+TC (red dots). For the Bouguer correction, the datum is at 500 m (dashed line in the bottom panel) and ρ=1.85 g/cc. Bottom: Topography of interface between the layers under the survey line.

Model 6: Model 6 is similar to Model 4 (i.e. flat base of the top layer), but with a third layer (lower layer from 0 m to -400 m; i.e. basement of the McArthur area). Also, after this the middle layer, which surrounds the alteration zone, will be the sandstone. This also has different vertical blocks in three different variants of the model. The interface between the upper (overburden) layer and the middle (sandstone) layer is again a plane at an elevation of 500 m. The interface between the middle (sandstone) layer and the lower (basement) layer is a plane et 0 m (sea level). The approximate locations of these layers as well as their densities are taken from Wood and Thomas (2002). For this model, three different scenarios (A, B and C) are considered.

Model 6A: In Model 6A (Figure 5.14), the sea level (0 m) is considered as the reference ellipsoid. Therefore, the densities below 0 m (actually the densities of the units in the third layer) are relative density with respect to 2.67 g/cc. In this variant of Model 6, I assume that the third (lower) layer has a constant density of 2.67 g/cc, and hence a relative density of 0 g/cc. The cylinder now has a positive real density more than the real density of the middle layer (Figure 5.15). Therefore, the cylinder shows up as a positive contribution to the Bouguer anomaly. Figure 5.15 indicates the importance of the TC. There is a significant difference between the Bouguer anomaly after BC and the Bouguer anomaly after BC+TC. In this figure for the BC I consider the interface between the upper and the middle layer as the datum (500 m), and after BC and TC I get an acceptable result. However, the base level of the Bouguer anomaly is not around 0 mGal. Figure 5.16 represents the Bouguer anomaly after BC and TC when I consider sea level (0 m) as the datum in the BC for two densities ρ=1.85 g/cc and ρ=2.67 g/cc. It can be clearly seen that considering a density of 2.67 g/cc

is not a good choice.

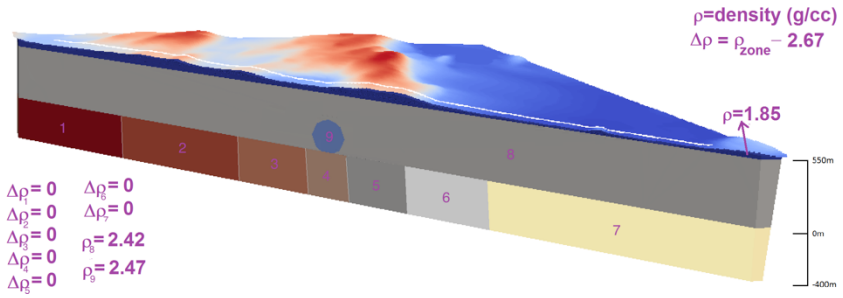

Figure 5.14: Model 6A; Reference ellipsoid and Bouguer correction datum are located at 0 m and 500 m elevations, respectively. The lowest layer has a relative density of 0 g/cc.

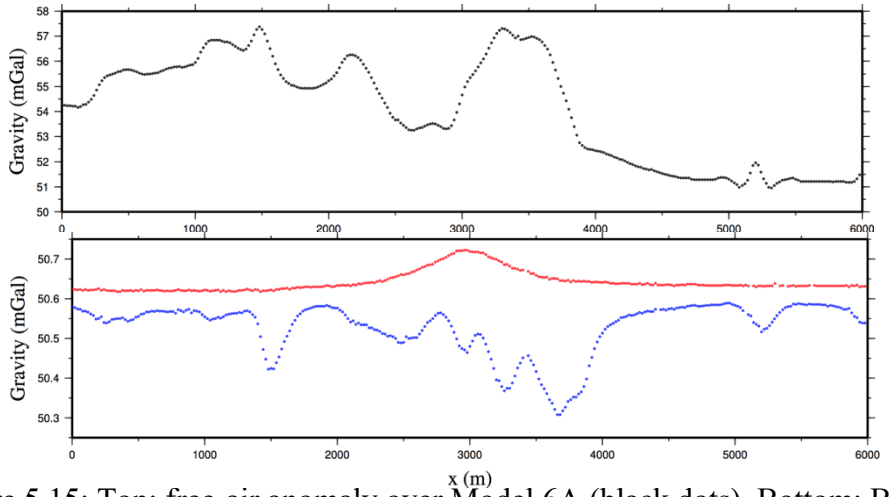

Figure 5.15: Top: free-air anomaly over Model 6A (black dots). Bottom: Bouguer anomaly over Model 6A after BC (blue dots) and after BC+TC (red dots). For the Bouguer correction, the datum is at 500 m and ρ=1.85 g/cc.

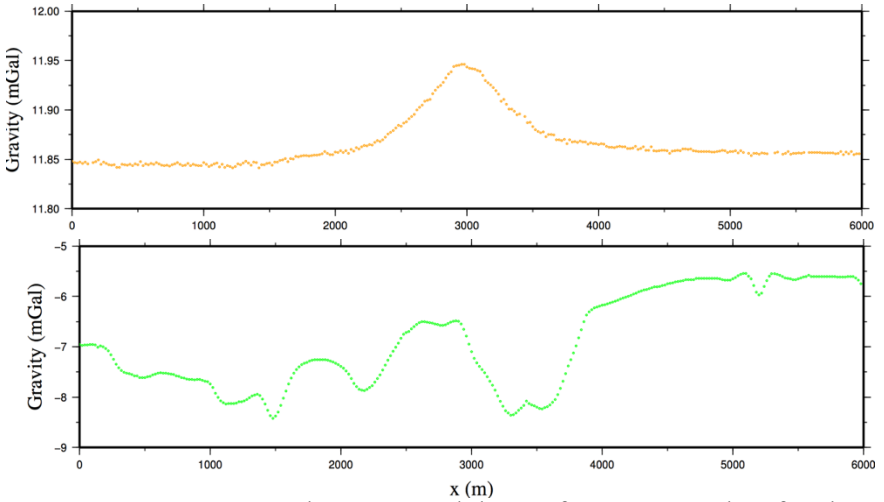

Figure 5.16: Bouguer anomaly over Model 6A after BC+TC, but for the Bouguer correction with the datum at 0 m and two densities: ρ=1.85 g/cc (top - orange dots) and ρ=2.67 g/cc (bottom – green dots).

Model 6B: The base level of the Bouguer anomaly of Model 6A is unexpectedly too far from a value close to 0 mGal (as can be seen it is around 50 mGal; Figure 5.15). This can be solved by considering the same datum for both the reference ellipsoid and Bouguer correction which is the same as the correct datum mentioned in Section 3.2.4. Thus, for Model 6B, I consider the interface between the upper and middle layer (which is at 500 m) as the reference ellipsoid. Thus, the structures under 500 m in the model have a relative density (actually the densities of the units in the second and third layers in addition to the cylinder anomaly; Figure 5.17). The Bouguer anomaly (after BC+TC) in Figure 5.18 shows a profile where the anomaly of the cylinder is apparent when the datum is at 500 m and ρ=1.85 g/cc, as the signature of the cylinder anomaly can be clearly seen. Note that I considered a density for the Bouguer correction which is the same as the density of the materials of the upper layer (i.e. the density of overburden located above the reference ellipsoid). Also, I considered the same datum for the reference ellipsoid and Bouguer correction.

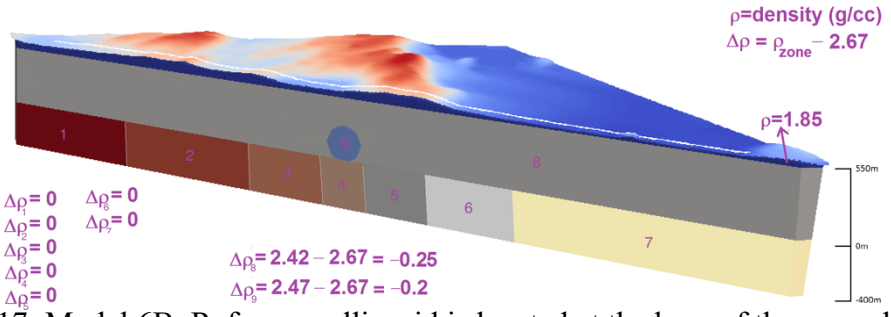

Figure 5.17: Model 6B; Reference ellipsoid is located at the base of the upper layer, and for the Bouguer correction two scenarios (0 m and 500 m) are considered for datum. The lowest layer has a relative density of 0 g/cc.

I now investigate the impact of not having an accurate value for the density of the upper (overburden) layer used in the BC. Thus, I try two values (ρ=1.7 g/cc and ρ=2 g/cc) for density which are close to the accurate value (ρ=1.85 g/cc). The results are shown in Figure

5.19. It can be seen that those approximate densities don't show the anomaly of the cylinder. This shows the importance of getting the density that is used in the Bouguer correction as close as possible to the density of the material that the topography is going up and down through.

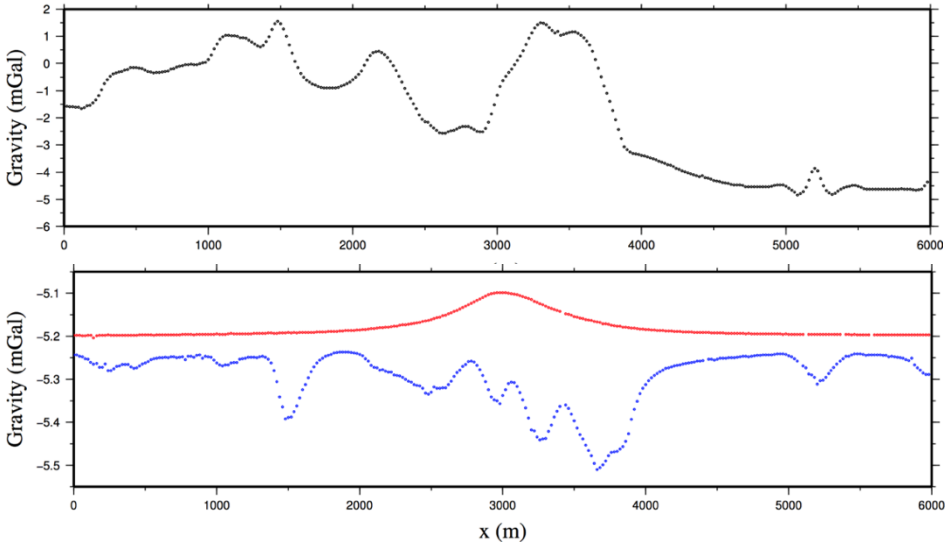

Figure 5.18: Top: free-air anomaly over Model 6B (black dots). Bottom: Bouguer anomaly over Model 6B after BC (blue dots) and after BC+TC (red dots). For the Bouguer correction, the datum is at 500 m and ρ=1.85 g/cc.

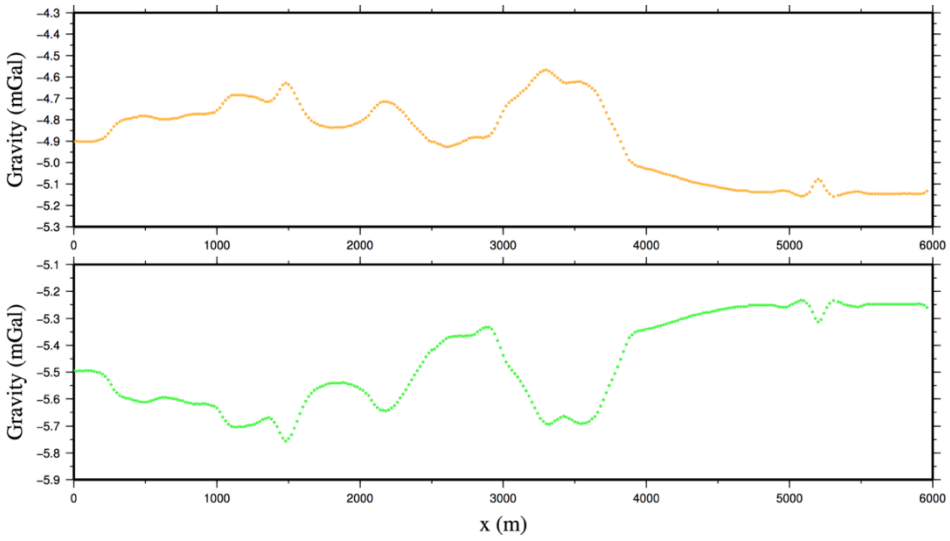

Figure 5.19: Bouguer anomaly over Model 6B after BC+TC for the Bouguer correction using the datum at 500 m and with two densities: ρ=1.7 g/cc (top - orange dots) and ρ=2 g/cc (bottom – green dots).

Now, assume that for Model 6B the location of the base of the upper layer is unknown to be used in the BC. Therefore, I consider an arbitrary datum for the BC at 0 m elevation. The Bouguer anomaly (after BC+TC) in Figure 5.20 shows that for a datum at 0 m in the BC, ρ=1.85 g/cc gives a much better result than ρ=2.67 g/cc. For the BC when the datum is at 0 m, I again try two values (ρ=1.7 g/cc and ρ=2 g/cc) for the density which are close to the true value (of the upper layer; ρ=1.85 g/cc). The results are shown in Figure 5.21. It can be seen that a good estimate of density in the BC is necessary for obtaining a good result even when I did not consider a correct level for the datum.

However, there is a static shift in the Bouguer anomalies in Figures 5.20 and 5.21 around -40 to -60 mGal which is due to considering a datum for the BC (0 m) lower than the reference ellipsoid. This happened because for the BC I considered a density of 1.85 g/cc for all the structures above 0 m elevation while from 0 m to 500 m the structures had small values of the relative density ($\Delta\rho_8$=-0.25 g/cc and $\Delta\rho_9$=-0.2 g/cc ; Figure 5.17) as they are located under the reference ellipsoid. Thus, when the BC is subtracted from the free-air data, actually a slab with a thickness of 500 m (from 0 m to 500 m) and a density of 1.85 g/cc is subtracted which has a small value of the relative densities.

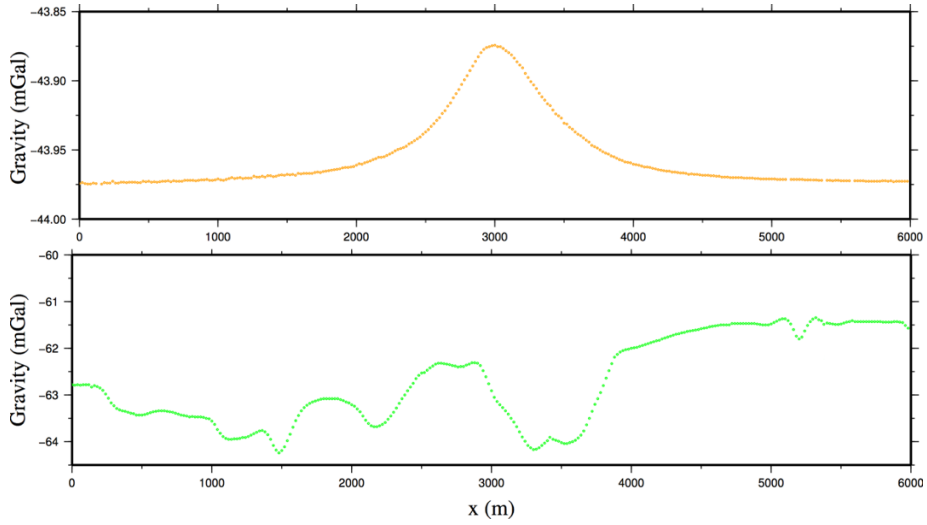

Figure 5.20: Bouguer anomaly over Model 6B after BC+TC for the Bouguer correction using the datum at 0 m and with two densities: ρ=1.85 g/cc (top - orange dots) and ρ=2.67 g/cc (bottom – green dots).

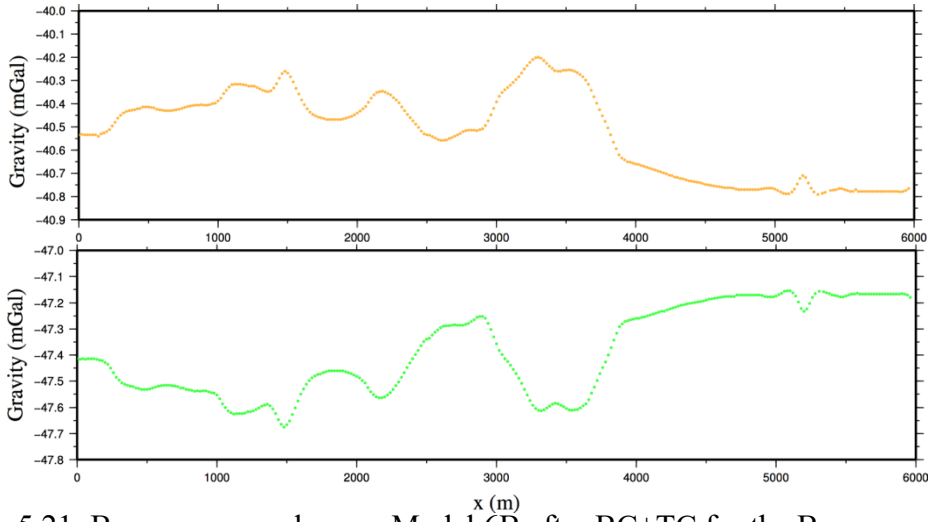

Figure 5.21: Bouguer anomaly over Model 6B after BC+TC for the Bouguer correction using the datum at 0 m and with two densities: ρ=1.7 g/cc (top - orange dots) and ρ=2 g/cc (bottom – green dots).

Model 6C: Model 6C is similar to Model 6B, but in this model I consider different densities for the vertical blocks in the lower layer (Figure 5.22). These blocks represent the different geological structures in the basement (see Figure 5.3 and 5.17). In Figure 5.23, for the BC a datum of 500 m and a density of 1.85 g/cc are considered. The graphs show that the

different densities in the lower layer have a big effect on the gravity data. The subsequent graphs in Figure 5.24 emphasize that for the BC with a datum at 0 m, a density of 2.67 g/cc is not a good choice as there is no similarity between this graph (with a density of 2.67 g/cc) and the graph in Figure 5.23 (with a density of 1.85 g/cc). Also, this graph is following the same pattern of the variations of topography (but in the opposite direction which means by increasing topography the data is decreasing and vice versa; see Figure 5.7). Note that in Figure 5.24 the constant shift is again present as expected.

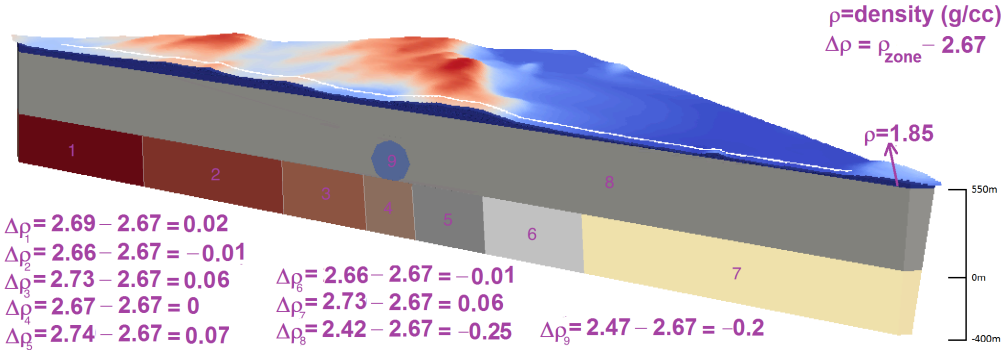

Figure 5.22: Model 6C; the reference ellipsoid is located at the base of the upper layer, and for the Bouguer correction two scenarios (0 m and 500 m) are considered for datum. The lowest layer has blocks with different relative densities.

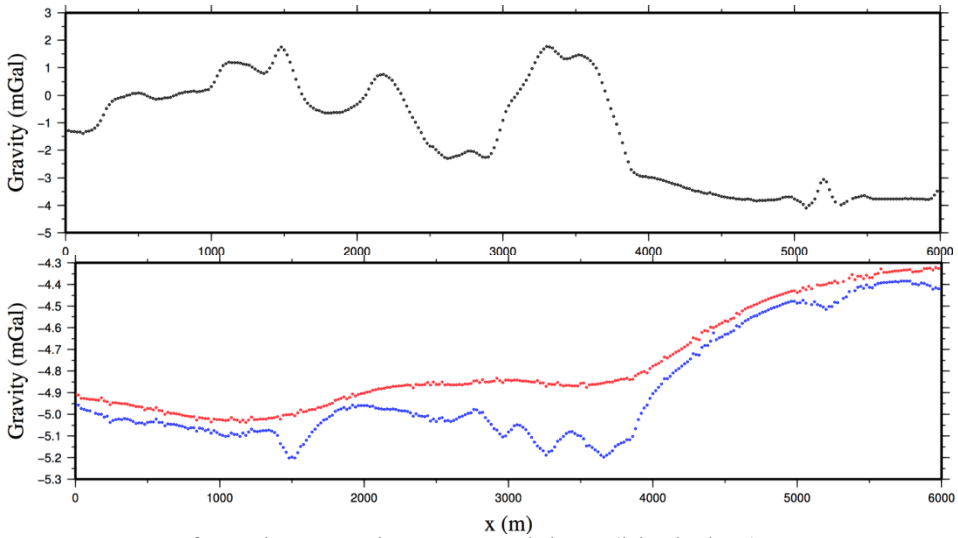

Figure 5.23: Top: free-air anomaly over Model 6C (black dots). Bottom: Bouguer anomaly over Model 6C after BC (blue dots) and after BC+TC (red dots). For the Bouguer correction, the datum is at 500 m and ρ=1.85 g/cc.

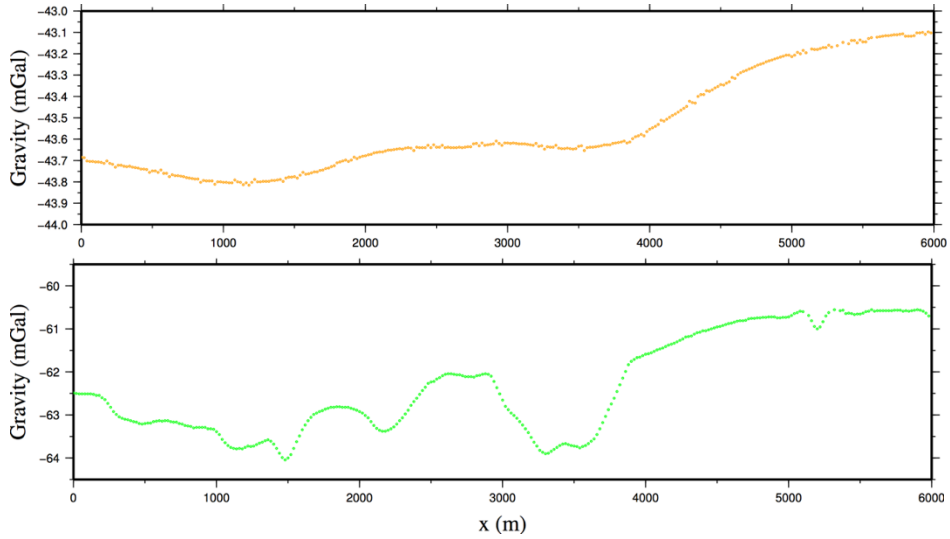

Figure 5.24: Bouguer anomaly over Model 6C after BC+TC for the Bouguer correction using the datum at 0m and with two densities: ρ=1.85 g/cc (top - orange dots) and ρ=2.67 g/cc (bottom – green dots).

Model 7: Model 7 is similar to Model 6C, but in this model based on Wood and Thomas (2002) the thickness of the lower layer was increased from 400 m to 4500 m (Figure 5.25). By this work, the effect of the thickness of the model on the computed data can be investigated (Figure 5.26). For the Bouguer correction, the datum is at 500 m and ρ=1.85 g/cc. By comparing Figures 5.23 and 5.26, it can be seen that both free-air and Bouguer anomalies are shifted around 5 mGal for Model 7 which is due to the increasing of the thickness of the model. However, in both figures the signature of the cylinder anomaly cannot be seen because it is masked by the variations of the density of the basement blocks. Also, it can be seen that the Bouguer anomaly of Model 7 is a little bit smoother than Model 6C. This is because, by increasing the thickness of basement blocks to depth, longer wavelength components from the deeper parts of the blocks are now contributing to the response. Therefore, the summation of these longer wavelengths gives a smoother data in which the variation of amplitude is less sharp.

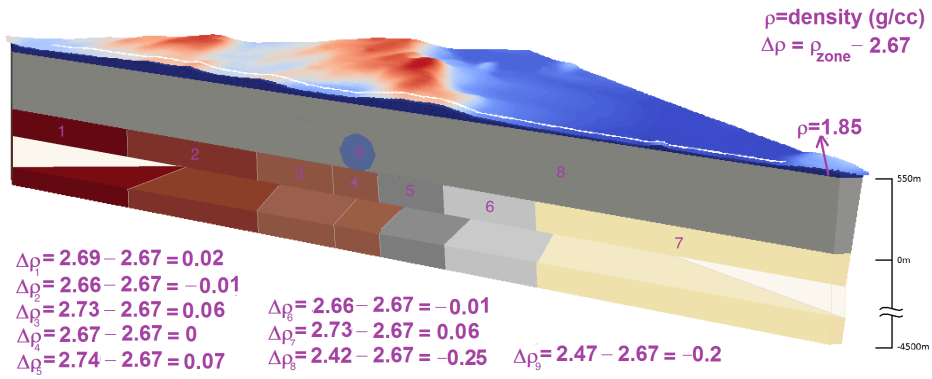

Figure 5.25: Model 7; For the Bouguer correction, the datum is at 500 m and ρ=1.85 g/cc. The thickness of the lowest layer which has different blocks with different relative densities has increased.

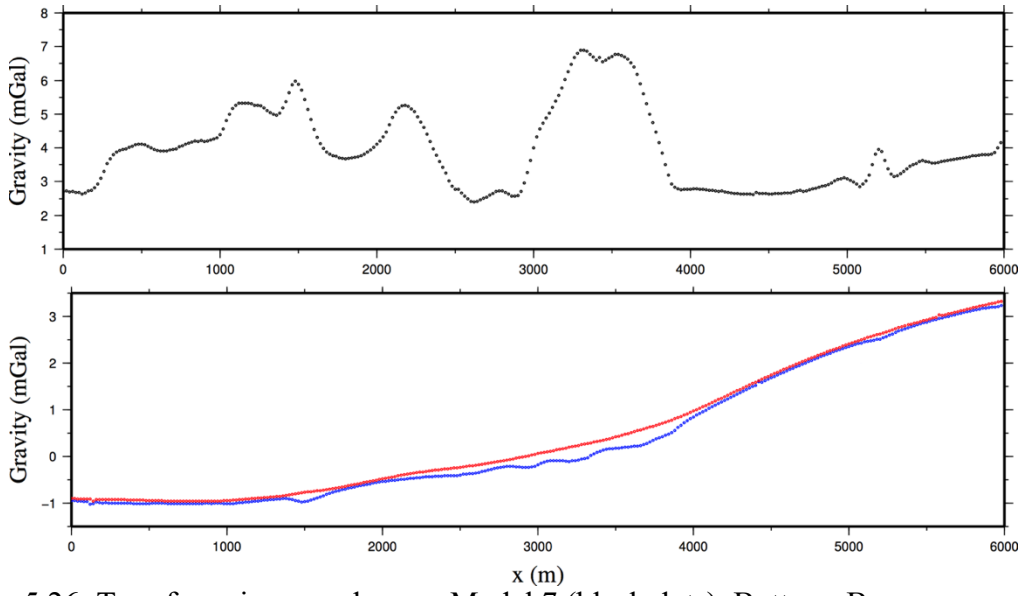

Figure 5.26: Top: free-air anomaly over Model 7 (black dots). Bottom: Bouguer anomaly over Model 7 after BC (blue dots) and after BC+TC (red dots). For the Bouguer correction, the datum is at 500 m and ρ=1.85 g/cc.

Model 8: Model 8 is similar to Model 7, but it has realistic interfaces between the layers (Figure 5.27). Thus, both the base of overburden and top of basement (unconformity) are not planar in Model 8. These changes are made using the available drill-hole data (see Section 2.2 and Figure 2.2). Also, instead of the cylinder the irregular density anomaly is used (see Section 5.2).

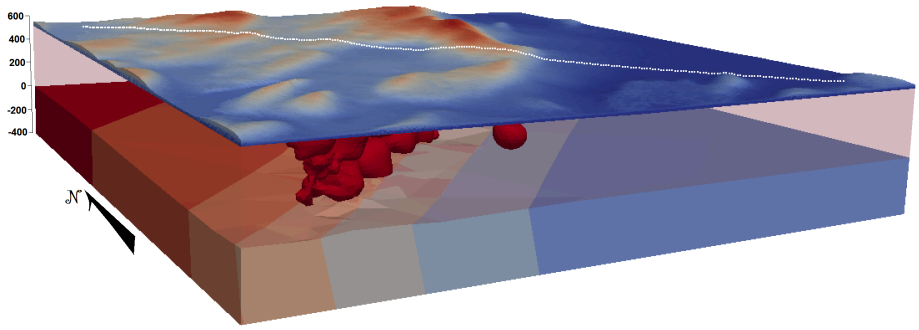

Figure 5.27: A 3D perspective view of Model 8 (to the depth -400 m). This model has an irregular density anomaly as well as realistic topography for the interfaces between the layers.

Model 8A: For Model 8, I investigate two variations (8A and 8B) in which the irregular anomaly (#9 in Figures 5.28 and 5.32) within the middle (sandstone) layer is two times larger in Model 8B than in Model 8A.

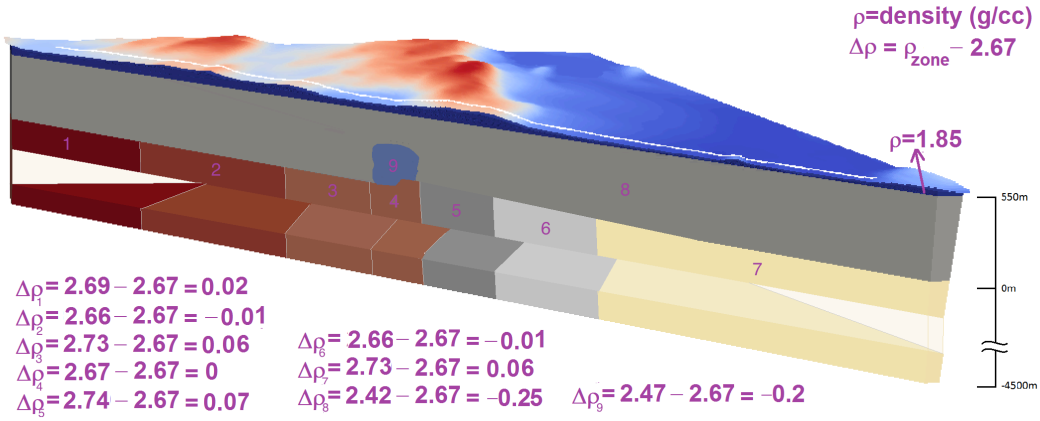

Figure 5.28: Model 8A; This model has a small irregular density anomaly as well as realistic interfaces between the layers.

It can be seen that the small variation in the data due to the anomaly within the middle layer (which is modelling the alteration zone) is very small compared with the variation due to the heterogeneous lower layer (i.e., basement; Figure 5.29). Also, there are sharp variations due to the topography of the two interfaces between upper and middle layers and less sharp variations due to the middle and lower layers (Figure 5.30). In Figure 5.31 the

individual contributions of the upper layer (i.e., overburden) and the lower layer (i.e., basement) are shown. Also shown are the data for the complete model after removing the contribution of the upper layer which is similar to the Bouguer anomaly (BC+TC) as expected.

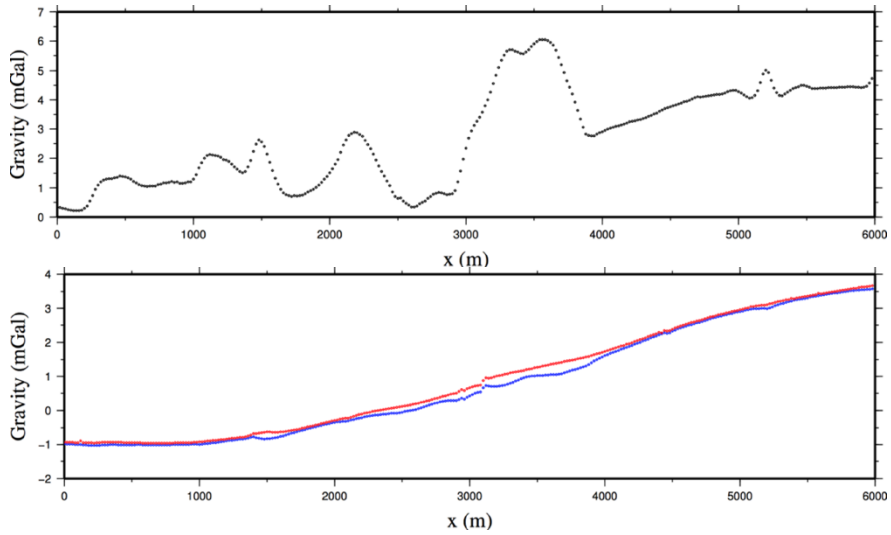

Figure 5.29: Top: free-air anomaly over Model 8A (black dots). Bottom: Bouguer anomaly over Model 8A after BC (blue dots) and after BC+TC (red dots). For the Bouguer correction, the datum is the interface between the upper and lower layers and ρ=1.85 g/cc.

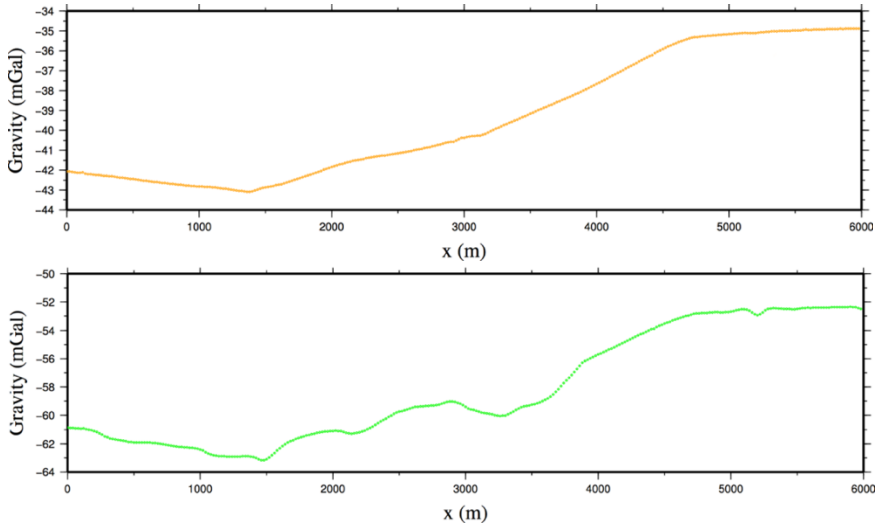

Figure 5.30: Bouguer anomaly over Model 8A after BC+TC for the Bouguer correction using the datum at 0 m and with two densities: ρ=1.85 g/cc (top - orange dots) and ρ=2.67 g/cc (bottom – green dots).

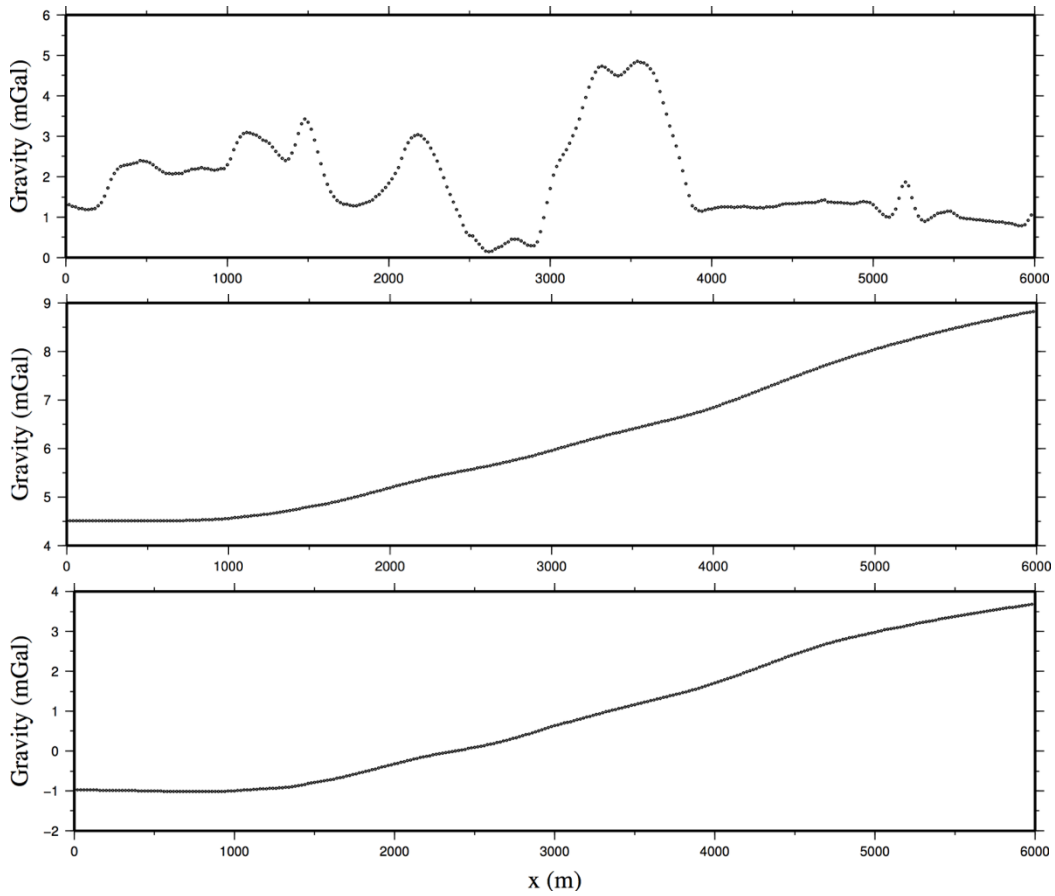

Figure 5.31: Top: Gravity signature of the upper layer (overburden) along the survey line on the topography. Middle: Gravity signature of the lower layer (basement) along the survey line on the topography. Bottom: Gravity data along the survey line on the topography for the entire model after removing the upper layer (overburden) contribution.

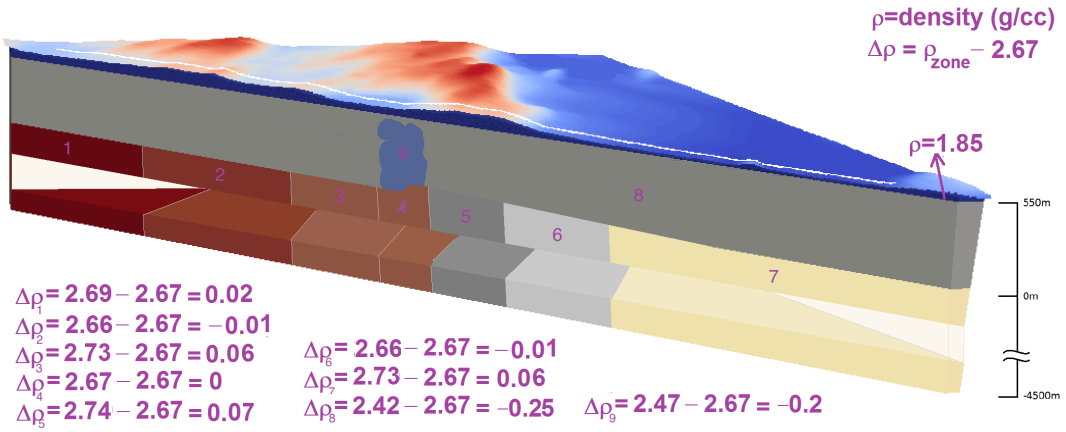

Figure 5.32: Model 8B; This model has a large irregular density anomaly as well as realistic interfaces between the layers.

Model 8B: In Model 8B the anomaly (#9 in Figure 5.32) in the middle (sandstone) layer is larger in width and vertical extent (same density). Comparing the data due to the two Models, 8A and 8B, shows an increase of 0.1 mGal in the amplitude of gravity data for Model 8B (Figure 5.33).

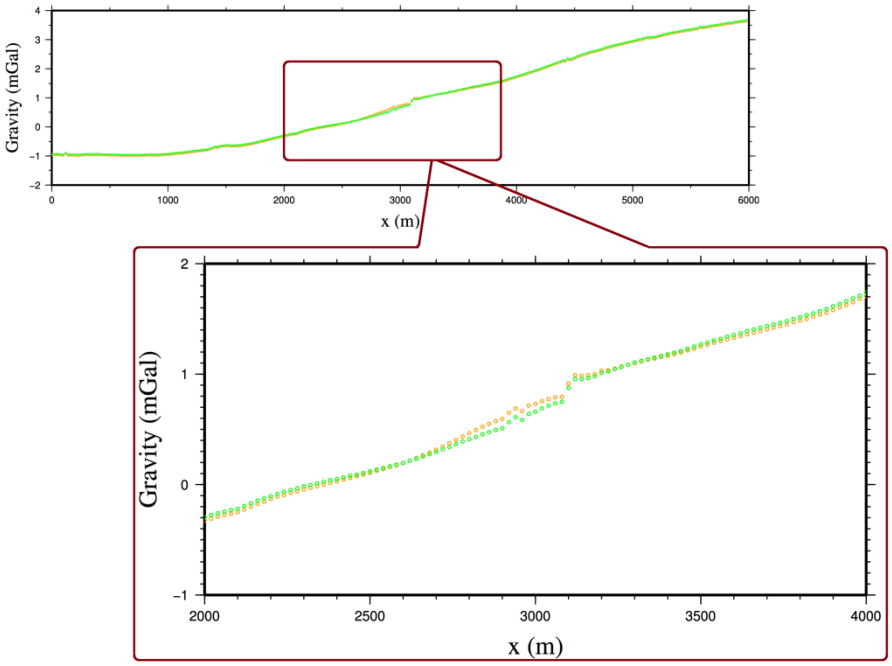

Figure 5.33: Comparing the Bouguer anomaly (BC+TC) for the two Models 8A (green) and 8B (orange). It can be seen that they are similar except in the middle of the profile where the 8B data are 0.1 mGal larger than the 8A data.

5.4 Modelling of free-air and Bouguer anomalies (McArthur area #2)

As mentioned before, the structure of the basement is the main difference between scenarios (#1) and (#2). For Model (#2), the density model was made based on Wood and Thomas (2007; Figures 5.34 and 5.35). In this model, the effect of the (different) basement on gravity data is investigated. Gravity data (free-air and Bouguer anomalies) were computed for representative 3D models of the McArthur area. The images of the 3D models in this section again show the central 5 by 5 km. The actual 3D models used for the

computations had a size of 500 by 500 km in order to avoid any effect of the edges on the gravity data. The total thickness of these models was 5000 m based on the results of the previous section. Gravity data were computed at 20 m intervals along a 6 km line across the model over the topography. The tetrahedral mesh has around 320,000 cells starting with an edge size of 20 m on the surface. Note that, as mentioned before, in the gravity forward modelling the quality of mesh, number and size of the cells have no effect on the results (data).

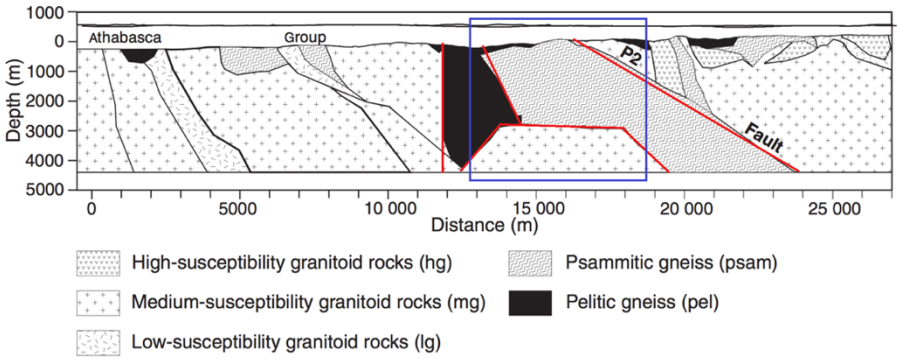

Figure 5.34: McArthur geological section from Thomas and Wood (2007). Blue square shows the part which forms the basis of the models considered here. Red lines show the modelled interfaces between the blocks. Small zones and variations are ignored in the modelling.

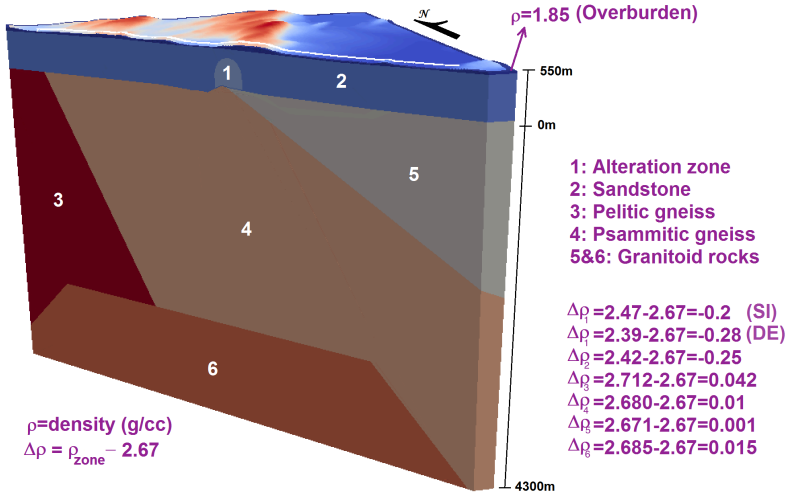

Figure 5.35: Density model including different geological structures based on Wood and Thomas (2007). Basement blocks are adapted from Figure 5.34. SI: silicification; DE: desilicification.

Two different scenarios, named DE (desilicification) and SI (silicification), are considered. Also, instead of the irregular density (derived from SWIR) used in previous Models (Model 8; Figure 5.27) a cylinder anomaly is used for this new model as the alteration zone. The density of the alteration zone in Model DE is 0.03 g/cc less than the sandstone, and in Model SI is 0.05 g/cc more than the sandstone. The base of the overburden is considered as datum for the reference ellipsoid and the Bouguer correction. The structures above the reference ellipsoid have real densities while the structures below the reference ellipsoid have relative density. The relative densities were with respect to 2.67 g/cc. Therefore, overburden has a real density of 1.85 g/cc and the lower layers have a relative density. This model has realistic topography as well as realistic interfaces for the base of overburden and the top of basement (unconformity). The unconformity has a step of more than 50 m where it is intersected by the fault (the interface between block #4 and block #5 in Figure 5.35). A density of 1.85 g/cc in applied for the BC.

Model DE: In this model a density of 2.39 g/cc (a relative density of -0.28 g/cc) is considered for the alteration zone. Figures 5.36 and 5.37 show the gravity data for the DE scenario. It can be seen that the free-air anomaly is dominated by variations in topography. The Bouguer anomaly (Figure 5.36) shows a decrease in the middle of the profile that is due to the alteration zone. Other variations, specially a large step at 3000 m, in the Bouguer anomaly along the profile can be due to the variations in the interface between overburden and sandstone. Also, in Figure 5.37 gravity data after removing overburden contribution shows a decrease in the middle of the profile (between 2500 m and 4000 m) which is due to the alteration zone. The overburden signature was calculated by the forward modelling.

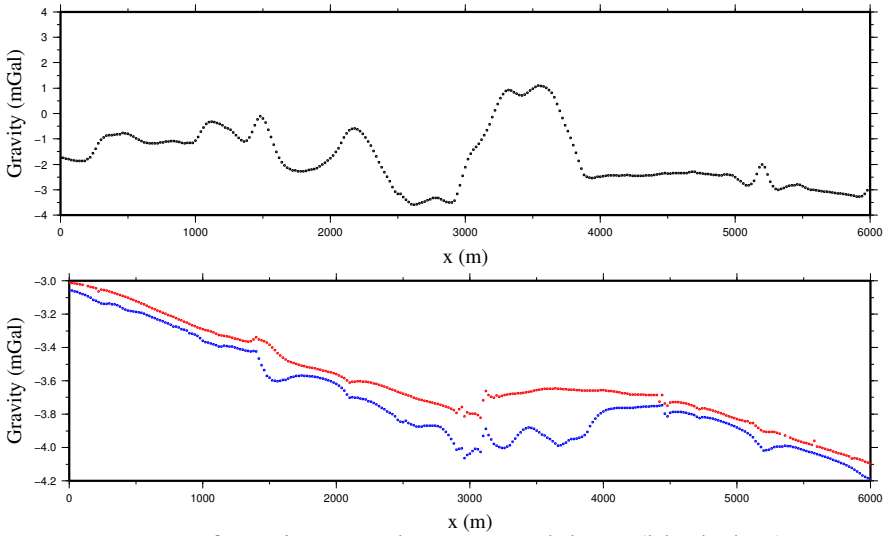

Figure 5.36: Top: free-air anomaly over Model DE (black dots). Bottom: Bouguer anomaly over Model DE after BC (blue dots) and after BC+TC (red dots). For the Bouguer correction, the datum is the interface between the upper and lower layers and ρ=1.85 g/cc.

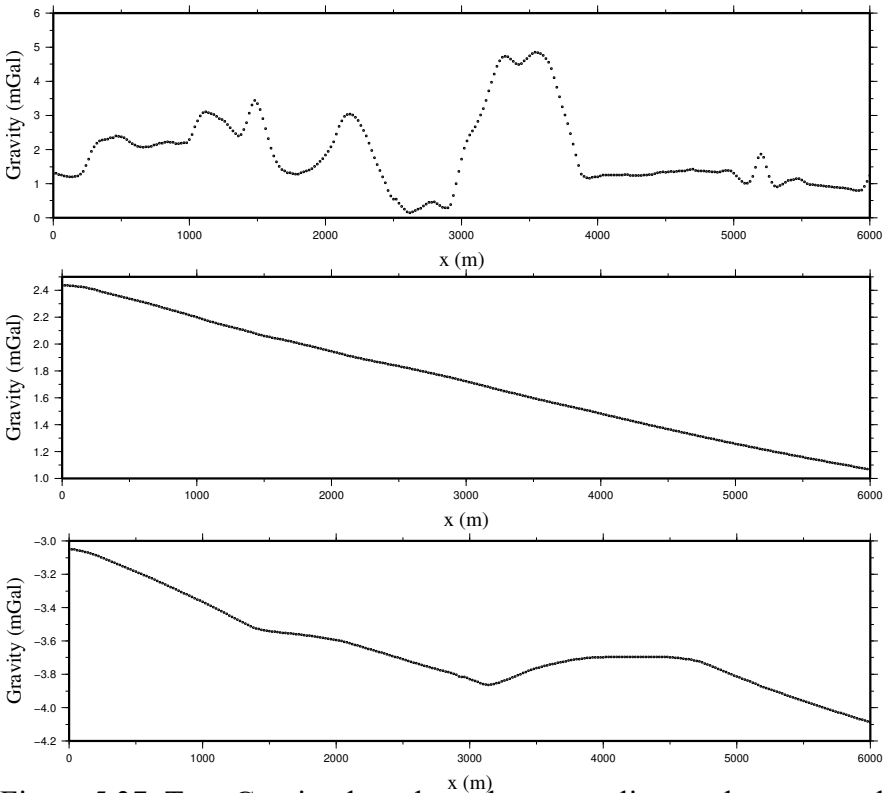

Figure 5.37: Top: Gravity data along the survey line on the topography for the overburden. Middle: Gravity data along the survey line on the topography for the basement. Bottom: Gravity data along the survey line on the topography for the entire model after removing overburden contribution.

Model SI: In this model, a density of 2.47g/cc (a relative density of -0.2) is considered for the alteration zone. Figures 5.38 and 5.39 show the gravity data for the SI scenario. Similar to the previous model, the free-air anomaly is strongly influenced by variations of topography. The Bouguer anomaly shows an increase in the middle of the profile that is due to the alteration zone. A large step at 3000 m in the Bouguer anomaly is due to the variations in the interface between overburden and sandstone. The Bouguer anomaly (Figure 5.38) shows an increase in the middle of the profile that is due to the alteration zone. Also, in Figure 5.39 gravity data after removing overburden contribution shows an increase in the middle of the profile (between 2500m and 4000m) which is due to the alteration zone as well.

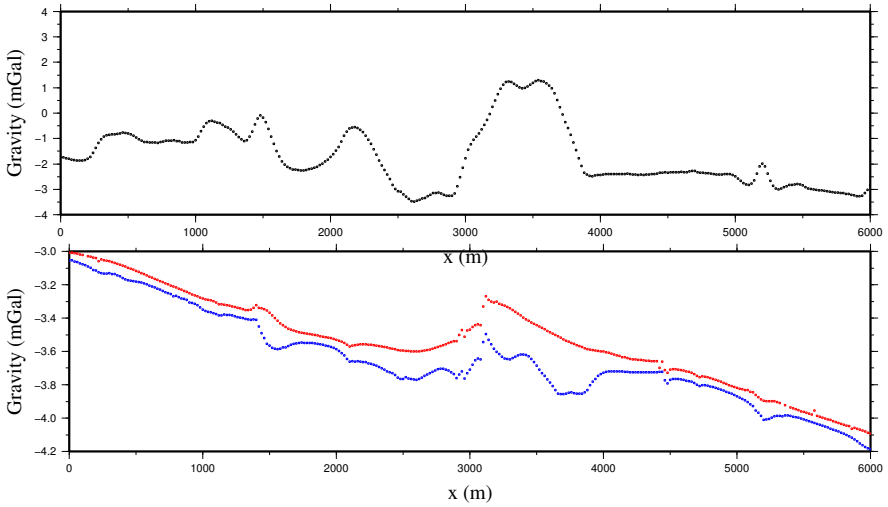

Figure 5.38: Top: free-air anomaly over Model SI (black dots). Bottom: Bouguer anomaly over Model SI after BC (blue dots) and after BC+TC (red dots). For the Bouguer correction, the datum is the interface between the upper and lower layers and ρ=1.85 g/cc.

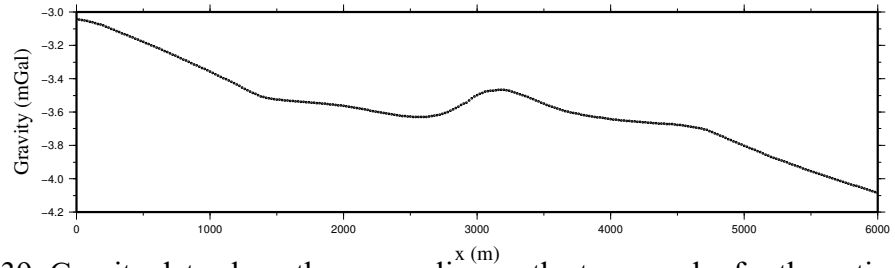

Figure 5.39: Gravity data along the survey line on the topography for the entire model after removing overburden contribution.

It can be seen that considering the interface between overburden and sandstone as the reference ellipsoid is a good choice (however it is not flat) as the signature of the alteration zone can be clearly seen in the Bouguer anomaly and the free-air anomaly after removing the overburden contribution.

I also investigated a case in which the datum for the reference ellipsoid and the Bouguer correction is flat and is located at 450 m elevation for both Models DE and SI. Therefore, the overburden and the upper part of the sandstone has a real density of 1.85 g/cc and 2.42 g/cc, respectively; whereas the lower layers have a relative density.

Model DE: Figure 5.40 shows the gravity data for the DE scenario in which the datum for the reference ellipsoid and the Bouguer correction is located at 450 m elevation, and a density of 2.39 g/cc (a relative density of -0.28 g/cc) is considered for the alteration zone. It can be seen that the free-air anomaly is dominated by variations in topography. Variations in the Bouguer anomaly along the profile are due to the variations in the interface between the overburden and the sandstone. No variation can be seen in the Bouguer anomaly as well as the free-air anomaly associated with the alteration zone after removing the overburden contribution.

Model SI: Figure 5.41 shows the gravity data for the SI scenario in which the datum for the reference ellipsoid and Bouguer correction is located at 450 m elevation, and a density of 2.47 g/cc (a relative density of -0.2 g/cc) is considered for the alteration zone. The Bouguer anomaly shows an increase in the middle (between 2500 m and 3500 m) of the profile that is due to the alteration zone. But, no clear variation can be seen in the free-air

anomaly after removing the overburden contribution associated with the alteration zone. But, note that as long as there is a density contrast between the alteration and sandstone, both the positive and negative contrast must produce a gravity response even if it is very small and not easy to find.

For the McArthur area model (Figure 5.35), it is not possible to consider a flat datum for the reference ellipsoid higher than the base of the overburden (somewhere in the overburden). Because, in some places the elevation of the highest point of the base of overburden is more than the elevation of the lowest point of the topography in other places (see Figure 5.42). In the model in Figure 5.35, the topography varies from 506 m to 624 m, while the base of the overburden varies from 494 m to 550 m.

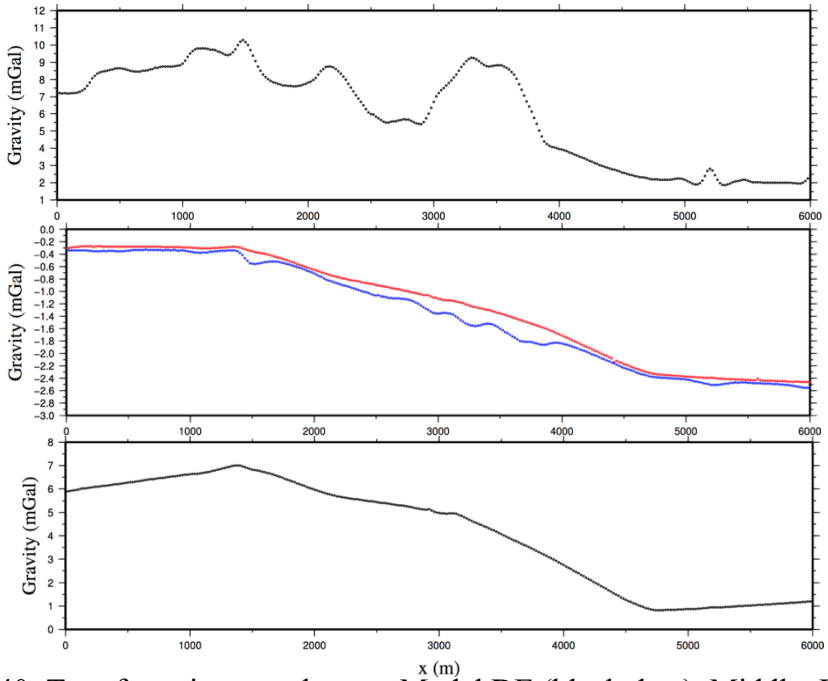

Figure 5.40: Top: free-air anomaly over Model DE (black dots). Middle: Bouguer anomaly over Model DE after BC (blue dots) and after BC+TC (red dots). For the Bouguer correction, the datum is at 450 m elevation and ρ=1.85 g/cc. Bottom: gravity data along the survey line on the topography for the entire model after removing overburden contribution.

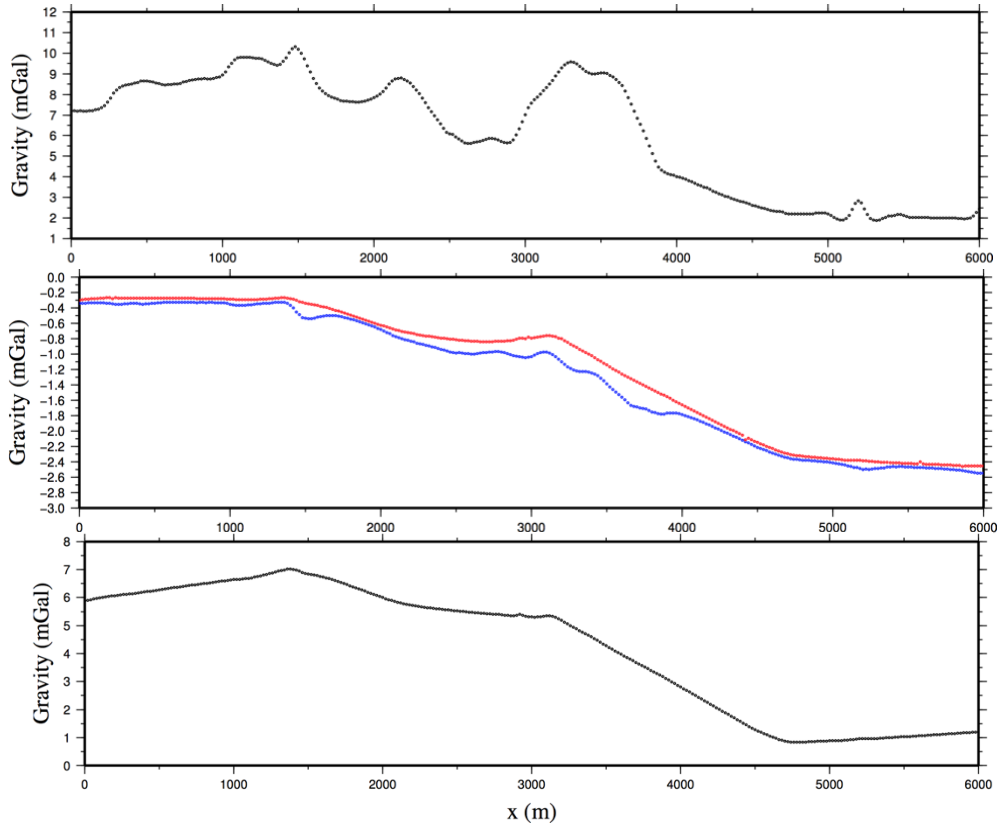

Figure 5.41: Top: free-air anomaly over Model SI (black dots). Middle: Bouguer anomaly over Model SI after BC (blue dots) and after BC+TC (red dots). For the Bouguer correction, the datum is at 450 m elevation and ρ=1.85 g/cc. Bottom: gravity data along the survey line on the topography for the entire model after removing overburden contribution.

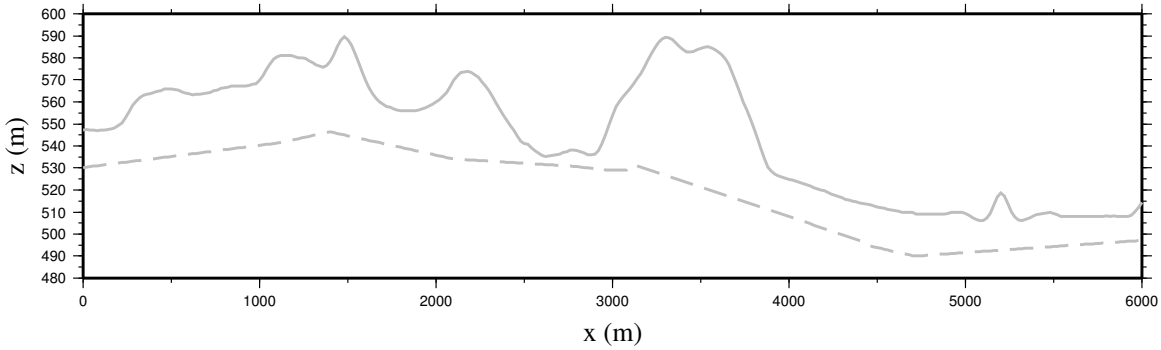

Figure 5.42: Topography along the survey line (solid line), and the interface between the overburden and sandstone under the survey line (dashed line).

Figure 5.41 shows also that a variation less than 10 m in the base of overburden can provide a similar response to the alteration signature. New research (CMIC-Footprints project; see Section 2.5.2) shows that the density of the alteration zone can vary over a wider range from 2.2 g/cc (desilicification) to 2.6 g/cc (silicification). This means that a larger response (amplitude) related to the alteration zone might be seen in the Bouguer anomaly.

5.5 Conclusions

In this chapter, I was working to build realistic models taking into account changes in multiple factors such as datum, variable interfaces and structures that are estimated or speculated and these are taken into account in forward modelling. Also, the relative benefits of the free-air anomaly and the Bouguer anomaly were examined by synthetic models. Different models were made to investigate the contribution of different geological structures of the McArthur River area in gravity data. The sequence of these models from simple to complicated give a better understanding of the signature of the geological structures on gravity data. It was shown that the free-air data are dominated by the variations of topography and not useful. Also, the basement has a significant effect on the Bouguer anomaly. And, the density contrast between sandstone and alteration is an important factor for detecting the alteration signature in the Bouguer anomaly. Therefore, it is not easy to provide a minimum contrast that is needed in order to resolve the alteration zone as the depth and density of other structures have a very large effect on the results. If it is possible to remove the overburden signature from the gravity data, there can be more

factors (e.g. topography between the overburden and sandstone) which are able to mask the alteration signature.

It was shown that the location of the datum in the Bouguer correction has no significant effect on the Bouguer anomaly. But, a good estimate of density of overburden is necessary for obtaining a good result even when there is a poor approximation for the datum in the Bouguer correction.

Chapter 6

Modelling and Inversion of Seismic Refraction and Gravity Data of the McArthur River Area

6.1 Introduction

Seismic refraction (see Section 3.4) is one of the best geophysical methods to investigate the interface between shallow layers. It can also yield the seismic velocity of the geological structures between the interfaces (Telford et al. 1976; Sheriff and Geldart, 1995; Kearey et al., 2002). In this research, seismic refraction data were synthetized for a 2D model. Inversion (see Section 4.5) was applied on the synthetic data to find the base of the overburden. The inversion approach used in this research is that of Lelièvre et al. (2012). This uses the minimum structure approach in which an objective function is minimized using a Gauss-Newton method. For the joint inversion, I have mostly used the clustering fuzzy c-mean method in which I can specify a relationship between the physical properties that lies in discrete clusters (Paasche and Tronicke, 2007). 2D joint (as well as independent and constrained) inversion of seismic refraction and gravity data is assessed as a means of reliably mapping overburden thickness, enabling density anomalies from deeper mineralization and alteration to be reconstructed through gravity inversion. Results show

that the seismic refraction data provides an accurate estimation of the base of the overburden in the joint Earth model, which in turn leads to an accurate density distribution in the same model. However, this approach would be expensive on a realistically large scale.

In this chapter, 2D models of the McArthur area are made to synthetize the seismic refraction (first-arrival traveltime) data followed by the inversion of synthetic data to reconstruct the true model. Different Earth models will be investigated such as a two-layer model and a drumlin-shape model. Also, the joint inversion method will be assessed by considering and adding the gravity method. Finally, a constrained gravity inversion will be used to reconstruct the alteration zone by getting help from the independent and joint inversion models of seismic refraction. All these processes will be applied on the real data as well. Since there is no real seismic refraction data in the McArthur-Millennium area, I have used the first-arrival traveltime data obtained from the 3D seismic reflection data of the Millennium area.

6.2 Synthetic modelling and inversion of seismic refraction

In this section, synthetic modelling and inversion of seismic refraction data are investigated over different models. Figure 6.1 represents the topography of the McArthur-Millennium corridor. There are many drill-holes in the corridor which are mostly located close to the faults (e.g. the P2 fault in McArthur area). A straight survey line crossing a few drill-holes is chosen for the modelling. In the model, the variation of topography and the base of overburden are obtained from drill-hole data. Inset in Figure 6.1 shows the location of the

survey line. The variation of overburden thickness is not only due to the variable topographic surface, which is the outcome of glacial events, but also due to the variable interface between overburden and sandstones (Figure 6.2).

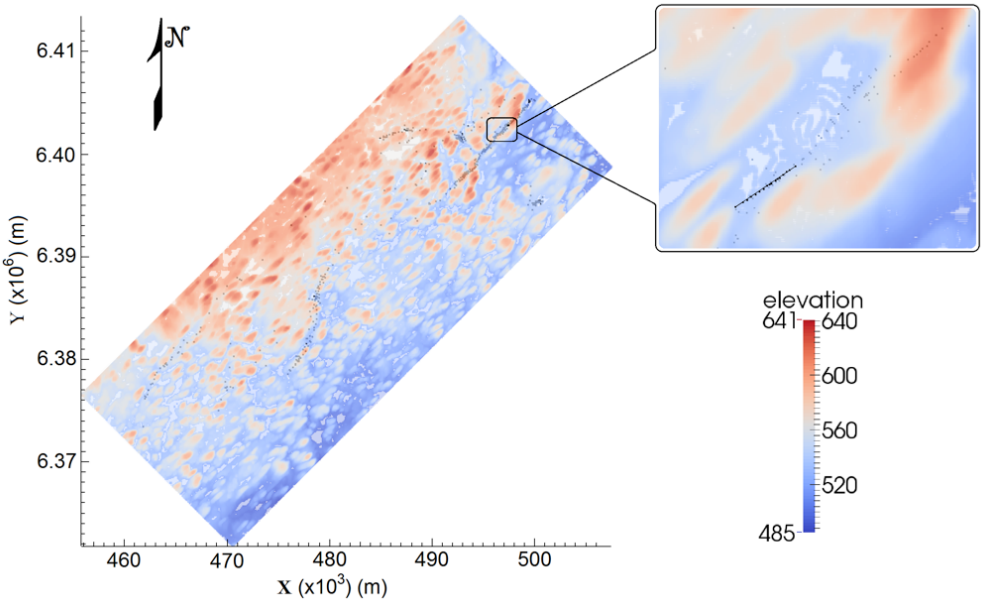

Figure 6.1: Topography of the McArthur-Millennium corridor. Inset shows location of survey line (black line) and seismic sources for synthetic modelling study.

6.2.1 Two-layer model

A vertical section was made for the synthetic model using real drill-hole data (Figure 6.2). Two layers are considered in which the upper layer is the overburden and the lower layer is sandstones. Appropriate slownesses were specified for these two layers. The overburden and the sandstones have a slowness of 0.00025 s/m and 0.000625 s/m, respectively (see Section 2.5.1). Then, the forward modelling code (Lelièvre et al., 2011; see Section 4.3) is run in order to generate the seismic first-arrival traveltime data. In order to keep this synthetic modelling similar to the real surveys, distances between receivers (geophones)

and sources are 2 m and 50 m, respectively. In this chapter, using a code of Lelièvre and Farquharson (2015) a Gaussian random noise of standard deviation equal in magnitude to 1% of a datum is added to the synthetic traveltime data. Also, Figure 6.2 illustrates the propagation of a wavefront (traveltime contours) belonging to one of the sources, and related seismic rays.

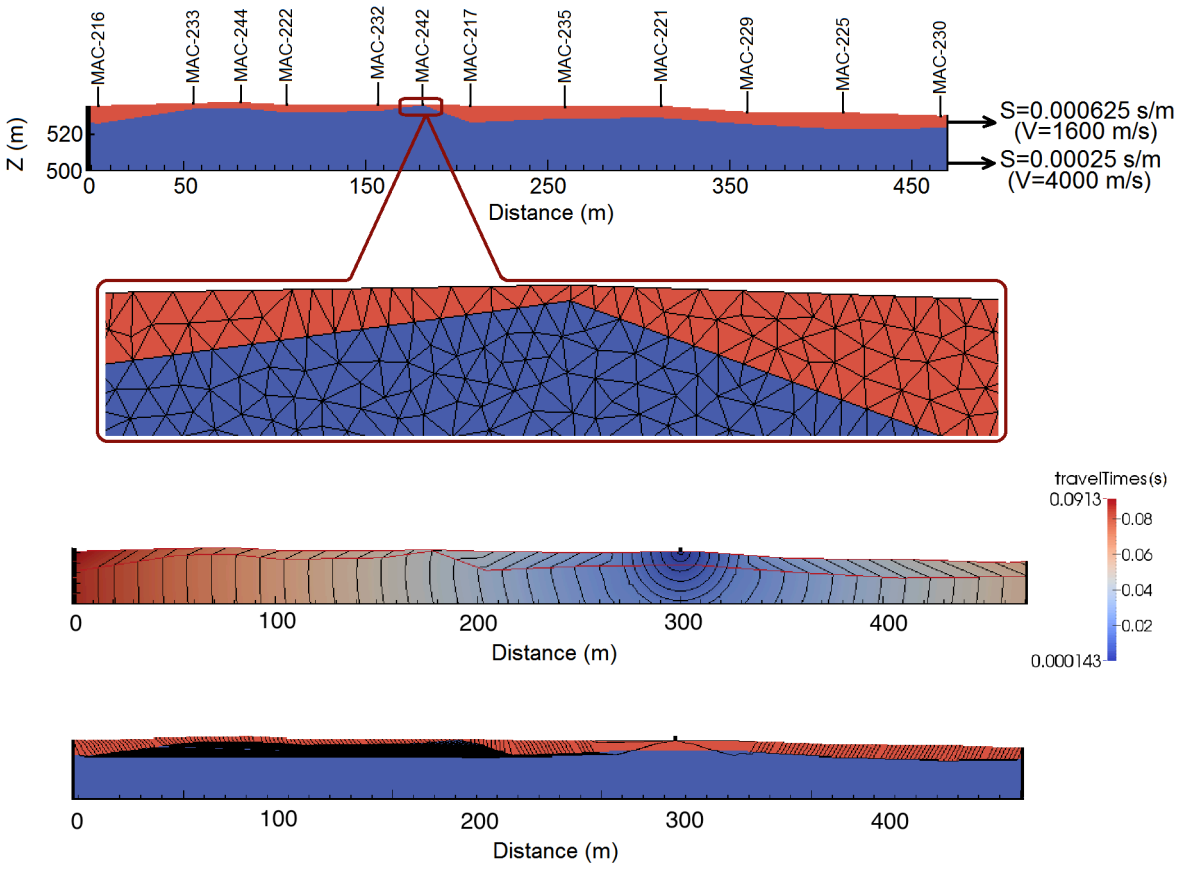

Figure 6.2: Top: model of glacial sediments (red, slow) over sandstone (blue, faster) based on true topography and base of glacial sediments interpolated between boreholes (labelled), and as an inset the triangular mesh used for the modelling. Middle: propagation of a wavefront (traveltime contours) associated with one of the sources. Bottom: seismic traces between receivers and one of the sources.

In all the inversions in this chapter, for the data misfit, the value of ω reached 1 while a value less than one is considered for the *chifact* (see Section 4.5). This leads to a desirable fit. Also, a small value of 10^{-5} is considered for the initial trade-off parameter value. For the inversion of gravity data, the distance weighting is considered. Also, no reference model is considered in the inversions except in the constrained inversions described towards the end of this chapter. The mesh used in all the inversions extends a larger distance laterally than what is shown in the figures in order to decrease the effect of the edge of the mesh on the computed data.

After considering suitable values for inversion parameters, the inversion code (Lelièvre et al., 2012) was run for the synthetic traveltime data-set using both L2-norm and L1-norm methods (Figure 6.3). The model obtained from the inversion process using the L2-norm displays an acceptable agreement with the true model in which the depth is reasonably estimated (Figure 6.3 top panel). But, the interface between the two layers is not sharp and obvious, which is due to the smoothing nature of the L2-based regularization used in this inversion. In order to ameliorate this problem, the L1-based approach was also used (Figure 6.3 bottom panel). As can be seen, small variations in the glacial sediments–sandstones contact are remarkably well reproduced, and the interface is sharp. However, the number of iterations (and subsequently the run-time) in the L1-based inversion is much more than the L2-based inversion. The run-time for L2 is around 2 hours (for 11 iterations), while the run-time for L1 is more than 4 hours (for 24 iterations).

Figure 6.4 shows the traveltime-distance plots of the refraction data computed for the models constructed by the inversions as well as the synthetic observed refraction data-set

provided to the inversion. The fit between the observed and calculated data is good and mostly acceptable. For the L2-norm and the L1-norm, the inversion process started with an ω value of 1447.3 and 1168.7, and stopped when they reached to 1.042 and 1.028, respectively (see Section 4.5). Models are constructed with more than 40,000 triangle cells, in which the maximum area of cells is limited to 1 square metre. The advantage of small cells is seen where the thickness of the layers is very small, as it can be seen in Figure 6.2 in the model between 100 m and 200 m. Although small cells increase the run-time, they increase the resolution and accuracy. Small cells give the inversion freedom to put interface and changes of slowness where required to without being constrained by cell boundaries. The interface under the two last stations in both sides is not resolved because the refracted wave beneath these locations is not measured (see Figure 3.14).

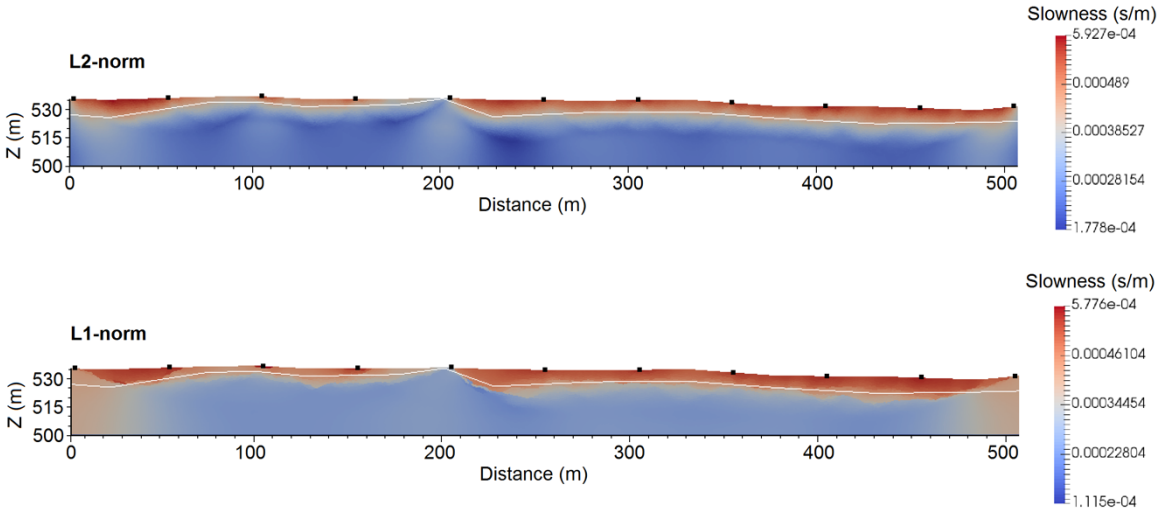

Figure 6.3: Earth model constructed from inversion of synthetic seismic data along the line shown in Figure 6.2 using L2- and L1-norm. Locations of sources indicated by squares. White line indicates the glacial sediments-sandstone contact in the model used to synthesize the data for this example.

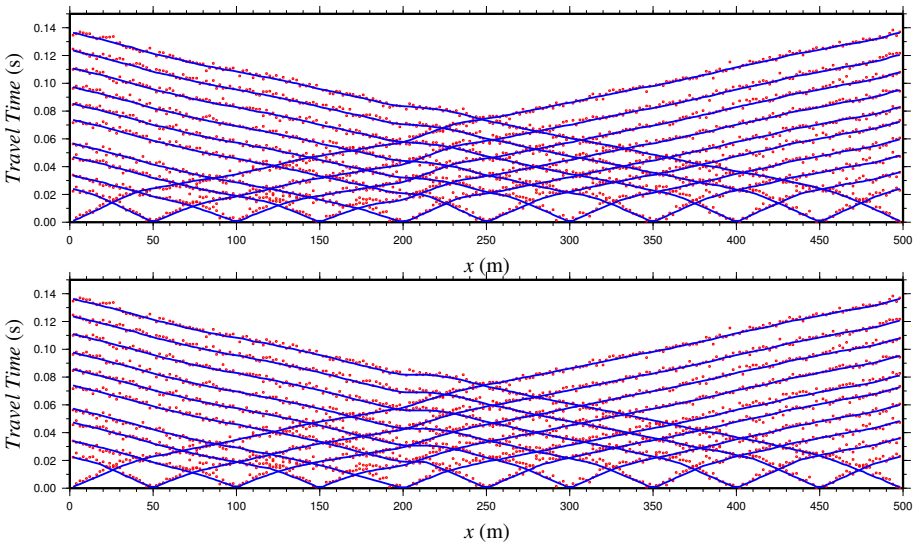

Figure 6.4: Traveltime-distance plot of refraction data belonging to the forward modelling used in the inversion code (red) and data calculated from the inversion model (blue) for both L2-norm (top) and L1-norm (bottom) models in Figure 6.3. One percent random noise is added to the synthetic data on this and all subsequent plots in this chapter.

6.2.2 Drumlin-shape models

In order to test the modelling and inversion for different structures, a few models were made for drumlin-shape models as the McArthur-Millennium corridor is dominated by streamlined deposits such as drumlins (Figures 6.5, 6.6 and 6.7). Physical properties were kept the same as for the previous model; however, the shape and thickness of overburden is different in these models. The difference between them are in the shape of the interface between glacial sediments and sandstones as the base of the glacial sediments has a topography due to the abrasion caused by glacial motions. In Figure 6.5, small variations were considered for the interface, whereas Figures 6.6 and 6.7 demonstrate bulge and trough shapes for the interface, respectively. Forward and inversion modellings for these models were similar to those for the model in Figure 6.3, where distances between receivers (geophones) and sources were kept as 2 m and 50 m, respectively. It can be seen that

inversion results (using L2-norm method) show a good agreement with the true synthetic models, and there is a good fit between observed and calculated data.

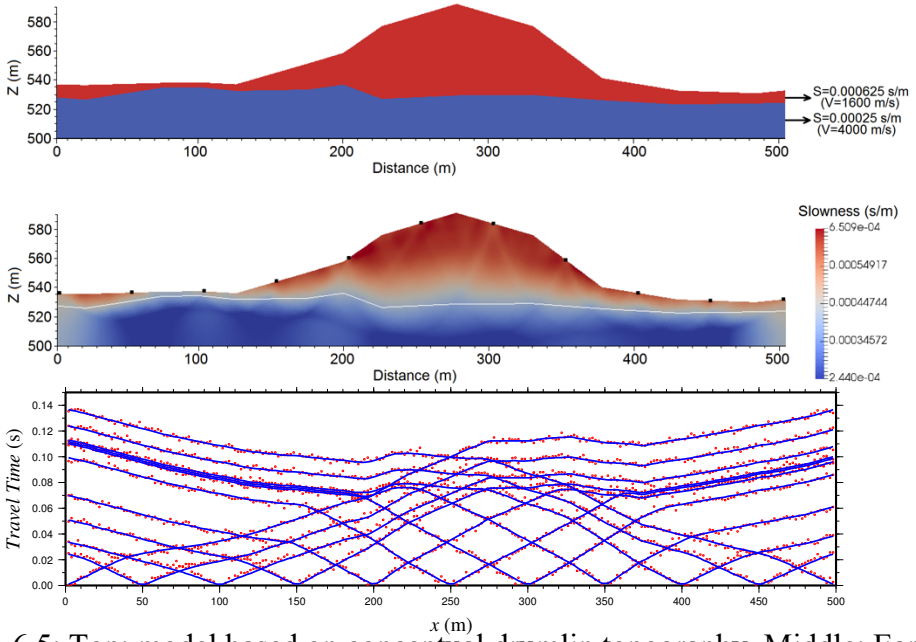

Figure 6.5: Top: model based on conceptual drumlin topography. Middle: Earth model constructed from L2-norm inversion of synthetic seismic data. White line indicates the glacial sediments-sandstone contact. Bottom: Traveltime vs distance plot of refraction data for true model (red) and data calculated from the inversion result (blue).

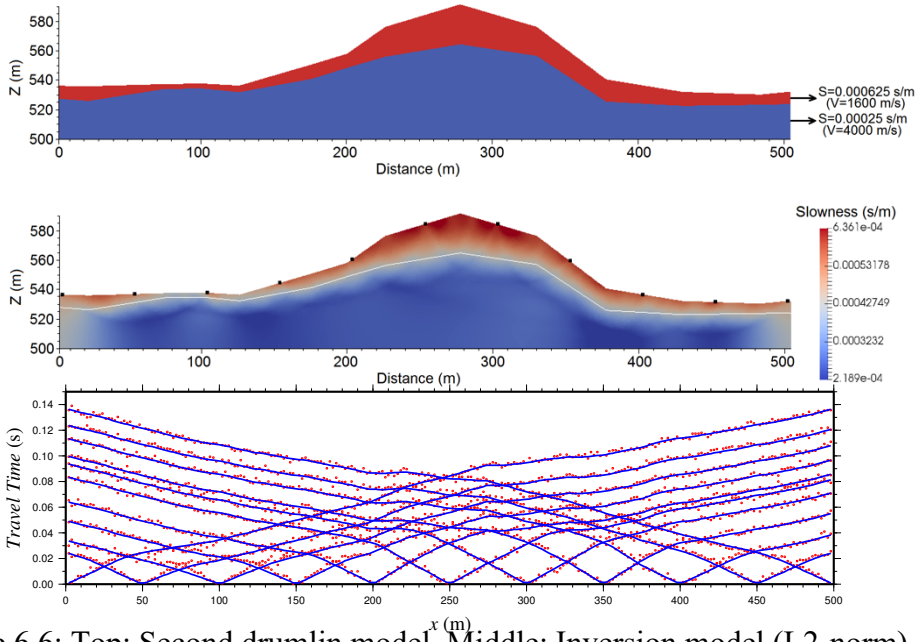

Figure 6.6: Top: Second drumlin model. Middle: Inversion model (L2-norm). Bottom: Traveltime vs distance plot of refraction data for true model (red) and for inversion result (blue).

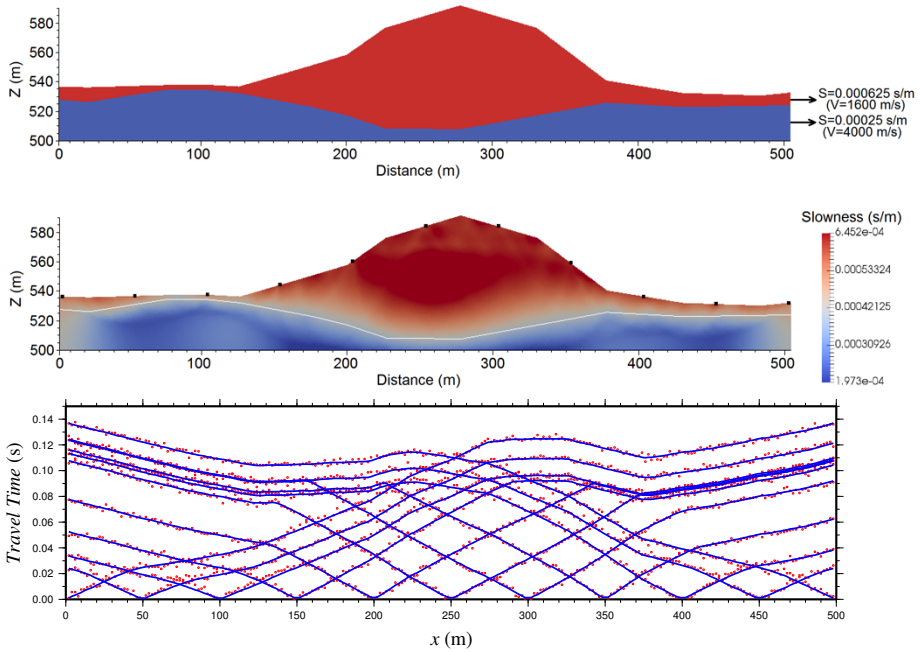

Figure 6.7: Top: Third drumlin model. Middle: Inversion model (L2-norm). Bottom: Travel-time vs distance plot of refraction data for true model (red) and for inversion result (blue).

6.2.3 Blind-layer model

A blind layer is a low-velocity layer in which rays cannot be critically refracted (see Section 2.5.1 and 3.4.3). This leads to an overestimation of the depth to underlying interfaces. The assumption that velocity increases with depth may not always be valid. The real indication of a blind layer in the McArthur area is shown in Figure 2.12 where the lower layer in the glacial sediments (which is unconsolidated stratified sand and gravel) can have a lower seismic velocity than the upper layer in the glacial sediments (which is unconsolidated stratified tills). Thus, a synthetic model is made with a blind layer case which is represented in Figure 6.8. In this model, distances between receivers (geophones) and sources are 5 m and 20 m, respectively. The middle layer has a lower velocity than the upper layer. The difference between observed and calculated data for the inversion illustrates a good fit,

whereas the inversion vertical section shows an overestimation and a very fuzzy, indistinct base of the overburden/blind layer of the depth (see Figure 6.8). The bind layer was not captured as well.

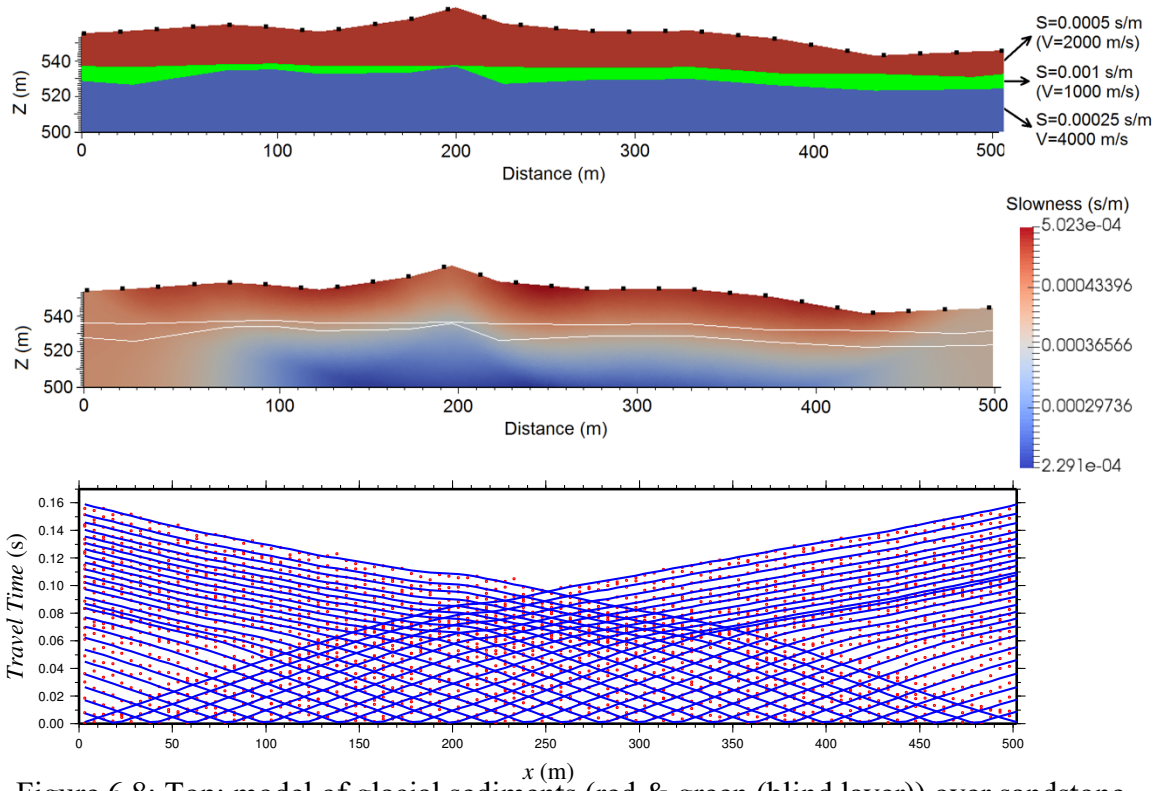

Figure 6.8: Top: model of glacial sediments (red & green (blind layer)) over sandstone (blue, faster) based on conceptual topography. Middle: Inversion model (L2-norm). Bottom: Traveltime vs distance plot of refraction data for true model (red) and for inversion result (blue).

6.3 Joint inversion of synthetic seismic refraction and gravity data

Another effective method to determine the subsurface structure using geophysical data is joint inversion (see Section 4.5). The joint inversion is applied to the drumlin model shown in Figure 6.5. The mesh used for this joint inversion is laterally and vertically more extensive than what is shown in the figures. Two layers are considered in which the upper layer is the glacial sediments (v=1600 m/s and d=2 g/cc; in this chapter the density will be

shown with "d" as ρ is used for the coupling factor) and the lower layer is sandstone (v=4000 m/s and d=2.42 g/cc). Using the code of Lelièvre and Farquharson (2015) a Gaussian random noise with a standard deviation equal in magnitude to 1% of a datum is added to both synthetic traveltime and gravity data. Figure 6.9 (second panel) shows results from the independent inversions of gravity data for this drumlin-shaped model using the L2-norm. There is a good fit between observed and calculated data. However, the density vertical section in particular does not resemble the true model (Figure 6.9).

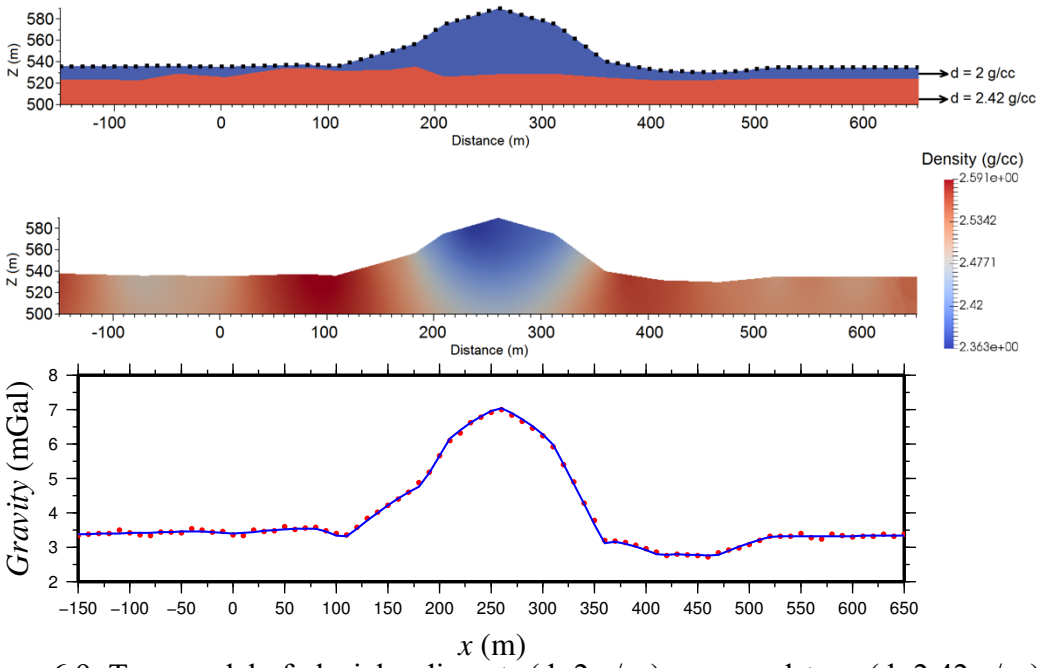

Figure 6.9: Top: model of glacial sediments (d=2 g/cc) over sandstone (d=2.42 g/cc) based on conceptual topography (drumlin; Figure 6.5). Middle: Earth models constructed from independent inversions (L2-norm) of synthetic gravity data along an 800 m line. Bottom: gravity data for the true model (red) and data calculated from the inversion result (blue).

In order to solve this problem, the joint inversion of seismic refraction and gravity data is used (Figures 6.10 to 6.13). The joint inversion method tries to leverage good seismic sensitivity to the glacial sediments–sandstones contact to build accurate glacial sediment

layers in the density model. The simultaneous inversion of two geophysical data-sets (i.e. seismic refraction and gravity data; see Sections 3.2 and 3.4) is intended to produce a single Earth model consistent with both data sets. In this chapter, the clustering fuzzy c-mean method is used for the joint inversion method to simultaneously invert the two data sets by including a term in the objective function which links the two physical properties (see Section 4.5). Because there are two layers in the true model, two clusters are defined with average physical properties corresponding to the two main geological structures: glacial sediments (density=2 g/cc; slowness:0.000625 s/m), sandstone (density=2.42 g/cc; slowness:0.00025 s/m). A coupling factor of ρ=1 is considered. Values larger than ρ=1 were tested for the coupling factor as well, but the results were not as good as for ρ=1. Therefore, they are not shown in this thesis. By increasing the coupling factor, the similarity between the models increases, but the number of iterations (convergence) as well as the run-time will increase. For the joint inversion of gravity and seismic data the joint inversion after preheating (JaP) is used, and one stage is used for heating the coupling factor (see Section 4.5).

Figure 6.10 shows the model for a coupling factor of ρ =1. The fit between observed and predicted data is good (Figure 6.11), and the approximate location of the interface can be seen. In comparison to the independent inversions, the density model is much improved (Figure 6.9). The variation of the various terms in the objective function (see Section 4.5) for the joint inversion model is shown in Figure 6.12. In total, 237 iterations are done in the "JaP" inversion process (see Section 4.5) of which 82 were used for pre-heating (shown by the grey area in Figure 6.12). The run-time was 542 hours for a mesh with 468,000 cells.

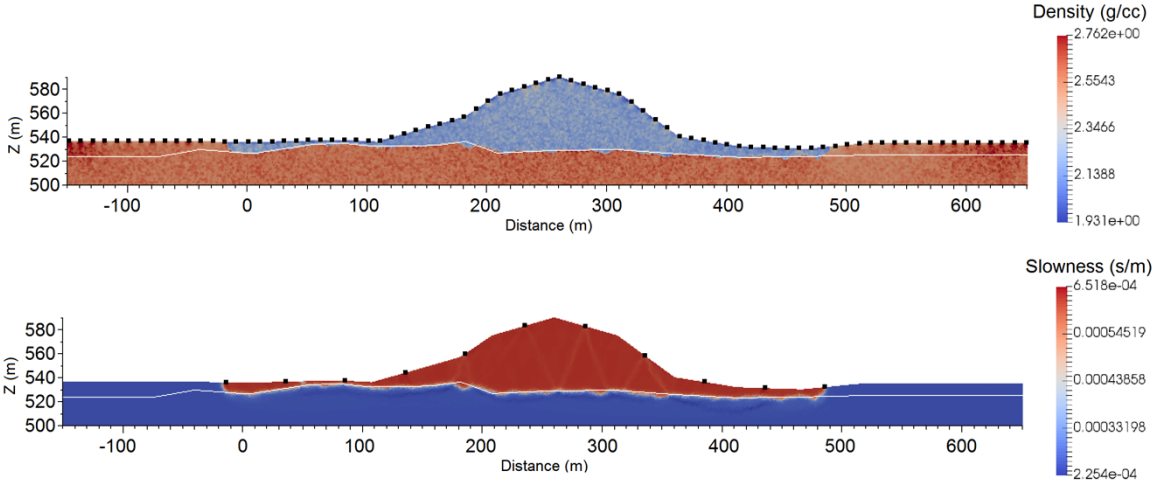

Figure 6.10: Density (top) and slowness (bottom) models constructed from joint inversion of seismic and gravity data (coupling factor ρ =1; L2-norm). Locations of seismic sources and gravity observation locations are indicated by black squares. White line indicates the glacial sediments-sandstone contact.

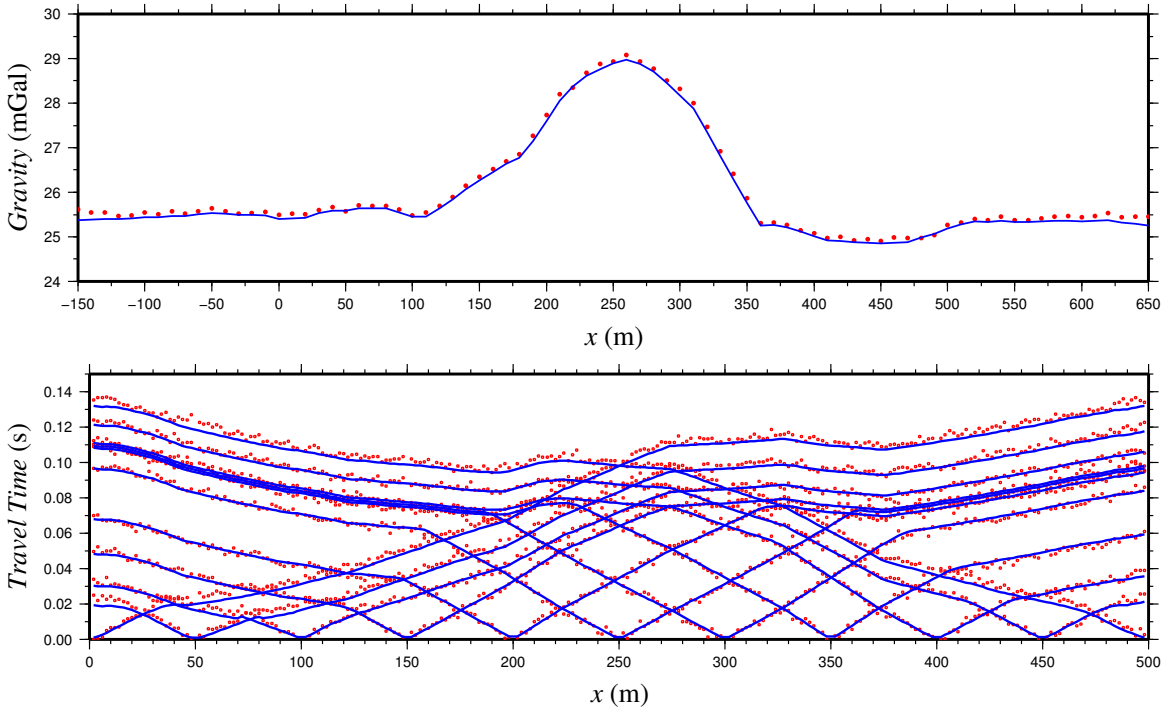

Figure 6.11: Gravity and seismic refraction data for the true model (red) and data for the joint inversion result (blue; ρ =1).

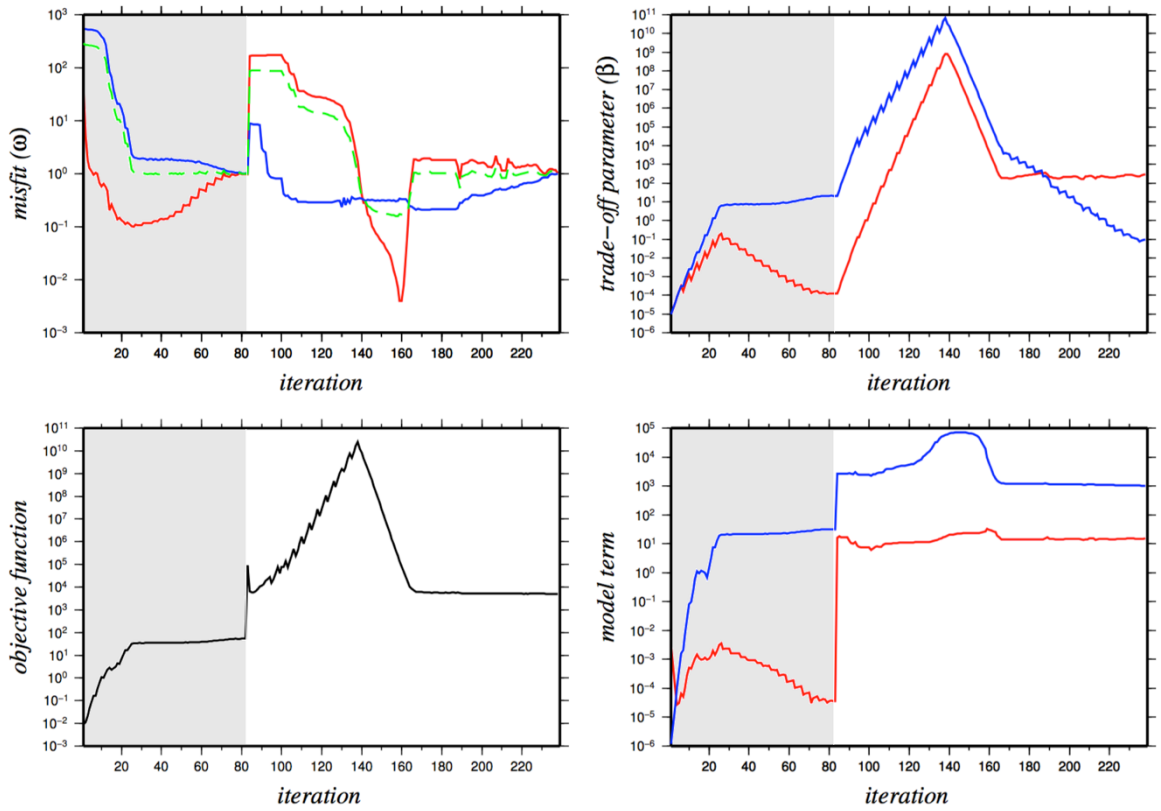

Figure 6.12: Variations of the different parts of the objective function such as data misfit (ω; top-left), trade-off parameter (β; top-right), objective function ($\mathbf{\Phi}$; bottom-left) and model term (ϕ_m; bottom-right) at iterations for the joint inversion of gravity (red) and seismic refration (blue) data for ρ=1. Green color shows the "average ω" (see Section 4.5). Grey area shows the pre-heating part, and the white area shows the joint inversion part.

Figure 6.13 illustrates the physical properties (slowness versus density) obtained after the independent and joint inversions. Physical properties belonging to each cell are indicated by a blue spot. For the independent inversion, no clusters are generated, while two clusters can be seen for the joint inversion results which represent the physical properties of upper (s=0.000625 s/m and d=2 g/cc; "s" is defined as the symbol for slowness) and lower (s=0.00025 s/m and d=2.42 g/cc) layers. As mentioned, the inversion mesh was larger than is shown in the pictures. The slowness values were more uniform than the density values in the extended parts (which are not shown in the pictures) while

the density was gradually changing. This can be seen as the horizontal extensions (lines) in the joint inversion scatter plot.

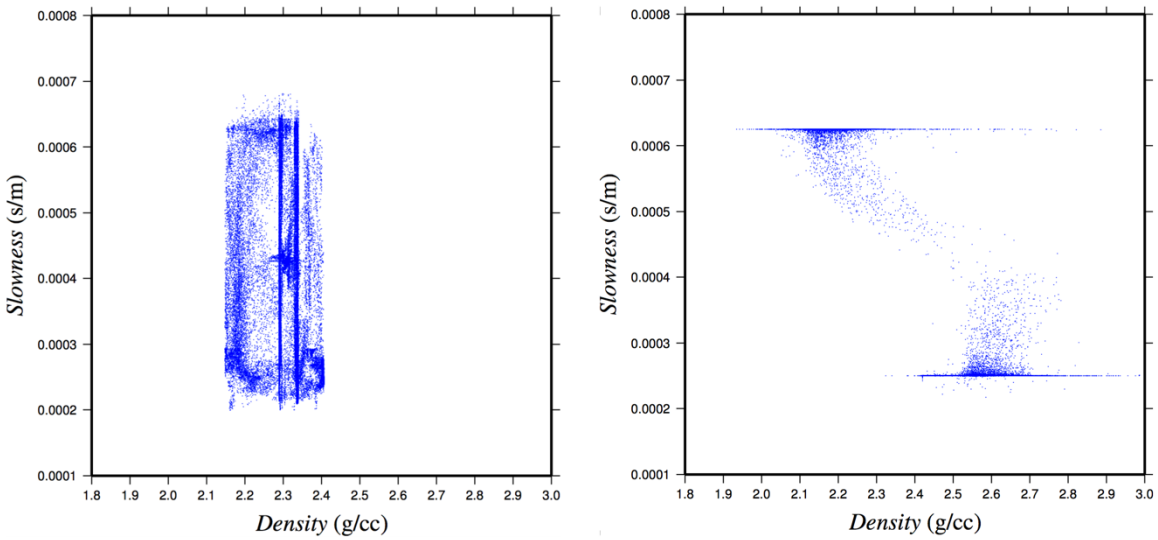

Figure 6.13: Physical properties (slowness versus density) obtained after the joint inversion (right; Figure 6.10) as well as the independent inversions that produced the models in Figures 6.5 and 6.9 (left).

Next, a more complicated model is investigated. For this purpose, a drumlin shaped model is made containing three geological structures: glacial sediments (#1 in Figure 6.14), sandstone (#2 in Figure 6.14) and alteration zone (#3 in Figure 6.14). After considering appropriate physical properties (i.e. density and slowness), seismic first-arrival traveltime data as well as gravity data were synthesized using the code of Lelièvre et al. (2011). As can be seen in Figure 6.15, the seismic data have no chance of seeing the alteration zone as it is too deep in this model. The contribution of the different structures to gravity data is shown in Figure 6.16. The increased density of the alteration zone relative to the sandstone (i.e., Δd=0.18 g/cc) increases the magnitude of gravity data as much as 0.2 mGal.

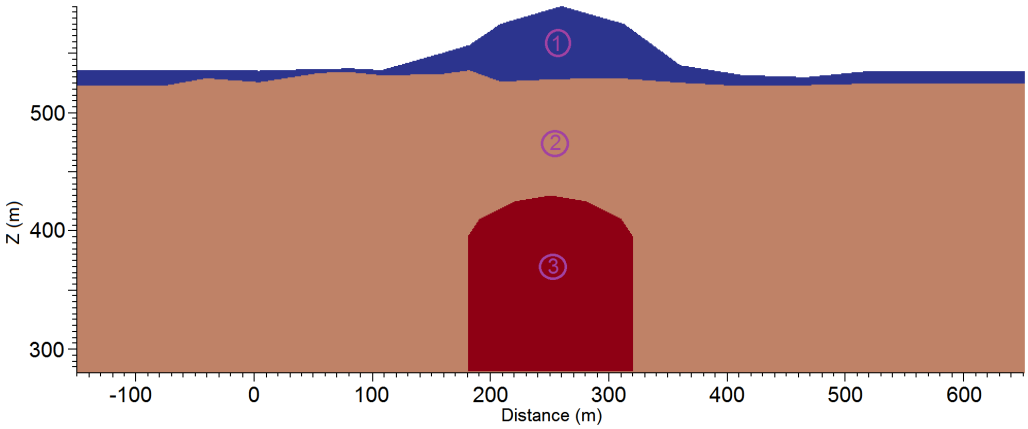

	Density(g/cc)	Slowness(s/m)
①	2	0.000625
②	2.42	0.00025
③	2.6	0.0002

Figure 6.14: Drumlin shaped model with an anomaly (alteration zone) at depth.

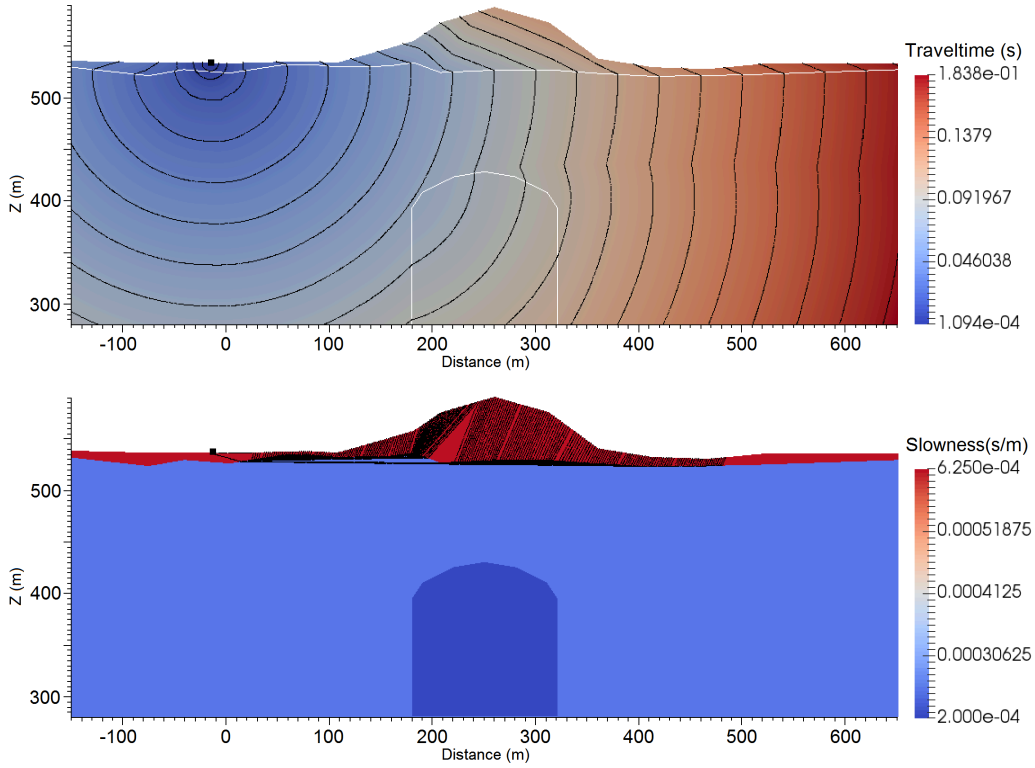

Figure 6.15: Propagation of a wavefront (traveltime contours; top) belonging to the first source from left (black dot), and seismic rays between this source and receivers (bottom).

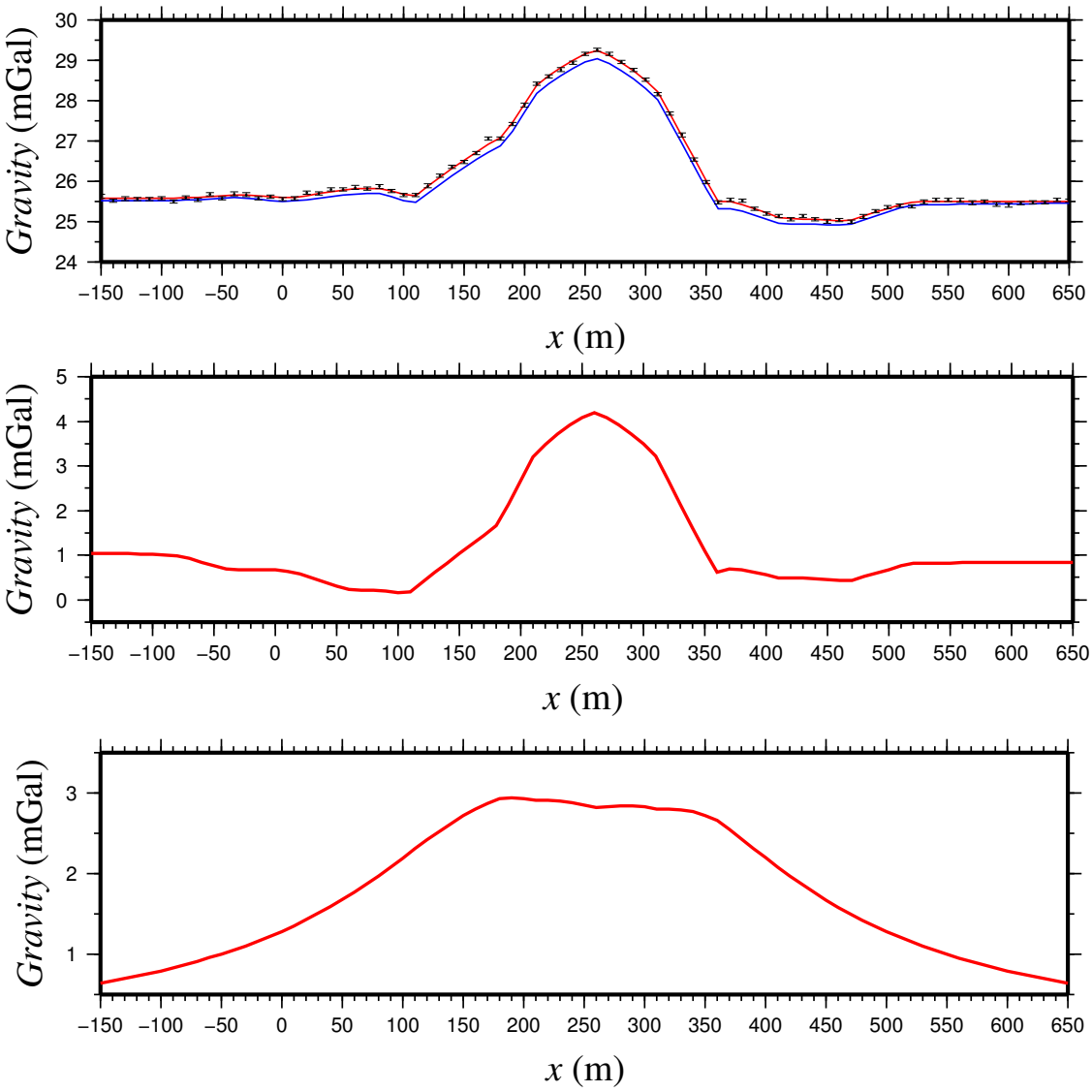

Figure 6.16: Top: red line shows gravity data for the model shown in Figure 6.14. Error bars show the uncertainty and data after adding 1% noise. Blue line shows gravity data for the model shown in Figure 6.14 i.e., with only two layers (alteration zone is removed). Middle: overburden signature. Bottom: alteration zone signature.

Independent inversions were performed for gravity data using the L2 norm (Figure 6.17) as well as for seismic data using both L2-norm (Figure 6.18) and L1-norm methods (Figure 6.19) using the code of Lelièvre et al. (2012). The mesh used for the inversion extends a greater lateral distance than is shown in the figures in order to decrease the effect of the edge of mesh on the data especially gravity data. The slowness vertical sections show a good agreement with the original model in the upper part of the model. However, the alteration zone is not recognized. The density vertical section does not show a deep alteration zone either. However, the fit between observed and calculated data for all the models is good.

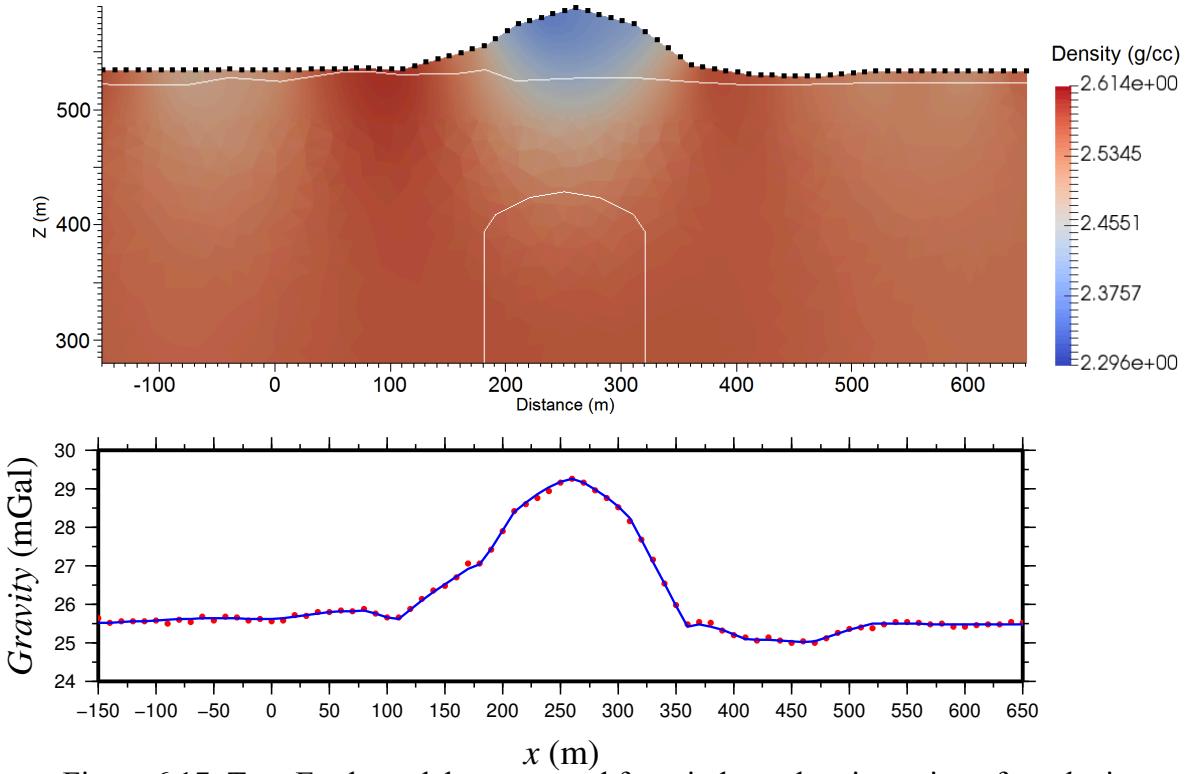

Figure 6.17: Top: Earth model constructed from independent inversion of synthetic gravity data (L2-norm). Bottom: Gravity data for the true model (red) and data calculated from the inversion result (blue).

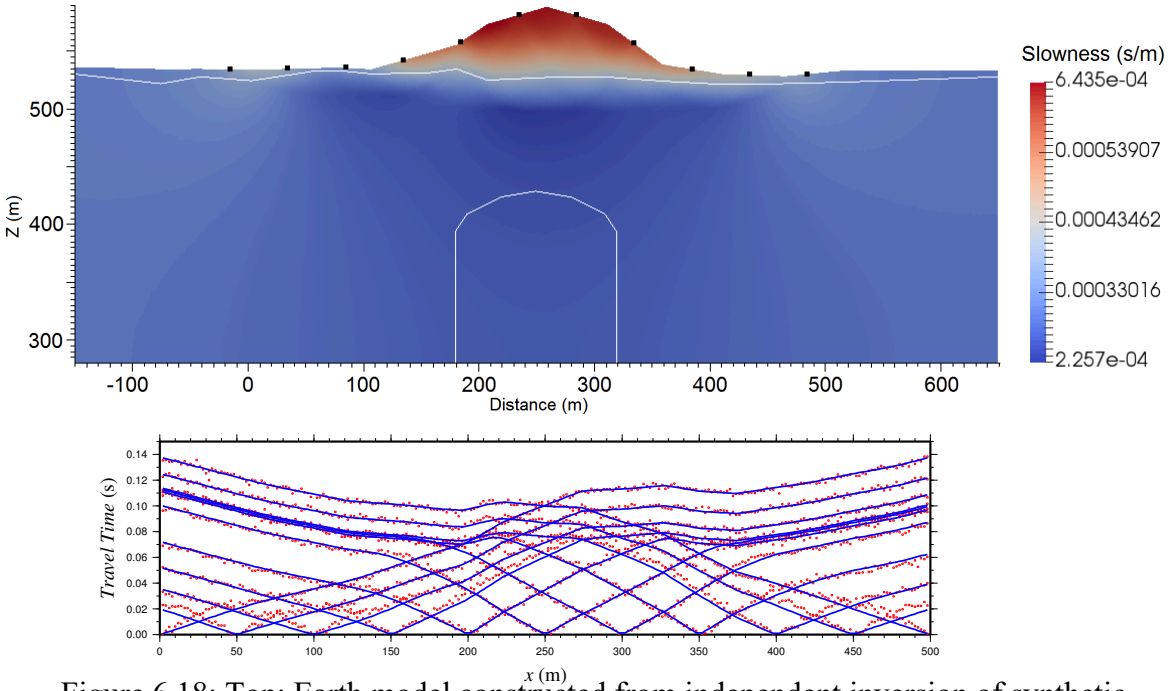

Figure 6.18: Top: Earth model constructed from independent inversion of synthetic seismic data using L2-norm. Bottom: Refraction data for the true model (red) and data calculated from the inversion result (blue).

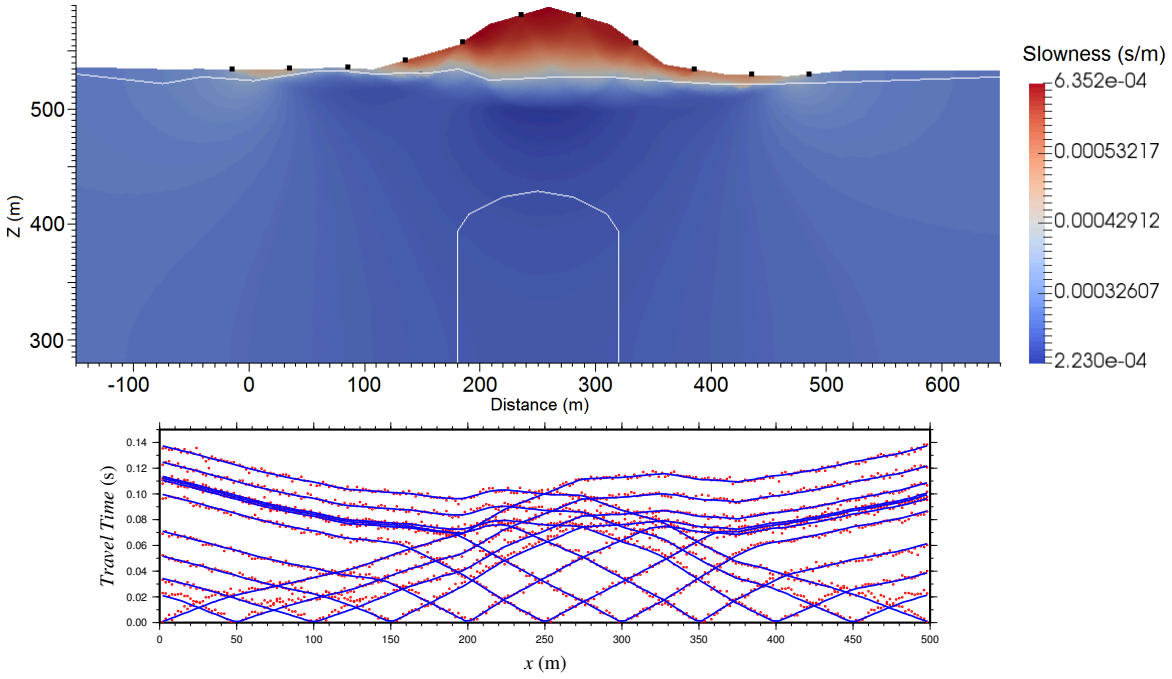

Figure 6.19: Top: Earth model constructed from independent inversion of synthetic seismic data using L1-norm. Bottom: Refraction data for the true model (red) and data calculated from the inversion result (blue).

In order to improve the results, the joint inversion method is used. Figure 6.20 shows the slowness and density models obtained by joint inversion using a coupling factor of ρ=1. Two clusters were defined from prior information for the joint inversion, namely, for upper layer: s=0.000625 s/m and d=2 g/cc; for lower layer: s=0.00025 s/m and d=2.42 g/cc. However, initially three clusters were considered (with an alteration zone as the third cluster). This forced the code to generate a third anomaly at depth while there was no signature of alteration zone in the seismic data. This was tested by a model which had no alteration zone but three clusters were considered in the joint inversion. It was seen that an artificial anomaly is constructed in the inversion model using the third cluster (alteration zone) when no anomaly was present in the synthetic model. Therefore, in this modelling only two clusters were considered.

A total of 81 iterations were required without pre-heating prior to the inversion in one stage (see Section 4.5). The run-time was around 287 hours. The fit to the data is reasonable (Figure 6.21), and the approximate location of the base of the overburden can be clearly seen in Figure 6.20. In comparison to the independent inversion of the gravity and seismic refraction data (Figures 6.17 to 6.19), the density and slowness models are much improved. But, the alteration zone is not yet identified. The variation of the various terms of the objective function (convergence curves) for the joint inversion models are shown in Figure 6.22. Figure 6.23 illustrates the physical properties (slowness versus density) obtained after the joint inversion for the models in Figure 6.20. Physical properties belonging to each cell are indicated by a blue spot (around 468,000 cells). It can be seen that two clusters are made.

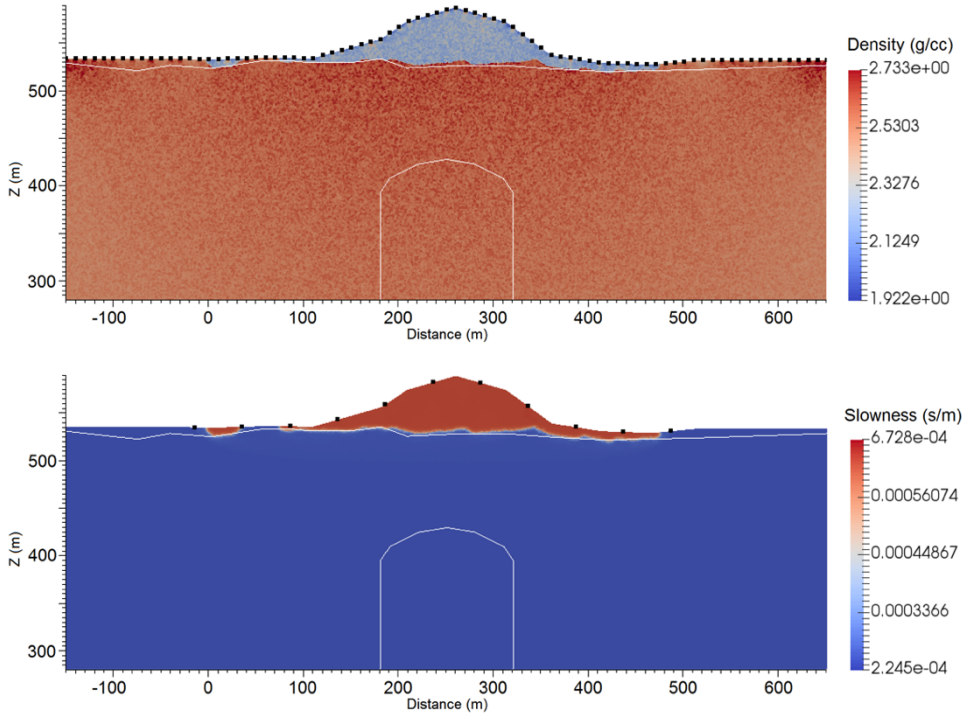

Figure 6.20: Density (top) and slowness (bottom) models constructed from joint inversion of seismic and gravity data (coupling factor ρ =1). Locations of sources are indicated by black squares. White lines indicate the glacial sediments-sandstone contact, and the white arch shaped line in the contact of alteration zone at depth.

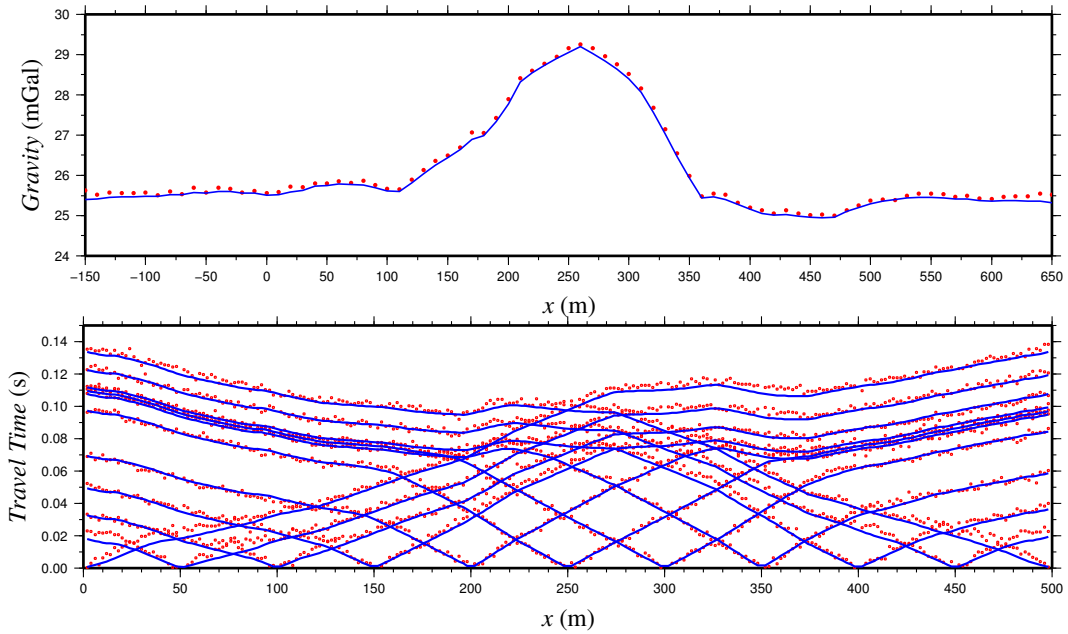

Figure 6.21: Gravity and seismic refraction data for the true model (red) and data for the joint inversion result (blue; ρ =1).

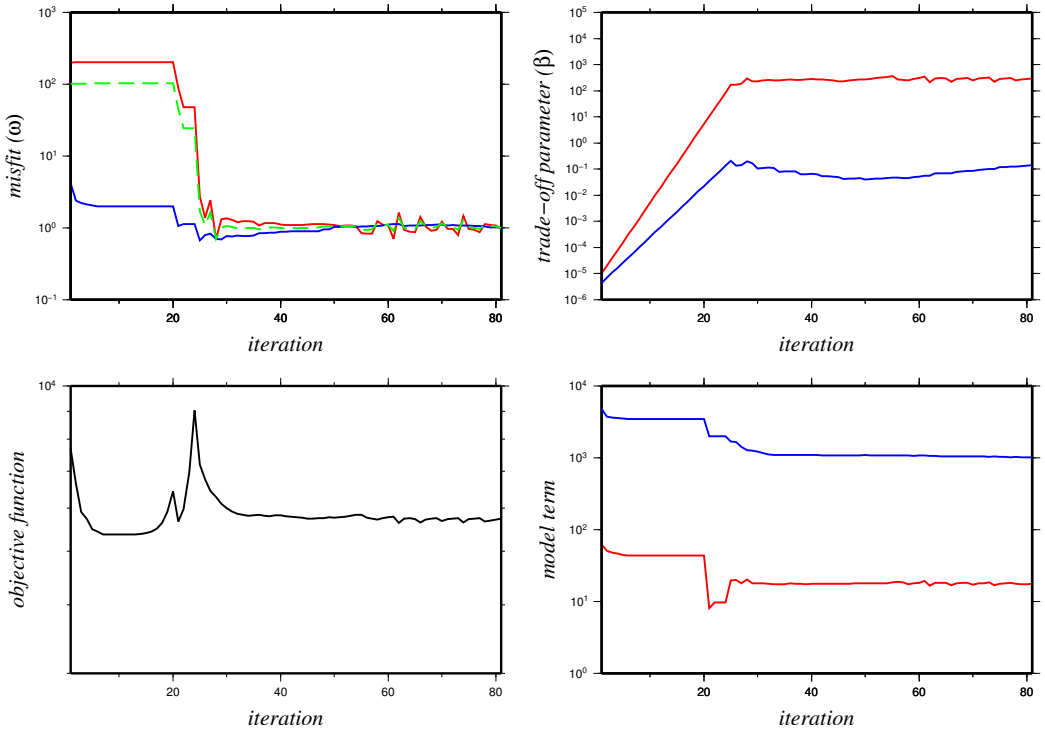

Figure 6.22: Variations of different parts of the objective function such as data misfit (ω; top-left), trade-off parameter (β; top-right), objective function ($\mathbf{\Phi}$; bottom-left) and model term (ϕ_m; bottom-right) at iterations for the joint inversion of gravity (red) and seismic refraction (blue) data for ρ=1. Green color shows the "average ω" (see Section 4.5). Pre-heating is not used for this joint inversion.

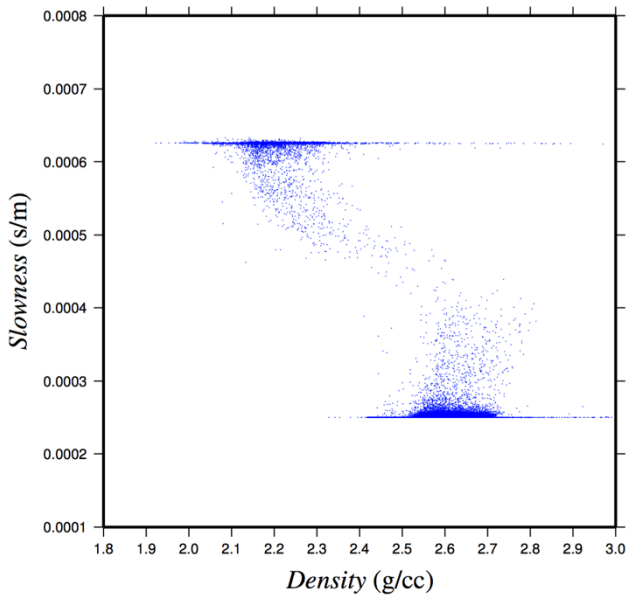

Figure 6.23: Physical properties (slowness versus density) obtained after the joint inversion. Two clusters can be seen which represent the physical properties of overburden (s=0.000625 s/m and d=2 g/cc) and sandstone (s=0.00025 s/m and d=2.42 g/cc).

To try to improve the ability to resolve the density model at depth, a constrained inversion is performed to compare with the joint inversion (see Section 4.5). For this purpose, the thickness and density of the overburden structure as well as the upper part of sandstone (above 500 m) which have been determined from the joint inversion models are used as a guide for the constraint in an independent gravity inversion. For the constrained inversion, a single value for the density of overburden cells (2 g/cc) and sandstone cells (2.42 g/cc) was fixed. This helps the code reconstruct the other geological structures (i.e. the alteration zone) below the overburden. Figure 6.24 shows that the overburden part as well as the upper part of the sandstone have a uniform density, and the alteration zone can be seen in the centre of the model.

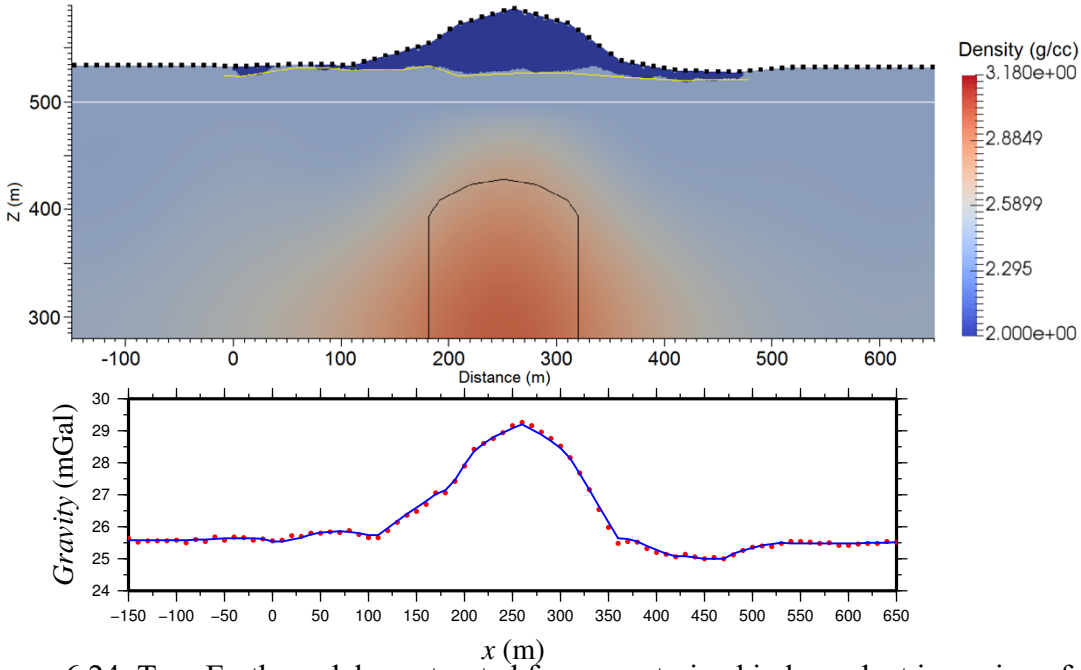

Figure 6.24: Top: Earth model constructed from constrained independent inversion of synthetic gravity data (L2-norm). The constrained zone is located above the white line in which the overburden and the top sandstone obtained from joint inversion results have a fixed value during the inversion. The black line and yellow line show the location of the true alteration zone and the true base of overburden, respectively. Bottom: gravity data for the true model (red) and data calculated from the inversion result (blue).

6.4 Real data example from Millennium area

The combination of joint gravity–travel-time inversion followed by constrained gravity inversion was then applied to real data from the Millennium area in the Athabasca Basin. First arrival travel-times for a 3D reflection seismic survey and ground gravity data from the Millennium area of the Athabasca Basin were the two sets of data used here (Figure 6.25).

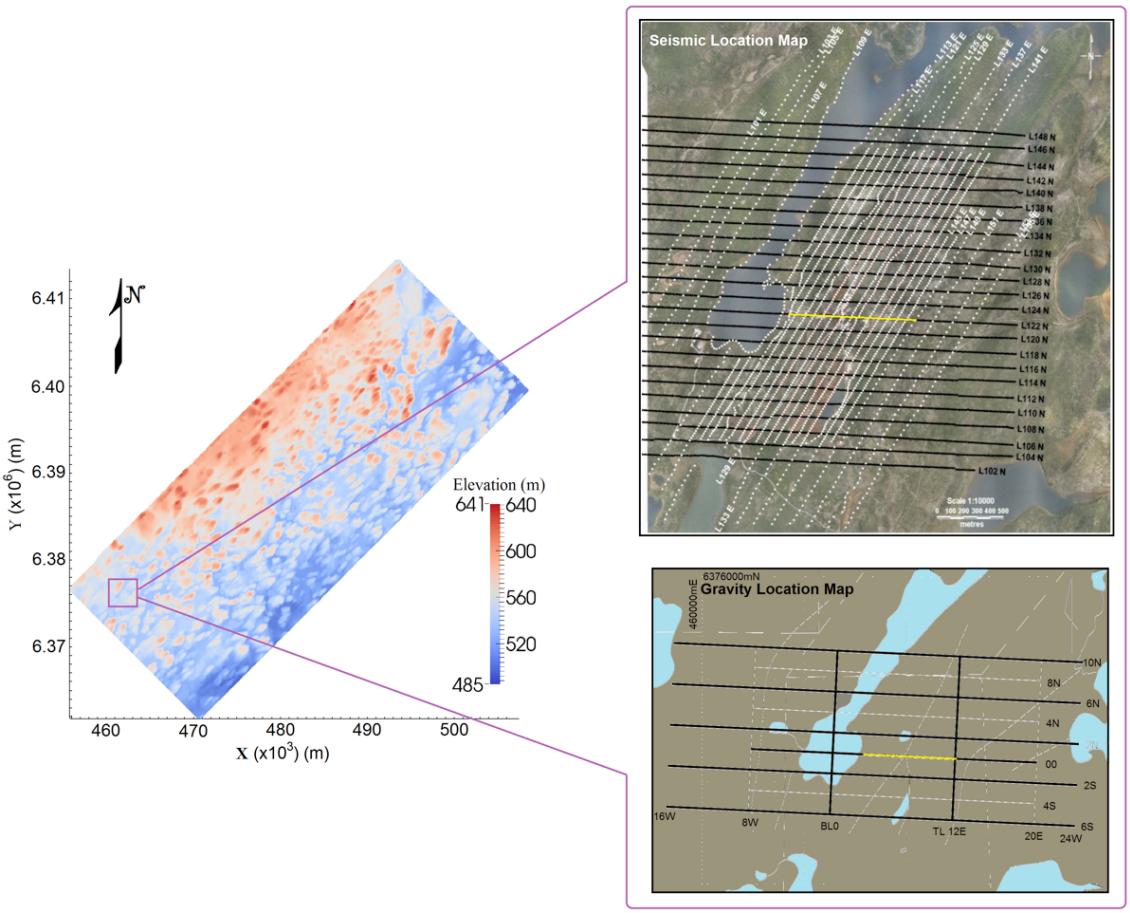

Figure 6.25: Topography of the McArthur-Millennium corridor (left). The inset shows the locations of the survey lines for the seismic and gravity surveys at the Millennium area. The yellow lines show the profile of data used in this research. Top right: seismic source lines (white) and seismic receiver lines (black). Bottom right: ground gravity profiles (black).

Ground gravity data were acquired over Millennium area by Patterson Mining Geophysics Ltd. for Cameco Corporation in 2003 (Patterson Mining Geophysics Ltd., 2003). Data were collected at 50 m station intervals along each line (Figure 6.25). All data were de-noised and corrected by Patterson Mining Geophysics Ltd.. A part of one of the survey lines with a length of 950 m was chosen for the 2D inversions here (Figure 6.25).

3D reflection seismic data were acquired over the Millennium area in the Athabasca Basin by Vibrometric Canada Limited, Kinetex and Uppsala University, in cooperation, for Cameco Corporation in 2006 and 2007 (Figure 6.25; Vibrometric Canada Limited, 2007). The goal of the 3D reflection survey was to map layering in the sandstones and the unconformity, and to image steeply dipping structures and alteration zones. All pre-processed data was sent to Uppsala University where the 3D processing was performed. A part of a seismic profile, with a length of around 950 m and a receiver spacing of 14 m, was chosen for the inversion in this research with a length of around 950 m and a receiver spacing of 14 m. The shot spacing was variable from 40 m to 140 m. Both the chosen seismic and gravity profiles were located along the same E-W line over the Millennium mine. The 3D seismic reflection data was of sufficiently good quality for picking the first travel-time arrivals, as the shot gather in Figure 6.26 illustrates.

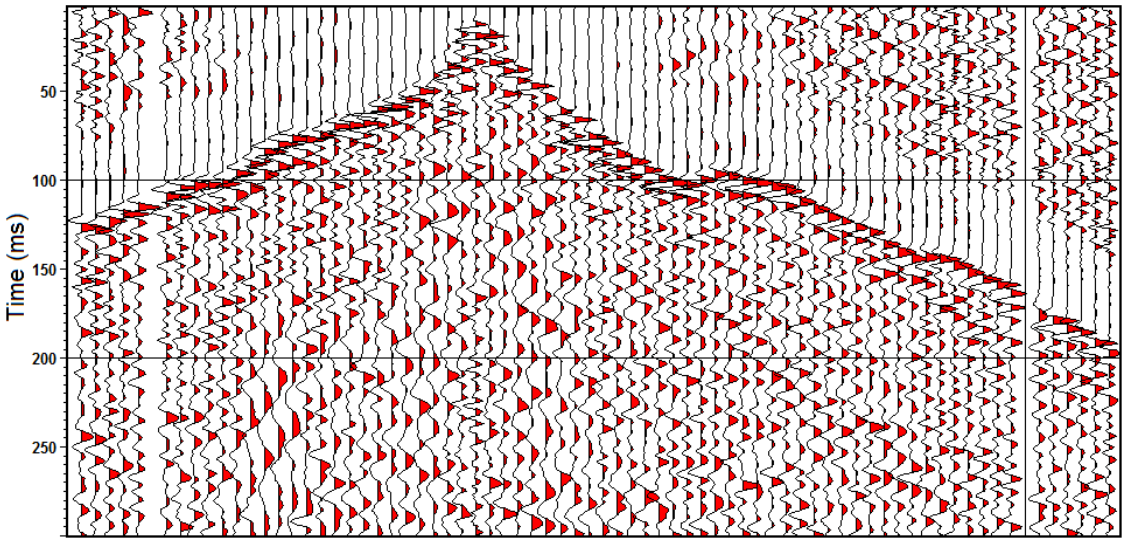

Figure 6.26: One of the shot gathers (#131185 of patch #5) from which the first-arrival travel times used for the travel-time inversion were obtained.

Independent inversions were first performed for the gravity data and the seismic data. Based on what was learned from the synthetic example, I did not attempt to construct densities at depth until the constrained inversion at the end. The constructed models for the independent inversions, and the observed and predicted data, are shown in Figures 6.27 and 6.28, respectively. The mesh used for the inversions had 10,167 triangular cells with a maximum cell size of 10 m^2. The mesh is laterally larger than what is shown in the figures. Since I am not trying to construct the deep alteration zones in these initial inversions, meshes with a smaller vertical extend were used. Uncertainties of 5% were considered as being appropriate. The independent inversions were terminated when the target misfit of ω=1 was achieved (see Chapter 4.5). Free-air gravity data, which are dominated by the variations in topography, were inverted. As expected, the density model mostly comprises artefacts correlating with the topography (Figure 6.27). However, as it can be seen from the model in Figure 6.28, the travel-time inversion separated out the overburden from the

sandstone reasonably well, although the interface between these two layers is not sharp. The fit between observed and calculated data for both models is good.

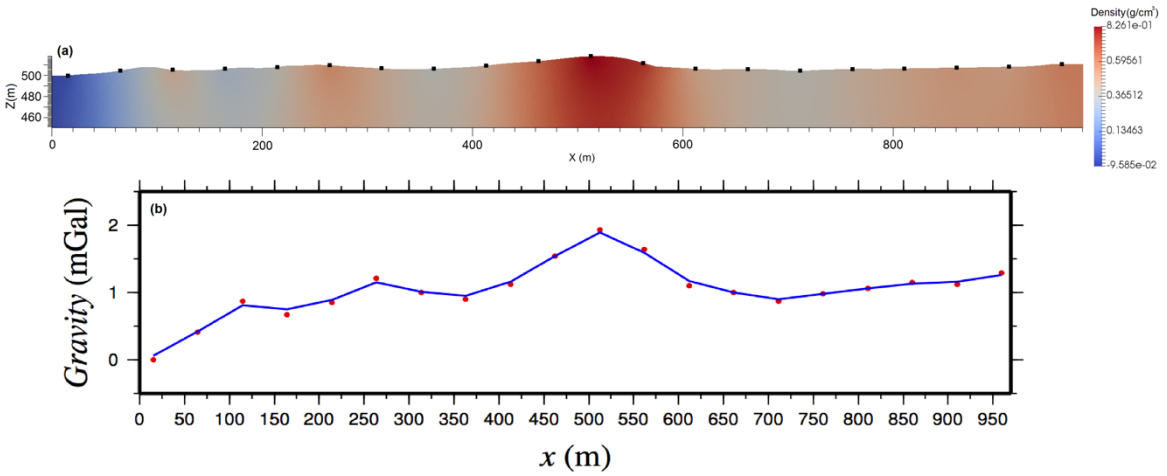

Figure 6.27: (a) The Earth model constructed from the independent inversion of the gravity data from over Millennium. (b) Observed (red) and calculated (blue) gravity data.

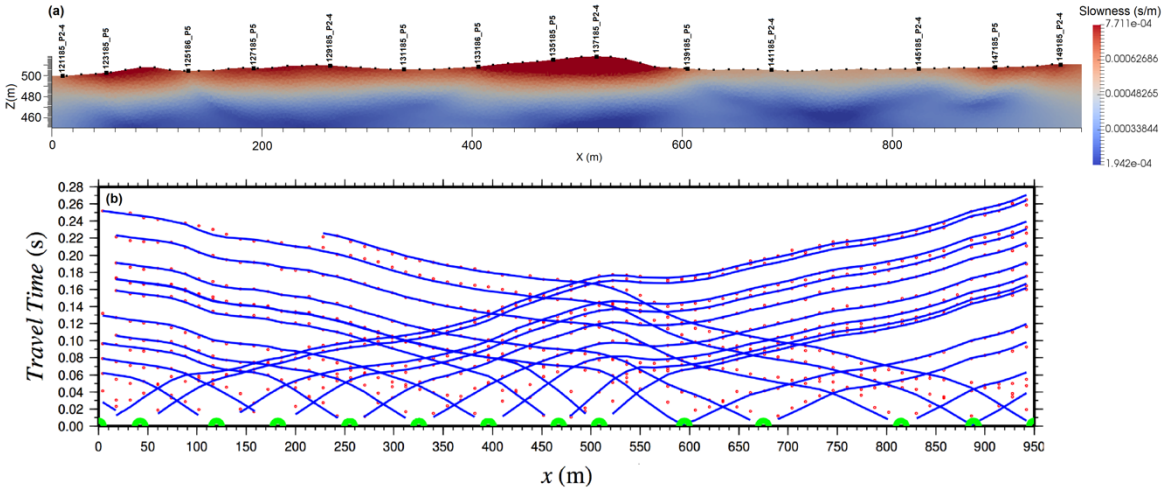

Figure 6.28: (a) The Earth model constructed from the independent inversion (using L2-norm) of the seismic travel-time data from Millennium. The 14 shots and 68 receivers for this data-set are shown by the large and small black dots, respectively. The labels of the large black dots give the shot numbers. (b) Observed (red) and calculated (blue) seismic refraction data. Green dots show the shot locations.

A 2-cluster joint inversion was then performed. Given the results of the synthetic example, no attempt at this stage was made to construct density variations at depth. Since a clustering method is being used as the coupling in the joint inversion, appropriate values of density are required to specify the clusters. Since it is anomalous gravity that is being inverted, and this is the case even for the free-air anomaly data use here, estimates of the true densities are not appropriate for all parts of the model. To determine appropriate densities a forward modelling study was carried out. The interface between overburden and sandstones was fixed (at 490 m), and a range of densities and anomalous densities investigated. It was found that values of 2.0 g/cc for the overburden (i.e., the real density) and -0.25 g/cc for the sandstones (=2.42-2.67 g/cc; i.e., an anomalous density) gave a range of synthesized data between 0.39 and 1.87 mGal, which is a similar range to that of the data to be inverted (0.0 to 1.93 mGal). This choice of real density for the overburden and anomalous density for the sandstones corresponds to the reference ellipsoid for the free-air anomaly values being approximately at the base of the overburden. The two clusters for the joint inversion were therefore 0.000625 s/m and 2 g/cc for the overburden and 0.00025 s/m and -0.25 g/cc for the sandstones.

A range of different coupling factors were tried, with ρ=1 giving the best balance between the two data-types in the inversion. Figure 6.29 shows the slowness and density models obtained by the joint inversion using a coupling factor of ρ=1. In the joint inversion process, 57 iterations were performed and the run-time was 3.71 hours. In Figure 6.29, the white line shows the interface between overburden and sandstone that was derived from these models. The four yellow squares show the true locations of the base of overburden in

four drill-holes that are on this profile. There is clearly a good match between the base of overburden determined from the joint inversion and the true values. The fit to the data is good (Figure 6.30). The variation of the various terms of the objective function (convergence curves) for this joint inversion are shown in Figure 6.31. Figure 6.32 illustrates the physical properties (slowness versus density) obtained after the joint inversion that generated the models in Figure 6.29; two clusters are clearly apparent.

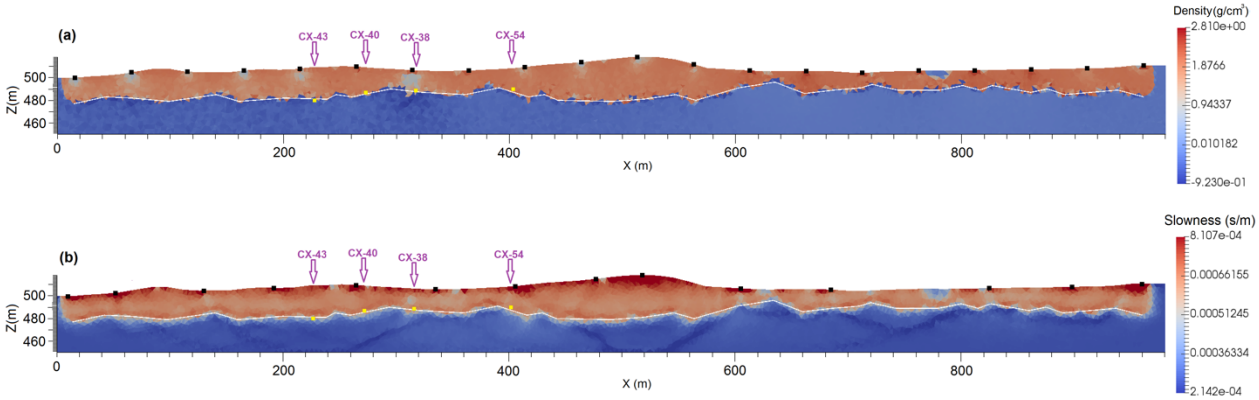

Figure 6.29: Density (a) and slowness (b) models constructed from a joint inversion of the seismic and gravity data from Millennium using a coupling factor of ρ=1. The locations of the seismic sources are indicated by black squares. The white line indicates the glacial sediments-sandstone contact interpreted from these models. The four yellow dots show the locations of the base of overburden obtained from drill-hole data (CX-38, CX-40, CX-43 and CX-54).

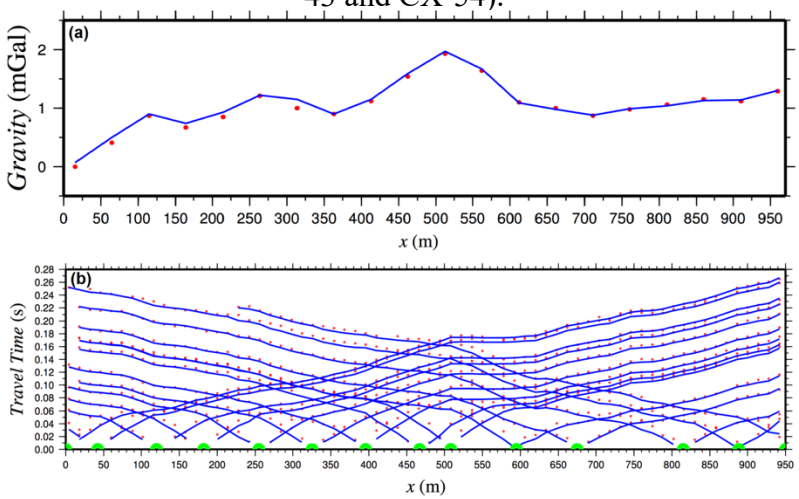

Figure 6.30: The real gravity and seismic travel-time data for the true model (red) and data (blue) computed from the models constructed by the joint inversion (and shown in Figure 6.29). Green color shows the shot locations.

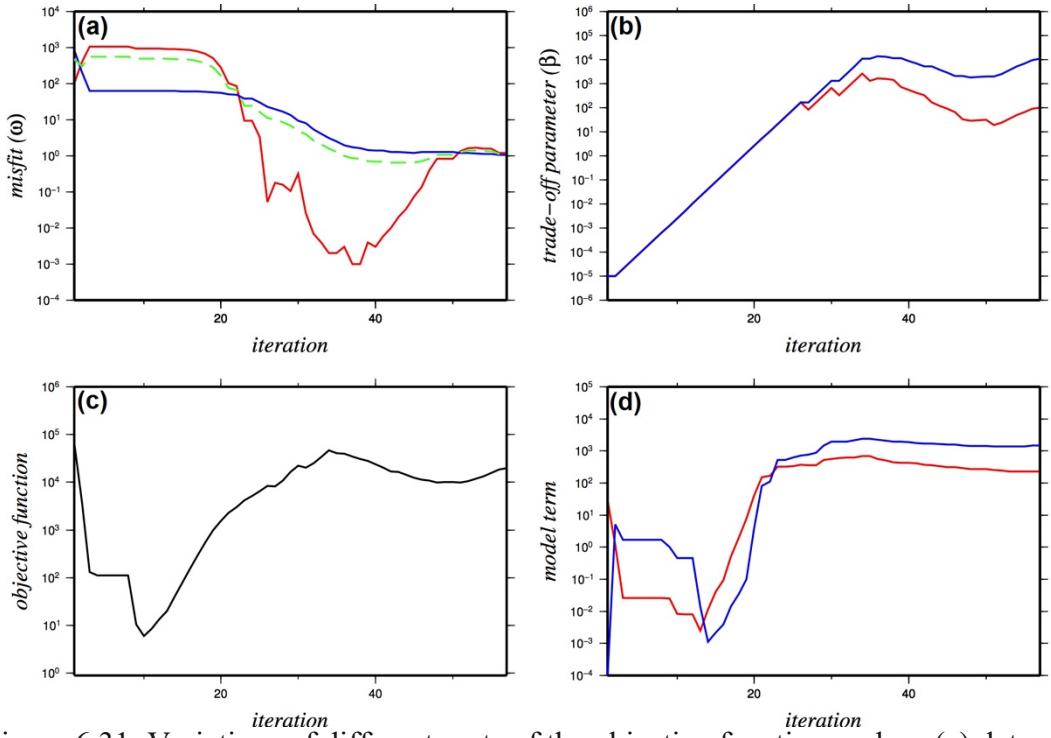

Figure 6.31: Variations of different parts of the objective function such as (a) data misfit (ω), (b) trade-off parameter (β), (c) objective function ($\mathbf{\Phi}$) and (d) model term (ϕ_m) at iterations for the joint inversion of the real gravity (red) and seismic refraction (blue) data for ρ=1. Green color shows the average ω.

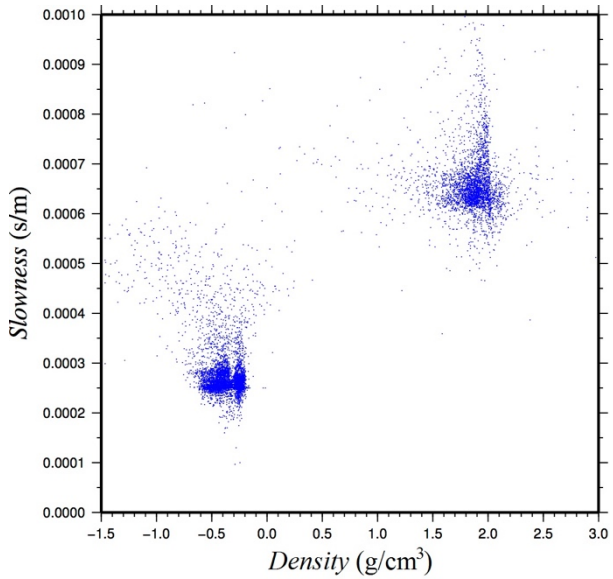

Figure 6.32: The physical properties values (slowness versus density) in the models constructed by the joint inversion, with each dot representing one cell. Two clusters can be seen which correspond to the physical properties of the overburden (s=0.000625 s/m and d=2 g/cc) and the sandstone (s=0.00025 s/m and d=-0.25 g/cc).

The base of overburden interpreted from the joint inversion results (see the white line in Figure 6.29) was then used to constrain an independent gravity inversion. Three layers were considered for the constraints which, from top to bottom, were as follows: 1- a layer (overburden) from surface to the base of overburden which was obtained from the joint inversion results. The density of these overburden cells (2 g/cc) was fixed during the inversion; 2- a layer that can safely be assumed to be sandstone from the base of overburden to the depth of 450 m (which was the base of joint inversion mesh). The density of the cells of this layer (-0.25 g/cc) was fixed during the inversion; 3- a layer from 450 m to the bottom of the model for which a wide range of density values is used as constraints (as lower and upper bounds). As mentioned before, one of the main alteration zones in the Millennium area is desilicification which has a lower density than the host (sandstone). In Figure 6.33, an anomaly (indicated by the black line) can be seen in the center of the model with a decrease in the density which can be interpreted as desilicification.

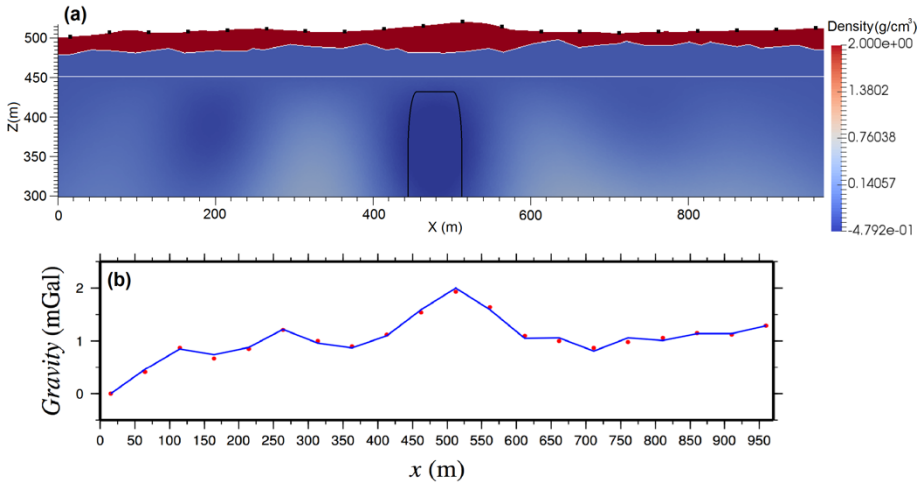

Figure 6.33: (a) The Earth model constructed from the constrained independent inversion of the real gravity data. The white lines show the base of the overburden obtained from the joint inversion and the base of a layer which is assumed to be sandstone without any alteration zone. The black line shows the location of the desilicification zone that is known to exist under this profile. (b) The real (red) and calculated (blue) gravity data.

6.5 Conclusions

In this chapter, it was shown that the independent inversion of seismic refraction data can be considered one of the best methods for determining the subsurface interfaces while gravity data is poor in this respect. There are many methods to improve the inversion results such as joint and constrained inversions. For this purpose, I initially tested joint inversions for two different coupling factors, and then applied constraints derived from joint inversion to an independent gravity inversion. For these inversions on synthetic data, different models relevant to the McArthur area are generated. The first modelling includes a two-layer model made based on the drill-hole data. Also, a drumlin-shaped model was generated to investigate the effect of topography on the inversions. This model had different scenarios in which the interface between the layers has topography. In addition to a blind layer model, a model was made which includes an alteration zone as well. Independent and joint inversions were able to reconstruct the interfaces but not the alteration zone. To try to improve the density model at depth, a constrained inversion was performed on the gravity data using overburden physical properties derived from the joint inversion. Therefore, I have demonstrated through realistic synthetic examples that the joint inversion of gravity data with seismic refraction data can accurately reconstruct the base of overburden in the joint Earth model, and hence the densities of the overburden and underlying bedrock. Also, the constrained gravity inversion can help to detect the alteration zone at depth.

I have illustrated the effectiveness of this process using a synthetic example, and successfully applied it to real data from the Athabasca Basin over the Millennium area.

Drill-hole data showed that the predicted interface from the joint inversion is correct. The result of the constrained independent gravity inversion clearly showed an anomaly with less density at the middle of the profile over the Millennium mine which can be interpreted as a desilicification zone.

Chapter 7

Modelling and Inversion of Magnetic and Gravity Data of the McArthur River Area

7.1 Introduction

In this chapter, 3D inversion of magnetic and gravity data is performed on both synthetic and real data in order to map overburden thickness as well as the density anomalies from deeper mineralization and basement. For the inversion methods, independent as well as joint and constrained methods will be investigated. For the synthetic modelling, the McArthur area is simulated as the real data (i.e., airborne gravity and magnetic data here) cover this area well. In the Athabasca basin, real gravity and magnetic data are dominated by the variations of topography (Figures 7.1 to 7.4). Data show that the magnetic response is closely related to the topography and glacial geology, and suggest that the magnetization of these features can be relatively uniform in some areas (Kornik, 1983). They also show that despite the heterogeneity of the glacial sediments, the free-air gravity data is strongly dominated by the topography variations which mask the signature of many other geological structures (except the long wavelength ones due to regional features). Airborne gravity data (Bell Gravity Data; Bell Geospace Limited, 2007) as well as airborne magnetic data

(Triaxial Magnetic Data; Goldak Airborne Surveys, 2007) are two sets of available data in this project (Figures 7.1 and 7.3).

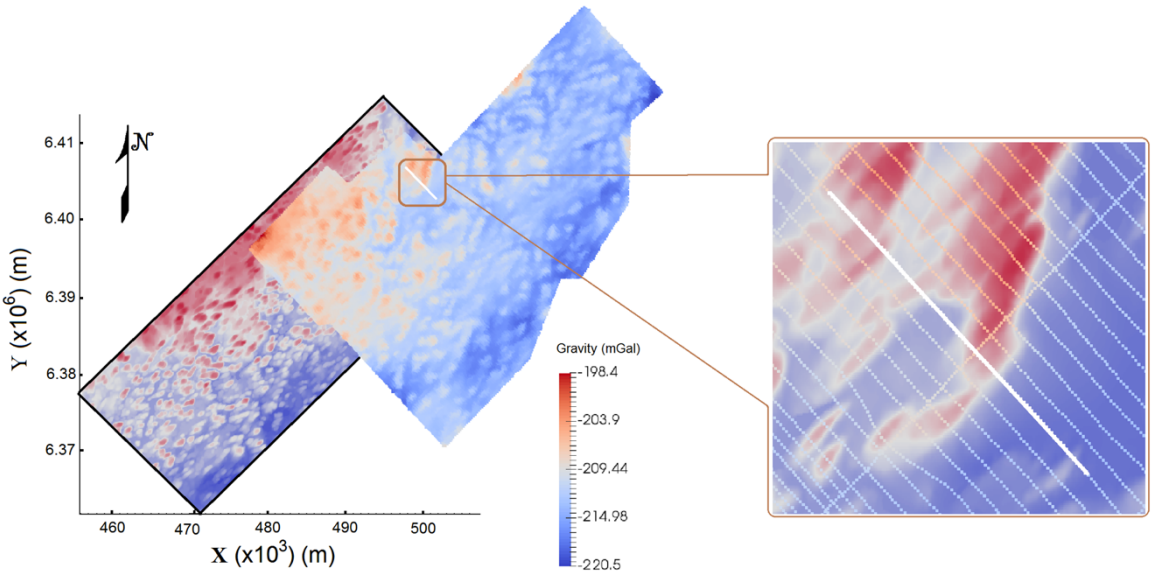

Figure 7.1: Left: topography of the McArthur-Millennium corridor (in the black frame) as well as Bell free-air gravity data (over the north part of area). Right: inset shows the topography of the McArthur area (5×5 km) as well as gravity profiles (dotted coloured lines) and selected survey line (white line).

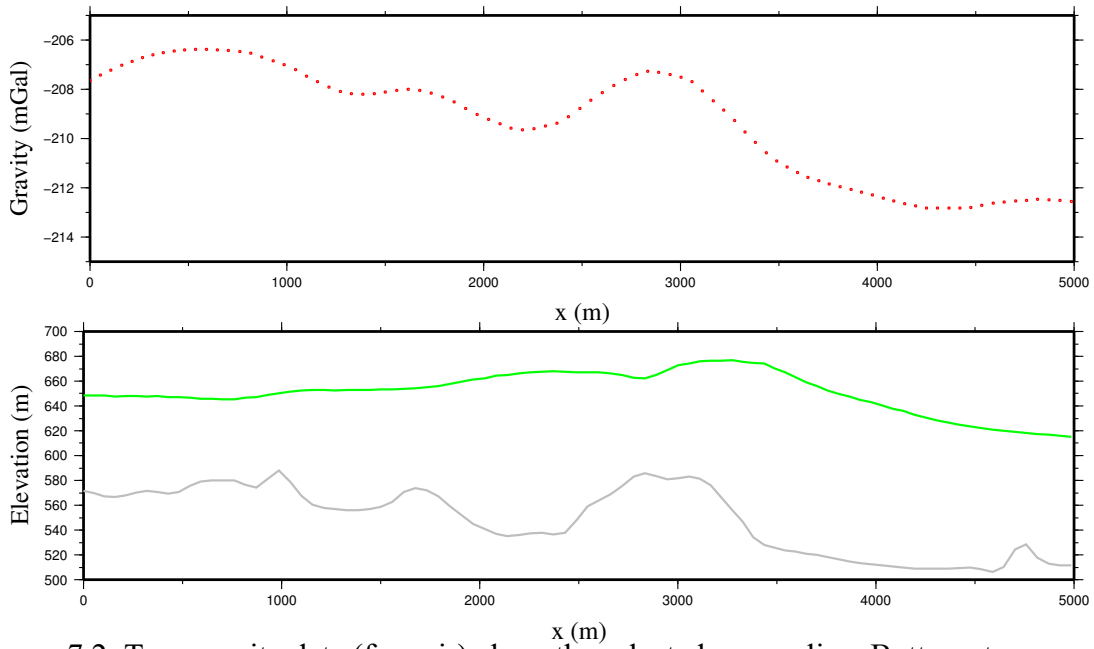

Figure 7.2: Top: gravity data (free-air) along the selected survey line. Bottom: topography under the selected survey line (grey), and airborne flight height (green).

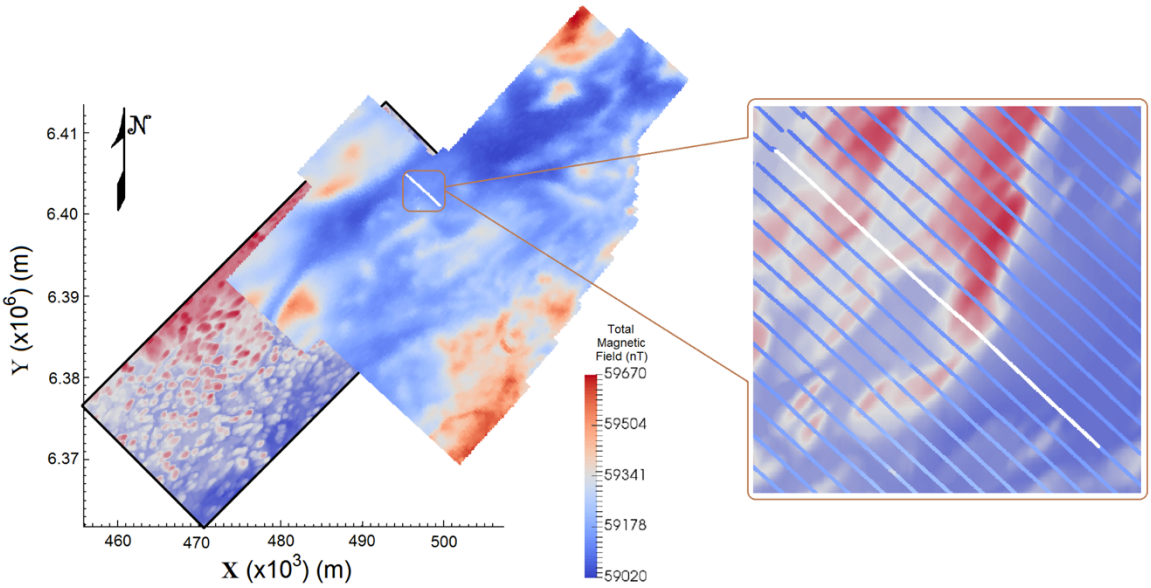

Figure 7.3: Left: topography of the McArthur-Millennium corridor (in the black frame; in left) as well as Triaxial magnetic data (over the north part of area). Right: inset shows the topography of the McArthur area (5×5 km) as well as magnetic profiles (parallel blue lines) and selected survey line (white line).

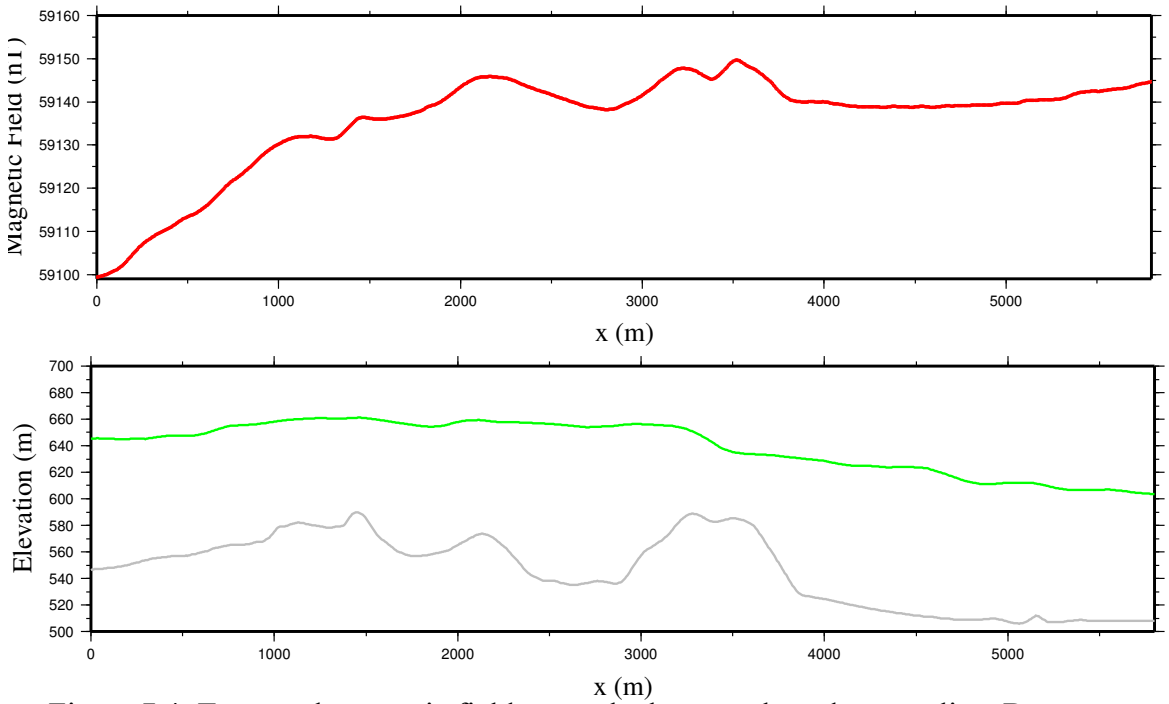

Figure 7.4: Top: total magnetic field strength along a selected survey line. Bottom: topography under the selected survey line (grey), and airborne flight height (green).

Bell gravity data, which includes airborne free-air data as well as airborne full tensor gravity gradiometry data (Air-FTG), was acquired over McArthur River, Read Lake and Rabbit Lake areas in the Athabasca Basin by Bell Geospace Limited for Cameco Corporation in 2007. The data was acquired using the FTG system which is installed in an aircraft. Data contain around 88,700 stations in a total 6568 line kilometres of data, while the station spacing and the profile spacing are around 50 m and 300 m, respectively. A radar altimeter system is deployed to measure the distance between the airplane and the ground. Along with the plane's altitude acquired via GPS, radar altimetry data can be used to produce a digital elevation model (DEM). The free-air data used in this research was the computed free-air gravity response from vertical integration of the vertical gravity gradient (G_{zz}; see Appendix D) anomaly field. All data were de-noised and corrected by Bell Geospace Limited (Bell Geospace Limited, 2007).

Triaxial magnetic data, which includes airborne total magnetic intensity data as well as airborne magnetic gradiometry data (derivative of the field in the three directions), was acquired (and was corrected) over McArthur River and Read Lake in the Athabasca Basin by Goldak Airborne Surveys (Goldak) on behalf of Cameco Corporation and comprises a total of 5433 line kilometres collected during in March 2007. The data were acquired using Geometrics G-822A optically pumped cesium vapour magnetometers (a triaxial system) with a sensitivity of 0.005 nT. The triaxial system has three magnetometers installed in an aircraft. Also, for acquiring the diurnal variations, a "GEM Systems GSM19W" proton precession magnetometer with a GPS time base was used as the magnetic base station. Two radar altimeters as well as a GPS system were also installed in the aircraft. Triaxial

magnetic data has around 676,500 stations, and the station spacing and the profile spacing are around 7 m and 300 m, respectively. During data acquisition, the geomagnetic field strength in the McArthur area was around 59500 nT, and geomagnetic field declination and inclination were around 12 and 80 degrees, respectively. The geomagnetic noise variations did not exceed 1 nT over a distance of 3000 m (Goldak Airborne Surveys, 2007). Parts of survey lines for both magnetic and gravity data are plotted in Figures 7.2 and 7.4. By comparing the variation in data and the topography under the survey lines, the topography signature on the data can clearly be seen.

7.2 3D synthetic modelling and inversion

In this section, gravity and magnetic data are synthesized for the McArthur area over a 3D model along a number of profiles (Figures 7.5 to 7.7). The McArthur area was chosen for the modelling as there is plenty of geological, geophysical and physical property data for this area (see Chapter 2). The model is the one based on the work of Wood and Thomas (2007; see Section 3.6) which was first described in Section 5.4. For the basement, different units of granitoid and gneiss rocks are considered (Figure 7.5). The basement is now very relevant to these magnetic and gravity data-sets unlike the data-sets considered in Chapter 6. Independent, joint and constrained inversions were performed in order to reconstruct density and susceptibility models. Note that, based on the modelling investigations (Chapter 5), the signature of the alteration zone is too subtle, thus it is not expected to be detected in the inversion results in this chapter. Physical property data as well as drill-hole data were used as constraints in the inversions (see Section 2.5).

There are 405 synthetic airborne observations generated at locations at a fixed elevation above sea level of 650 m that are used for gravity data along 5 profiles with station spacing and profile spacing of 50 m and 300 m, respectively. The same stations are used for synthetizing magnetic data. These survey specifications are based on those for the real data-sets (see Section 7.1). In the magnetic modelling (the same as for the real data), geomagnetic field strength, declination and inclination were considered to be 59500nT, 12 degrees and 80 degrees, respectively.

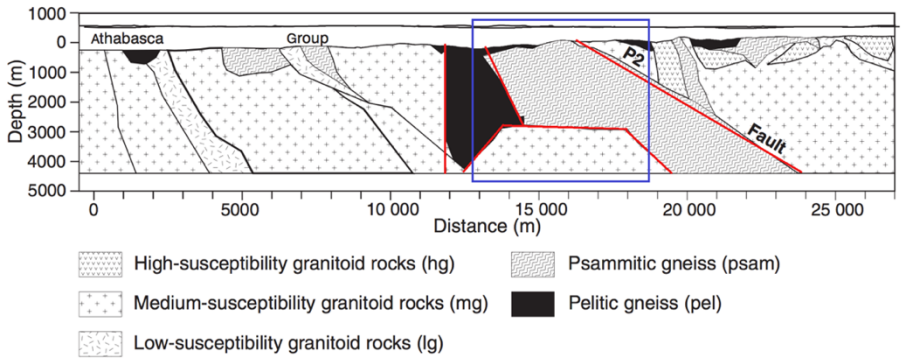

Figure 7.5: McArthur geological section (Thomas and Wood, 2007). Blue square shows the part which forms the basis of the models considered in this research. Red lines show the modeled interfaces between the blocks. Small zones and variations in the model are ignored in the modelling.

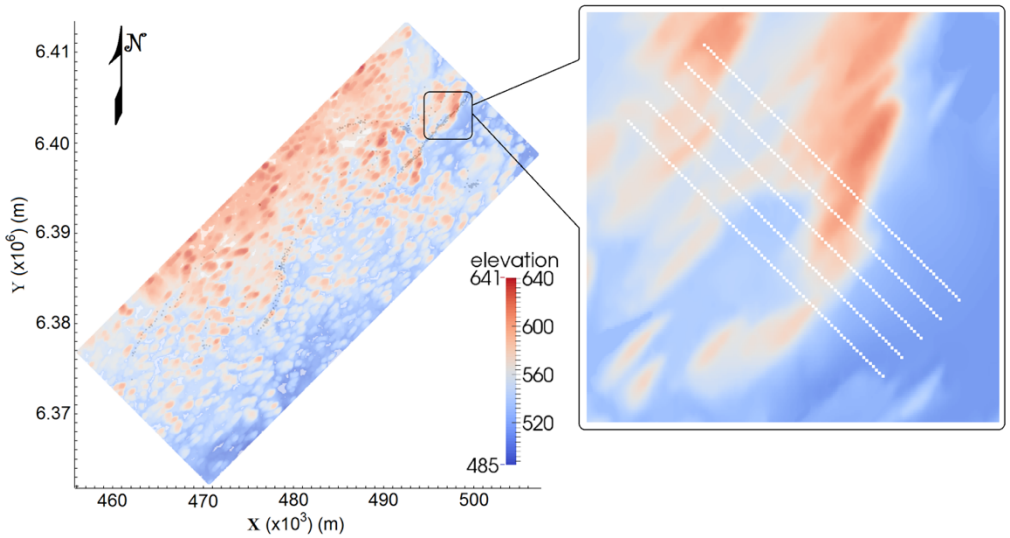

Figure 7.6: Topography of McArthur-Millennium corridor. Inset shows location of survey lines over the (modelled) McArthur area.

The gravity model with the densities of the various geological units is shown in Figure 7.7. The images shown here of the 3D models in this research show the central 5 by 5 km (Figure 7.6). The actual 3D models used for the computations had a size of 500 by 500 km in order to avoid any effect of the edges on the gravity data. The average total thickness of these models was 4850 m.

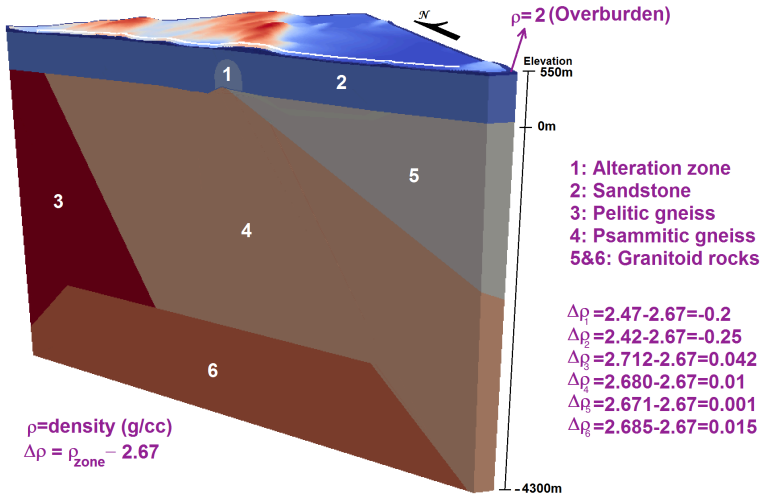

Figure 7.7: Density model including different geological structures based on Wood and Thomas (2007). Basement blocks are adapted from Figure 7.5.

In this model, a cylinder anomaly is considered as an altered sandstone body. Free-air gravity data were computed. As mentioned in Section 5.4, considering the undulating interface between the overburden and sandstone as the reference ellipsoid can be an acceptable choice. The layers (or structures) above the reference ellipsoid have real densities in the model while the layers (or structures) below the reference ellipsoid have relative density. The relative densities are with respect to 2.67 g/cc. Therefore, the overburden has a real density of 2 g/cc whereas the lower layers have a relative density. Figure 7.8 shows the synthetic free-air gravity for the survey lines considered here. This figure also shows the topography, and it is clear that the free-air data are predominantly

affected by the topography.

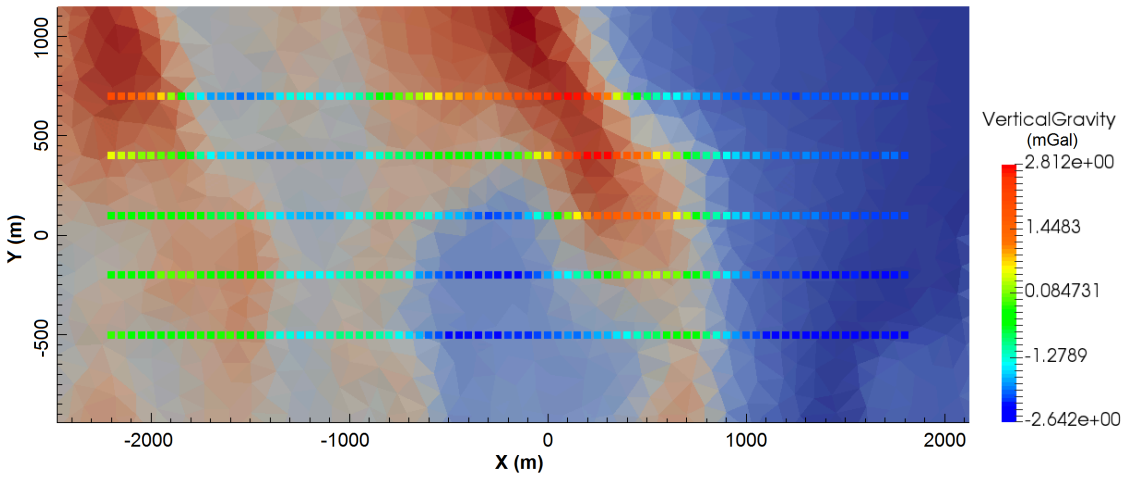

Figure 7.8: Synthetic gravity free-air data along the airborne survey lines after adding 1% noise over the topography of the McArthur area. Number of stations: 405. The background is the topography with red high and blue low.

The magnetic model with magnetic susceptibilities of the various geological units is shown in Figure 7.9. Magnetic data were computed along the same airborne survey lines used for the gravity modelling. The images of the 3D magnetic models in this research show the central 5 by 5 km. The magnetic susceptibility of the sandstone is approximately zero, so it is expected that the overburden and its variable thickness will strongly influence the magnetic data. Thomas and Wood (2007) considered the overburden as non-magnetic, but I assigned a value of 5×10^{-3} SI for the magnetic susceptibility of overburden based on values in the CMIC-Footprints database (see Section 2.5.3). Figure 7.10 shows the synthetized magnetic data. Similar to the gravity data, the magnetic data is strongly dominated by variations of topography. Units in the basement on the right (i.e., east) side of the P2 fault (body #5 in Figure 7.9) have higher magnetic susceptibility values than those on the left (i.e., west) side of the P2 fault (bodies #3 and #4 in Figure 7.9). The signature of this difference can be clearly seen in the right sides (east) of the magnetic profiles where

the magnetic data is significantly increased. The real magnetic and gravity data shown in Figures 7.2 and 7.4 demonstrate that the data is not too noisy. Therefore, using a code of Lelièvre and Farquharson (2015), a Gaussian random noise of standard deviation equal in magnitude to 1% of a datum is added to both synthetic gravity and magnetic data. This amount of the noise is selected from trial and error based on the comparison with the available real data.

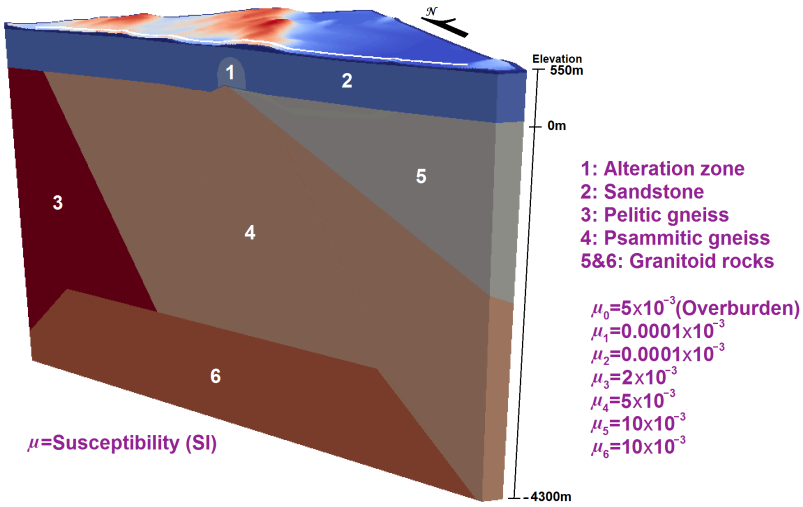

Figure 7.9: 3D magnetic susceptibility model including different geological structures based on Wood and Thomas (2007). Basement blocks are adapted from Figure 7.5.

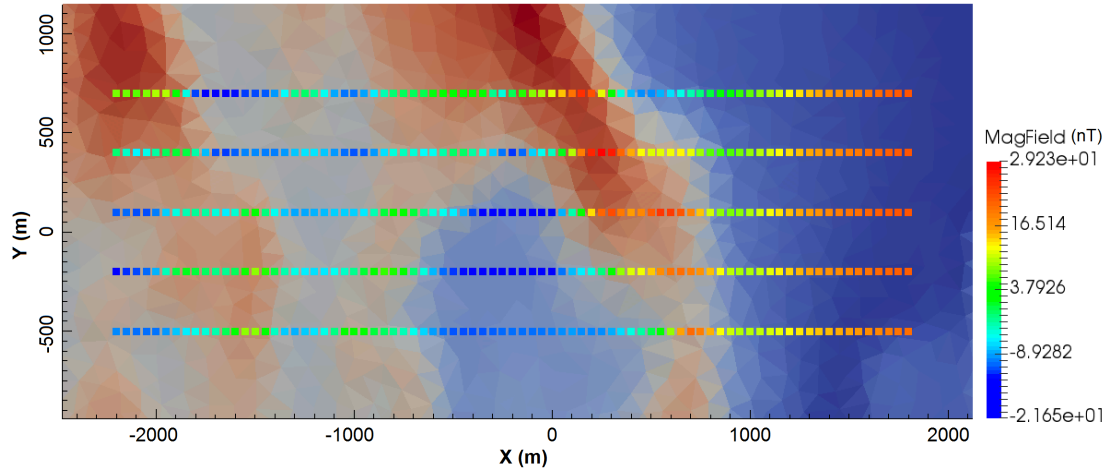

Figure 7.10: Total magnetic intensity along the airborne survey lines after adding 1% noise over the topography of the McArthur area. Geomagnetic field strength: 59500nT; geomagnetic field declination: 12 degrees; geomagnetic field inclination: 80 degrees; Number of stations: 405.

7.2.1 3D independent inversions of synthetic gravity and magnetic data

3D inversions are performed on the synthetized airborne gravity and magnetic data on a mesh shown in Figure 7.11. The smallest tetrahedral cells which are located at the surface have a small edge size of 30 m. As depth increases, the cell size increases. For the data misfit of inversions in this chapter, the value of ω reached 1 while a value of 0.05 is considered for the *chifact* (see Section 4.5). This means that a desirable fit is obtained. For the distance weighting, a value of 1.0 is assigned for w_z and w_p. Also, no reference model was considered in the inversions except in the constrained inversions discussed later.

Independent inversions were considered first, and then constrained inversions. Finally, the joint inversion was investigated as well as constrained joint inversion. Figures 7.11 and 7.12 show the block used for the inversions as well as the independent inversion results for magnetic and gravity data, respectively. The views of these models are the same as the view of the true model in Figure 7.7 (or 7.9). The mesh used for the independent inversions had about 28,000 tetrahedral cells. The normalized data residuals in Figure 7.13 show there is a good fit between the observed and calculated data.

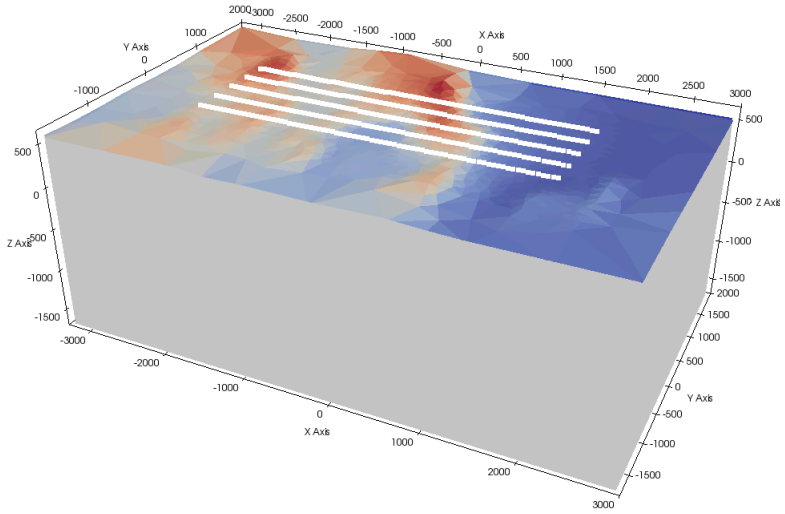

Figure 7.11: Block (rectangular cube ~6×4×2km) with tetrahedral cells used in the inversions. The topography of McArthur area can be seen on the surface as well as the airborne survey lines (white lines).

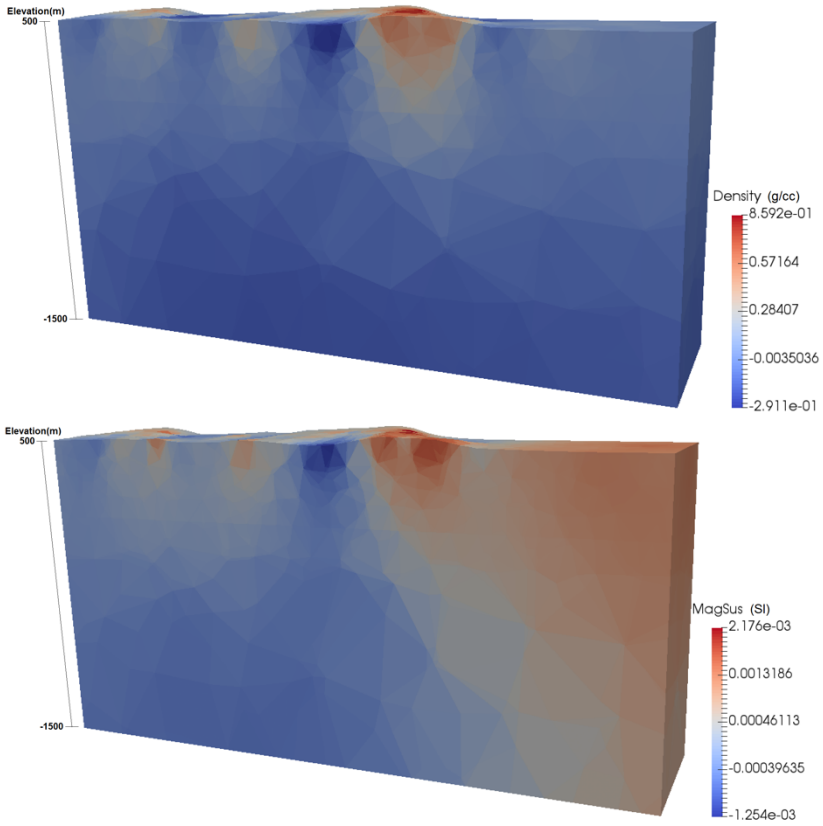

Figure 7.12: Vertical sections of independent gravity (top) and magnetic (bottom) inversion models.

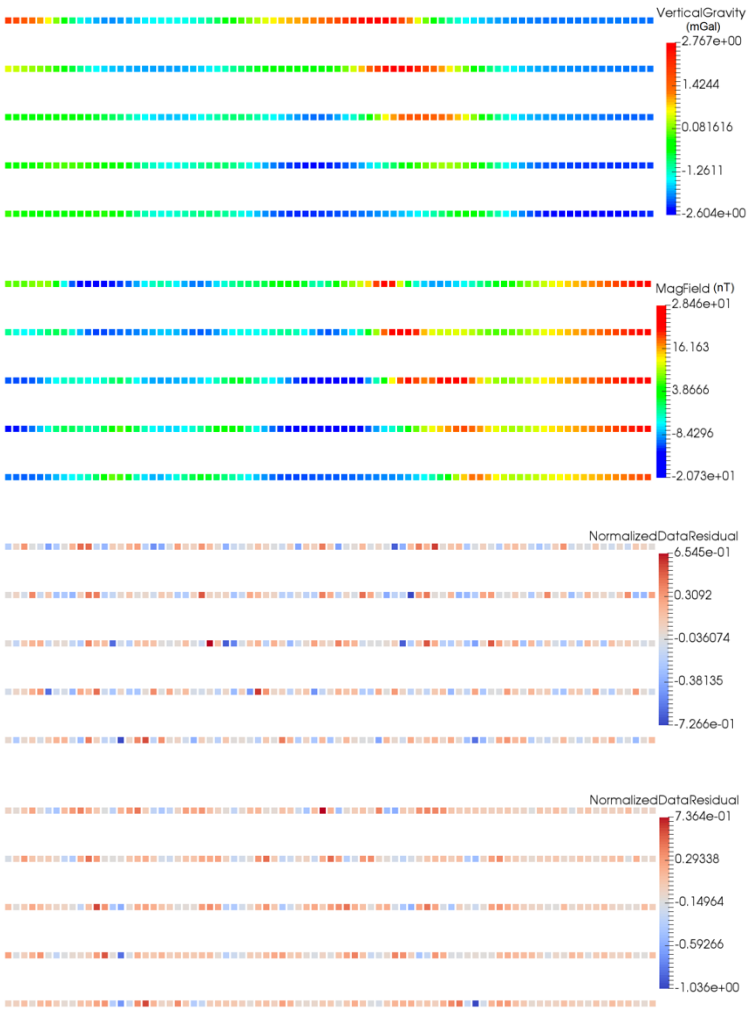

Figure 7.13: From top to bottom: gravity data calculated by the density model constructed by the independent inversion; magnetic data calculated by the susceptibility model constructed by the independent magnetic inversion; normalized data residual for the gravity model; normalized data residual for the magnetic model.

It can be seen that the independent inversions of gravity and magnetic data are not able to construct the true interfaces and geological blocks and layers properly. A reason for the poorness of these results is because of the poor inherent resolution and nonuniqueness of both gravity and magnetic data. Without any other information, the inversion does not really know where to put the density and susceptibility, especially when it is necessary to use absolute densities above the reference level and relative values below.

Since independent unconstrained inversions are very poor, I next consider constrained inversion. For this purpose, physical property data as well as depth information are used as constraints in the inversions, and for this purpose, a reference model was developed to include 4 layers. From top to bottom these are:

1- A layer that we are confident is all overburden from surface to an elevation above sea level of around 500 m that has fixed physical properties during the inversion process, e.g. here a density value of 2 g/cc and a magnetic susceptibility of 5×10^{-3} SI.

2- A layer that we are unsure of but is either overburden or sandstone from an elevation of 500 m above see level to 450 m. So, for the physical properties a wide range of values is considered as constraint (as lower and upper bounds).

3- A layer that we are confident is all sandstone from an elevation of 450 m to 50 m that has fixed physical properties during the inversion process, e.g. here a relative density value of -0.25 g/cc and a magnetic susceptibility of 0 SI.

4- A layer from 50m to the bottom of the model that we are unsure of but is either sandstone or basement. So, for the physical properties a wide range of values is considered as constraint (as lower and upper bounds).

The mesh used for the constrained independent inversions had about 533,000 tetrahedral cells. The results in Figure 7.14 show the constrained independent inversions for magnetic and gravity models. The constrained independent inversion results are better than the independent inversion results, especially the magnetic model in which the basement shows

the location of the P2 fault rather well. However, they are nevertheless not good reproductions of the true model and are not reliable. For example, the basement in the gravity model has a pattern suspiciously similar to the variations of the overburden thickness. Figure 7.15 (top) shows the shallow part of the model for the constrained magnetic inversion. The four layers are shown clearly in this figure. The red layer at the top and the blue layer in the middle are layers that we are confident are all overburden and sandstone, respectively (with fixed physical properties during the inversion process). Constrained results seem interesting, but the truth is that the constructed density anomalies in the basement have the same pattern of the overburden variations as can be seen in Figure 7.15 (bottom) in comparison with Figure 7.12. Figure 7.16 shows there is a good fit between the observed and calculated data.

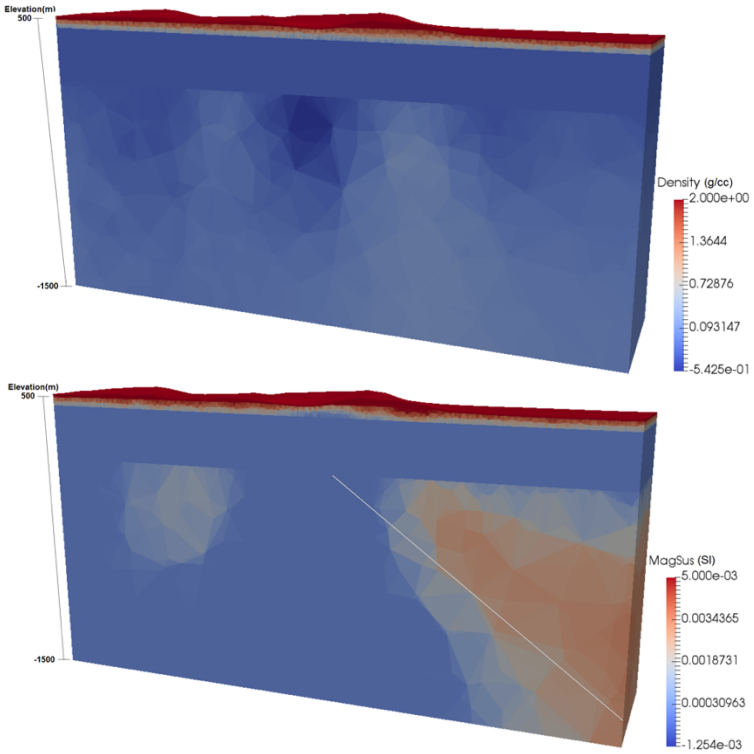

Figure 7.14: Vertical section of constrained independent gravity (top) and magnetic (bottom) inversion models. White line shows the approximate location of the P2 fault.

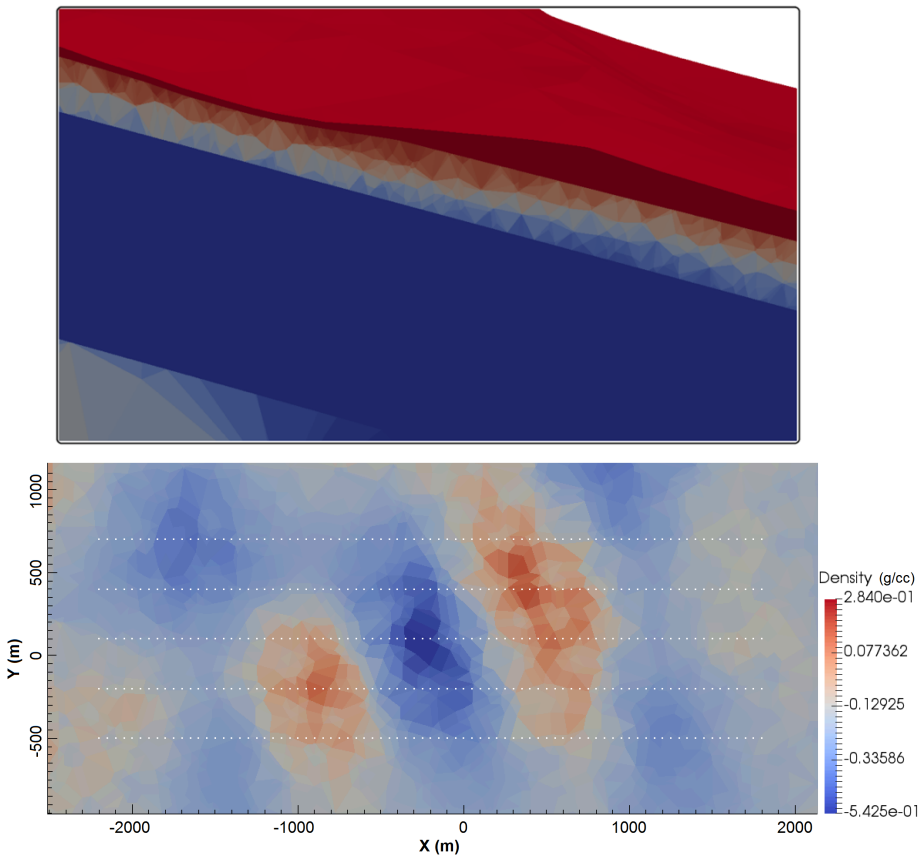

Figure 7.15: Top: a zoom-in on the magnetic section displayed in Figure 7.14 close to the surface. Bottom: a horizontal section of the gravity model at elevation -50 m under the survey lines. White dots show the survey lines.

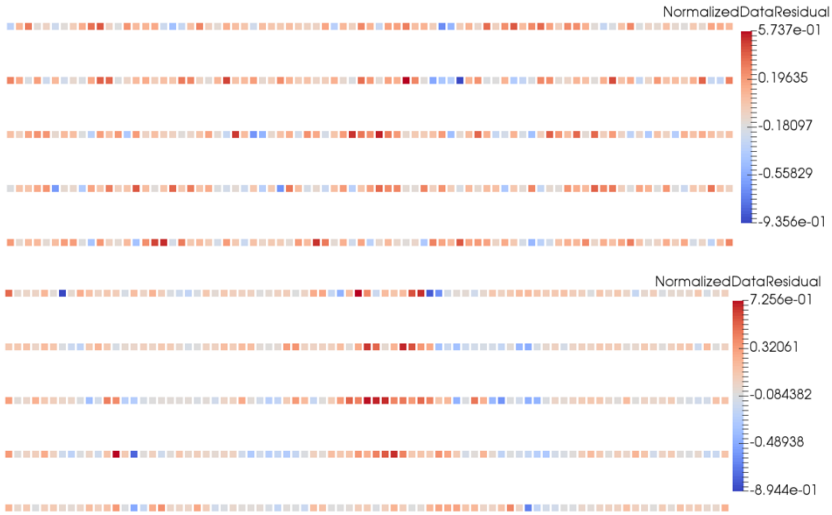

Figure 7.16: Top: normalized data residual for the gravity model. Bottom: normalized data residual for the magnetic model (for constrained independent inversions).

7.2.2 3D joint inversion of synthetic gravity and magnetic data

In order to improve the inversion results, joint inversion of gravity and magnetic data using different coupling factors is investigated. Since the results related to different coupling factors were able to reconstruct the model well, the results belonging to ρ=10 and ρ=1.0E+5 are shown as representing a small value and a large value. For this purpose, two different methods for coupling are used: the correlation method and the clustering fuzzy c-mean method (see Section 4.5). The mesh used for the joint inversions (except the constrained inversion) had about 28,000 tetrahedral cells. The JwP is used for all the joint inversions in this chapter, and one stage is used for heating the coupling factor (see Section 4.5). For the joint inversions in this chapter, a value of 700 is considered for the initial value of the trade-off parameter. This value was obtained as the final trade-off parameter from a few test runs with an initial trade-off parameter of 1.0. Therefore, the trade-off parameter value rather than going up (see Section 4.5) in the iterations starting from a small value to reach an appropriate value, it oscillates around 700 to find the best value. This can help not only to reduce the number of iterations as well as the run-time but to improve the results. Figures 7.17 and 7.24 show the joint inversion results for the correlation method for the two coupling factors of ρ=10 and ρ=1.0E+5. A higher coupling factor causes a greater similarity between the gravity and magnetic inversion models (not at the expense of the fit between calculated and observed data), but at the expense of a longer run-time. The run-times for the joint inversions (correlation method) of ρ=10 and ρ=1.0E+5 are 1 hour and 27 minutes for 13 iterations and 3 hour and 53 minutes for 38 iterations, respectively. For the results shown in Figures 7.17 and 7.21, the normalized data residuals shown in Figures

7.18 and 7.22 show there is a good fit between the observed and calculated data. Also, Figures 7.19 and 7.23 show the cross plot of densities and magnetic susceptibilities constructed using the joint inversion. The variations of the various terms of the objective function for the joint inversion model are shown in Figures 7.20 and 7.24.

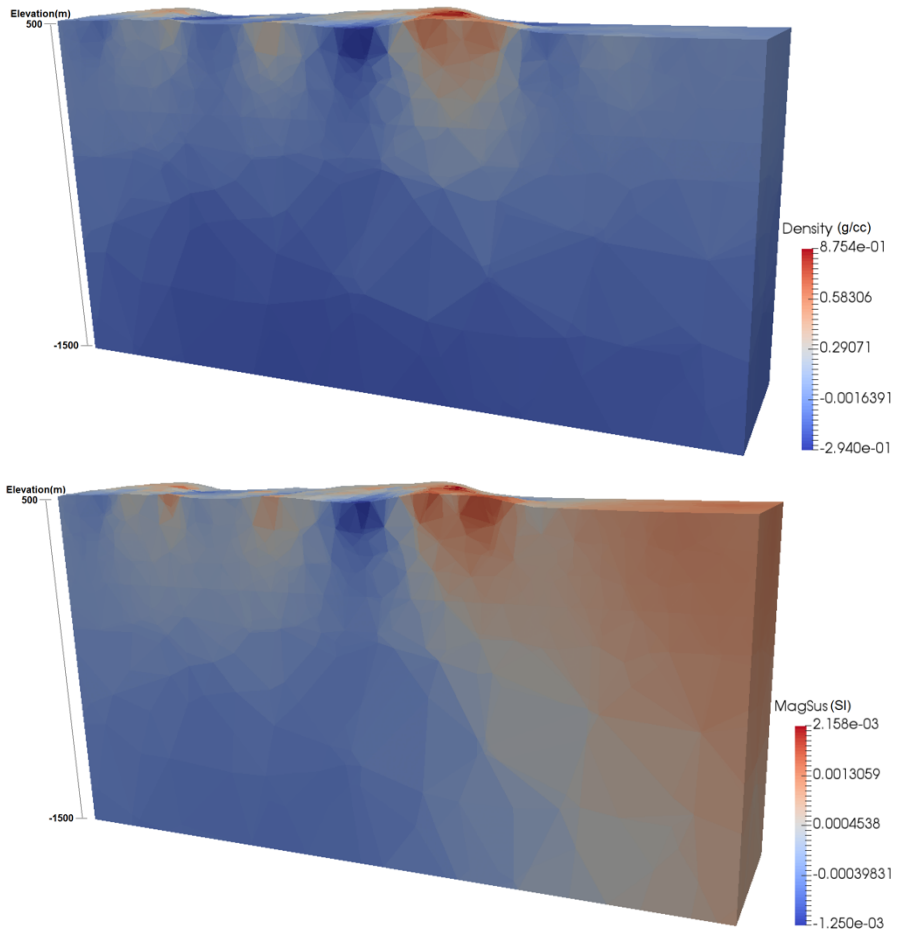

Figure 7.17: Vertical sections of the joint inversion models of gravity (top) and magnetic (bottom) data using correlation method for ρ=10.

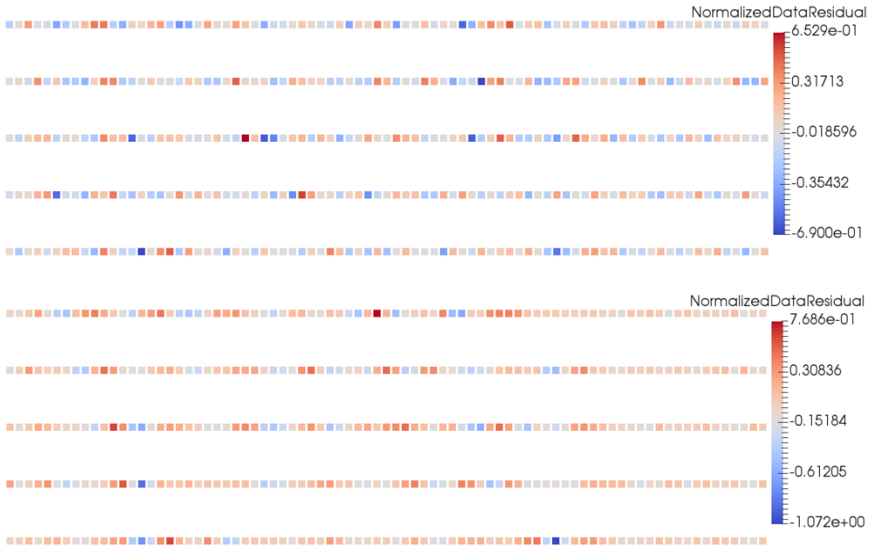

Figure 7.18: Top: normalized data residual for the gravity model. Bottom: normalized data residual for the magnetic model (correlation method for ρ=10).

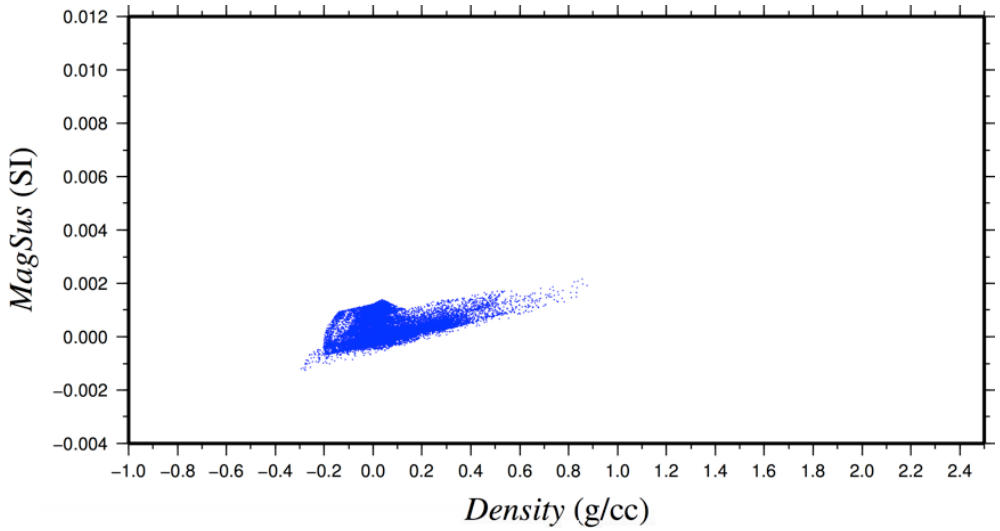

Figure 7.19: Physical properties (magnetic susceptibility versus density) obtained after the joint inversion using the correlation method for ρ=10. Each blue dot corresponds to a cell in the inversion mesh.

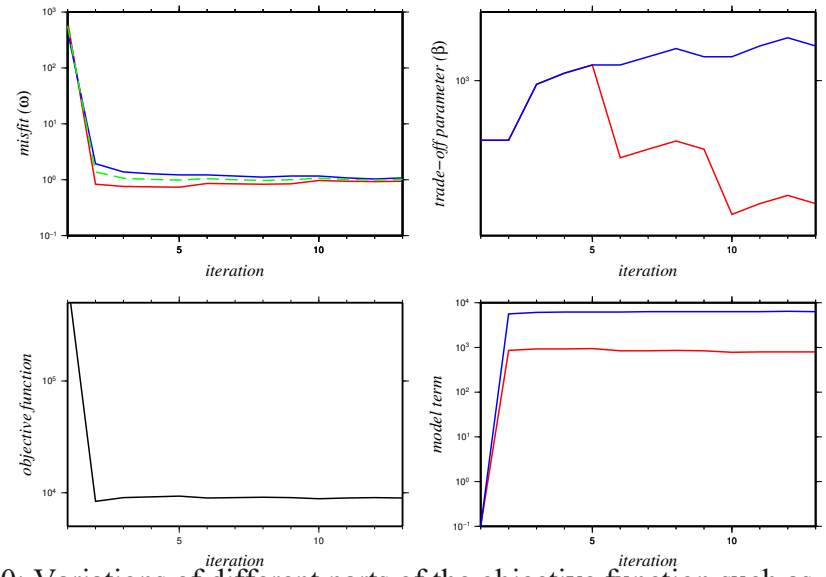

Figure 7.20: Variations of different parts of the objective function such as data misfit (ω; top-left), trade-off parameter (β; top-right), objective function ($\mathbf{\Phi}$; bottom-left) and model term (ϕ_m; bottom-right) at iterations for the joint inversion of gravity (red) and magnetic (blue) data using the correlation method for ρ=10. Green color shows the "average ω" (see Section 4.5).

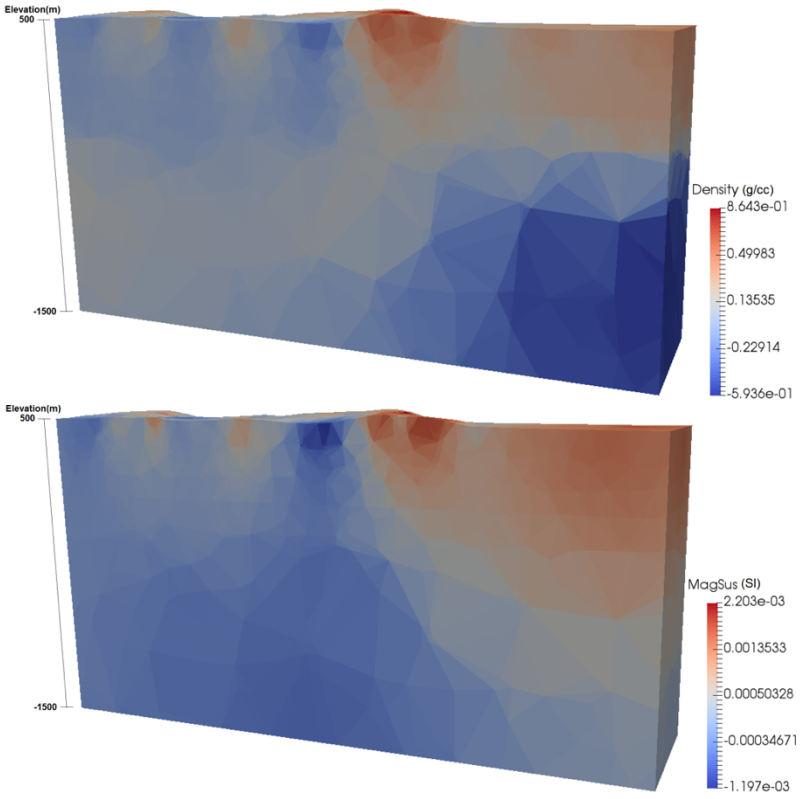

Figure 7.21: Vertical sections of the joint inversion models of gravity (top) and magnetic (bottom) data using correlation method for ρ=1.0E+5.

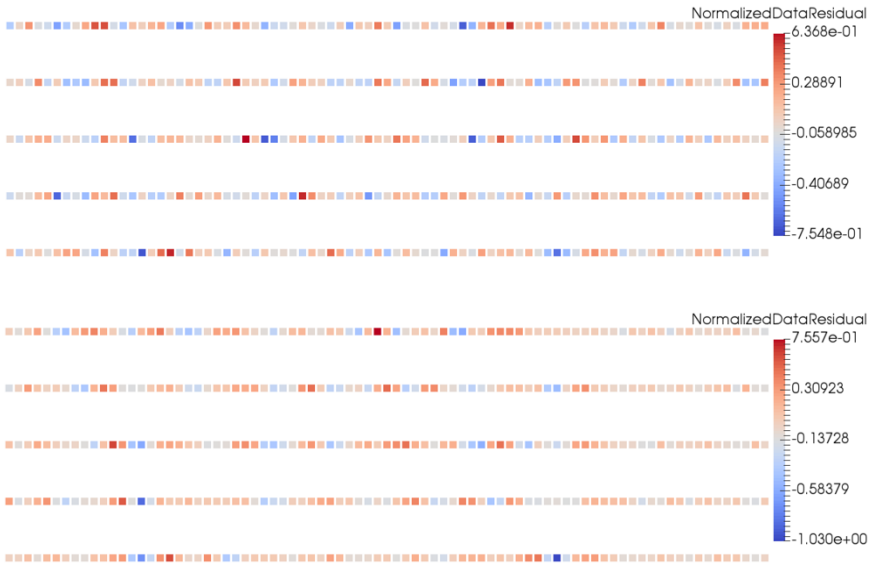

Figure 7.22: Top: normalized data residual for the gravity model. Bottom: normalized data residual for the magnetic model (correlation method for ρ=1.0E+5).

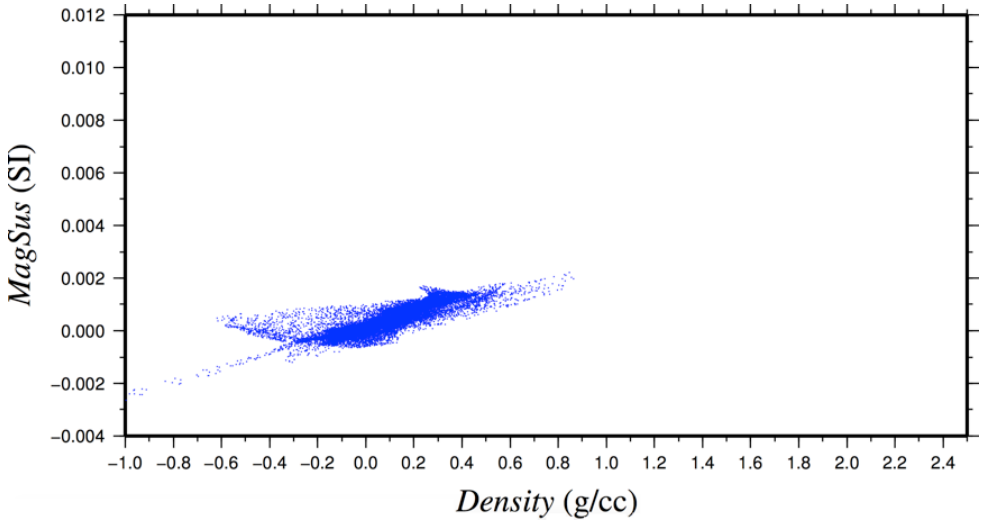

Figure 7.23: Physical properties (magnetic susceptibility versus density) obtained after the joint inversion using the correlation method for ρ=1.0E+5. Each blue dot corresponds to a cell in the inversion mesh.

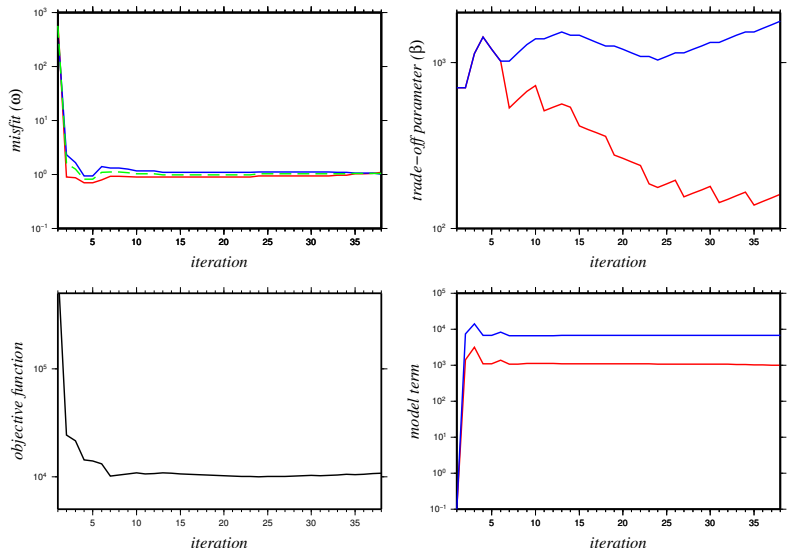

Figure 7.24: Variations of different parts of the objective function such as data misfit (ω; top-left), trade-off parameter (β; top-right), objective function ($\mathbf{\Phi}$; bottom-left) and model term (ϕ_m; bottom-right) at iterations for the joint inversion of gravity (red) and magnetic (blue) data using the correlation method for ρ=1.0E+5. Green color shows the average "ω".

Joint inversion results from the correlation method do not show results better than the independent inversions. In order to improve the inversion results the clustering method is used, for two scenarios: two clusters and three clusters. For the three cluster case I define three different clusters with average physical properties corresponding to the three main geological structures: overburden (density=2 g/cc; MagSus= 4×10^{-3} SI), sandstone (relative density=-0.25 g/cc; MagSus= 0 SI) and basement (relative density=0.0 g/cc; MagSus= 5×10^{-3} SI). For the two cluster case I omit the basement. Figures 7.25 to 7.28 show joint inversion results for a 2 cluster case with a coupling factor of 10, the normalized data residuals, the cross plot of the physical properties (magnetic susceptibility versus density) obtained after the joint inversion, and the variation of the various terms of the objective function, respectively. The constructed model shows much improvement over those from the independent inversions. The run-time was 1 hour and 57 minutes for 13 iterations.

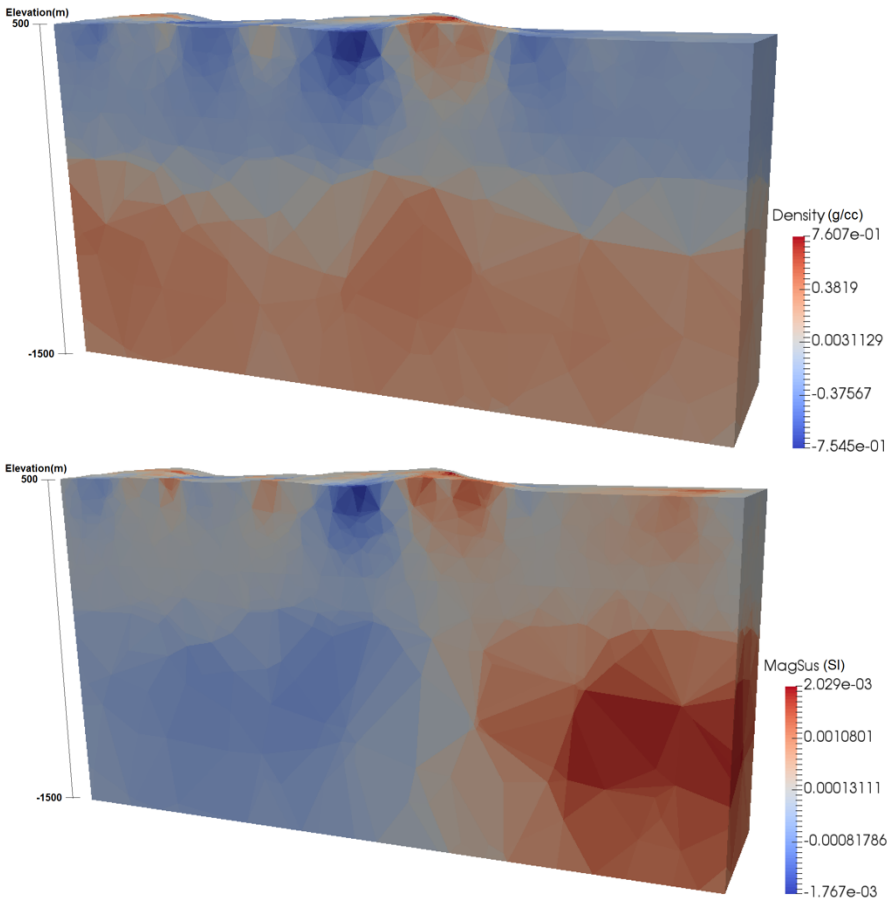

Figure 7.25: Vertical sections of the joint inversion models of gravity (top) and magnetic (bottom) data using clustering method (2 clusters) for ρ=10.

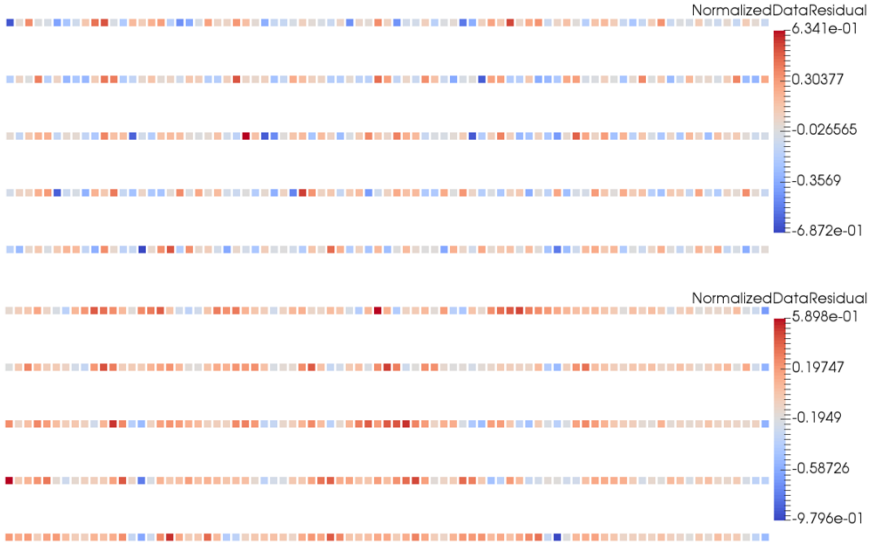

Figure 7.26: Top: normalized data residual for the gravity model. Bottom: normalized data residual for the magnetic model (clustering method; 2 clusters; ρ=10).

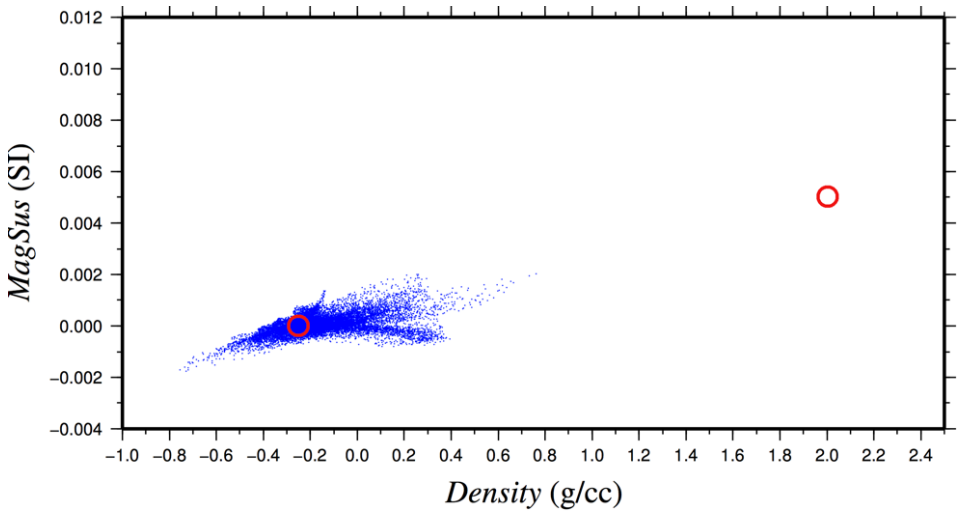

Figure 7.27: Physical properties (magnetic susceptibility versus density) obtained after the joint inversion using the clustering method (2 clusters) for ρ=10. Each blue dot corresponds to a cell in the inversion mesh. Red circles: the two initial clusters defined in the joint inversion (from right to left: overburden and sandstone).

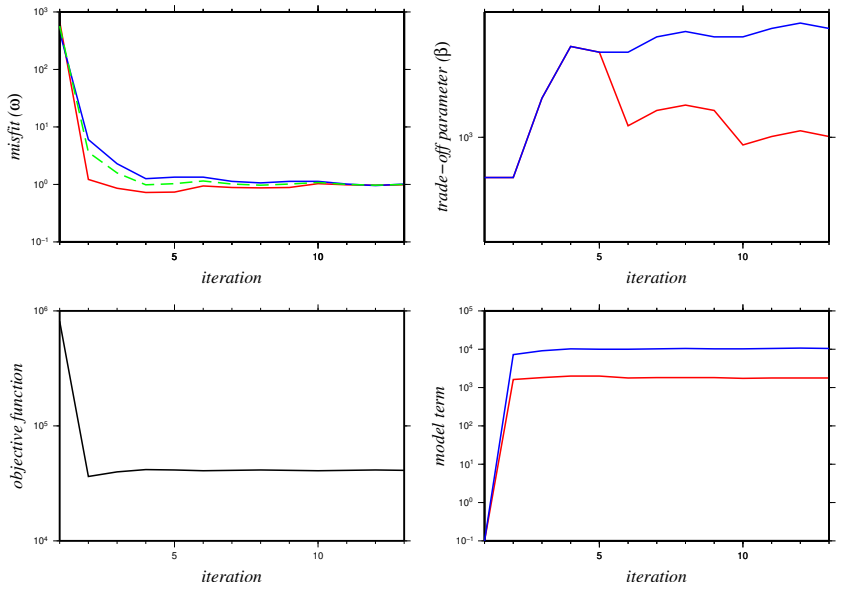

Figure 7.28: Variations of different parts of the objective function such as data misfit (ω; top-left), trade-off parameter (β; top-right), objective function ($\mathbf{\Phi}$; bottom-left) and model term (ϕ_m; bottom-right) at iterations for the joint inversion of gravity (red) and magnetic (blue) data using the clustering method (2 clusters) for ρ=10. Green color shows the average "ω".

It can be seen that three different layers are somewhat apparent in the joint inversion model (Figure 7.25). The non-zero susceptibility is concentrated in the overburden and basement, and there is a susceptibility of around 0SI in the middle layer that corresponds to the sandstone. The same situation can be seen in the density model in which the middle zone has a relative density of around -0.25 g/cc corresponding to the sandstone layer. Also it can be seen that the magnetic susceptibility on the left side of the basement is less than on the right side. These models match reasonably well the true models (see Figure 7.9). The approximate location of the unconformity can be clearly seen. In particular, the clustering joint inversion with two clusters is able to separate out the susceptibility and density in the basement.

Figures 7.29 and 7.30 show joint inversion results of the synthetic data for a three cluster case with a coupling factor of 10 as well as the normalized data residuals. This clustering does not seem better than for the 2 cluster case as the cluster of the overburden (as well as sandstone) is not generated. Figures 7.31 to 7.32 show the cross plot of the physical properties (magnetic susceptibility versus density) obtained after the joint inversion, and the variation of the various terms of the objective function as a function of the iteration number, respectively. The run-time was 1 hour and 23 minutes for 13 iterations.

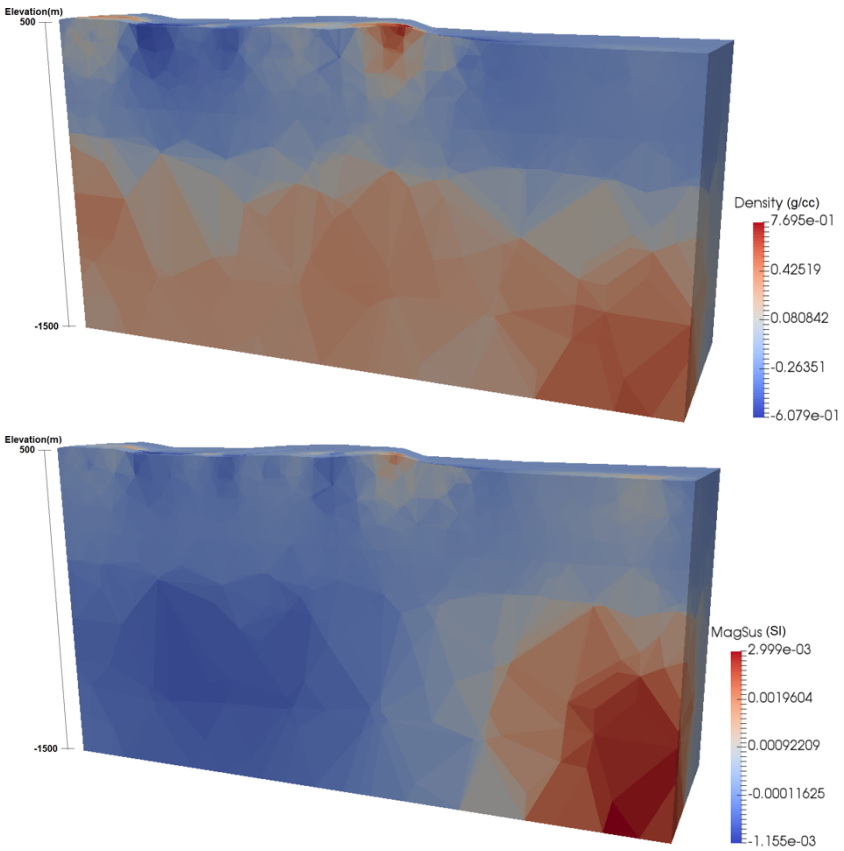

Figure 7.29: Vertical sections of the joint inversion models of gravity (top) and magnetic (bottom) data using clustering method (3 clusters) for ρ=10.

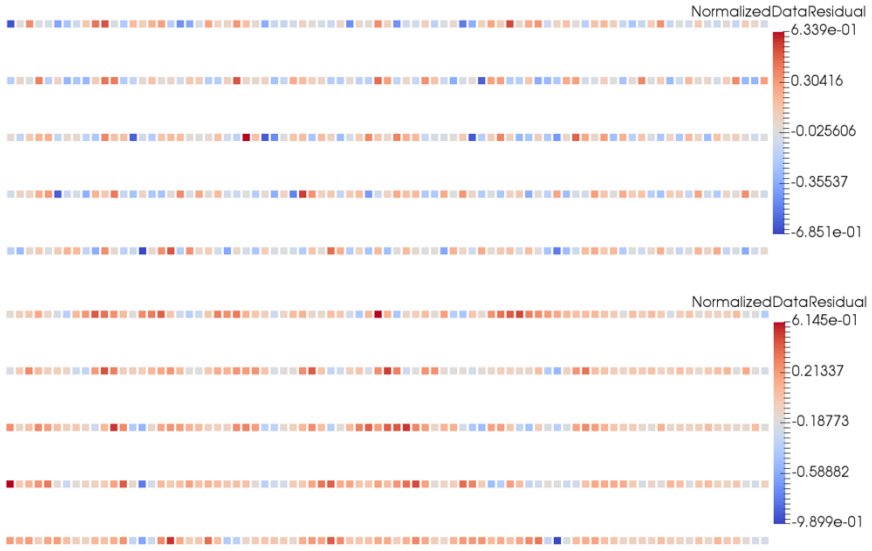

Figure 7.30: Top: normalized data residuals for the gravity model. Bottom: normalized data residual for the magnetic model (clustering method; 3 clusters; ρ=10).

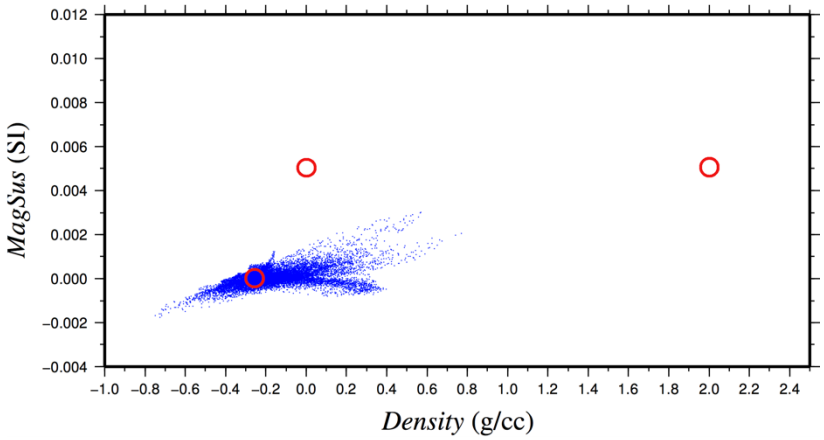

Figure 7.31: Physical properties (magnetic susceptibility versus density) obtained after the joint inversion using the clustering method (3 clusters) for ρ=10. Each blue dot corresponds to a cell in the inversion mesh. Red circles: the three clusters defined in the joint inversion (from right to left: sandstone, basement and overburden).

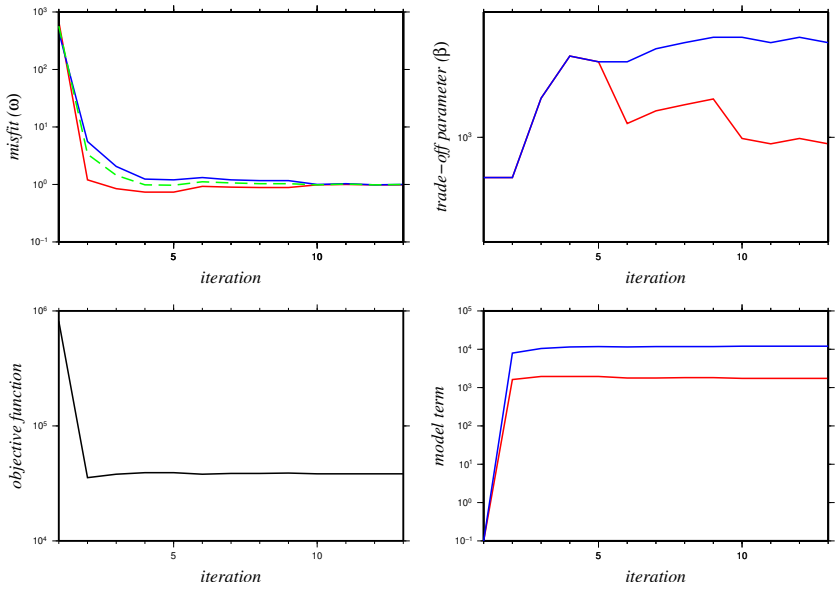

Figure 7.32: Variations of different parts of the objective function such as data misfit (ω; top-left), trade-off parameter (β; top-right), objective function ($\mathbf{\Phi}$; bottom-left) and model term (ϕ_m; bottom-right) at iterations for the joint inversion of gravity (red) and magnetic (blue) data using the clustering method (3 clusters) for ρ=10. Green color shows the average "ω".

It can be seen that the cluster method can generate the sandstone and basement structure as well as the unconformity location. But the overburden is still not imaged as a sharp

transition at the overburden/sandstone interface. To solve this problem, I use the constrained joint inversion. I consider a layer that I am confident is all overburden from surface to an elevation above sea level of around 500 m in which the physical properties are fixed during the inversion process (a density value of 2 g/cc and a magnetic susceptibility of 5×10^{-3} SI). The mesh had about 325,000 tetrahedral cells. The reason that unlike the constrained independent inversion I started with a mesh with 1 constrained layer rather than 2 constrained layers is to reduce the number of cells. Because by reducing the number of cells, the run-time will decrease. Therefore, I will initially start with a mesh with 1 constrained layer. If no satisfactory results are obtained, I will try a mesh with 2 constrained layers. Also, since it is the free-air data that is being inverted, it is expected that by constraining the layer/structure which has the absolute density value in the mesh, the code will be able to reconstruct other parts of the model as well as the base of overburden.

The code was initially run for ρ=10. The model constructed by this inversion was used as an initial model for both inversions for ρ=1.0E+5 and (again) ρ=10. Without considering this approach, the inversion for ρ=1.0E+5 stopped after 150 iterations with a run-time of 314 hours. Whereas, by considering this initial model, not only the run-time for ρ=1.0E+5 was reduced, but the results for ρ=10 were improved. The run-times for the joint inversions of ρ=10 and ρ=1.0E+5 were 33 hours and 35 minutes for 13 iterations and 48 hours and 12 minutes for 17 iterations, respectively. Figures 7.33 to 7.40 show the results for ρ=10 and ρ=1.0E+5 for this (1 layer) constrained joint inversion.

For the clustering method, a higher coupling factor gives a better clustering (see Figure

7.39). Thus, it is expected that this gives the better inversion for this model (but not necessarily for all models). In this research many models were made to investigate the clustering method, but only a few of them, which represent the range of results, are shown in this thesis. In one of these models, all clusters (6 clusters including overburden, sandstone, politic gneiss, psammitic gneiss, granitoid rocks and alteration zone) were considered for the joint inversion. The results for ρ=10 were similar to Figures 7.29 and 7.31. For ρ=1.0E+5, the structures reconstructed in the basement were similar to those in Figure 7.37 with sharper boundaries. The only improvement for ρ=1.0E+5 was related to the clustering in which all 6 clusters were made. Therefore, as mentioned a higher coupling factor gives a better clustering but not necessarily always the better inversion models.

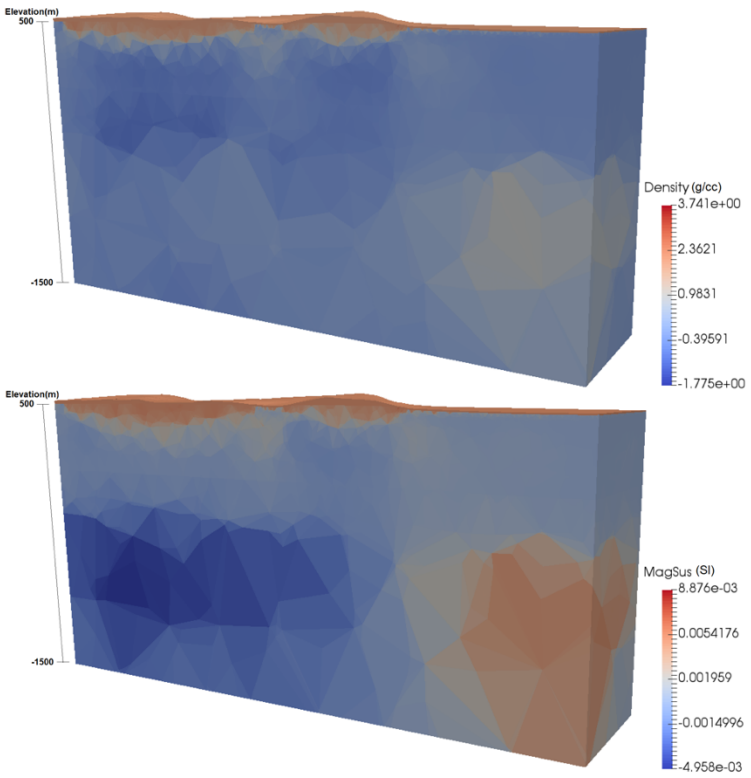

Figure 7.33: Vertical sections of the constrained (1 constrained layer) joint inversion models of gravity (top) and magnetic (bottom) data using clustering method (2 clusters) for ρ=10.

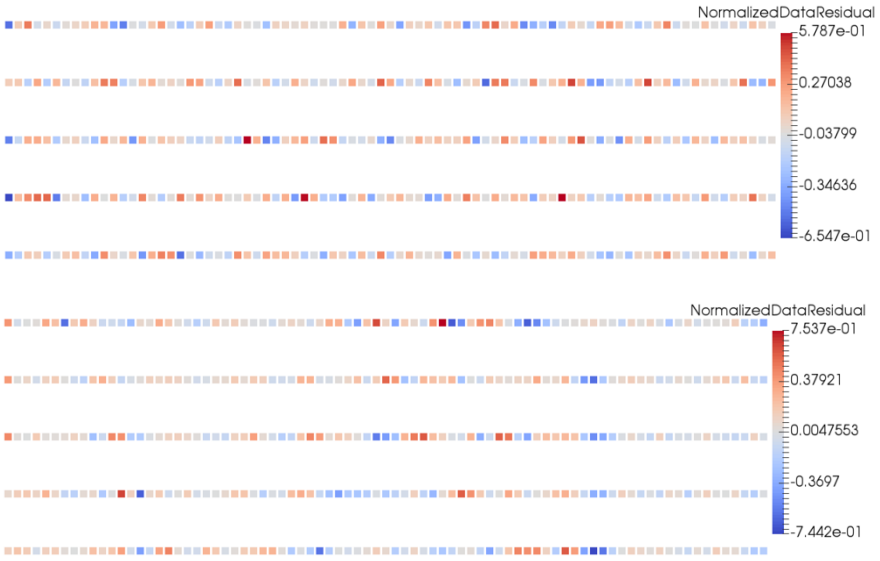

Figure 7.34: Top: normalized data residuals for the gravity model. Bottom: normalized data residual for the magnetic model (1 constraint; 2 clusters; ρ=10).

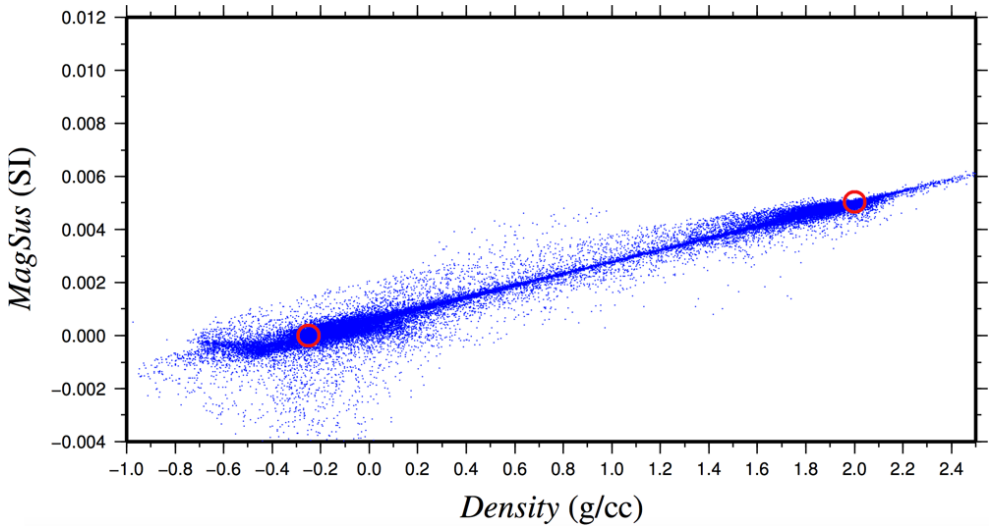

Figure 7.35: Physical properties (magnetic susceptibility versus density) obtained after the constrained (1 constraint) joint inversion. Each blue dot corresponds to a cell in the inversion mesh. Red circles: the two initial clusters defined in joint inversion.

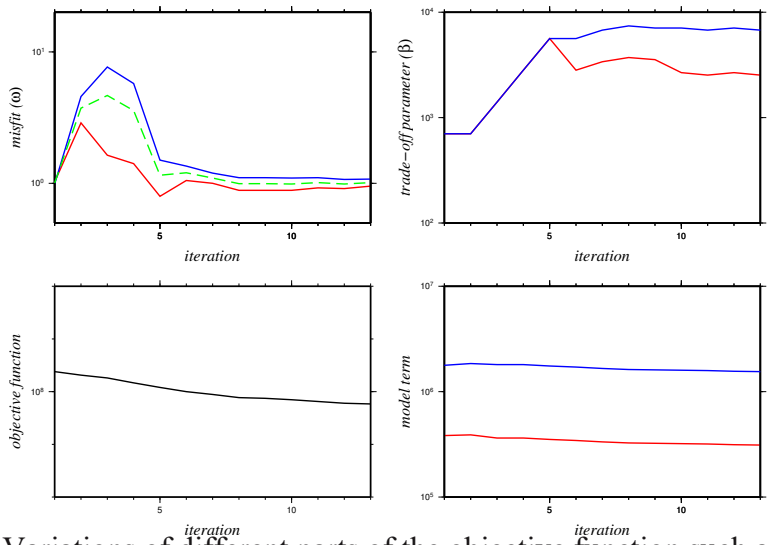

Figure 7.36: Variations of different parts of the objective function such as data misfit (ω; top-left), trade-off parameter (β; top-right), objective function ($\mathbf{\Phi}$; bottom-left) and model term (ϕ_m; bottom-right) at iterations for the joint inversion of gravity (red) and magnetic (blue) data using the clustering method (2 clusters; 1 constraint) for ρ=10. Green color shows the average "ω".

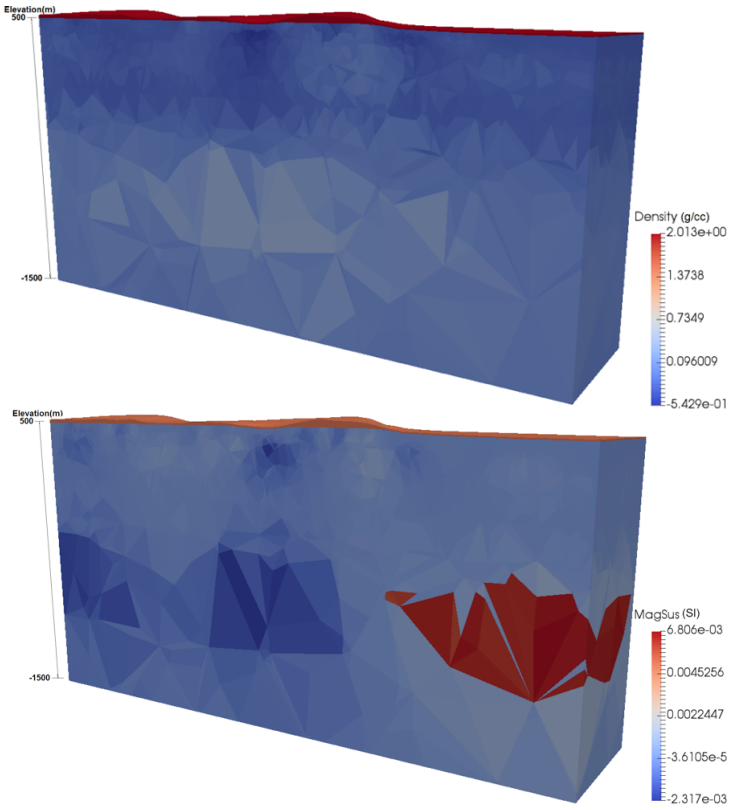

Figure 7.37: Vertical sections of the constrained (1 constraint) joint inversion models of gravity (top) and magnetic (bottom) data using clustering method (2 clusters) for ρ=1.0E+5.

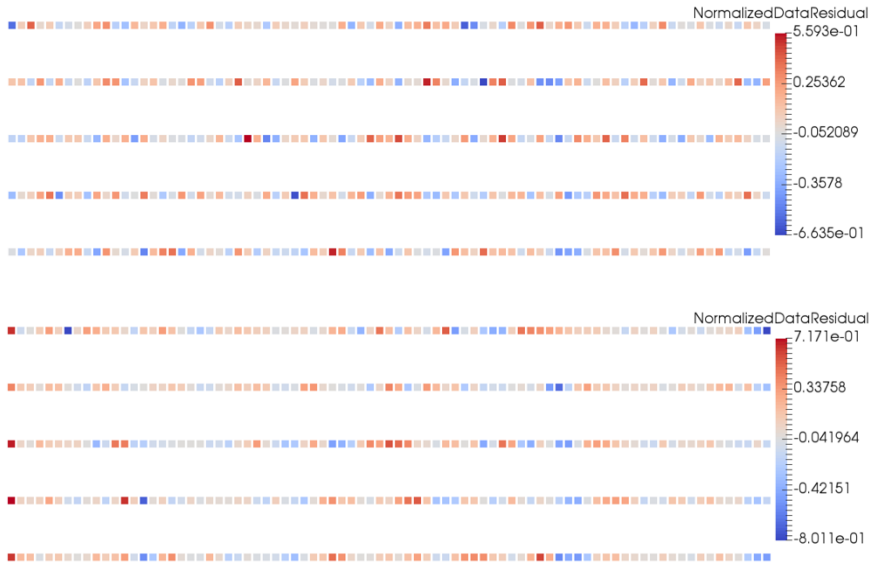

Figure 7.38: Top: normalized data residuals for the gravity model. Bottom: normalized data residual for the magnetic model (1 constraint; 2 clusters; ρ=1.0E^{+5}).

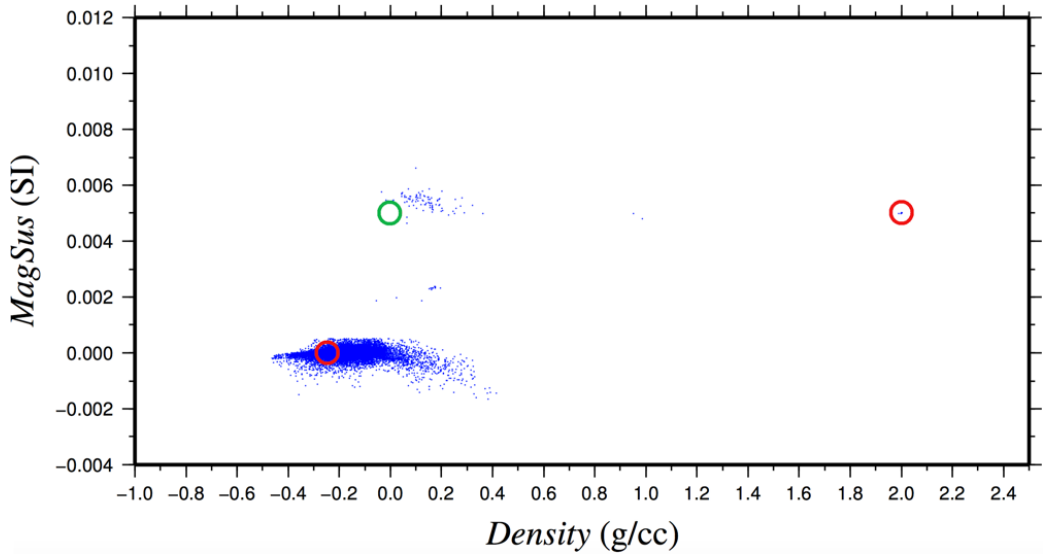

Figure 7.39: Physical properties (magnetic susceptibility versus density) obtained after the constrained (1 constraint) joint inversion. Each blue dot corresponds to a cell in the inversion mesh. Red circles: the two initial clusters defined in joint inversion. Green circle: basement cluster which was omitted in this 2 cluster joint inversion.

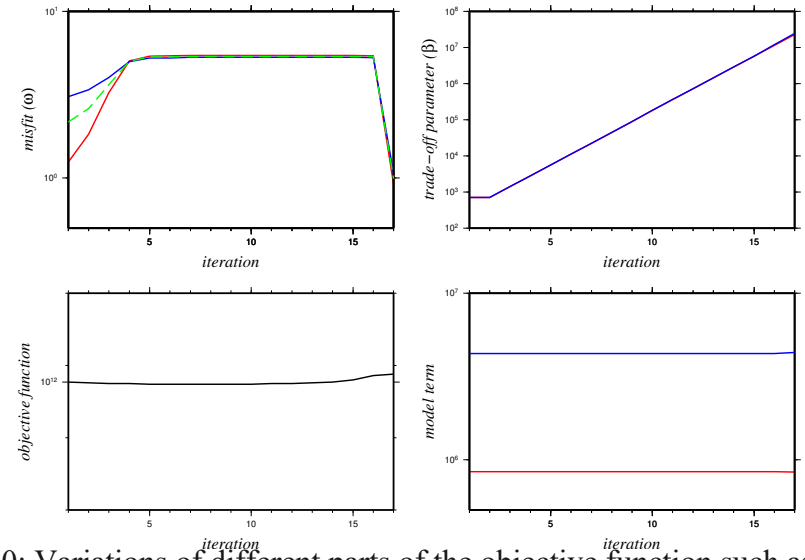

Figure 7.40: Variations of different parts of the objective function such as data misfit (ω; top-left), trade-off parameter (β; top-right), objective function ($\mathbf{\Phi}$; bottom-left) and model term (ϕ_m; bottom-right) at iterations for the joint inversion of gravity (red) and magnetic (blue) data using the clustering method (2 clusters; 1 constraint) for ρ=1.0E+5. Green color shows the average "ω".

Only two clusters (overburden and sandstone) were considered for the constrained joint inversions. But it can be seen that the clustering for ρ=1.0E+5 is better than that for ρ=10 as far as it has generated three distinct clusters (for overburden, sandstone and basement). The green circle in Figure 7.39 shows the location of the basement cluster. The clustering for ρ=10 is not too good, but the constructed models for ρ=10 are a little better than the results for ρ=1.0E+5, as the base of overburden is reconstructed better. The results for 3 cluster case are not shown here as they were very similar to the 2 cluster case without any improvement.

In an attempt to further improve the results, Figures 7.41 to 7.45 show the results when two layers with fixed physical properties are constrained during the joint inversion. From top to bottom the layers are:

1- A layer that can confidently be assumed to be the overburden from the surface to an elevation above sea level of around 500 m with fixed physical properties during the inversion process: here a density value of 2 g/cc and a magnetic susceptibility of 5×10^{-3} SI.

2- A layer that we are unsure of but is either overburden or sandstone from an elevation of 500 m to 450 m. So, for the physical properties a wide range of values is considered as constraint (as lower and upper bounds; i.e. -100 g/cc < density < 100 g/cc and -10000 SI < magnetic susceptibility < 10000 SI).

3- A layer that we are confident is all sandstone from an elevation of 450 m to 50 m with fixed physical properties: e.g. here a relative density value of -0.25 g/cc and a magnetic susceptibility of 0 SI.

4- A layer from 50 m to the bottom of the model that we are unsure of but is either sandstone or basement. So, for the physical properties a wide range of values is considered as constraint (as lower and upper bounds; i.e. -100 g/cc < density < 100 g/cc and -10000 SI < magnetic susceptibility < 10000 SI).

From Figures 7.41 and 7.42, it can be seen that the result for the overburden section has improved in the constrained (with 4 constrained layers) joint inversion results. Similar to the previous model (1 constraint model), an initial model is used in order to improve the results. The run-time for this constrained joint inversion (of ρ=10) was 89 hours and 52 minutes for 20 iterations. The mesh had about 533,000 tetrahedral cells.

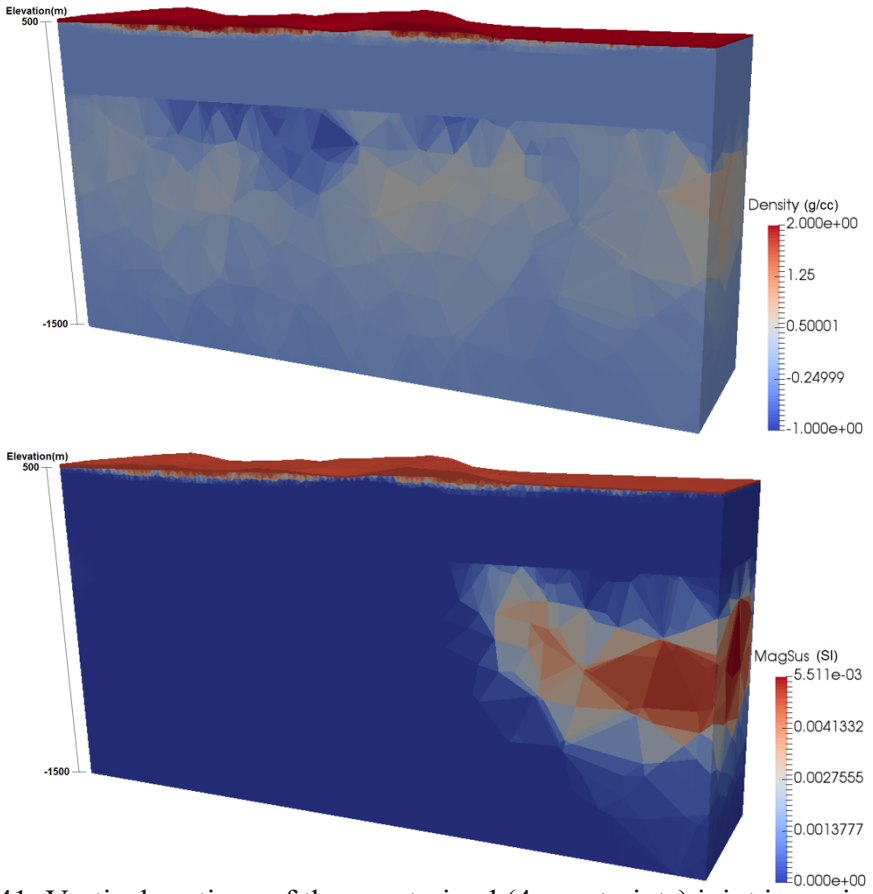

Figure 7.41: Vertical sections of the constrained (4 constraints) joint inversion models of gravity (top) and magnetic (bottom) data using clustering method (2 clusters) for ρ=10.

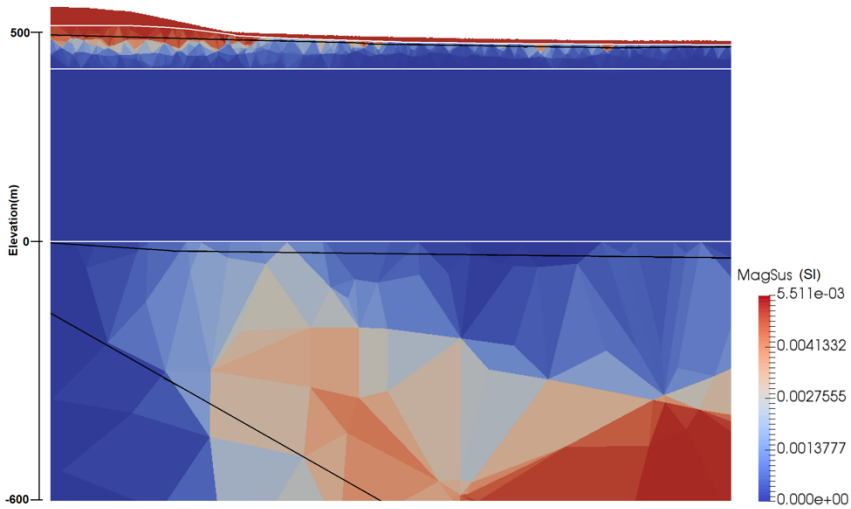

Figure 7.42: Part of the susceptibility model produced by the constrained (4 constraints) joint inversion. Three black lines (from top to bottom): true base of overburden, true unconformity and true P2 fault (true interface between blocks #4 and #5 in the basement). The white lines show where the bounds change.

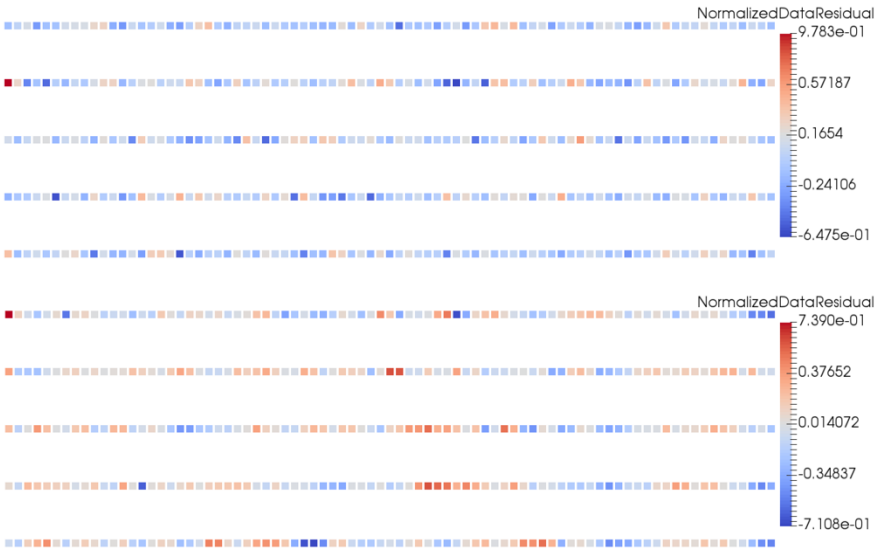

Figure 7.43: Top: normalized data residual for the gravity model. Bottom: normalized data residual for the magnetic model (4 constraints; 2 clusters; ρ=10).

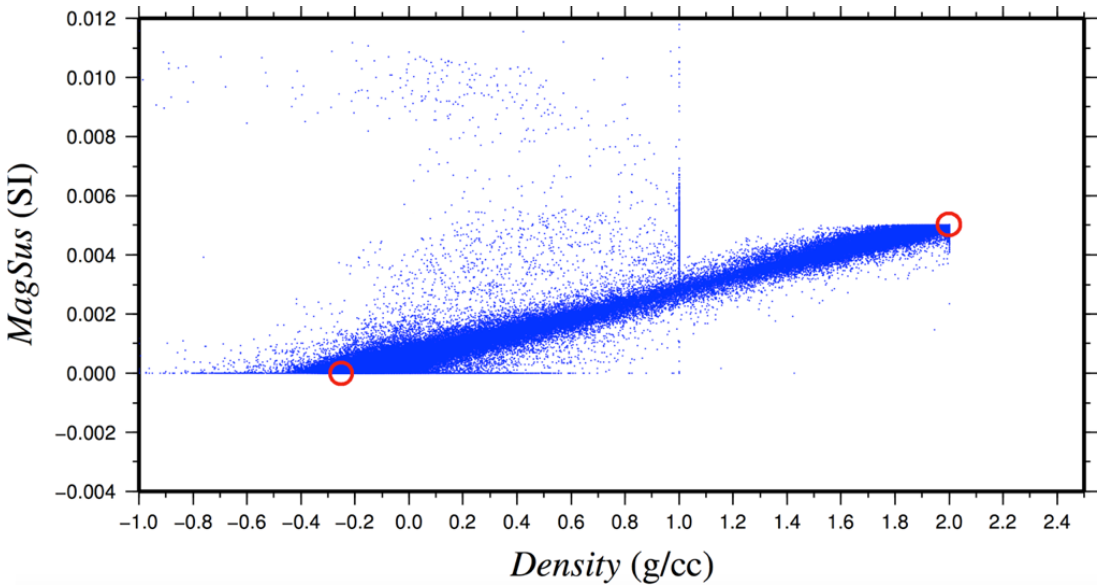

Figure 7.44: Physical properties (magnetic susceptibility versus density) obtained after the constrained (4 constraints) joint inversion. Each blue dot corresponds to a cell in the inversion mesh. Red circles: the two clusters defined in joint inversion.

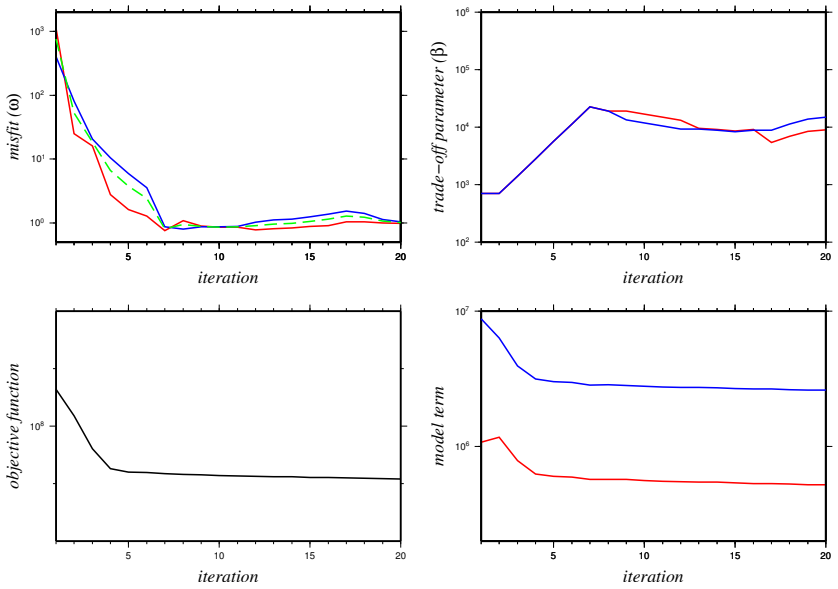

Figure 7.45: Variations of different parts of the objective function such as data misfit (ω; top-left), trade-off parameter (β; top-right), objective function ($\mathbf{\Phi}$; bottom-left) and model term (ϕ_m; bottom-right) at iterations for the joint inversion of gravity (red) and magnetic (blue) data using the clustering method (2 clusters; 4 constraints) for ρ=10. Green color shows the average "ω".

7.3 3D inversion of real gravity and magnetic data

In this section, 3D inversions of real gravity and magnetic data are performed for the McArthur area for a number of profiles. Independent and joint inversions are performed in order to construct density and susceptibility models. Physical property data are used as constraints in the inversions. Similar to the synthetic examples, for the distance weighting, a value of 1.0 is assigned for w_z and w_p. Also, a value of 0.05 is considered for the *chifact* value for both magnetic and gravity methods. Value of 1.0 and 700 are considered for the initial trade-off parameter of independent and joint inversions, respectively (see Section 7.2.2). For the inversions, appropriate uncertainties are probably about 5% of the ranges (Van Wijk et al., 2002). Since the gravity data is in the range [-212.96, -204.45] and the

magnetic data is in the range [-380.61, -330.71] (after removing the geomagnetic field value = 59500 nT), uncertainty values can be about 0.44 mGal and 2.5 nT for gravity and magnetic data, respectively. For levelling the data, simply removing the average value of data was the most sensible approach for both gravity and magnetic methods.

A part of the airborne free-air gravity data (from the Bell Gravity data-set) as well as airborne total magnetic field data (from Triaxial Magnetic data-set) were selected for the inversion with a station spacing and a profile spacing of around 50 m and 300 m, respectively (Figures 7.46 and 7.47; see Section 7.1). The data are almost in the same locations but not quite (see Figures 7.1, 7.3 and 7.46). During data acquisition, the geomagnetic field strength in McArthur area was 59500nT, and the geomagnetic field declination and inclination were around 12 and 80 degrees, respectively. Figure 7.47 shows that the gravity and magnetic data are strongly dominated by variations of topography. Also, the right side and left side of the magnetic profiles show a decrease and an increase in the magnetic data, respectively. These variations are a part of a long wavelength trend (see also Figure 7.4) which is due to the deep (i.e. basement) structures.

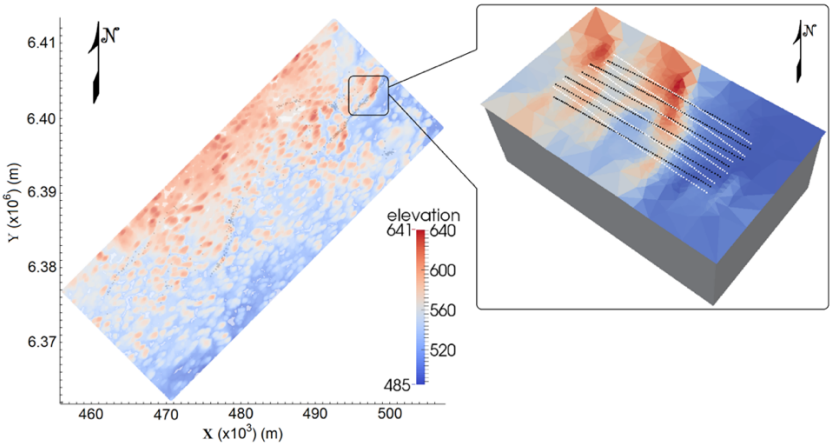

Figure 7.46: Topography of McArthur-Millennium corridor. Inset shows location of magnetic (black) and gravity (white) survey lines.

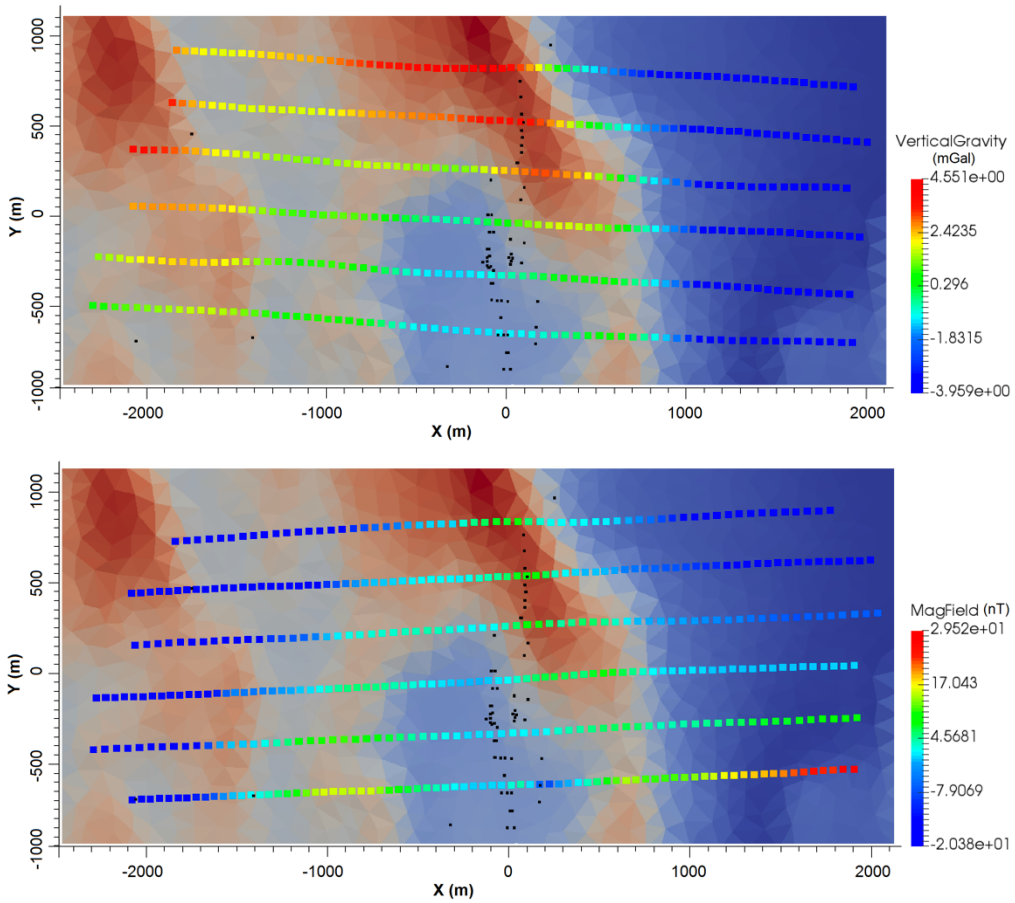

Figure 7.47: Free-air gravity data (top; in mGal) and magnetic data (bottom; in nT) over the McArthur River area (~4×2km). Data are dominated by variations in topography. Black dots show the location of drill-holes. The background image for both panels is elevation (and the same colour scale as in Figure 7.46).

3D inversions were performed for the real airborne gravity and magnetic data on a mesh using the L2-norm method. Similar to the synthetic examples, I started with independent inversions, then I investigated the results of joint inversion as well as constrained joint inversion. Figure 7.48 shows the independent inversion results for magnetic and gravity data. It can be seen that the independent inversions were not able to reconstruct the interface between the overburden and sandstone nor the basement structure. Figure 7.49 shows there is a good fit between the observed and calculated data. The mesh had about 28,000 tetrahedral cells.

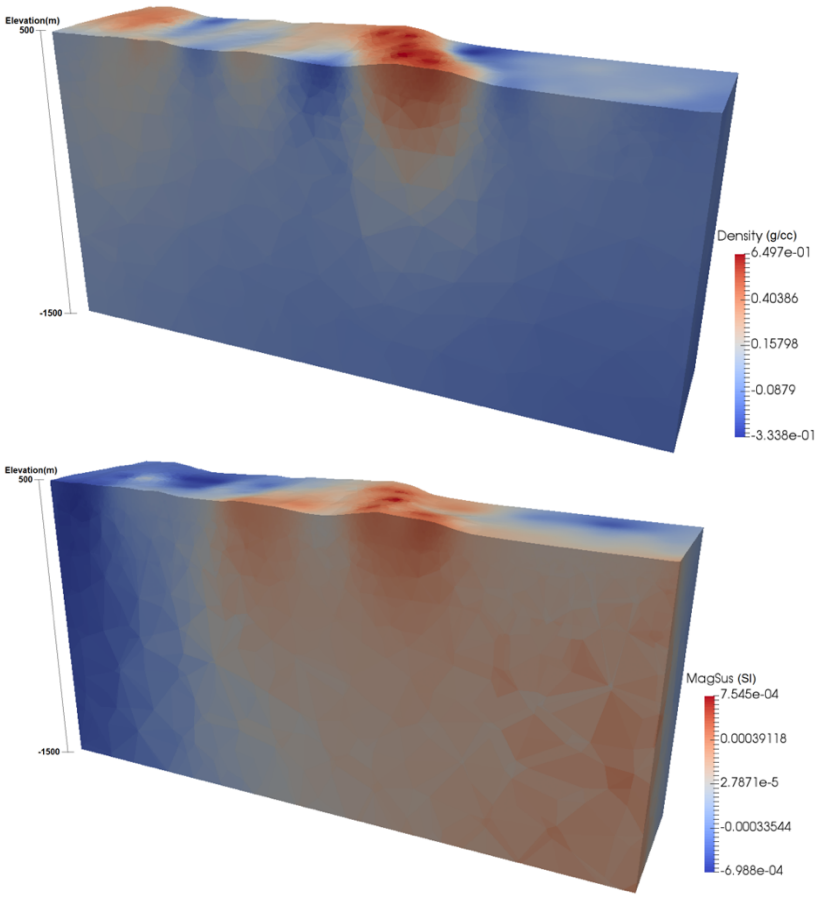

Figure 7.48: Vertical sections of independent gravity (top) and magnetic (bottom) inversion models for the real data.

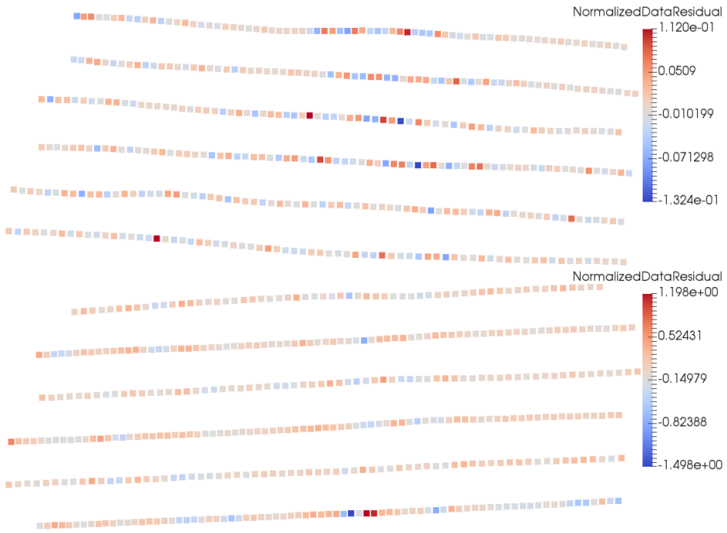

Figure 7.49: Top: normalized data residuals for the gravity model. Bottom: normalized data residuals for the magnetic model (for the independent inversions).

In order to improve the inversion results, joint inversion of gravity and magnetic data using the clustering method for a coupling factor of ρ=10 was applied (similar to the synthetic case in Section 7.8.2; Figure 7.25). For this purpose, two clusters were considered in which two different clusters with average physical properties corresponding to the two main geological structures were defined: overburden (density=2 g/cc; MagSus: 4×10^{-3} SI) and sandstone (relative density=-0.25 g/cc; MagSus: 0 SI). For the joint inversion results shown in Figure 7.50, the normalized data residuals shown in Figure 7.51 show there is a close fit between the observed and calculated data. Figure 7.52 shows the cross plot of densities and magnetic susceptibilities constructed using the joint inversion. Also, the variation of the various terms of the objective function for the joint inversion model are shown in Figure 7.53. The run-time for this joint inversion (of ρ=10) was 2 hours and 57 minutes for 13 iterations. The mesh had about 28,000 tetrahedral cells.

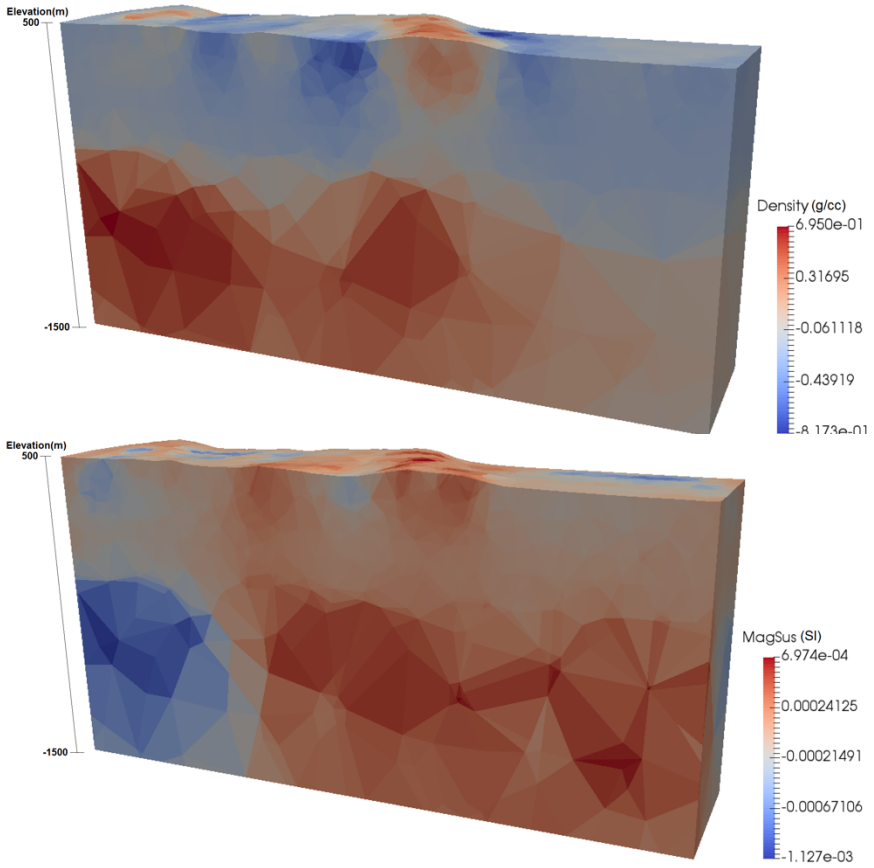

Figure 7.50: Vertical sections of the joint inversion models of real gravity (top) and magnetic (bottom) data using clustering method (2 clusters) for ρ=10.

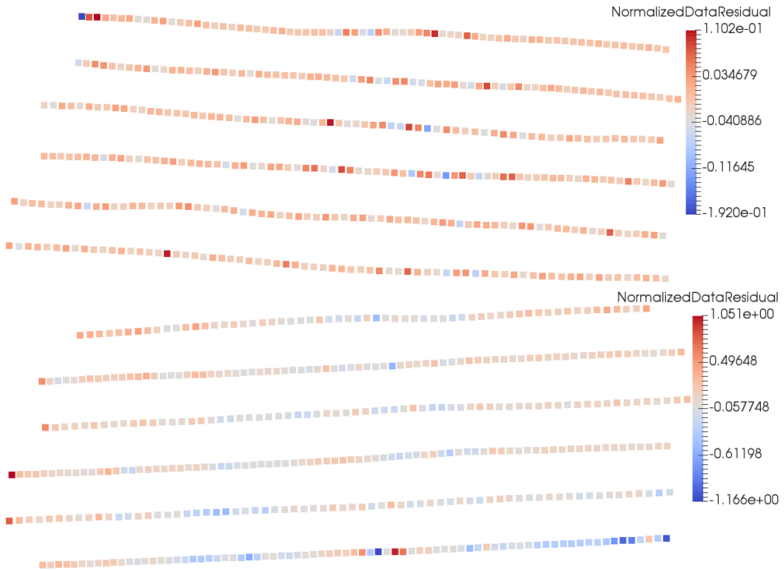

Figure 7.51: Top: normalized data residuals for the gravity model. Bottom: normalized data residuals for the magnetic model (clustering method; 2 clusters; ρ=10).

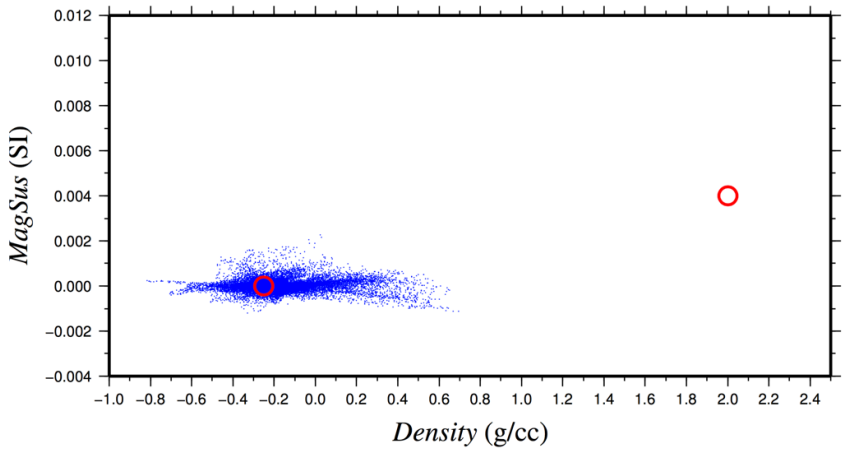

Figure 7.52: Physical properties (magnetic susceptibility versus density) obtained after the joint inversion of real data using the clustering method (2 clusters) for ρ=10. Each blue dot corresponds to a cell in the inversion mesh. Red circles: the two clusters defined in the joint inversion (from left to right: overburden and sandstone).

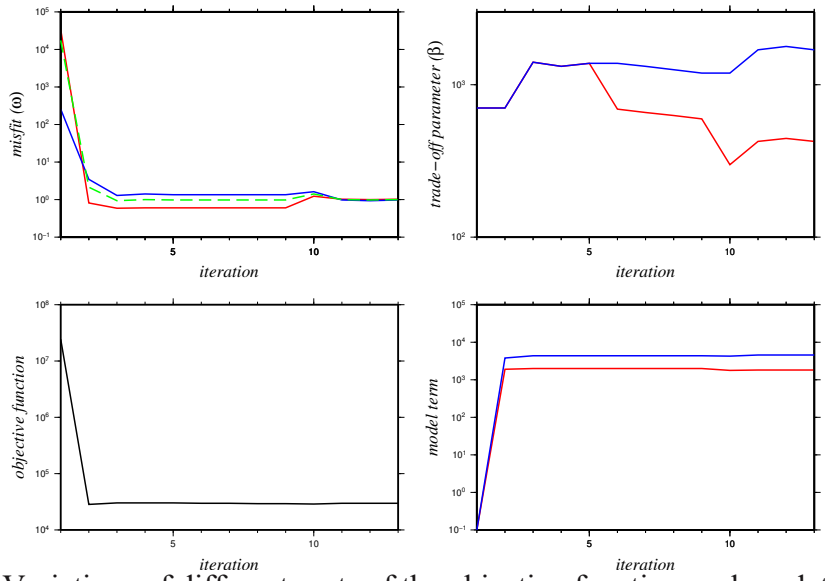

Figure 7.53: Variations of different parts of the objective function such as data misfit (ω; top-left), trade-off parameter (β; top-right), objective function ($\mathbf{\Phi}$; bottom-left) and model term (ϕ_m; bottom-right) at iterations for the joint inversion of real gravity (red) and magnetic (blue) data using the clustering method (2 clusters) for ρ=10. Green color shows the average "ω".

A susceptibility of around 0 SI is estimated for the middle layer that corresponds to the sandstone (Figure 7.50). The same situation can be seen in the density model in which the middle zone has a relative density of around -0.25 g/cc corresponding to the sandstone layer. The approximate location of the unconformity can be clearly seen, albeit a little deep.

In the basement zone the magnetic susceptibility on the left side is less than on the right side of the basement. As mentioned in Chapter 2, in the McArthur River area the magnetic susceptibility of rocks in the footwall of the P2 fault is less than that of the rocks in the hanging-wall. Therefore, in the inversion results the boundary between the low and high magnetic susceptibly in the basement can be interpreted as the approximate location of the P2 fault. In particular, the clustering joint inversion is able to separate out the susceptibility and density in the basement. But the overburden and sandstone interface is not resolved in a sharp manner.

To attempt to solve this problem, I use the 1-layer constrained joint inversion (similar to the synthetic case in Section 7.2.2; Figure 7.33). A layer is considered that can confidently be assumed to be overburden in which the physical properties are fixed during the inversion process (a density value of 2 g/cc and a magnetic susceptibility of 4×10^{-3} SI based on drill-hole information; Figures 7.54 to 7.57). The run-time for this constrained joint inversion (of ρ=10) was 49 hours and 34 minutes for 20 iterations. The mesh had about 325,000 tetrahedral cells which is significantly larger than the previous example as defining a narrow layer below the topography (as a constraint) causes the mesh generator "tetgen" to generate many (small) refined tetrahedral cells in that region. The 1-layer constrained joint inversion improved the results better than the joint inversion method as the base of overburden is imaged at the correct depth as a sharper interface.

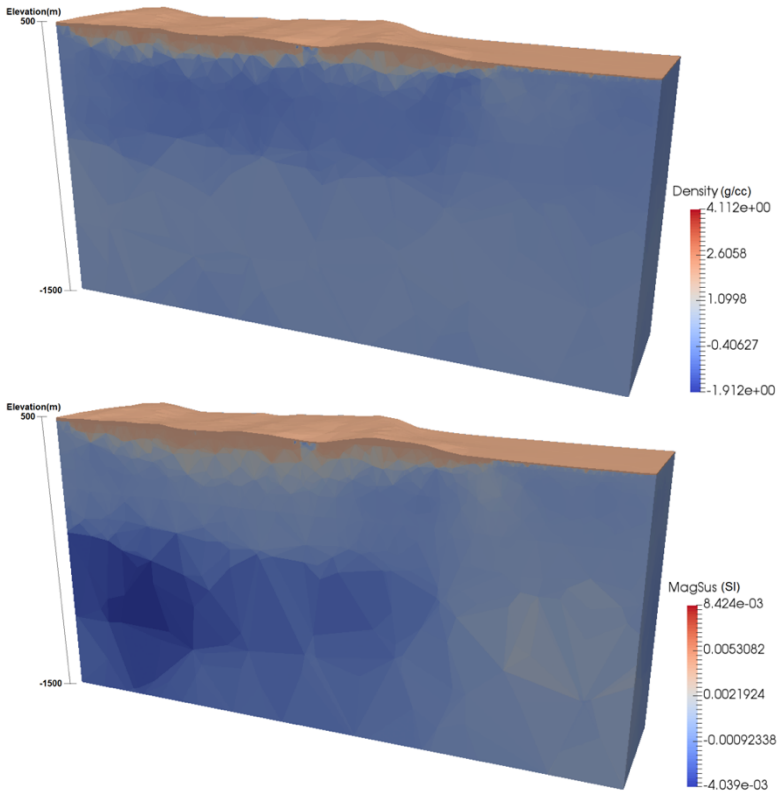

Figure 7.54: Vertical sections of the constrained (1 layer) joint inversion models of real gravity (top) and magnetic (bottom) data using clustering method (2 clusters) for ρ=10.

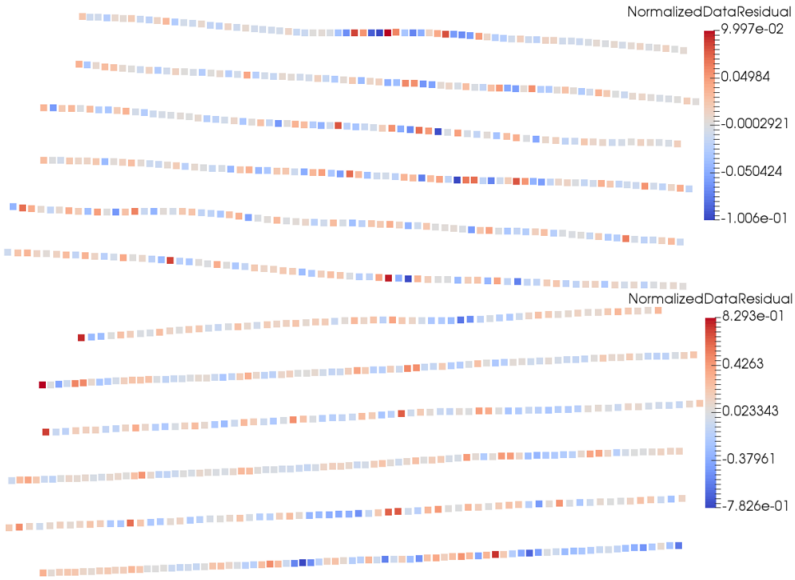

Figure 7.55: Top: normalized data residuals for the gravity model. Bottom: normalized data residuals for the magnetic model (1 constraint/layer; 2 clusters; ρ=10).

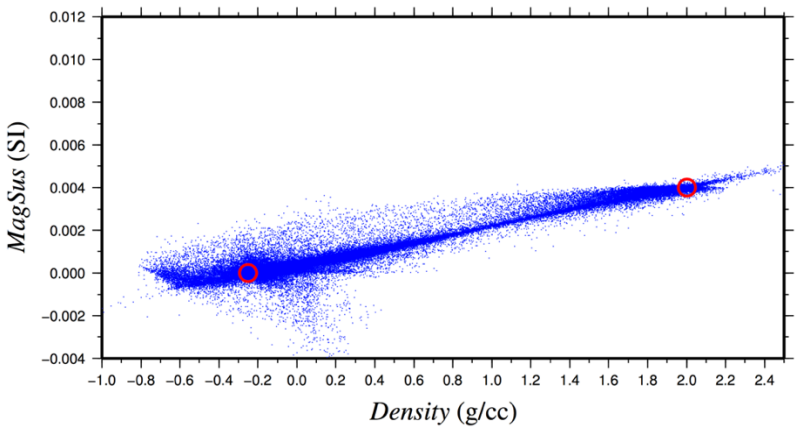

Figure 7.56: Physical properties (magnetic susceptibility versus density) obtained after the constrained (1 layer) joint inversion of real data. Each blue dot corresponds to a cell in the inversion mesh. Red circles: the two clusters defined in joint inversion.

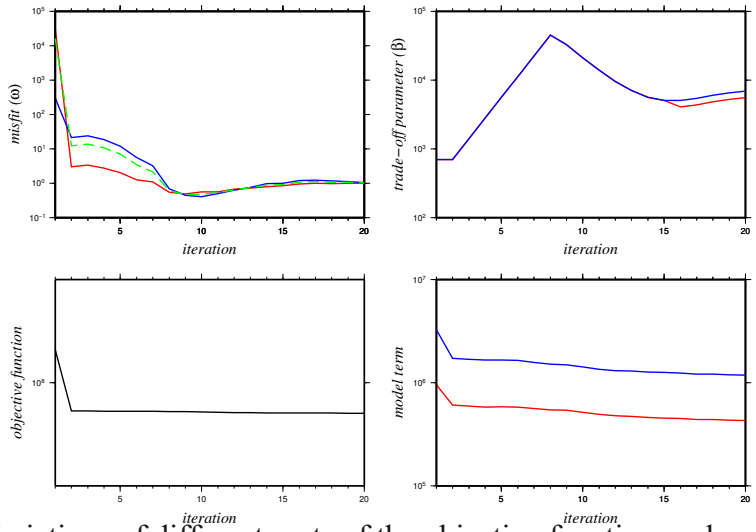

Figure 7.57: Variations of different parts of the objective function such as data misfit (ω; top-left), trade-off parameter (β; top-right), objective function ($\mathbf{\Phi}$; bottom-left) and model term (ϕ_m; bottom-right) at iterations for the joint inversion of real gravity (red) and magnetic (blue) data using the clustering method (2 clusters; 1 constraint) for ρ=10. Green color shows the average "ω".

I attempted to further improve the results using a constrained joint inversion and two layers with fixed physical properties (Figures 7.58 to 7.62). Similar to the synthetic case in Section 7.2.2 (Figure 7.41), the layers in the mesh were as follows: 1- A layer that can safely be assumed to be overburden with fixed physical properties during the inversion

process: e.g. here a density value of 2 g/cc and a magnetic susceptibility of 4×10^{-3} SI. 2- A layer that we are unsure of but is either overburden or sandstone. So, for the physical properties a wide range of values is considered as constraint possible between the lower and upper bounds. 3- A layer that we are confident is all sandstone from an elevation of 450 m to 50 m with fixed physical properties: e.g. here a relative density value of -0.25 g/cc and a magnetic susceptibility of 0 SI. 4- A layer from 50 m to the bottom of the model that we are unsure of but is either sandstone or basement, and hence for which a wide range of physical property values is possible between lower and upper bounds.

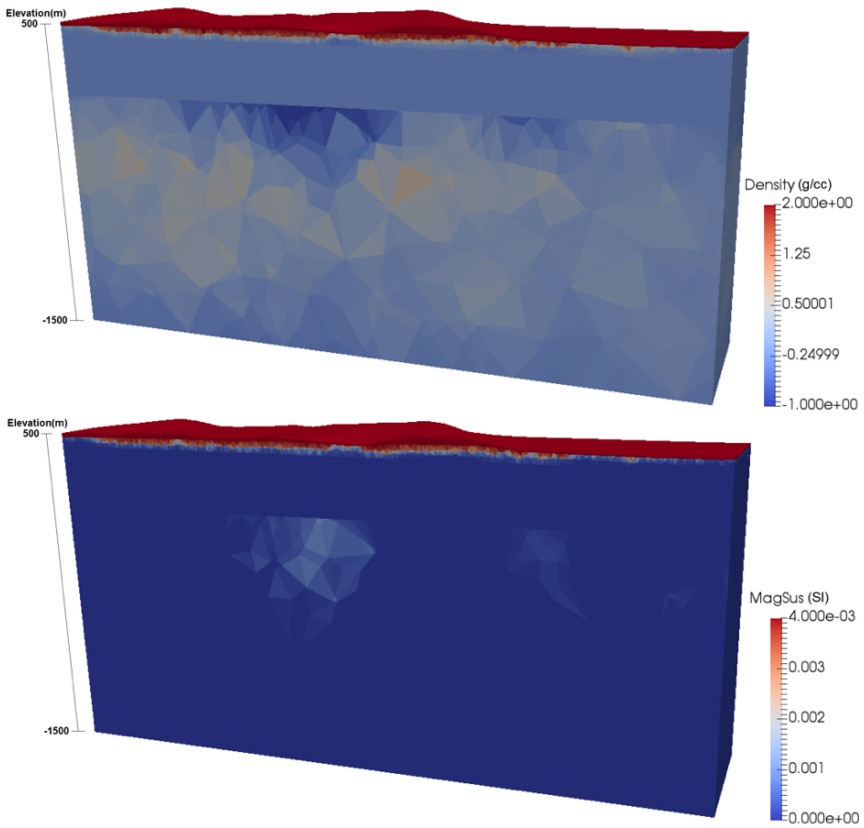

Figure 7.58: Vertical sections of the constrained (2 constraint) joint inversion models of real gravity (top) and magnetic (bottom) data using clustering method (2 clusters) for ρ=10.

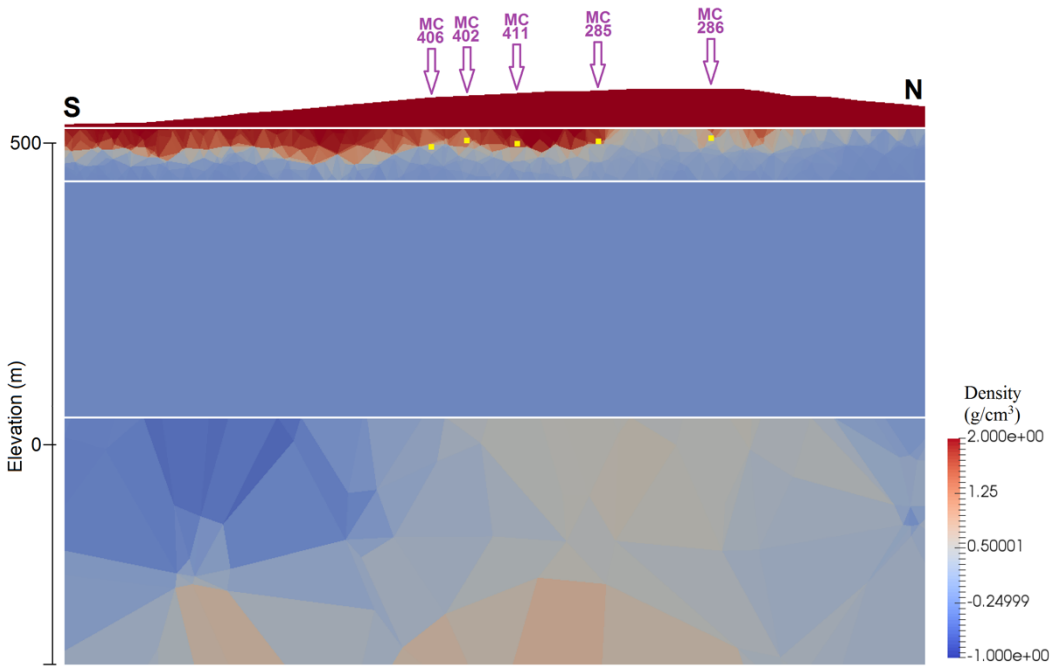

Figure 7.59: Part of the density model produced by the constrained (2 constraints) joint inversion. White lines show where the bounds change. The yellow dots show the true location of the base of the overburden from drill-holes MC-406, MC-402, MC-411, MC-285 and MC-286.

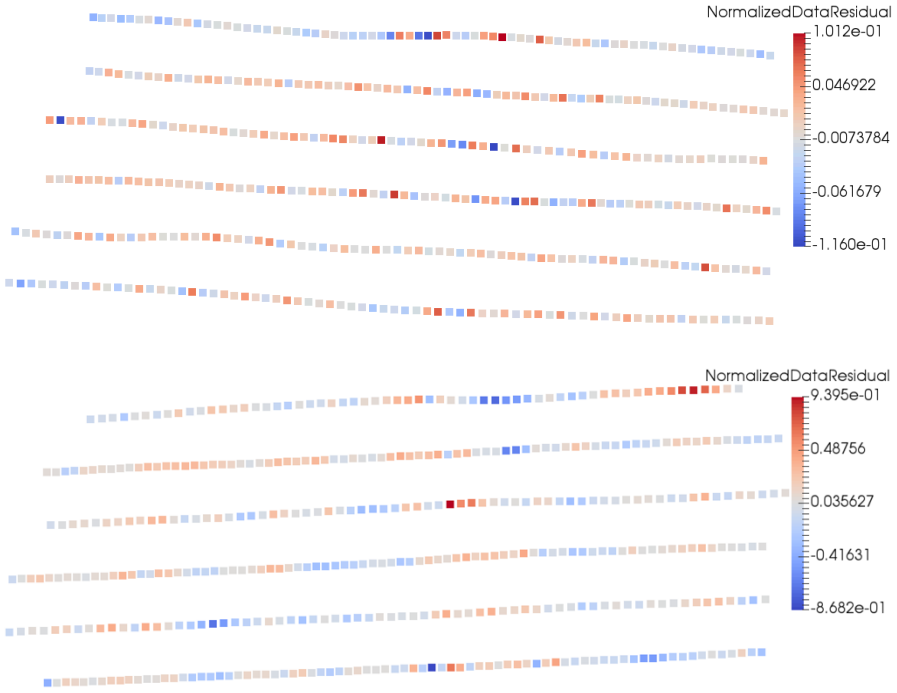

Figure 7.60: Top: normalized data residuals for the gravity model. Bottom: normalized data residuals for the magnetic model (4 constraints; 2 clusters; ρ=10).

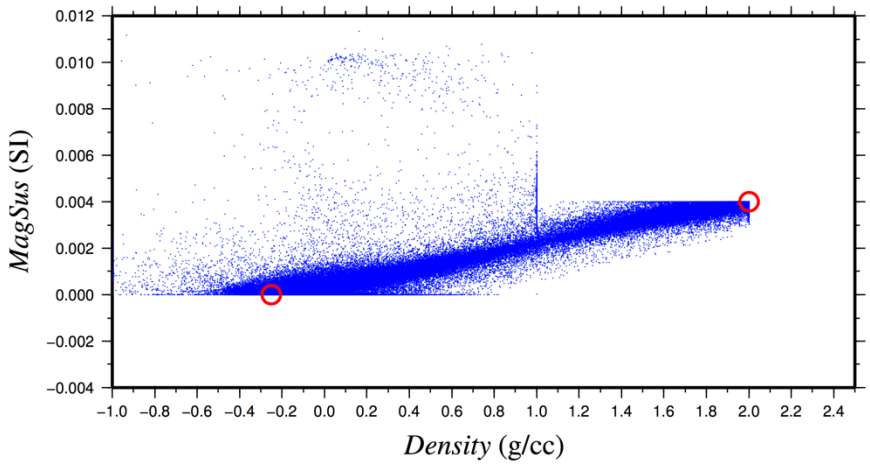

Figure 7.61: Physical properties (magnetic susceptibility versus density) obtained after the constrained (4 constraints) joint inversion of real data. Each blue dot corresponds to a cell in the inversion mesh. Red circles: the two initial clusters defined in joint inversion.

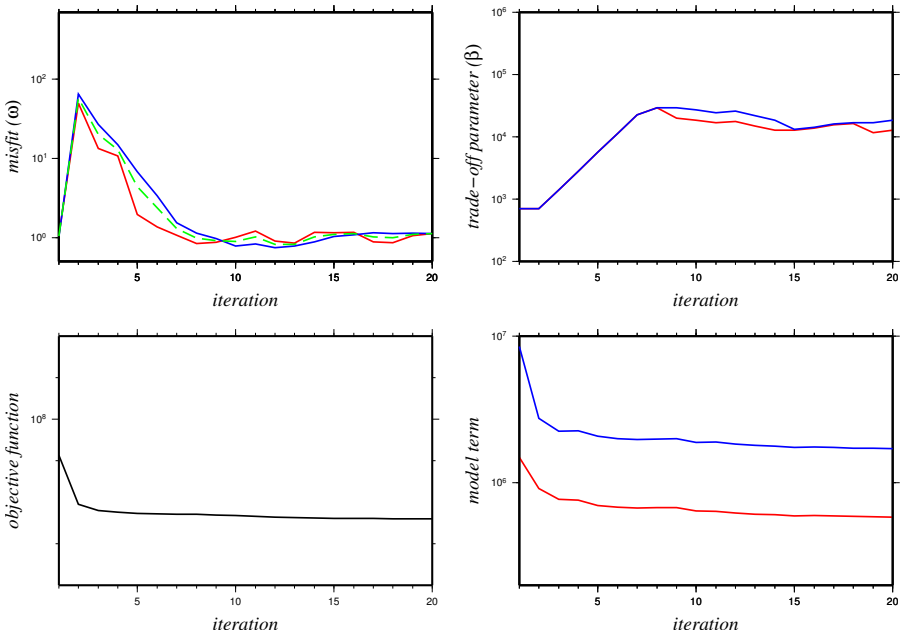

Figure 7.62: Variations of different parts of the objective function such as data misfit (ω; top-left), trade-off parameter (β; top-right), objective function ($\mathbf{\Phi}$; bottom-left) and model term (ϕ_m; bottom-right) at iterations for the joint inversion of real gravity (red) and magnetic (blue) data using the clustering method (2 clusters; 4 constraints) for ρ=10. Green color shows the average "ω".

The run-time for this constrained joint inversion (of ρ=10 with 4 constraints) was 110 hours and 8 minutes for 22 iterations. The mesh had about 533,000 tetrahedral cells which is larger than the previous example as defining additional layers/interfaces in the mesh caused "tetgen" to generate more refined tetrahedral cells in/around those layers/interfaces. Similar to the synthetic models (see Section 7.2.2), for the constrained inversions an initial model is found to improve the results and to reduce the run-time. It can be seen that the result for the overburden section has improved in the constrained joint inversion results. Also, most of the reconstructed parts of the overburden are located below the drumlins (Figure 7.59). This can be due to the presence of magnetic rocks (only) in the drumlins (see Section 2.5.3). This means that where the magnetic rocks are located a better reconstruction happens in the constrained joint inversion. Also, some depression in the base of the overburden in the reconstructed model can be due to poor quality/size of cells. There is no signature of the alteration zone in the inversion results.

7.4 Conclusions

In the Athabasca Basin, the free-air gravity data is dominated by the overburden signature. Although the separation of the regional signature (e.g., the basement signature) can be done by filtering methods or independent inversions, the signature of other features (e.g., signature of alteration zones) is strongly masked by the overburden signature. The magnetic data has the same features as it is a combination of both overburden and the basement signatures (sandstone is non-magnetic).

Independent inversion of gravity and magnetic data can be an appropriate method to

construct some subsurface structures, but not good enough to reconstruct the interfaces in a way similar to the seismic method. There are many methods to improve the inversion results. For this purpose, I initially tested different joint inversions, and then applied a constrained version of joint inversion on both synthetic and real data. In order to synthetize the gravity and magnetic data, a model for McArthur area was made including three main strata overburden, sandstone and basement. The basement is made of different blocks.

Independent inversion of gravity and magnetic data did not show good results. For the joint inversion, both correlation and fuzzy c-mean clustering methods were applied on the synthetic data. For the correlation method, the result had no improvement in comparison with the independent inversions. But, the clustering method showed better results in which the interface between the sandstone and basement was reconstructed but gradational. To improve the results, the constraints (from drill-hole data for real data) were applied on the joint inversions to construct the base of the overburden.

The constrained joint inversion using the clustering method shows the best results as the interface between the layers are sharper. The magnetic data has a significant role in the separation of the layers especially the overburden as the sandstone is a non-magnetic structure which helps in the joint inversions to separate the short wavelengths (i.e., overburden signature) from the long ones (i.e., basement signature). A summary of the research in this chapter is shown in Table 7.1. These processes were also applied on the real airborne gravity and magnetic data as well. Joint inversion of real data reconstructed the sandstone and basement well. Constrained joint inversion was also applied to the real airborne gravity and magnetic data which improved the (base of) overburden part.

However, no alteration zone was evident.

Table 7.1: A summary of the research done in this chapter based on the techniques used for reconstructing the geological structures (overburden, sandstone and basement).

	Overburden	Sandstone	Basement
Independent Inversion (gravity data)	Gradual	Gradual	moderate
Independent Inversion (magnetic data)	Gradual	Gradual	moderate
Constrained Independent Inversion (gravity data)	Gradual	Gradual	Sharp
Joint Inversion (correlation method)	Gradual	Gradual	moderate
Joint Inversion (clustering method)	Gradual	Sharp	Sharp
Constrained Joint Inversion (clustering method)	Sharp	Sharp	Sharp

Chapter 8

3D Modelling and 1D Inversion of Electromagnetic Data (Frequency Domain & Time Domain) of the McArthur River Area

8.1 Introduction

In this chapter, modelling and inversion of frequency domain (FDEM) and time domain (TDEM) electromagnetic methods are applied for overburden stripping and graphite exploration. As mentioned before, the uranium deposits are often found in the vicinity of conductive graphite in the Athabasca Basin. Also, the overburden can have low resistivity in the Athabasca Basin (see Section 2.5 and 3.6.5). However, I consider different resistivities for it in this research. It was initially thought that EM would be the main method to define overburden thickness, but then it was realized that there is not much of a conductivity contrast for the McArthur-Millennium corridor (adapted from CMIC-Footprints project). The work in this chapter may still be applicable to the Athabasca basin, but it is certainly relevant to overburden stripping in many other places.

In this chapter, 1D synthetic modelling and inversion of FDEM and TDEM methods will be initially studied for overburden stripping using codes EM1DFM (Farquharson and Oldenburg, 2000) and EM1DTM (Farquharson and Oldenburg, 2006). For the FDEM and TDEM methods, the helicopter-borne DIGHEM and VTEM systems with depth-detection capabilities for conductive anomalies of 150 m and 600 m are investigated, respectively. The DIGHEM system is a frequency-domain system which means it measures the secondary field in the presence of the primary field when the transmitter is emitting five frequencies in the range 900 Hz to 56000 Hz with a sinusoid waveform (Cain, 2000). The VTEM system is an off-time system which means it measures the voltage induced in the receiver loop in time-channels immediately after the current is switched off in the transmitter (Witherly et al., 2004).

Three different scenarios are considered for the modelling: overburden is more conductive than the sandstone; overburden is less conductive than the sandstone; and when there is no good conductivity contrast between overburden and sandstone. Also, for the FDEM method two cases are considered: overburden has magnetic susceptibility; and overburden has no magnetic susceptibility. Also, in this chapter 3D forward modelling is performed using a code of Ansari and Farquharson (2014). Then, the 1D inversion is done on the synthetic data to reconstruct the true model. Finally, the 1D inversion is applied to the real VTEM data (see Appendix E for the 1D inversion of real DIGHEM data from the CMIC Au project).

8.2 1D synthetic modelling and inversion of FDEM

One dimensional modelling and inversion of FDEM was done using EM1DFM (using the L2-norm; Farquharson and Oldenburg, 2000) for a model with two layers, namely, overburden and sandstone (half-space). Since the depth penetration of FDEM is less than 150 m, only these two layers are considered for the forward modelling. The output of the forward code is the secondary field normalized by the primary field in ppm. A resistivity of 2000 Ohm-m is used for the sandstone. For overburden three scenarios (700 Ohm-m, 1800 Ohm-m and 6000 Ohm-m) are considered. For each of these, three different thicknesses (5 m, 25 m and 100 m) are also considered (see Section 2.5). The scenario for overburden with a resistivity of 1800 Ohm-m is the most representative of the McArthur area in which there is a very weak conductivity contrast between overburden and sandstone. For magnetic susceptibility, two values of 0.005 SI and 0 SI are considered for overburden. A value of 0 SI is considered for sandstone. Thus, input files have different resistivity values as well as magnetic susceptibility values. A non-zero susceptibility for the overburden is reasonable in most parts of the Athabasca Basin (see Section 2.5.3). An elevation of 40 m is considered for the EM sensor height, and 2% noise is added to the data (Cain, 2000). The initial model for all the 1D inversions in this chapter is made of layers with different thicknesses increasing from surface to depth with a factor of 1.134. Also, a constrained inversion is applied to investigate its effect on the results (see Section 4.5), by using a reference model in which I assume the conductivity of the deepest layer in the inversion mesh. So its weight for the reference model is much higher than other layers.

Figures 8.1 to 8.3 show the true models as well as inversion results for the scenarios mentioned above when the magnetic susceptibility of the overburden is 0SI. Also, these figures show the results for the constrained inversions. Figures 8.4 to 8.6 show the results when the magnetic susceptibility of overburden is 0.005 SI. Figures 8.1 to 8.6 involve the results for the three different overburden thicknesses (5 m, 25 m and 100 m) since the variation of the overburden thickness in the McArthur-Millennium corridor is mostly in the range of 5 to 100 m. For the scenario in which the overburden is more conductive than the sandstone, the results are shown in Figures 8.1 and 8.4. Figures 8.2 and 8.5 show the results for the scenario in which there is a very weak conductivity contrast between overburden and sandstone. Also, Figures 8.3 and 8.6 show the results for the scenario in which the overburden is more resistive than the sandstone.

Note that the Fugro DIGHEM system uses five frequencies from 877Hz to 56110Hz with two coil configurations: coaxial (horizontal dipole; 1128Hz and 5087Hz) coil pairs and coplanar (vertical dipole; 877Hz, 7166Hz and 56110Hz) coil pairs. Coil separation (between receiver and transmitter) is 8 m except for 55840Hz which is 6.3 m. Receiver and transmitter coils have a diameter of about half a metre. The system measures both in-phase and quadrature parts (Fugro Airborne Surveys Corp., 2006). The skin depth for DIGHEM, calculated using Equation 4.38, for an overburden with a conductivity of 500 ohm-m from 900-50,000 Hz is approximately between 50 m and 350 m. For a resistive case (6000 ohm-m), the skin depth is approximately between 150 m and 1200 m. These skin depths greatly exceed the overburden thickness, and this situation can affect the sensitivity of the responses and the manner in which different frequencies provide independent information

on the overburden. But note that these values are calculated for a plane-wave case while dipolar skin depths are found to be much smaller than their plane-wave counterparts (Beamish, 2004). The real depth of exploration of a DIGHEM system is not more than 150 m.

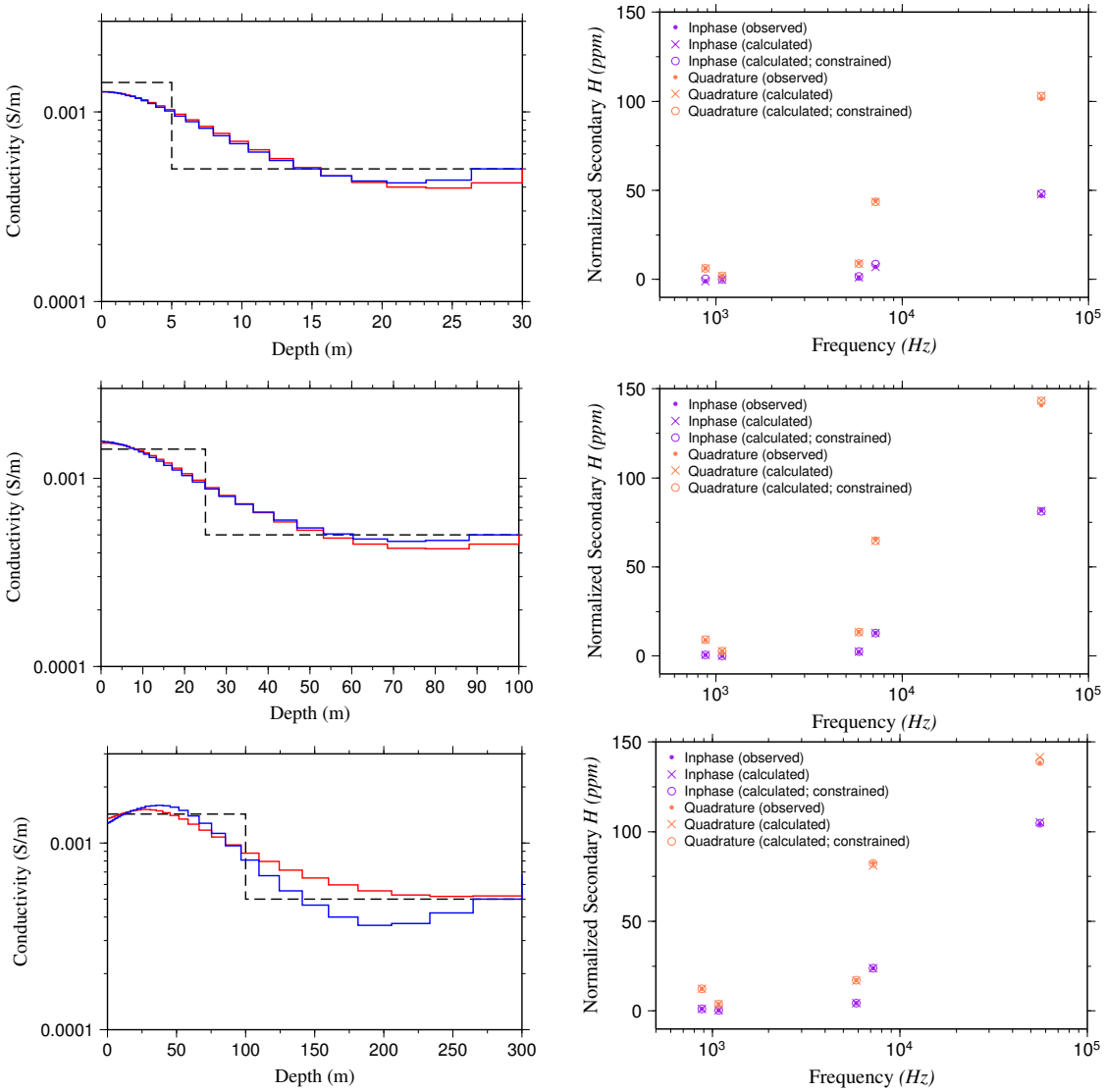

Figure 8.1: Left: true model (black dashed line), the result of inverting the synthetic data set from the true model (red line), and the constrained inversion result (blue line) for the model with the more conductive, non-susceptible overburden. Right: observed and calculated data. Overburden with different thicknesses 5 m (top), 25 m (middle) and 100 m (bottom) are investigated.

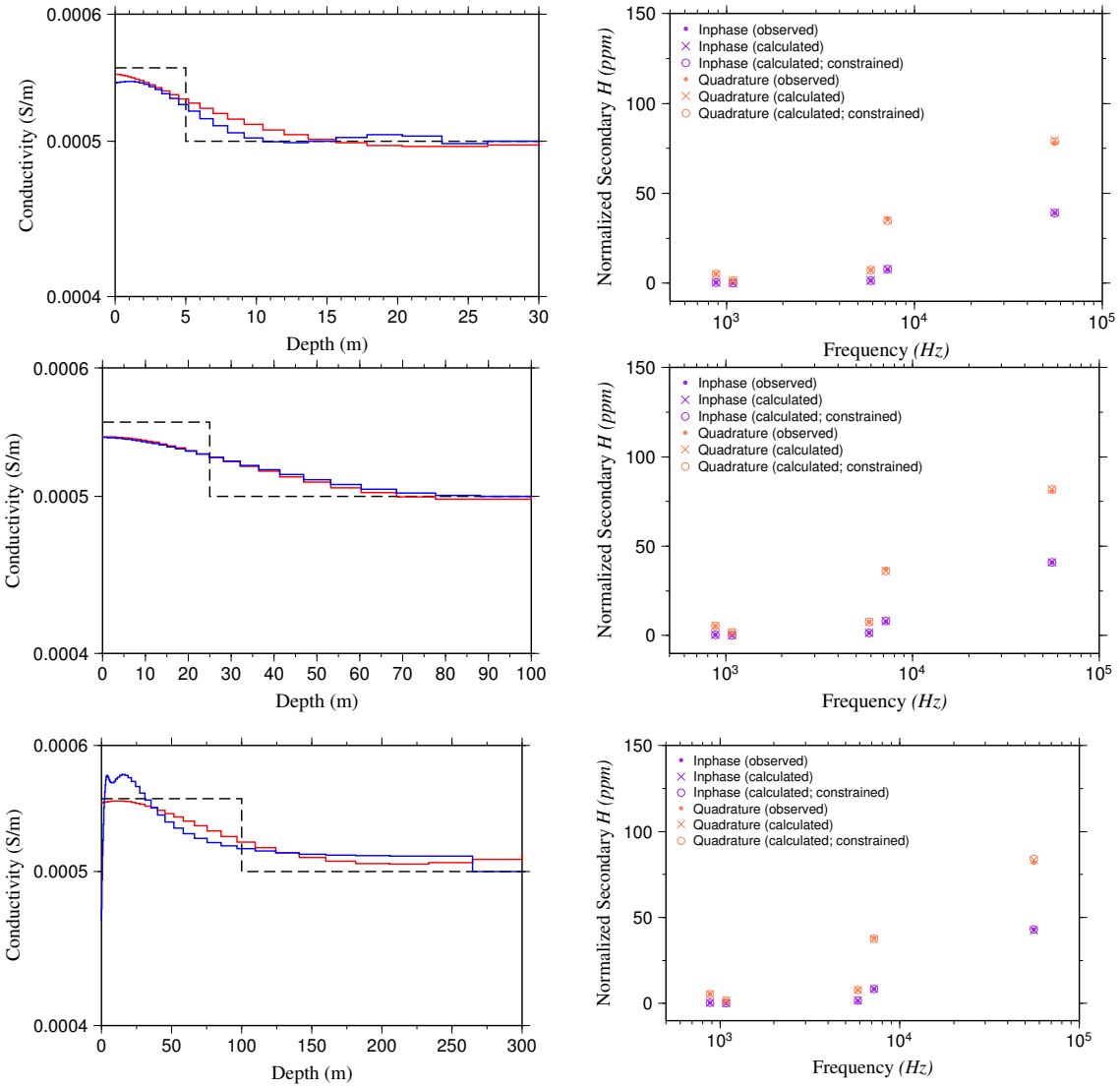

Figure 8.2: Left: true model (black dashed line), the result of inverting the synthetic data set from the true model (red line), and the constrained inversion result (blue line) for the model with the low conductivity contrast and non-susceptible overburden. Right: observed and calculated data. Overburden with different thicknesses 5 m (top), 25 m (middle) and 100 m (bottom) is investigated.

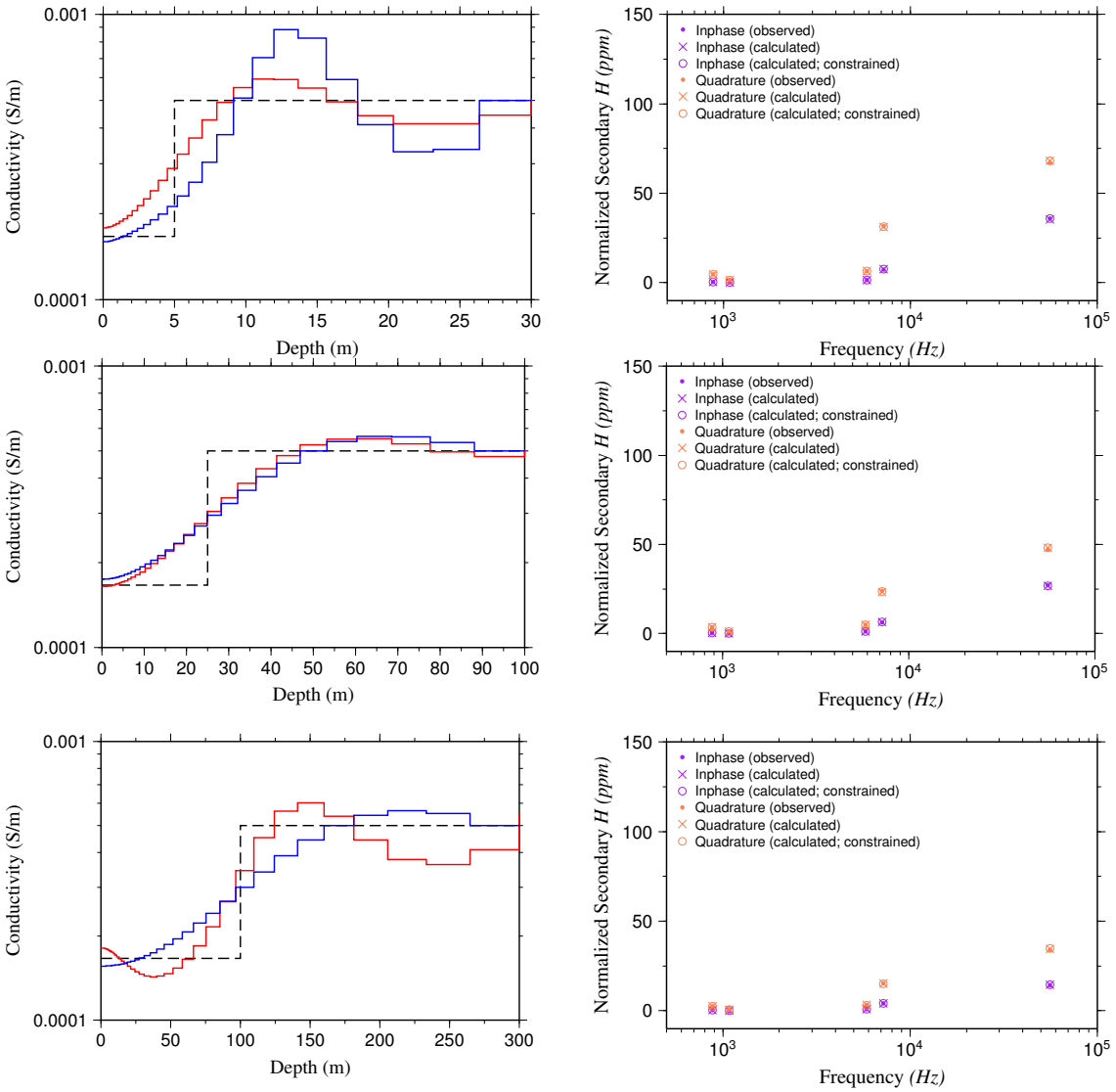

Figure 8.3: Left: true model (black dashed line), the result of inverting the synthetic data set from the true model (red line), and the constrained inversion result (blue line) for the model with the more resistive, non-susceptible overburden. Right: observed and calculated data. Overburden with different thicknesses 5 m (top), 25 m (middle) and 100 m (bottom) is investigated.

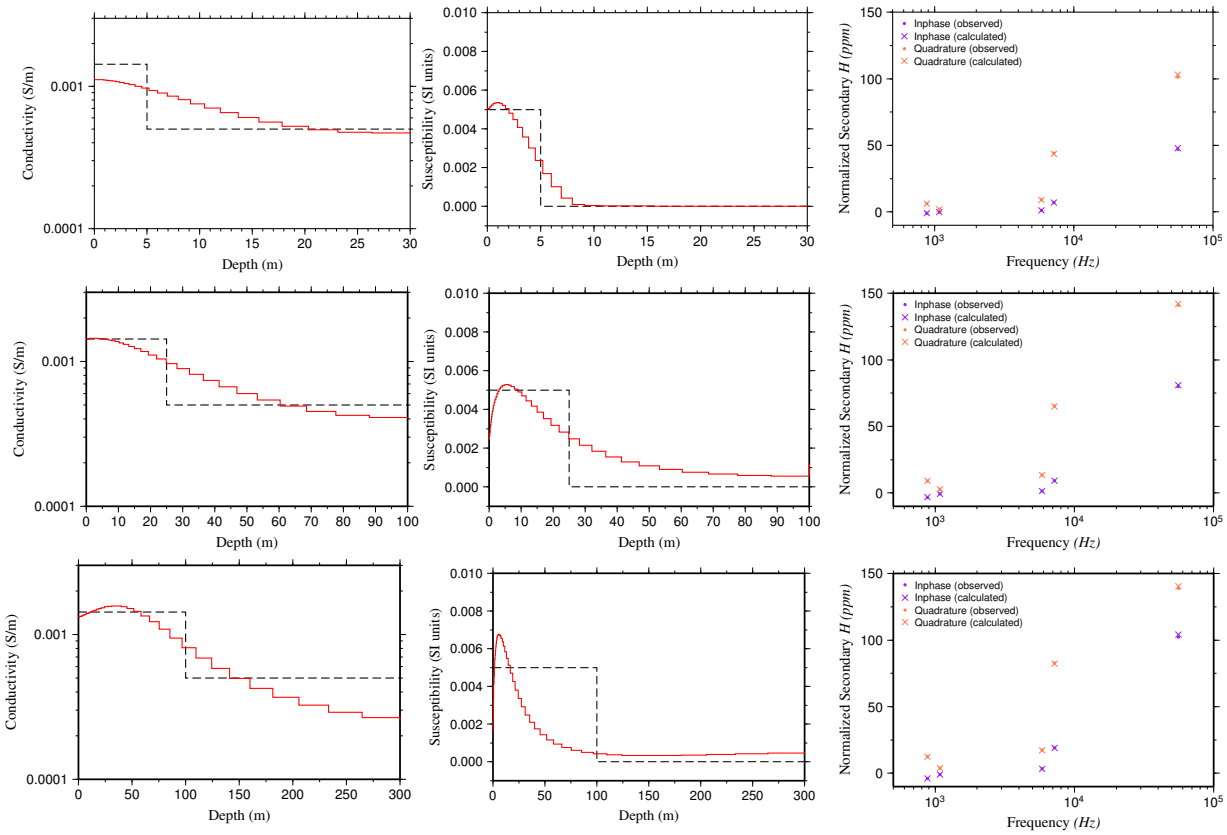

Figure 8.4: Left and middle: True model (black dashed line) and the result of inverting the synthetic data set from the true model (red line) for conductivity and magnetic models. Right: Observed and calculated data. Overburden with different thicknesses 5 m (top), 25 m (middle) and 100 m (bottom) is investigated.

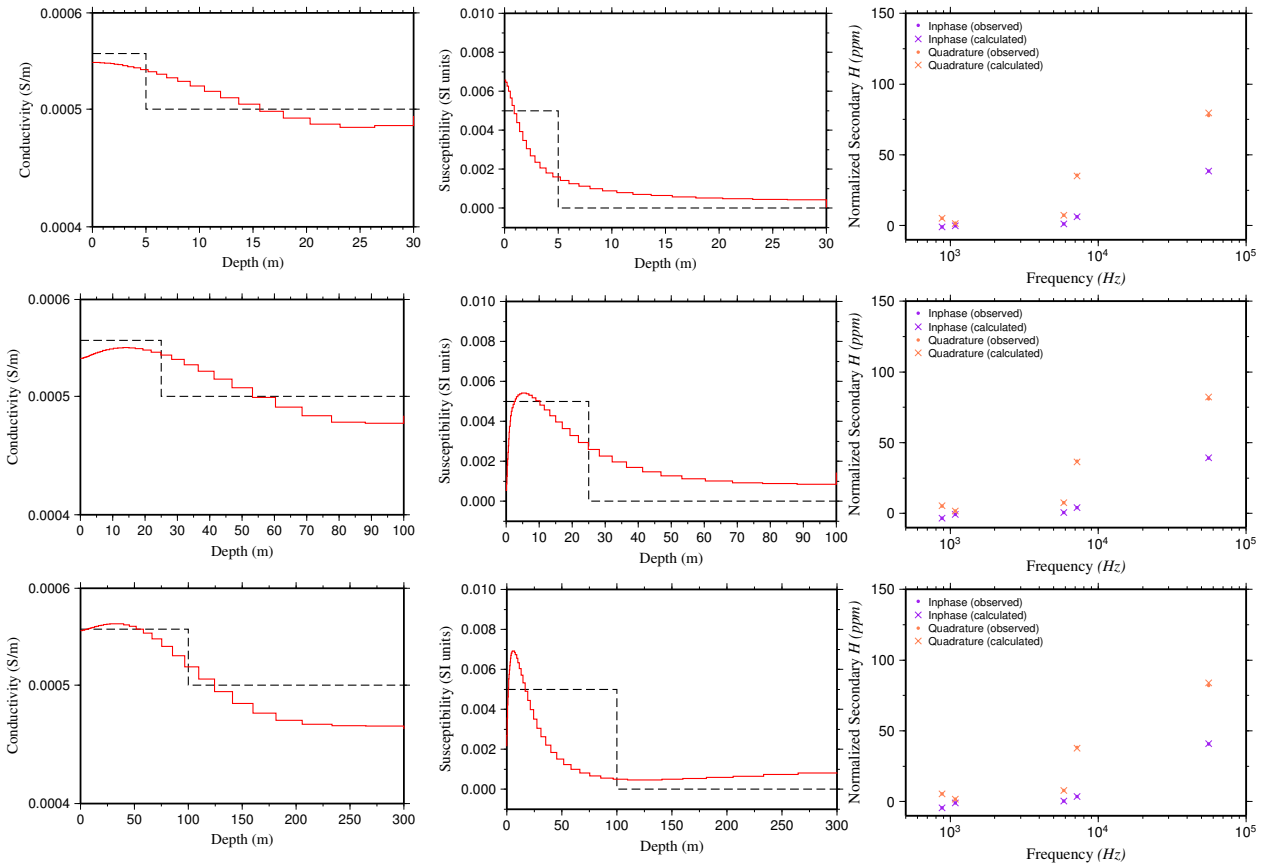

Figure 8.5: Left and middle: True model (black dashed line) and the result of inverting the synthetic data set from the true model (red line) for conductivity and magnetic models. Right: Observed and calculated data. Overburden with different thicknesses 5 m (top), 25 m (middle) and 100 m (bottom) is investigated.

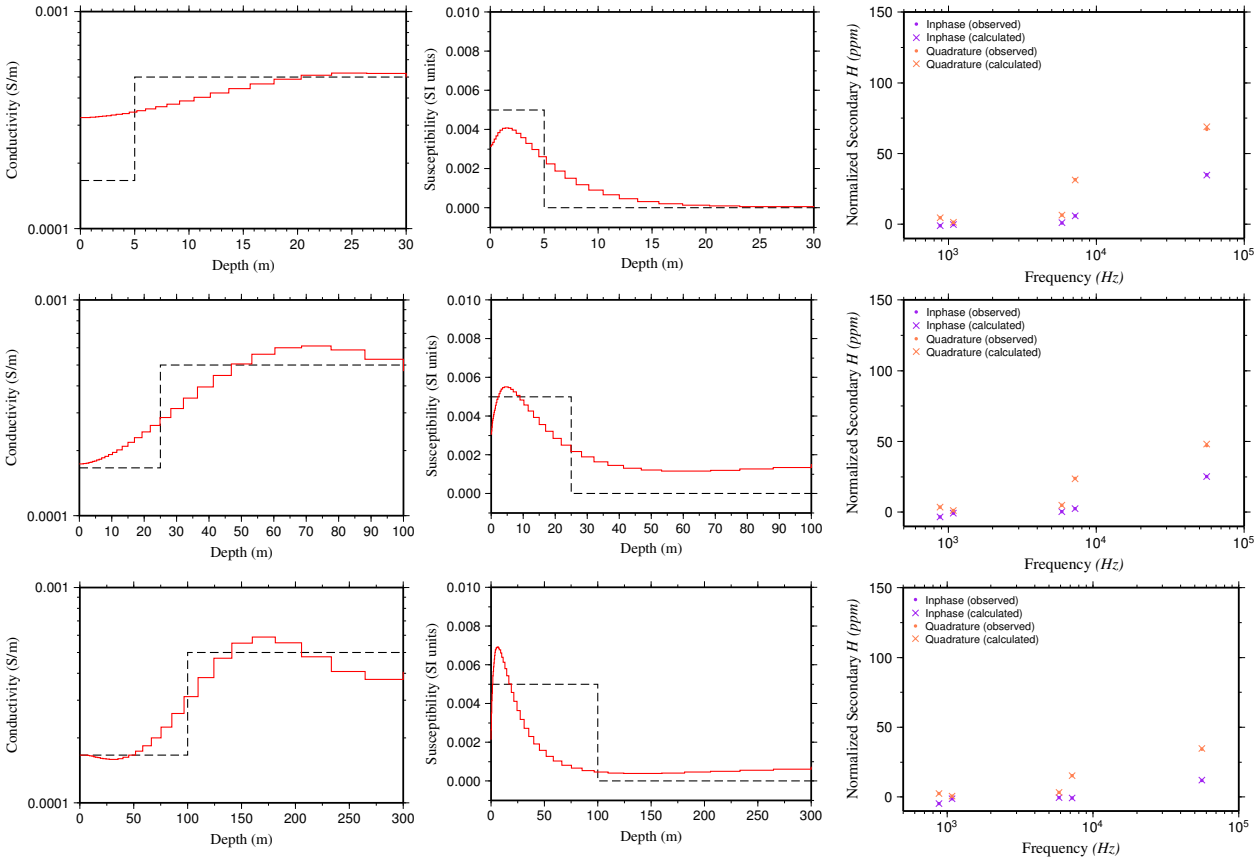

Figure 8.6: Left and middle: True model (black dashed line) and the result of inverting the synthetic data set from the true model (red line) for conductivity and magnetic models. Right: Observed and calculated data. Overburden with different thicknesses 5 m (top), 25 m (middle) and 100 m (bottom) is investigated.

For the constrained inversions, it was expected that the boundary between the layers would be reconstructed better and sharper. However, the results show that in most models it was not helpful. Also, accounting for the presence of the magnetic susceptibility in the overburden rocks does not improve the results. But, in total it can be said that the synthetic modelling and inversion results show that DIGHEM can be used for overburden stripping if there is a conductivity contrast between overburden and sandstones. Also, the variation of the various terms of the objective function for an inversion model are shown in Figure 8.7; all other inversions behave in a similar manner.

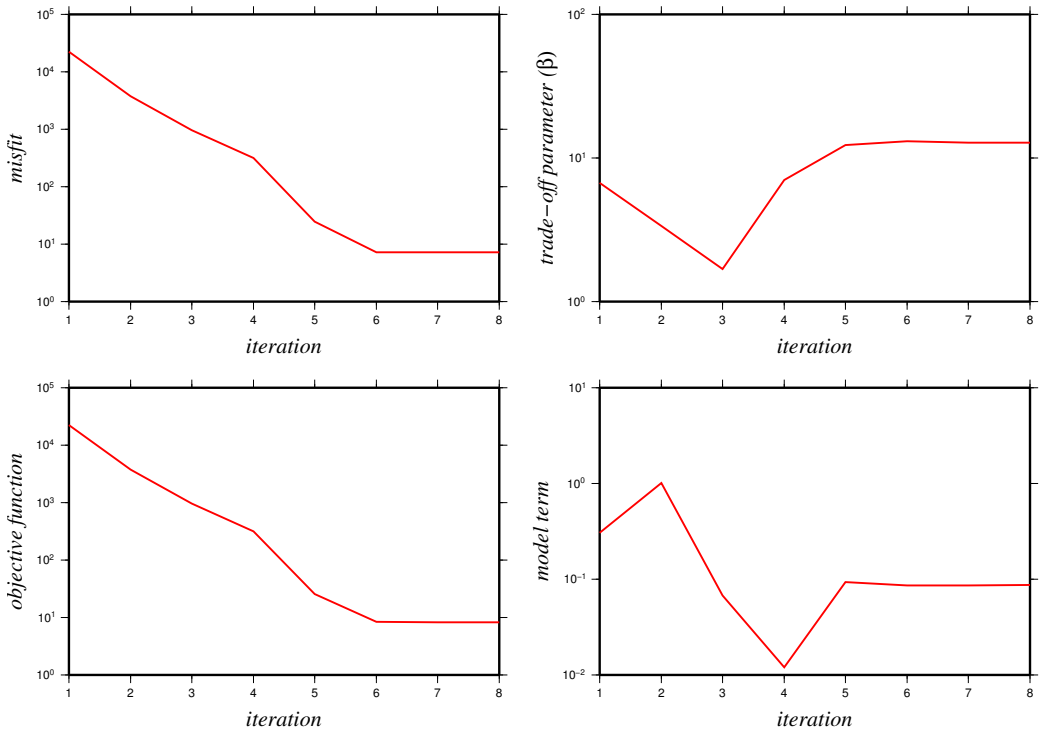

Figure 8.7: Variations of different parts of the objective function such as data misfit (ϕ_d; top-left), trade-off parameter (β; top-right), objective function (Φ; bottom-left) and model term (ϕ_m; bottom-right) at iterations for the inversion of synthetic DIGHEM data of the model in which the overburden thickness and resistivity are 5 m and 700 Ohm-m, respectively.

8.3 1D synthetic modelling and inversion of TDEM

1D modelling and inversion of TDEM is done using the EM1DTM code (Farquharson and Oldenburg, 2006) for two main scenarios: two layers (overburden and sandstone [half-space]; Figures 8.9 to 8.11); and four layers (overburden, sandstone, graphitic zone and basement [half-space]; Figures 8.12 to 8.14). These four layers are considered in the modelling as the uranium deposit in the Athabasca Basin is mostly located close to the graphitic fault and the unconformity between sandstone and basement (see Chapter 2). Also, the investigation depth for TDEM is deeper than FDEM (see Section 3.5). The EM1DTM code is able to invert the data using both L1-norm and L2-norm.

In this modelling, the sandstone, graphitic zone and basement have resistivities of 2000 Ohm-m, 50 Ohm-m and 20000 Ohm-m, respectively. But, for the overburden three different resistivities (700 Ohm-m, 1800 Ohm-m and 6000 Ohm-m) were considered. For each of them, three different thicknesses (5 m, 25 m and 100 m) were considered as well. In this modelling the graphitic zone has a thickness of 50 m, and 2% noise is added to the data (adapted from CMIC-Footprints reports; McCracken et al., 1984). Note that real graphitic structures/faults are not horizontal (see Section 2.3), however a horizontal graphitic layer is assumed here as that is all the code can handle. I just want to see if the supposedly deeper-seeing VTEM data can indeed see graphitic conductors at depth or not. An elevation of 30 m is considered for the height of the coils. The current waveform can have different shapes such as half-sine, square, triangular and trapezoidal shape. In this research, the current waveform for the 1D VTEM modelling has a shape of a trapezoid

similar to the current waveform of real VTEM data (Figure 8.8). The width of the transmitting time is 5.74 ms, and the earliest time datum is 21 μs after turn off.

Figures 8.9 to 8.11 show the true models as well as inversion (L1- and L2- norms) results for the three different resistivities of the overburden when the true model has two layers. Similar to these figures, Figures 8.12 to 8.14 show the results when the true model has four layers. Each figure involves the results for the cases in which the overburden has three different thicknesses.

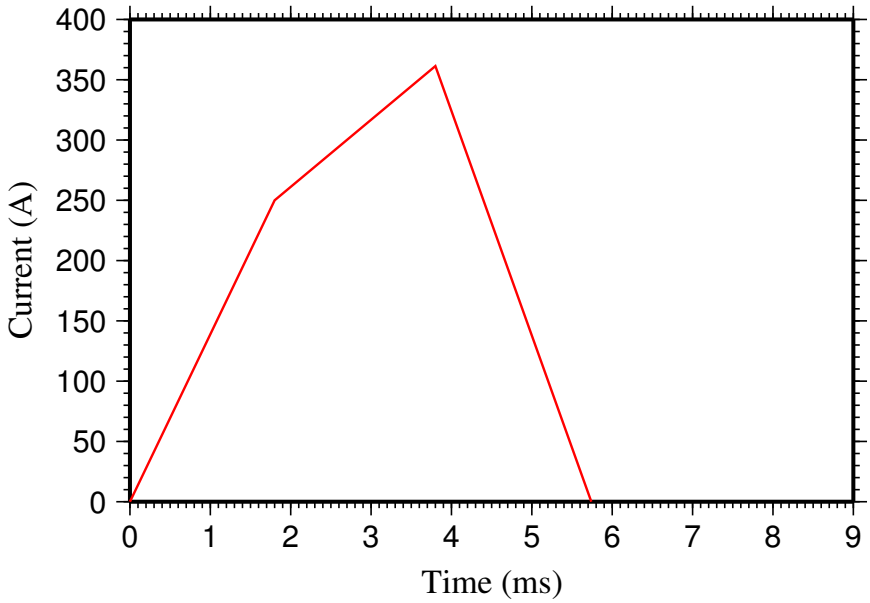

Figure 8.8: Transmitter current waveform for synthetic VTEM modelling.

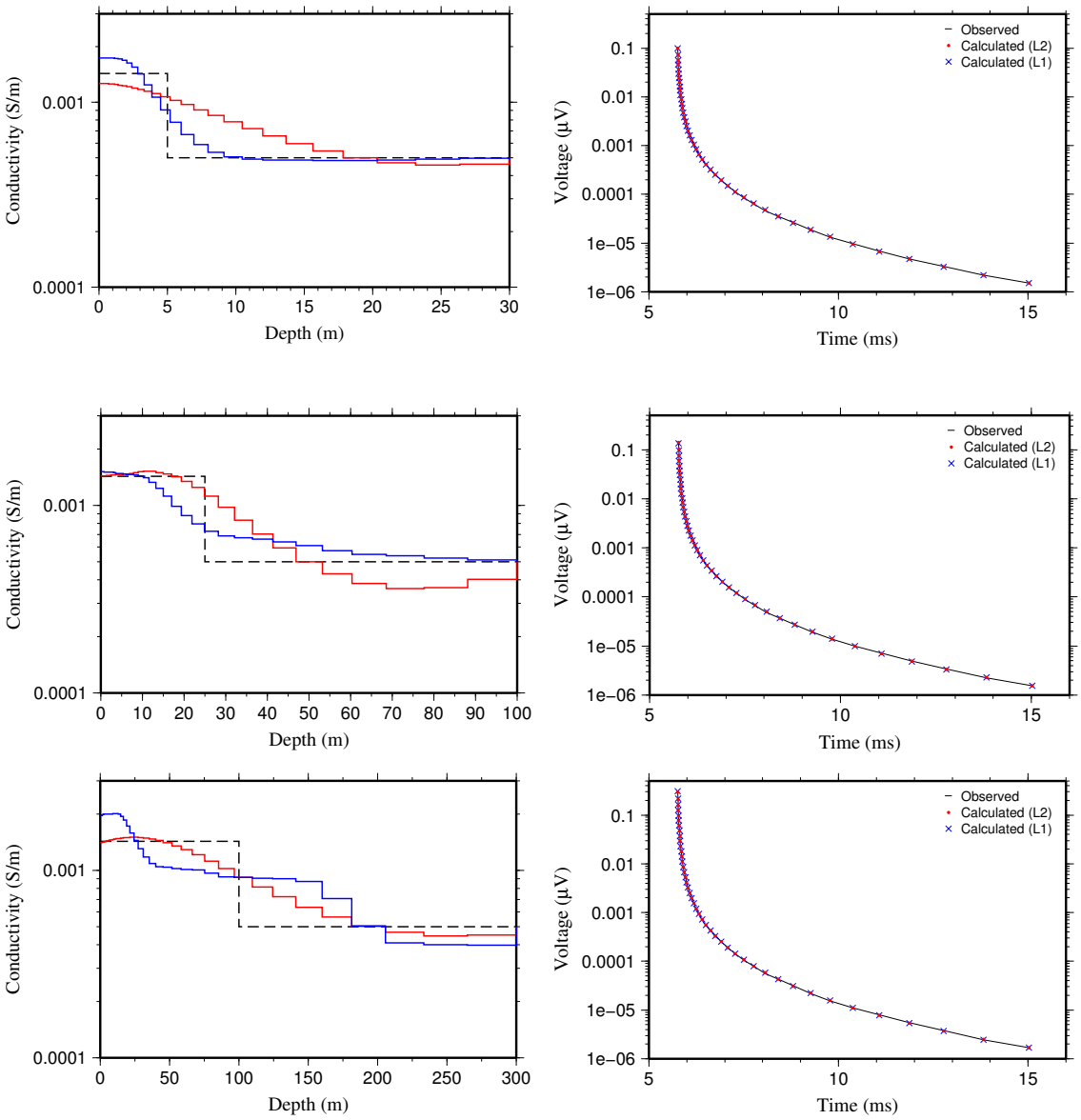

Figure 8.9: Left: true model (black dashed line), and inversion models for L2-norm (red line) and L1-norm (blue line) for the conductive overburden. Right: observed and calculated data. Different thicknesses of overburden 5m (top), 25m (middle) and 100m (bottom) are investigated.

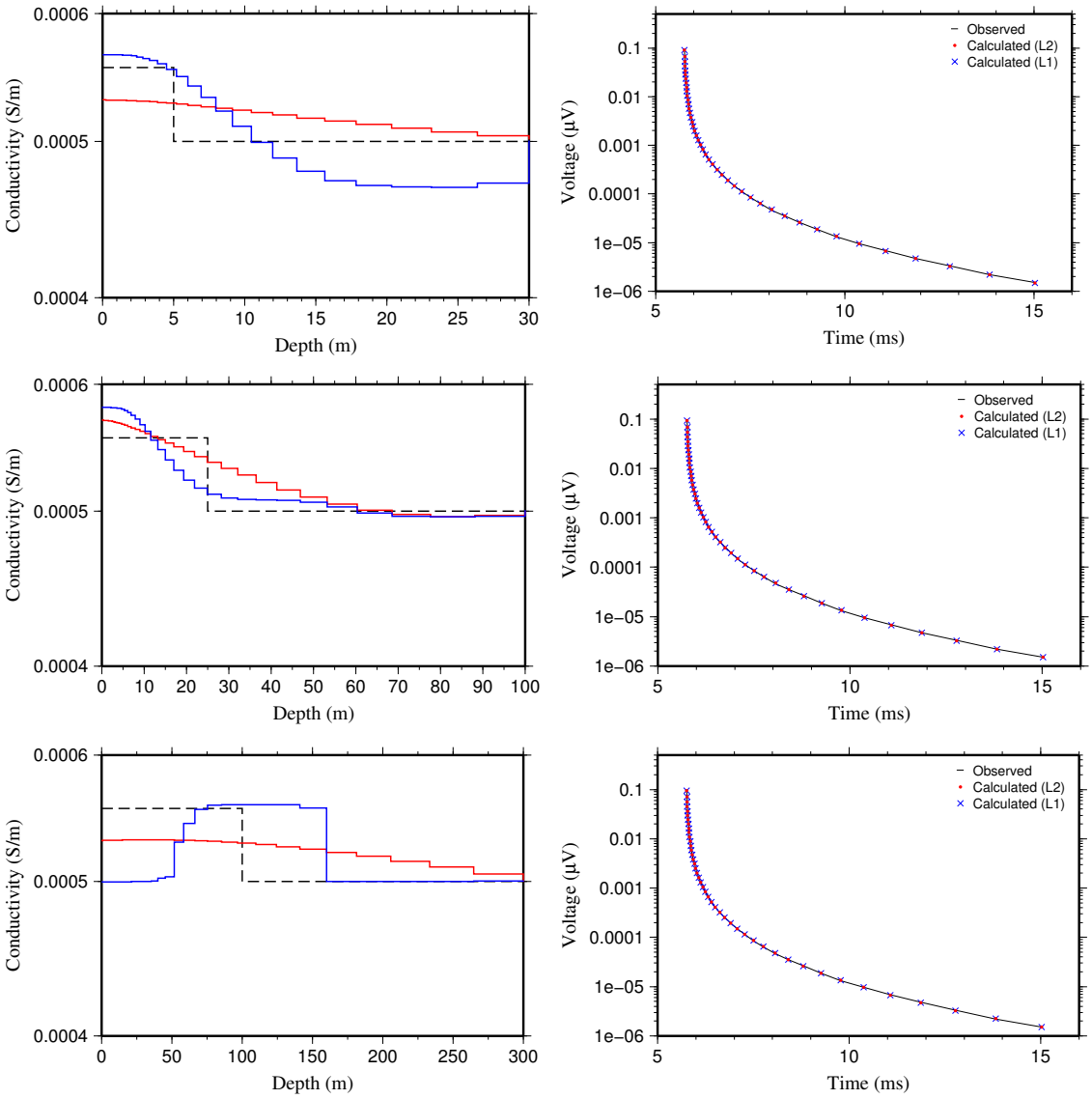

Figure 8.10: Left: true model (black dashed line), and inversion models for L2-norm (red line) and L1-norm (blue line) for a low contrast overburden. Right: observed and calculated data. Different thicknesses of overburden 5m (top), 25m (middle) and 100m (bottom) are investigated.

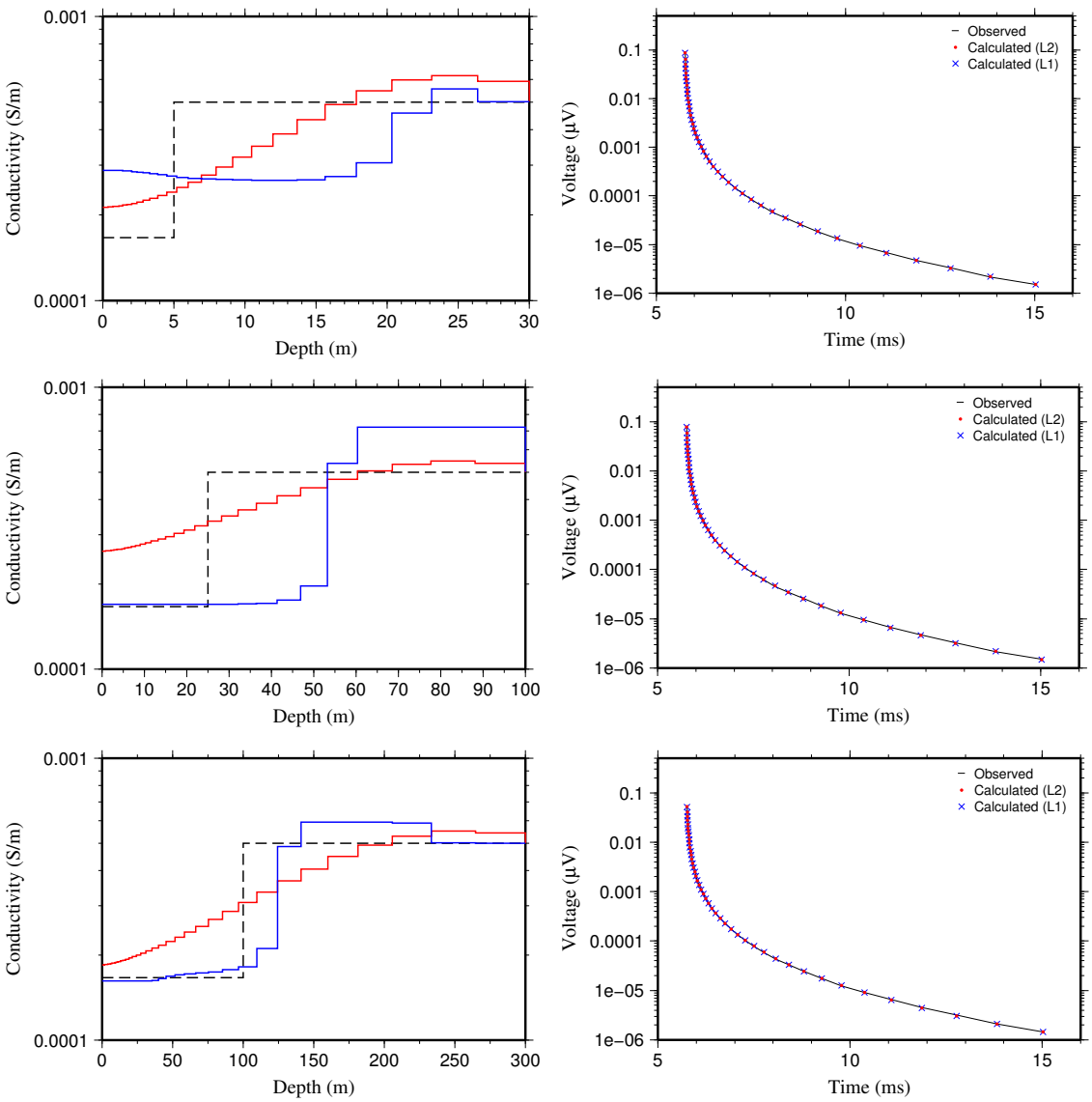

Figure 8.11: Left: true model (black dashed line), and inversion models for L2-norm (red line) and L1-norm (blue line) for resistive overburden. Right: observed and calculated data. Different thicknesses of overburden 5m (top), 25m (middle) and 100m (bottom) are investigated.

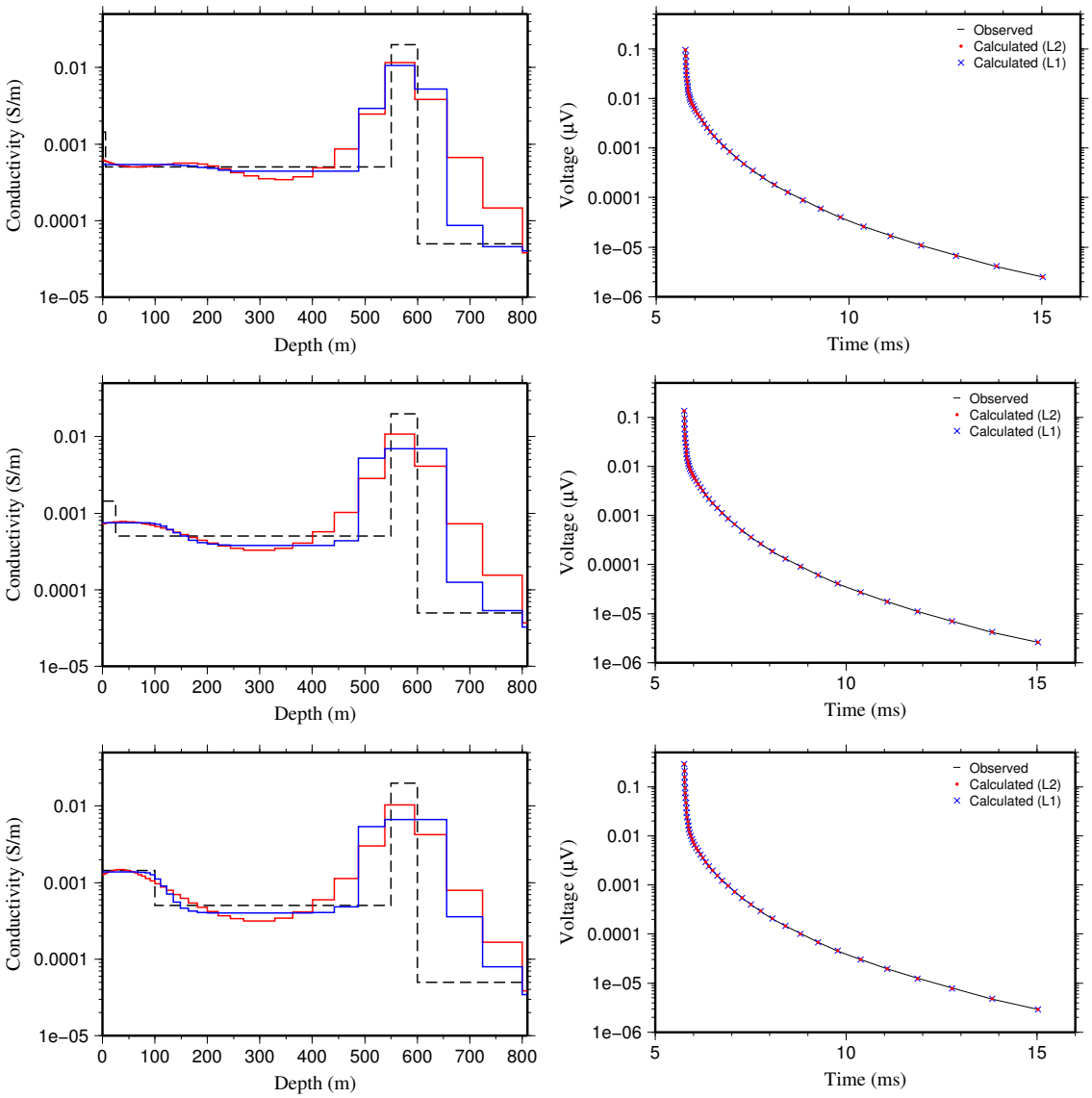

Figure 8.12: Left: true model (black dashed line), and inversion models for L2-norm (red line) and L1-norm (blue line) for the four-layer models with conductive overburden. Right: observed and calculated data. Different thicknesses of overburden 5m (top), 25m (middle) and 100m (bottom) are investigated.

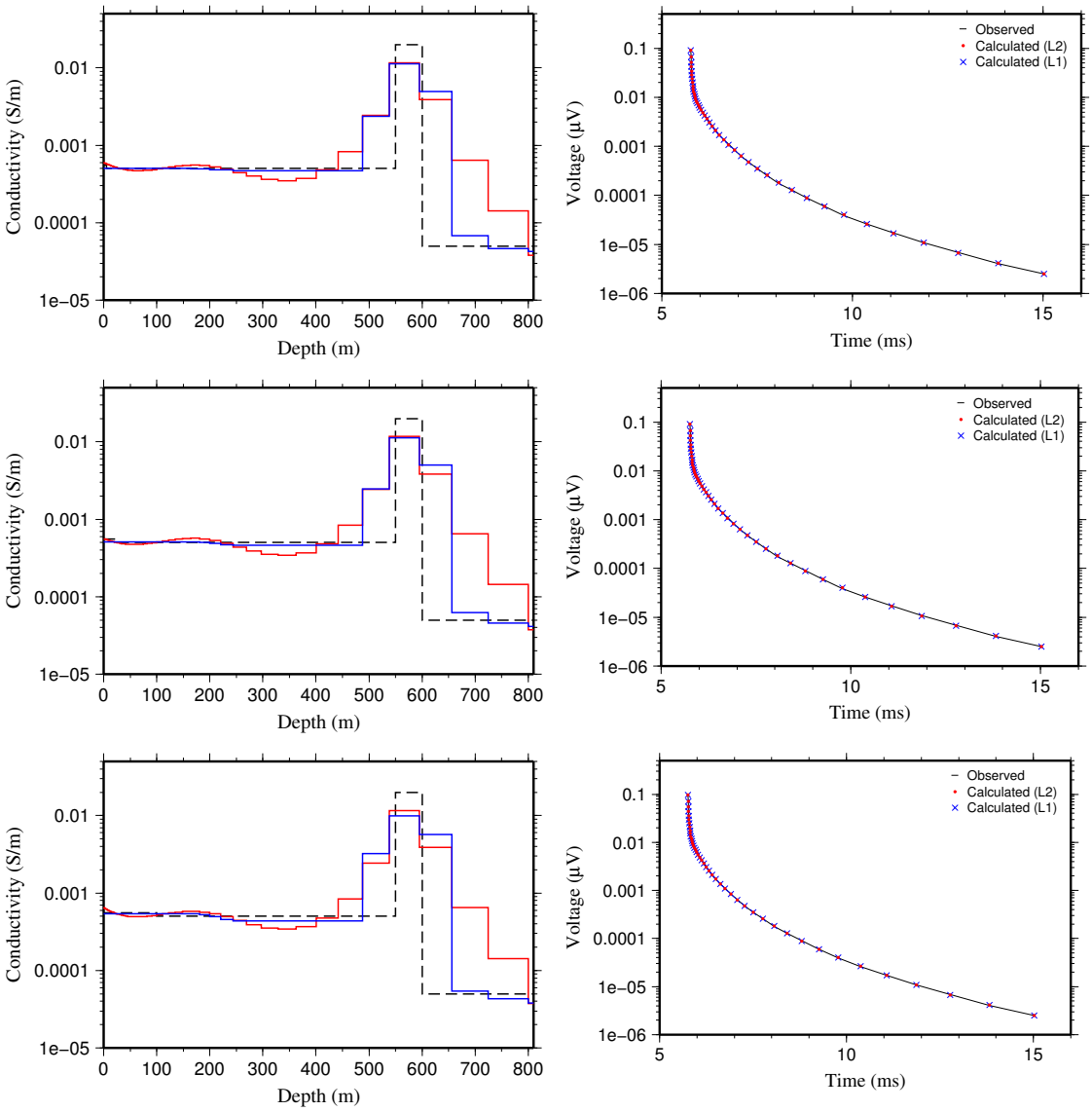

Figure 8.13: Left: true model (black dashed line), and inversion models for L2-norm (red line) and L1-norm (blue line) for the four-layer models with minimal overburden contrast. Right: observed and calculated data. Different thicknesses of overburden 5m (top), 25m (middle) and 100m (bottom) are investigated.

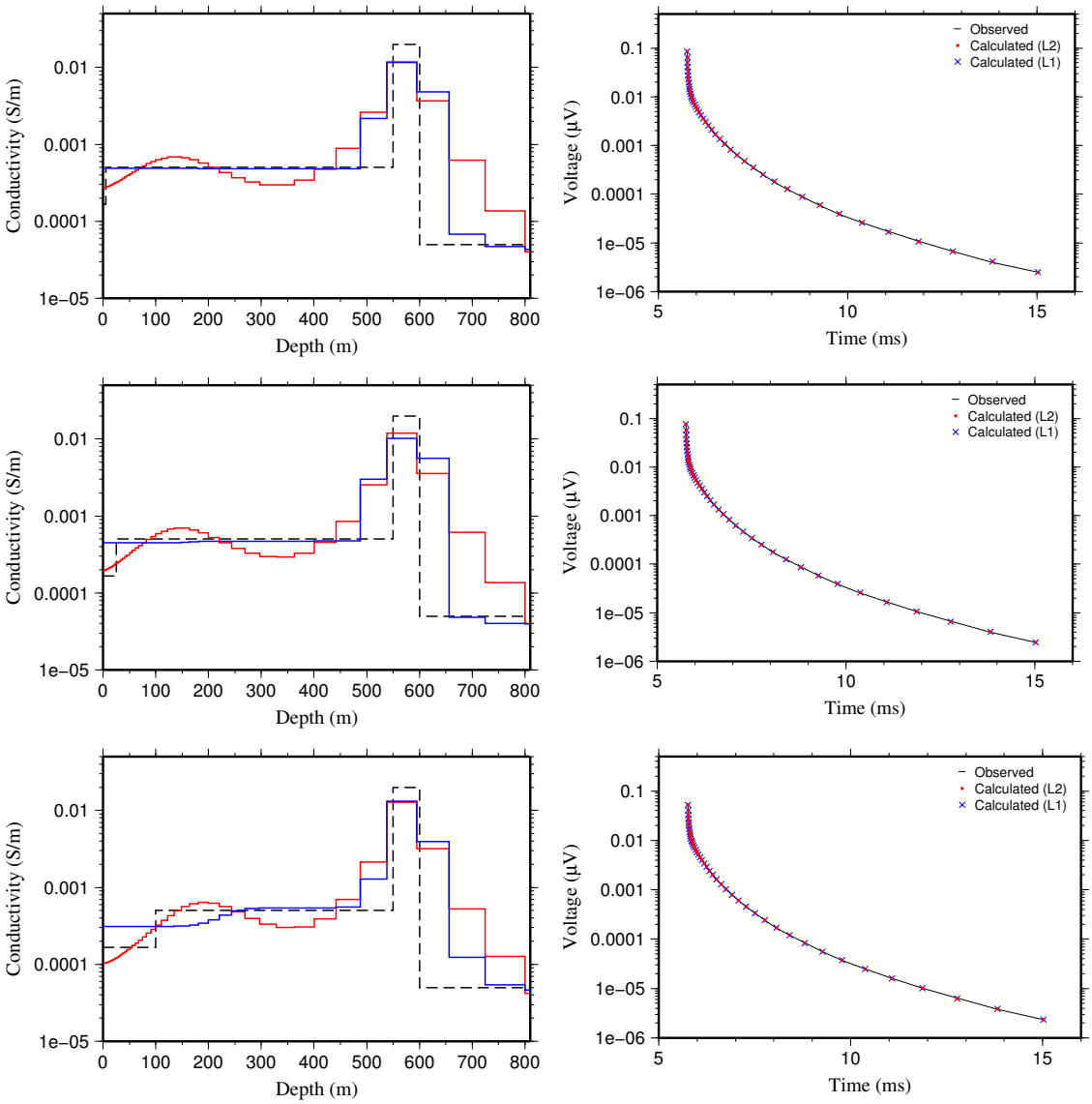

Figure 8.14: Left: true model (black dashed line), and inversion models for L2-norm (red line) and L1-norm (blue line) for the four-layer models with resistive overburden. Right: observed and calculated data. Different thicknesses of overburden 5m (top), 25m (middle) and 100m (bottom) are investigated.

It can be seen that the conductive graphitic zone is reconstructed well in the VTEM inversion results. As expected, by increasing the electrical resistivity contrast between layers the inversion results improve. Also, it can be seen that by increasing the conductivity of the layers which are close to the surface, the values of early-time responses are increasing. And, by increasing the conductivity of the layers at depth, the values of late-time responses are increasing. The variation of the various terms of the objective function for one of the inversion models are shown as a function of iteration in Figure 8.15; all other inversions behave in a similar manner.

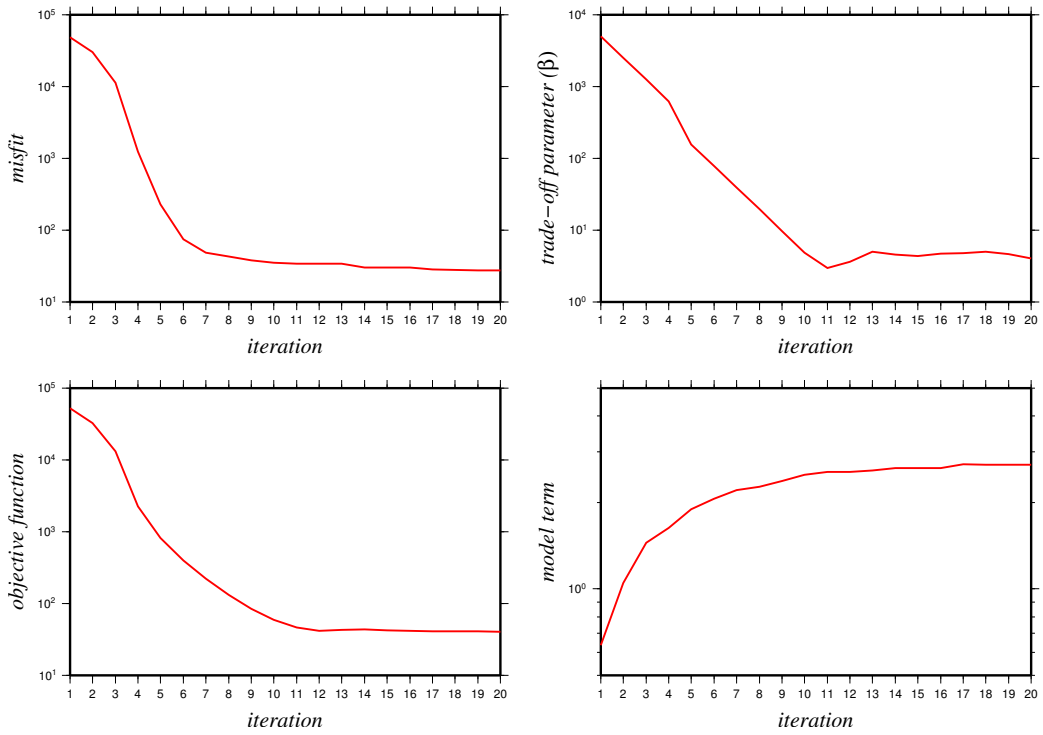

Figure 8.15: Variations of different parts of the objective function such as data misfit (ϕ_d; top-left), trade-off parameter (β; top-right), objective function (Φ; bottom-left) and model term (ϕ_m; bottom-right) at iterations for the inversion (L2-norm) of synthetic VTEM data of the (four layers) model in which the overburden thickness and resistivity are 5 m and 700 Ohm-m, respectively.

8.4 3D synthetic modelling and 1D inversion

For 3D modelling, a model (Figures 8.16 and 8.17) was made based on the most recent model in the CMIC-Footprint project (adapted from CMIC-Footprints project; generated by Kevin Ansdell, Ken Wasyliuk and Gerard Zaluski; entered into Gocad by Marc Vallée). The main difference between this model and models used previously in this thesis is in the basement structure in which the geological surfaces were built from updated geological sections and maps. It can be seen that the main geological structures in this model are overburden, sandstone, alteration zone, pelite, psammite, quartzite, granitoid gneiss and graphitic fault. The graphitic fault is the most conductive structure in this model.

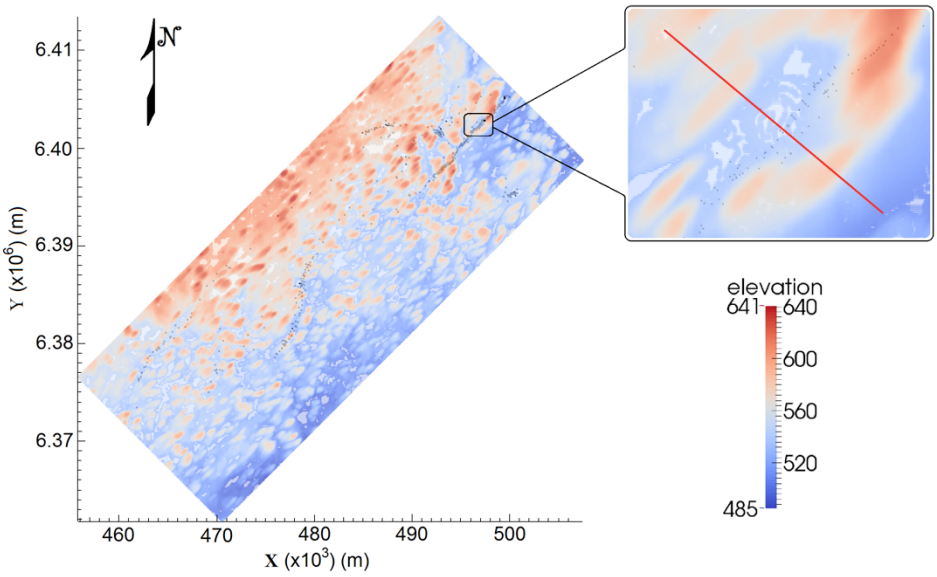

Figure 8.16: Topography of McArthur-Millennium corridor. Inset shows location of survey line (red line) considered for 3D EM modelling.

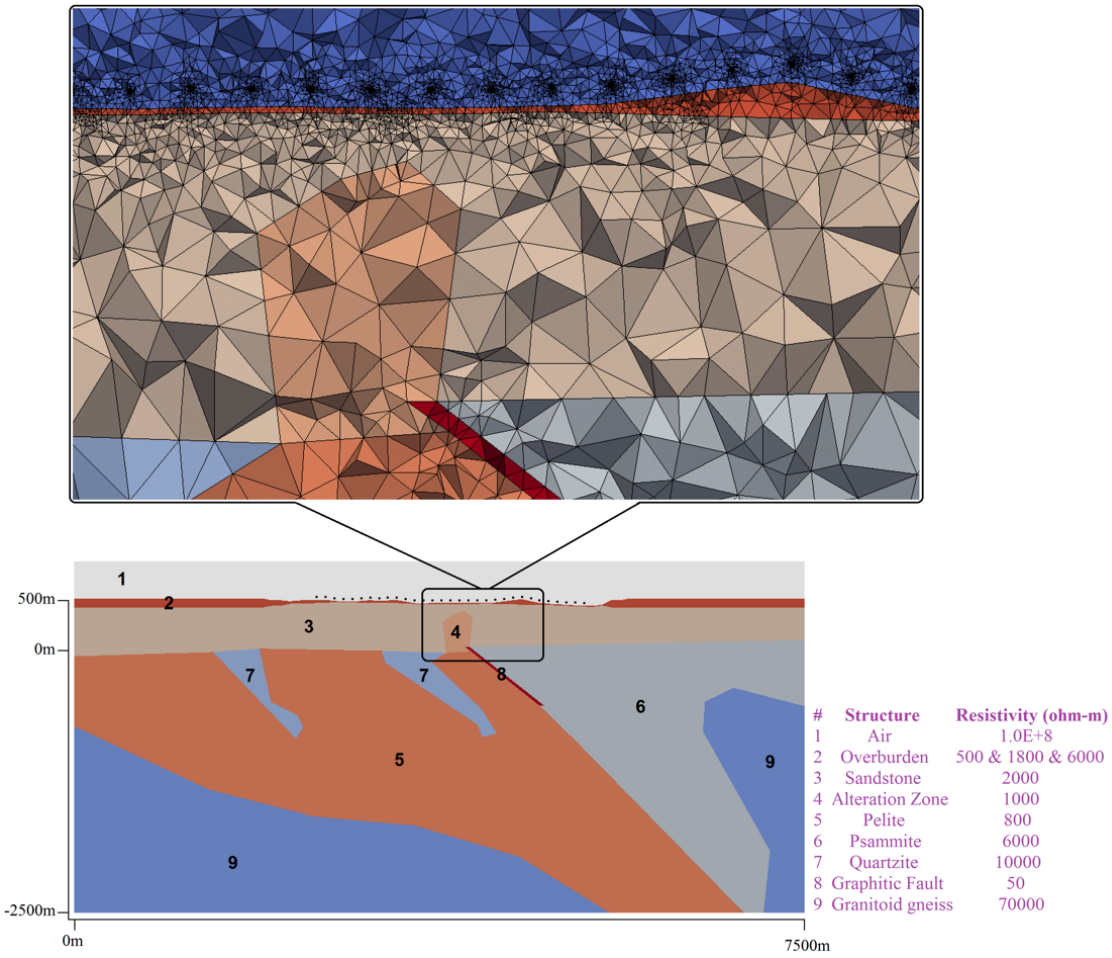

Figure 8.17: Constructed 3D geological structure under the profile (bottom), and tetrahedral mesh (top).

DIGHEM data for three different scenarios, in which overburden has three different resistivities 500, 1800 and 6000 Ohm-m, are calculated using CSEM3DFWD code (Ansari and Farquharson, 2014; see Section 4.4) along a profile with a station spacing of 100 m. Also, an elevation of 30 m is considered as the EM sensor height. A narrow zone with a thickness of around 40 m is considered as a graphitic fault with a resistivity of 50 Ohm-m (adapted from CMIC-Footprints reports).

One dimentional inversion was applied to the 3D synthetic data. For the inversion of data, a 5% noise is considered as uncertainty so this amount of noise was added into the data before inversion. Figures 8.18 to 8.20 show the inversion results for the above-mentioned overburden conductivity scenarios. DIGHEM data (secondary field normalized by the primary field in ppm) include both in-phase and quadrature parts for five frequencies in the range 880 Hz to 55840 Hz. The fit between the observed and calculated data is good. The inversion results show that the overburden base is reconstructed well when there is a good contrast between overburden and sandstone. Also, the conductive alteration zone is not reconstructed as it is located at a depth to which the EM fields (at the frequencies considered) are no longer sensitive. These inversion results show that DIGHEM can be used for overburden conductivity estimation, but not thickness estimation when there is not a strong conductivity contrast.

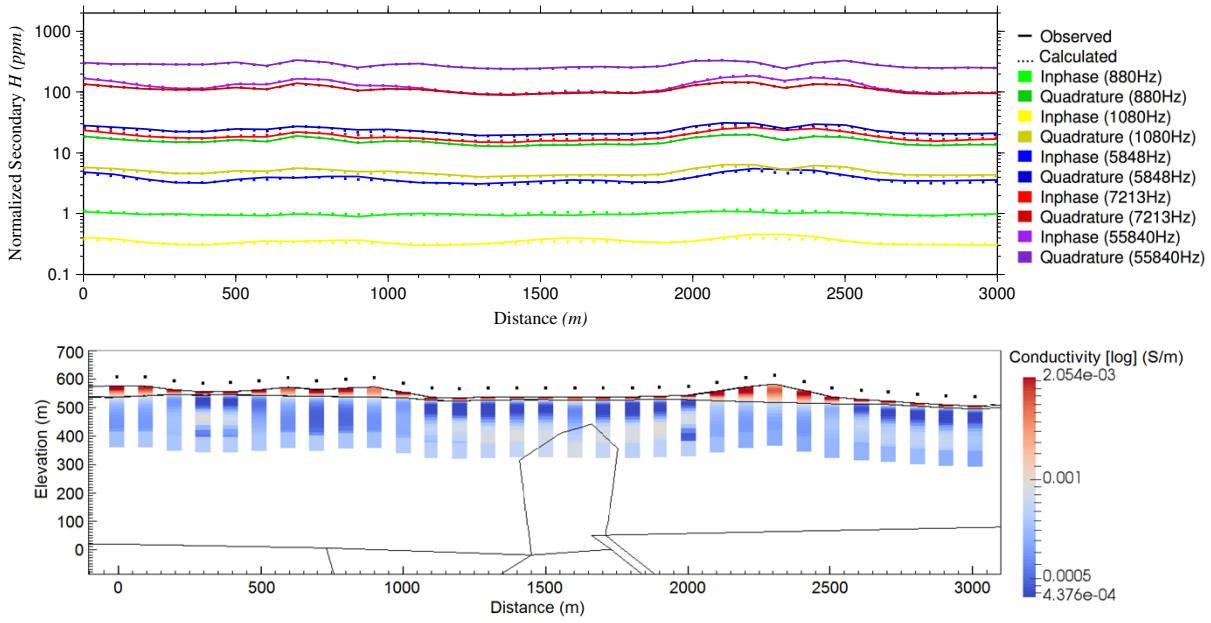

Figure 8.18: Top: observed and calculated data. Bottom: true model (black lines), and 1D inversion results for each station along the profile. True overburden has a resistivity of 500 Ohm-m.

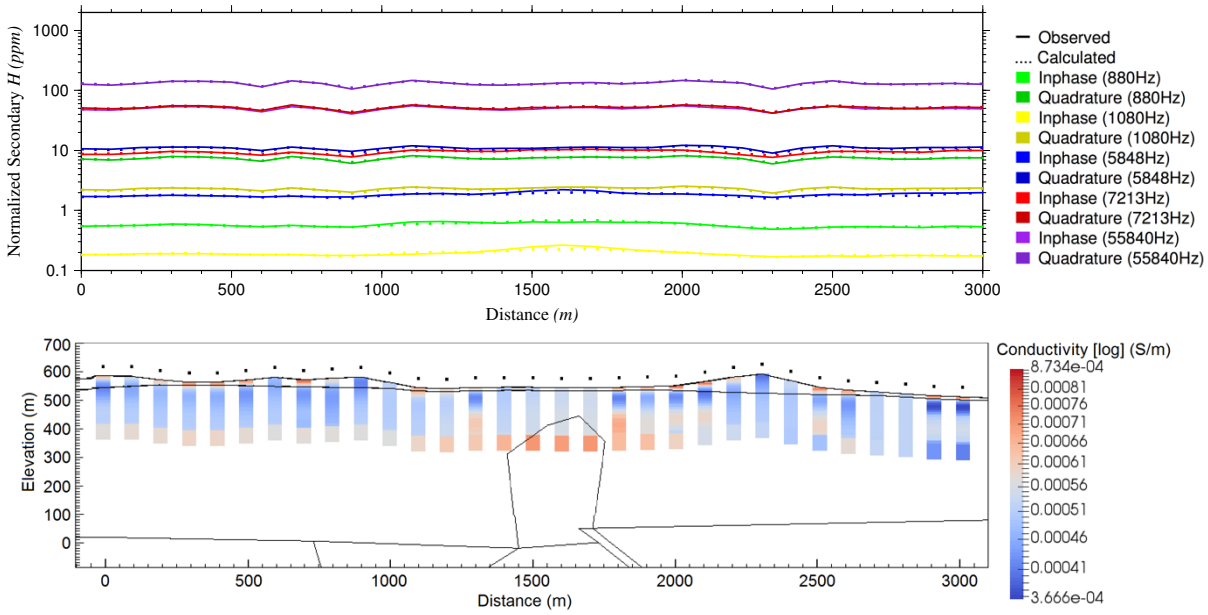

Figure 8.19: Top: observed and calculated data. Bottom: true model (black lines), and 1D inversion results for each station along the profile. True overburden has a resistivity of 1800 Ohm-m.

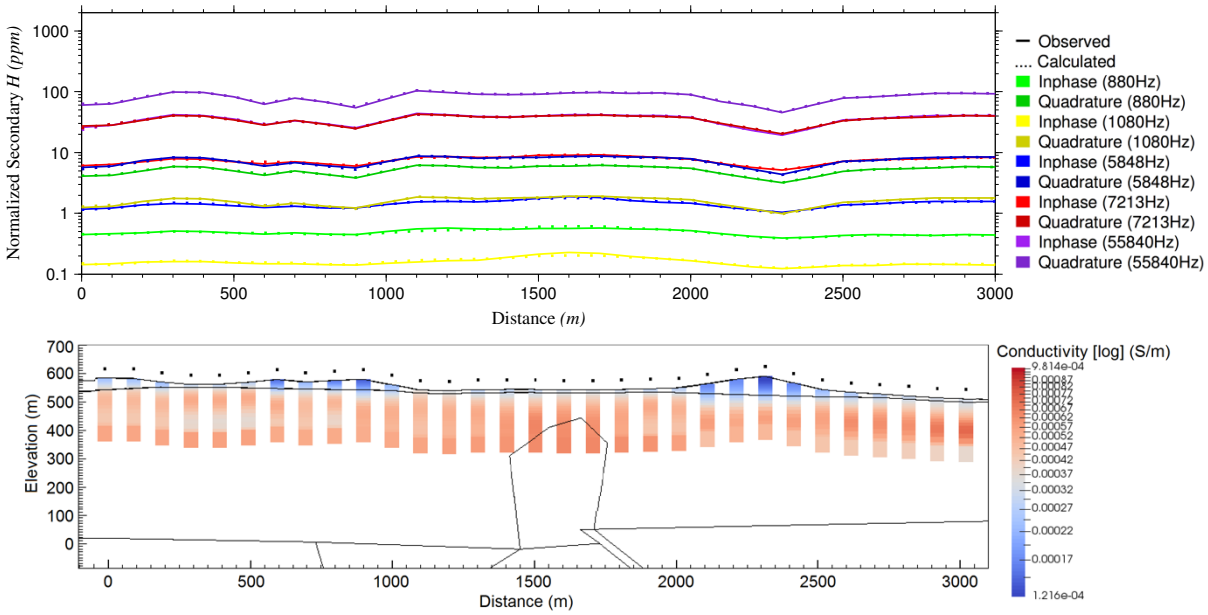

Figure 8.20: Top: observed and calculated data. Bottom: true model (black lines), and 1D inversion results for each station along the profile. True overburden has a resistivity of 6000 Ohm-m.

For 3D VTEM, the same geological model used for the DIGHEM system was used. Responses were computed initially in the frequency domain using CSEM3DFWD code (Ansari and Farquharson, 2014) along a profile with a station spacing of 100 m. Time-domain voltages were calculated using Fourier transform (i.e., dB/dt; see Section 4.4; Newman et al., 1986; Jones et al., 2016) using 160 frequencies over a range from 1 Hz to 30 MHz. VTEM data for three different scenarios were considered, in which overburden has three different resistivities 500, 1800 and 6000 Ohm-m. Also, an elevation of 30 m is used for the EM system height. A dipole moment and a current of 1 Am^2 and 1 A is considered for the modelling, respectively. Since the data are transformed from frequency domain to time domain, the current waveform (by default) has a shape of a square (Figure 8.21). The width of the transmitting time is 5.74 ms, and the earliest time datum is 21 μs after turn off. One dimensional inversion is applied on the data. For the inversion of data, a variable range of noise from 0.5% (for early times) to 100% (for late times) is considered as uncertainty (Figure 8.22). Figures 8.23 to 8.25 show the inversion results for the mentioned scenarios. It can be seen that the base of overburden reconstructed by the VTEM method is not as good as the DIGHEM method. But, as the conductivity contrast increases, the inversion results improve. The inversion results show that the VTEM method can be used to see the conductive anomalies to a certain depth and with a certain conductivity contrast, as the conductive overburden can be seen in some of these synthetic models but not the conductive graphite. Here, only a depth of 200 m is considered for mapping the depth of inversion results.

For EM modelling, the mesh should be refined especially at the receiver points and, in order to have an appropriate mesh, each tetrahedron should have as close to equal edges and angles as possible. This is possible but by increasing the refinement, the number of cells increases. In order to avoid memory limitations, the number of cell cannot be increased (and consequently the refinement) easily. Also, the refinement for the receiver can be controlled by considering a small cell (a fine tetrahedron with the edge size of 1 m) at receiver points. This causes the other cells around the receiver point to be small and refined. The maximum refinement was applied in the modelling by considering the limitation of the number of cells (up to one million cells). Nevertheless, responses for very low frequencies were noisy and so some of them were removed before transforming to the time domain. These low frequencies have a large relative effect on the data especially the late-time measurements.

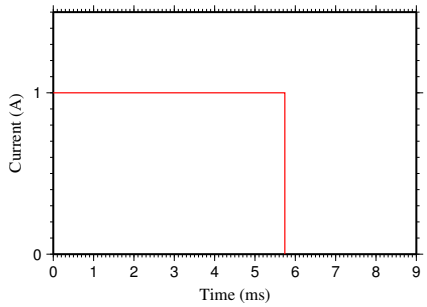

Figure 8.21: Transmitter current waveform for 3D synthetic VTEM modelling.

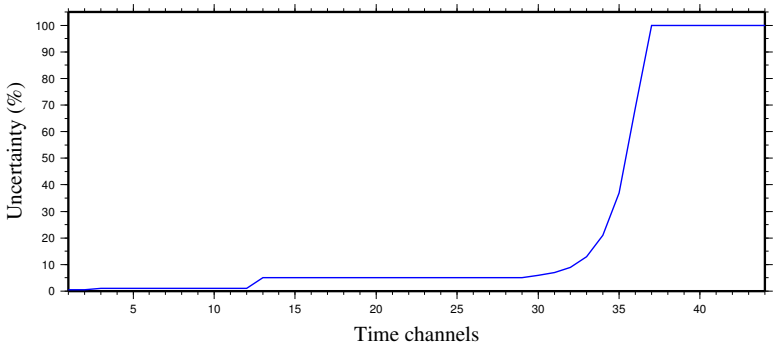

Figure 8.22: Curve shows the uncertainty values in percentage assigned to the 44 off-time channels.

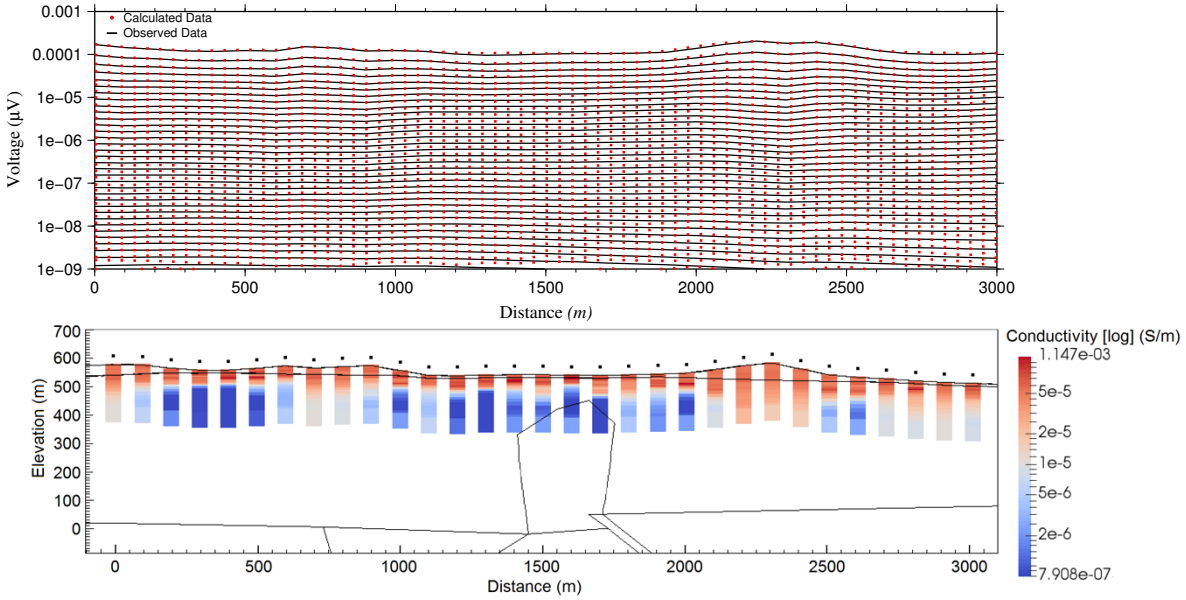

Figure 8.23: Top: observed and calculated data. Bottom: true model (black lines), and 1D inversion results for each station along the profile. True overburden has a resistivity of 500 Ohm-m.

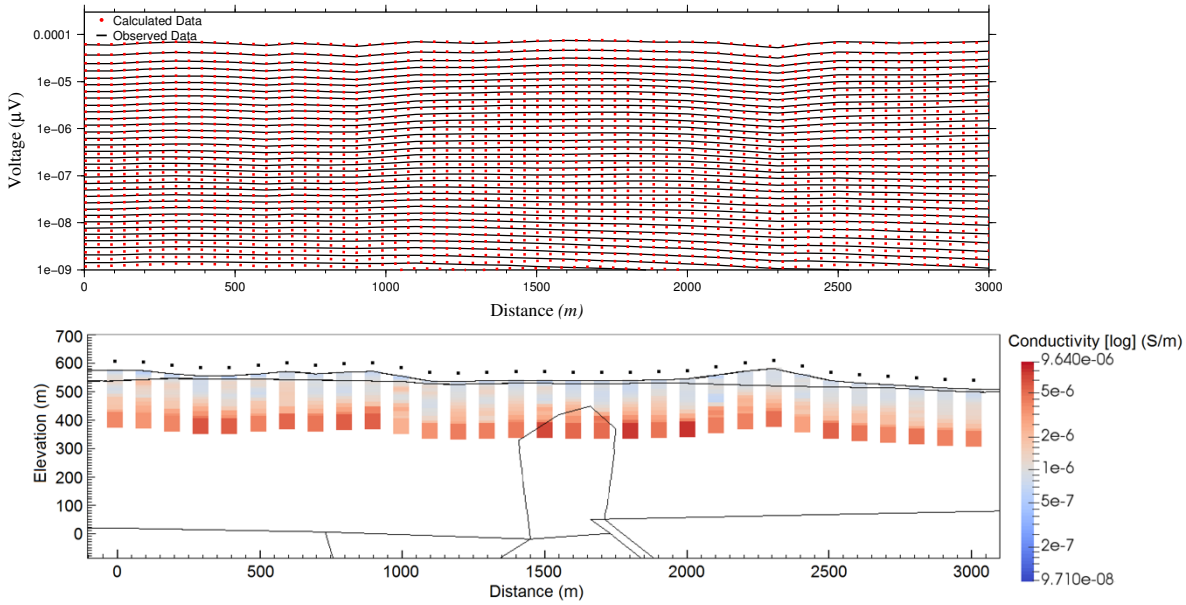

Figure 8.24: Top: observed and calculated data. Bottom: true model (black lines), and 1D inversion results for each station along the profile. True overburden has a resistivity of 1800 Ohm-m.

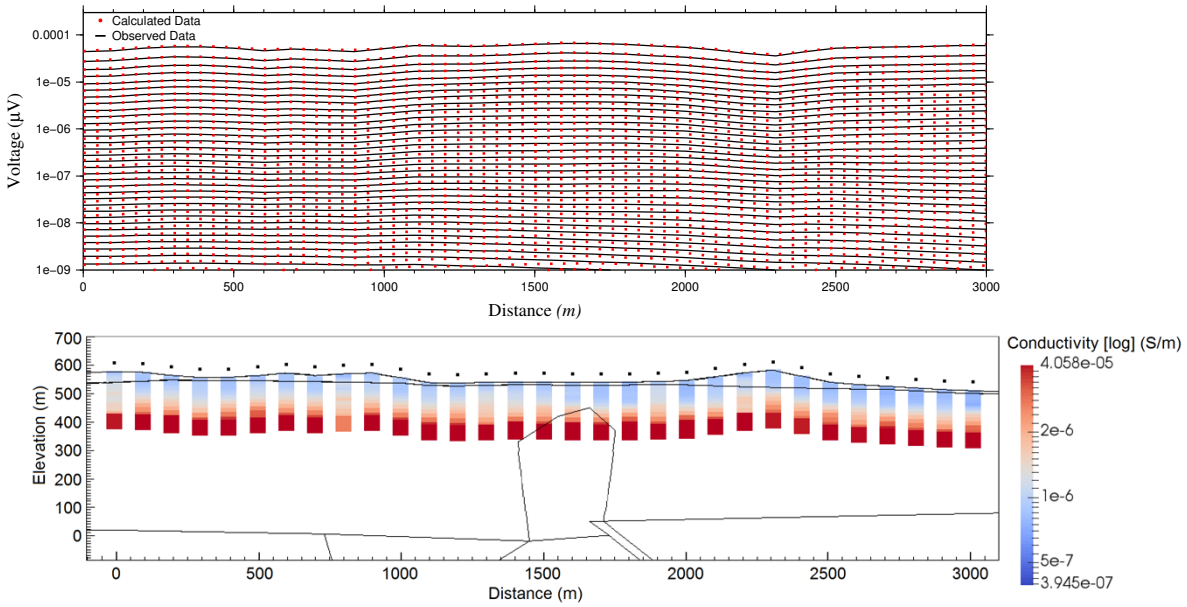

Figure 8.25: Top: observed and calculated data. Bottom: true model (black lines), and 1D inversion results for each station along the profile. True overburden has a resistivity of 6000 Ohm-m.

8.5 1D inversion of real VTEM data

One dimensional inversion was applied to the real VTEM data along a part of a profile with 1260 stations over the McArthur River area. The VTEM system specifications as used in the CMIC Footprints project are shown in Table 8.1.

Table 8.1: VTEM system specifications

Transmitter		Receiver	
Loop diameter	35 m	**X coil diameter**	0.32 m
Effective loop area	3848 m^2	**Number of turns**	245
Number of turns	4	**Effective coil area**	19.69 m^2
Base frequency	30 Hz		
Peak current	361.59 A	**Z coil diameter**	1.2 m
Pulse width	5.74 ms	**Number of turns**	100
Waveform shape	Trapezoid	**Effective coil area**	113.04 m^2
Peak dipole moment	1,391,561 nIA		
Average EM bird terrain clearance	31 m above the ground		

The transmitter current waveform (first pulse) has the shape of a trapezoid, and the off-time starts at 5.74 ms (Figure 8.26). VTEM data (for the time gate number 10) for more than 380,000 stations with a total area coverage of 250 km^2 are shown in Figure 8.27. Figure 8.27 also shows the particular line that is inverted.

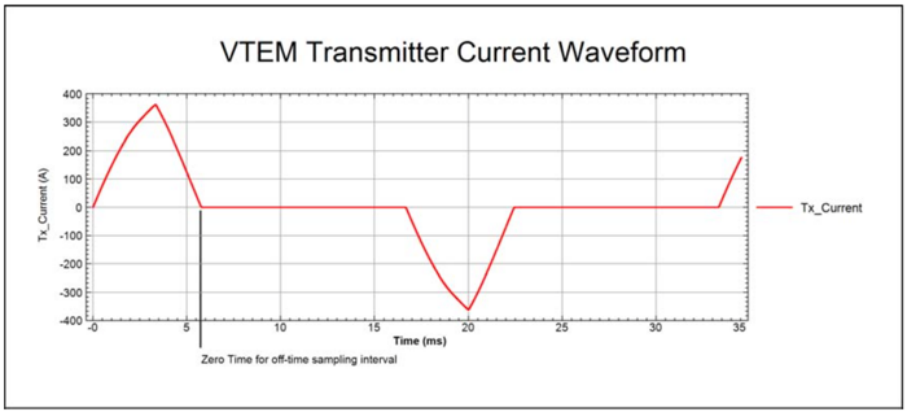

Figure 8.26: Waveform for real VTEM system (Geotech Ltd., 2013).

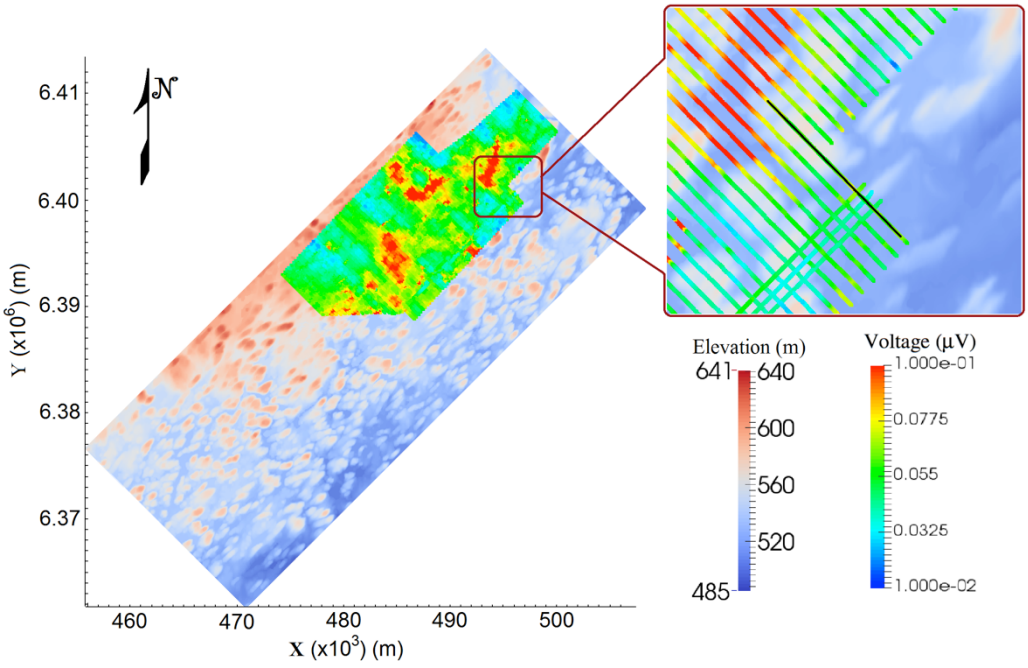

Figure 8.27: VTEM data for the time gate number 10. Inset shows location of survey line (black line) chosen for 1D inversion.

The late-time measurements were noisy. Therefore, the data were filtered using non-linear filtering and smoothing of the data with a moving average filter by Reza Mir (taken from CMIC-Footprints project). One dimensional inversion using the L2-norm was applied on the filtered real VTEM data (Figure 8.28). The same uncertainties applied for the inversion of 3D synthetic data (Figure 8.22) were used for the inversion of real data. There is a similarity between the 1D inversion model and the resistivity depth imaging (RDI) model (adapted from Geotech Ltd., 2013; Figure 8.29). RDI is a quick technique to convert EM profile decay data into an apparent resistivity section, by deconvolving the measured TDEM data. Figures 8.30 and 8.31 respectively show the 1D inversion model and the convergence curves for one of the stations.

The 1D inversion results show three main structures: 1- The first one is a conductive layer at the bottom of the model below -100m elevation which is almost certainly due to the noise in the late-time measurements. This can be explained as follows. An increase in conductivity at depth tends to increase the late-time measurements, and from Figure 8.30 it can be seen that late-time measurements are noisy, and this noise acts to increase the measured values at the late times in a way similar to the effect of a deep conductor. Thus, the inversion code for this data in order to fit the calculated data with the observed data, shift the calculated data upward. This increase in the value of calculated data is done by generating a (artifact) conductive layer at depth. 2- The second feature is a conductive zone starting from a depth of 0 m on the right side of the model between 2000 m and 3000 m. This zone is located around the P2 fault; thus this could be a signature of the graphitic zone. 3- The third feature is a narrow conductive layer close to the surface. The real location of

the interface between overburden and sandstone in shown with a black dot using the data from drill-hole RL-73. Although this conductive layer is close to the interface between overburden and sandstone, this interpretation does not make geological sense for this case as there is not a good contrast between the overburden and sandstone. Also, it seems too consistent all the way along the profile to be considered as, for example, a water table.

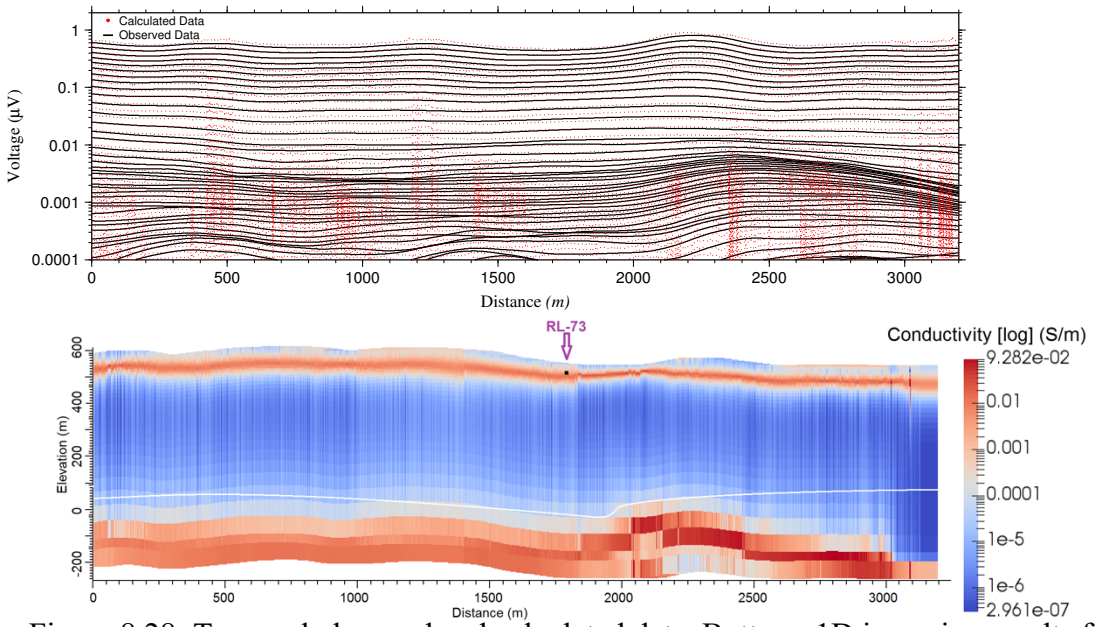

Figure 8.28: Top: real observed and calculated data. Bottom: 1D inversion results for around 1200 stations along a profile. Approximate location of unconformity (white line), and the true location of the overburden base from drill-hole RL-73 (black dot).

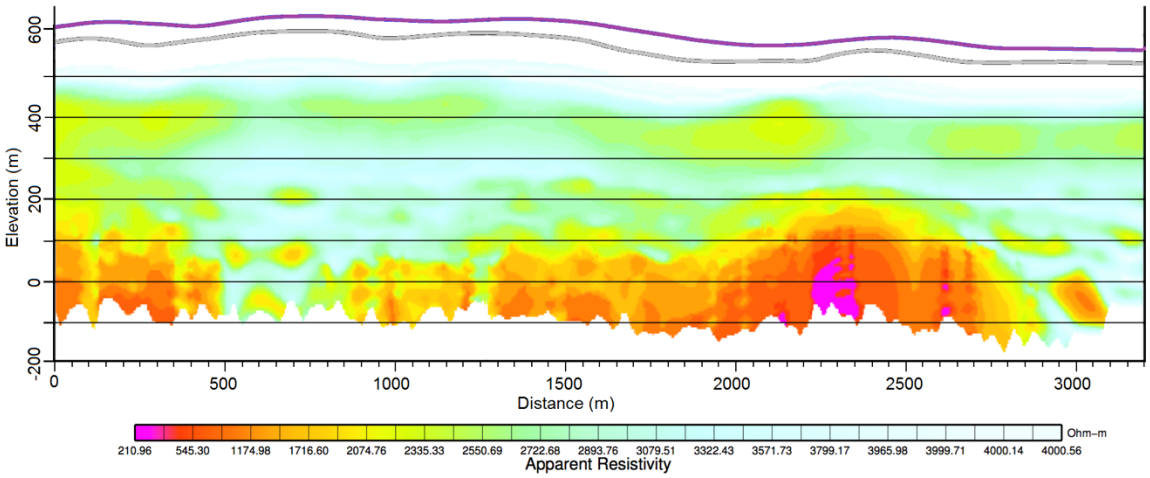

Figure 8.29: Resistivity depth imaging (RDI) done by deconvolving measured TDEM data (Geotech Ltd., 2013). Grey and purple lines on the top show topography and airborne survey line, respectively.

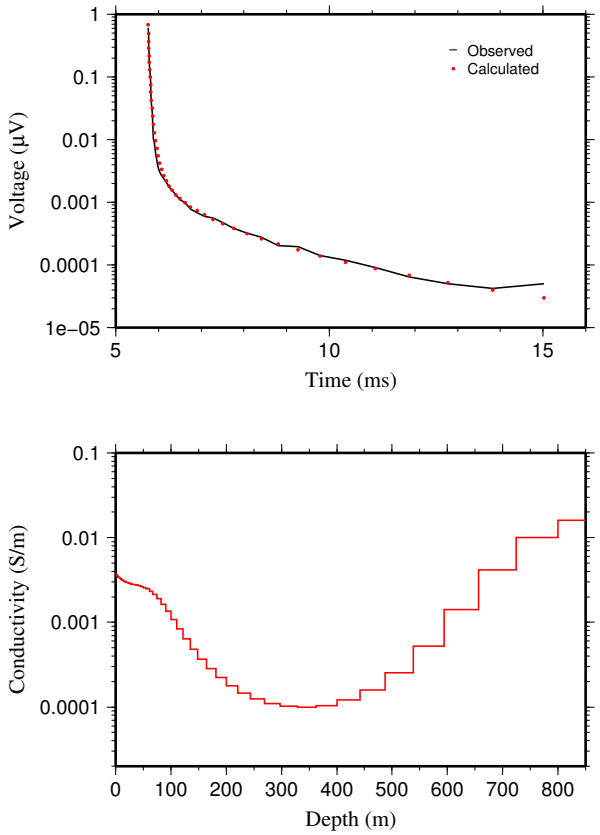

Figure 8.30: Top: observed and calculated data for a station of real VTEM data. Bottom: 1D inversion model.

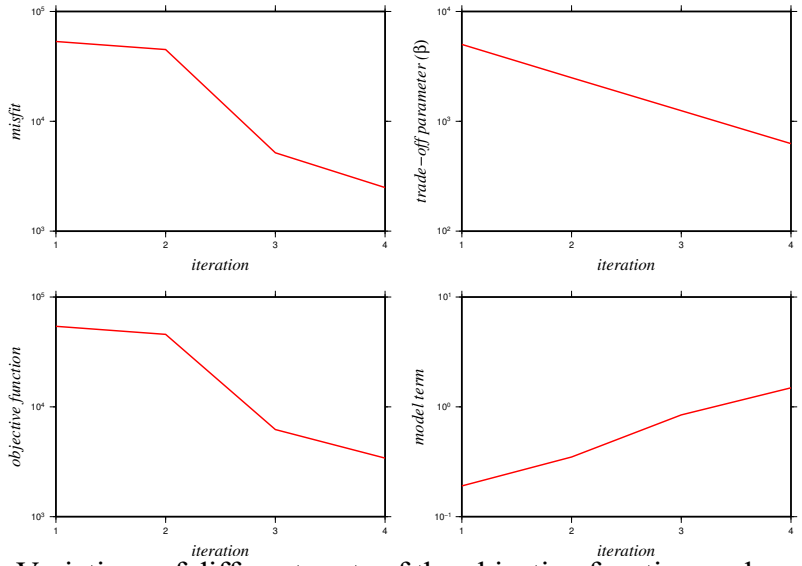

Figure 8.31: Variations of different parts of the objective function such as data misfit (ϕ_d; top-left), trade-off parameter (β; top-right), objective function (Φ; bottom-left) and model term (ϕ_m; bottom-right) at inversion iterations for the model in Figure 8.30.

8.6 Conclusions

Electromagnetic methods can be used for a wide range of subsurface explorations. EM can be divided in two waveform categories: frequency domain and time domain. Both of them are investigated in this chapter for airborne cases. For the frequency domain and time domain, DIGHEM and VTEM data were considered, respectively.

One dimensional and 3D forward modelling, and 1D inversion, were considered here. For the 1D DIGHEM case, a model with two layers was investigated in three scenarios in which the upper layer (overburden) had different conductivities. The inversion results show that DIGHEM data can be used for the overburden thickness estimation when the contrast is strong. However, the boundary between layers is not sharp which is due to the smooth transition (of conductivity) of the L2-based regularization used in the inversions. Use of drill-hole data can be helpful to obtain a sharper boundary. For example, the true interfaces

obtained from drill-hole data should be found and then the average conductivity of these points on the inversion models should be calculated. Finally, this average conductivity could be used for the other inversion models as the conductivity at the boundary.

For the 1D VTEM case, two models, one with two layers and the other with four layers, were investigated in three scenarios in which the upper layer (overburden) had different conductivities. Also, DIGHEM and VTEM data were synthetized for a 3D model of the McArthur area. Results showed that DIGHEM data are better than VTEM data for overburden thickness estimation when the contrast is strong while the VTEM data are better for reconstructing deep conductive structures. One dimensional inversion was applied on the real VTEM data showed some conductive zones, especially a conductive zone close to the P2 fault which can be related to the graphite fault zone. Other apparent conductive zones are probably due to noise, although the agreement of the depth of the conductive zone with the overburden thickness warrants some further investigations, perhaps with ground EM or physical properties investigations at these depths.

Chapter 9

Summary and Conclusion

The Athabasca Basin, Canada, has around 20% of the world's uranium. The uranium deposits are not easily detectable by geophysical methods as they are small in size and some are located at significant depth. But, they are surrounded by large alteration zones which have the potential to be good targets for the gravity method. Also, they often are located adjacent to graphitic faults which are good targets for electromagnetic (EM) methods. Seismic can image the unconformity and the basement faults where uranium is mostly deposited.

The focus of this project was on the eastern Athabasca Basin, McArthur-Millennium corridor, which has the world's largest high-grade uranium deposits at depths of 500-800 m where basement faults intersect the unconformity. Overburden in the region is dominated by Quaternary glacial deposits. The problem is that the overburden signature in the geophysical data, especially in the gravity data, masks the signature of the deeper geological structures such as alteration zones. In this research, four geophysical methods (seismic refraction, gravity, magnetic and electromagnetic methods) were investigated for stripping out the overburden response in order to determine the location of the uranium mineralization with more precision.

The approach taken throughout the thesis was synthetic modelling and inversion in which models representing the real-life situations were built, data were computed for these models, and then these data were inverted. Testing was done by considering the various components of the models individually or in various combinations to assess the relative importance of the various contributions to the geophysical data-sets. I also investigated and tested joint and cooperative inversion methods, especially with information from one data-type helping out the inversion of another data-type. Thus, for the inversion 2D and 3D independent, constrained and joint methods were applied to synthetic data representing the the McArthur-Millennium site. Then the best inversion methods obtained from synthetic modelling were applied to the available real data.

Due to the sensitivity of the seismic method to spatial changes of seismic velocities in the subsurface, the independent inversion of the seismic refraction data is a useful method for overburden stripping, whereas the independent gravity inversion is a weak method for this purpose because of poor depth resolution as well as the non-uniqueness of interpretation. Thus, joint inversion of gravity and seismic refraction data was tested which was able well to reconstruct the variable thickness of the overburden. The seismic refraction data essentially enable the inversion to reconstruct the base of the overburden. After determining the thickness of the overburden using the joint inversion, synthetic modelling showed that the constrained independent inversion of gravity data can illustrate the location of alteration zone at depths. Some issues such as blind layers and attenuation can make the seismic refraction method problematic by not allowing recovery of the true overburden model. However, in this thesis the inversion (especially the joint inversion) of seismic

refraction data is found the most effective method for finding the base of the overburden.

Independent inversions of magnetic and gravity data are not suitable methods for overburden stripping as these methods both have a poor resolution. The joint inversion of magnetic and gravity data was able to reconstruct the basement blocks, the sandstone and the unconformity, however the base of overburden cannot be sharply resolved. But, the constrained joint inversion of magnetic and gravity data showed that is a reasonable method for overburden stripping, however the alteration zone is not yet reconstructed. There are different mathematical methods for the joint inversion, but the best results were obtained using the "fuzzy c-mean clustering" method.

EM methods were applied to determine the location of the interface between overburden and sandstone as well as the location of the graphitic faults. For this purpose, both frequency domain (FDEM) and time domain (TDEM) methods were tested. The specific systems considered for FDEM and TDEM methods are airborne DIGHEM and VTEM methods, respectively. Results showed that DIGHEM method and VTEM method can be considered as a method for overburden stripping and detecting the graphitic faults, respectively. Note that there may not always be a sufficient conductivity contrast between the overburden and the sandstones in the McArthur area to allow this to work. However, overburden over basement is a ubiquitous problem, and often there will be a conductivity contrast, and so the use of EM could work.

This project, as a part of the larger CMIC Footprints project, has access to comprehensive geophysical data-sets, physical property data and geological information as

well as access to the results from other researchers in this project. A summary of my research based on the geophysical methods and techniques used in this thesis is shown in Table 9.1. It shows that the effect of the overburden on the gravity data can be removed using constraints from other geophysical methods in order to allow the residual gravity to be used to define alteration zones. Among the geophysical methods, the seismic refraction method works much better than the other methods such as electromagnetic and magnetic methods, however in a real large scale it would be an expensive method.

Table 9.1: A summary of the research done in this thesis.

	Seismic Refraction (2D)	Gravity (2D)	Gravity (3D)	Magnetics (3D)	DIGHEM (1D/3D)	VTEM (1D/3D)
Independent Inversion	Synthetic and real data. Successful (for the overburden stripping) if dense shot locations and simple model.	Synthetic and real data. Poor results for the overburden stripping.	Synthetic and real data. Poor results for the overburden stripping, and good results for reconstructing the deep structures such as basement.	Synthetic and real data. Poor results for the overburden stripping, and good results for reconstructing the deep structures such as basement.	Synthetic and real data. Good results for the overburden stripping (1D and 3D modellings & 1D inversions).	Synthetic and real data. Good results for the overburden stripping if there is a good conductivity contrast. Good results for deep conductive structures such as graphitic faults.
Constrained Independent Inversion	Not considered.	Synthetic and real data. Good for reconstructing the deep structures such as alteration zones (overburden thickness which was constructed using the independent seismic refraction inversion results was considered as the constraint)	Synthetic data only. Poor results for the overburden stripping (based on the drill-hole data, parts of overburden and sandstone thicknesses were considered as constraints).	Synthetic data only. Poor results for the overburden stripping (based on the drill-hole data, parts of overburden and sandstone thicknesses were considered as constraints).	Not considered.	Not considered.
Joint Inversion	With gravity; Synthetic and real data. Good (for the overburden stripping) if moderately dense shot locations, and simple model.	With seismic refraction; Synthetic and real data. Good results for the overburden stripping.	With magnetic; synthetic and real data. Better results than the independent inversions for the overburden stripping, but still not acceptable. Good results for reconstructing the deep structures such as sandstone, unconformity and basement.	With gravity; synthetic and real data. Better results than the independent inversions for the overburden stripping, but still not acceptable. Good results for reconstructing the deep structures such as sandstone, unconformity and basement.	Not considered.	Not considered.
Constrained Joint Inversion	Not considered.	Not considered.	With magnetic; synthetic and real data. Good results for the overburden stripping as well as for reconstructing the deep structures such as sandstone, unconformity and basement.	With gravity; synthetic and real data. Good results for the overburden stripping as well as for reconstructing the deep structures such as sandstone, unconformity and basement.	Not considered.	Not considered.

Bibliography

Aario, R. and Peuraniemi, V., 1992, Glacial dispersal of till constituents in morainic landforms of different types; in Proceedings of the Third International Drumlin Symposium, (ed.) R. Aario and H. Heikkinen; Geomorphology v. 6, p. 9–25.

Alexandre P., K. Kyser, D. Thomas, P. Polito and J. Marlat, 2007. Geochronology of unconformity-related uranium deposits in the Athabasca Basin, Saskatchewan, Canada and their integration in the evolution of the basin. Miner Deposita, DOI 10.1007/s00126-007-0153-3.

Allard, M., 2007, On the origin of HTEM species, In "Proceedings of Exploration 07: Fifth Decennial International Conference on Mineral Exploration" edited by B. Milkereit, 355-374.

Annesley, I.R., Madore, C., and Portella, P., 2005, Geology and thermotectonic evolution of the western margin of the Trans-Hudson Orogen: Evidence from the eastern sub-Athabasca basement, Saskatchewan: Canadian Journal of Earth Sciences, v. 42, p. 573-597.

Ansari, S., and Farquharson, C. G., 2014, 3D finite-element forward modeling of electromagnetic data using vector and scalar potentials and unstructured grids: Geophysics, 79, no. 4, E149–E165.

Averill, S.A., 1976a, Geikie River east, Saskatchewan; overburden drilling report for Conwest Canadian Uranium Exploration, Joint Venture; in Saskatchewan Industry and Resources Mineral Assessment File No. 74H-0017, 71 p.

Bamford, D., Nunn, K., Prodehl, C. and Jacob, B., 1978, LISPB-IV. Crustal structure of northern Britain. Geophys. J. R. astr. Soc., 54, 43–60.

Bauer, K., G. Munoz and I. Moeck, 2012, Pattern recognition and lithological interpretation of collocated seismic and magnetotelluric models using self-organizing maps: Geophysical Journal International, 189, 984–998.

Beamish, D., 2004, Airborne EM skin depths, Geophysical prospecting 52, 439-449.

Bell Geospace Limited, 2007, Report of acquisition and processing of Air-FTG data over McArthur river, Read Lake and Rabbit Lake in the Athabasca Basin, Saskatchewan, Canada, 42p.

Bernier, S., 2004, Stratigraphy of the Late Paleoproterozoic Manitou Falls Formation, in the Vicinity of the McArthur River Uranium Deposit, Athabasca Basin, Saskatchewan, Canada: M.Sc. thesis, Laurentian University, Sudbury, Ontario, 184 p.

Bhattacharya B. K., 1966, Two-dimensional harmonic analysis as a tool for magnetic interpretation. Geophysics, 30, 829–857.

Blakely, R.J., 1995, Potential Theory in Gravity and Magnetic Applications. Cambridge University Press, Cambridge.

Börner, R. U., 2010, Numerical modelling in geo-electromagnetics: Advances and challenges, Surveys in Geophysics, 31, 225–245, doi: 10 .1007/s10712-009-9087-x.

Bracewell, R., 1965, The Fourier transform and its applications: McGraw-Hill.

Cain, M. J., 2000, DIGHEM EM/Magnetic survey for Cream Minerals LTD. Nootka island, British Columbia, Fugro Airborne Survey report, 94p.

Campbell, J.E. and Flory, G., 1999, Cameco Corporation: till geochemical and Quaternary geological investigations on the Dawn Lake project properties (part of NTS 64L-4,-5 and 74I-1,-8,-9); in Saskatchewan Industry and Resources Mineral Assessment File No. 74I01-0091, 39 p.

Campbell, J. E., Shieves, R. B. K. and Klassen R. A., 2002. Integrated field investigations of airborne radiometric spectral domains, NEA-IAEA test area, eastern Athabasca Basin: A preliminary report, Summary of Investigations 2002, v2, Saskatchewan Geological Survey, Saskatchewan Industry Resources, Miscellaneous Report 2002-4.2, Paper D-2.

Campbell, J.E., 2007, Quaternary geology of the eastern Athabasca Basin, Saskatchewan; in EXTECH IV, Geological Survey of Canada, Bulletin 588, p. 211–228.

Card, C.D., 2006, Remote predictive map for the basement to the western Athabasca Basin: Saskatchewan Industry and Resources, Preliminary Geological Map, Open File 2006-45, scale: 1:500 000.

Carter-McAuslan, A., 2013, Joint inversion of geologically realistic, synthetic Earth models. M.Sc. thesis, Memorial University of Newfoundland, St. John's, NL, Canada, 356 p.

Carter-McAuslan, A., Farquharson, C.G., 2016, Predictive Mapping using Self-Organizing Maps: An example of mapping the Mid-Continent Rift at Depth; SEG International Exposition and 86th Annual Meeting, Dallas, Texas. p. 5643-5647.

Cerveny, V., and Ravindra, R., 1971, Theory of Seismic HeadWaves. University of Toronto Press.

CGG, 2014, HeliFALCON airborne gravity gradiometer survey; Project Number: 14021, Saskatchewan, Canada, 31p.

Clement, W.G., 1972, Basic principles of two-dimensional digital filtering, Geophysical Prospecting, pp. 125-145.

Connard, G., Couch, R. and Gemperle, M., 1983, Analysis of aeromag- netic measurements from the Cascade Range in central Oregon, Geophysics, 48, 376-390.

Costa, I.S.L., Tavares, F.M., Oliveira, J.K.M., 2019, Predictive lithological mapping through machine learning methods: a case study in the Cinzento Lineament, Carajás Province, Brazil. Journal of the Geological Survey of Brazil vol 2, no 1, 26-36.

Cowan, D. R., and Cowan, S., 1993, Separation filtering applied to aeromagnetic data. Exploration Geophysics, v. 24, pp. 429-436.

Cracknell M., Reading A., McNeill A.W, 2014, Mapping geology and volcanic-hosted massive sulfide alteration in the Hellyer-Mt Charter region, Tasmania, using Random Forests (TM) and Self-Organising Maps. Australian Journal of Earth Sciences, 61, 287-304. https://doi.or g/10.1080/08120099.2014.858081

Craik, D. J., 1995, Magnetism: principles and applications, Wiley, 468p.

Davies, J., Mushayandebvu, M. and Smith, I.R., 2004, Magnetic detection and characterization of Tertiary and Quaternary buried channels; SEG International Exposition and 74th Annual Meeting, Denver, Colorado. p. 734-737.

Demsar, J., T. Curk, A. Erjavec, C. Gorup, T. Hocevar, M. Milutinovic, M. Mozina, M. Polajnar, M. Toplak, A. Staric, M. Stajdohar, L. Umek, L. Zagar, J. Zbontar, M. Zitnik, and B. Zupan, 2013, Orange: Data mining toolbox in python: Journal of Machine Learning Research, 14, 2349– 2353.

Domzalski. W., 1956, Some problems of shallow refraction investigations. Geophysics. Props., vol 4, no:2, 140-166.

Earle, S. and V. Sopuck, 1989. Regional lithogeochemistry of the eastern part of the Athabasca Basin uranium province, Saskatchewan; in . Muller-Kahle , E., ed.,Uranium resources and geology of North America: International Atomic Energy Agency, TECDOC-500, p. 263 – 269.

Ekblom, H., 1973, Calculation of linear best Lp-approximations, BIT, 13, 292-300.

Ekblom, H., 1987, The L1-estimate as limiting case of an Lp-or Huber-estimate, in Y. Dodge, ed., Statistical data analysis based on the L1-norm and related methods: Elsevier Science Publ. Co., Inc., 109–116.

Everett, M.E., and Meju., M.A., 2005, Near-Surface controlled-source electromagnetic induction: background and recent advances, p.157-184. In Y. Rubin and S.S. Hubbard (ed.) Hydrogeophysics. Springer, Dordrecht, the Netherlands.

Farquharson, C. G., and J. A. Craven, 2009, Three-dimensional inversion of magnetotelluric data for mineral exploration: An example from the McArthur River uranium deposit, Saskatchewan, Canada: Journal of Applied Geophysics, 68, no. 4, 450–458, doi: 10.1016/j.jappgeo.2008 .02.002.

Farquharson, C.G., and Oldenburg, D.W., 1998, Non-linear inversion using general measures of data misfit and model structure: Geophys. J. Int., 134, 213–227.

Farquharson, C.G., and Oldenburg, D.W., 2000, EM1DFM; A Program Library for Forward Modelling and Inversion of Frequency Domain Electromagnetic Data over 1D Structures, Version 1.0, Developed by the UBC- Geophysical Inversion Facility, Department of Earth and Ocean Sciences, University of British Columbia, Vancouver, British Columbia.

Farquharson, C.G., and Oldenburg, D.W., 2004, A comparison of automatic techniques for estimating the regularization parameter in nonlinear inverse problems, Geophysical Journal International, 156, 411–425.

Farquharson, C.G., and Oldenburg, D.W., 2006, EM1DTM; A Program Library for Forward Modelling and Inversion of Time Domain Electromagnetic Data over 1D Structures, version 1.0, Developed by the UBC- Geophysical Inversion Facility, Department of Earth and Ocean Sciences, University of British Columbia, Vancouver, British Columbia.

Farquharson, C.G, 2008. Constructing piecewise-constant models in multidimensional minimum-structure inversions, Geophysics, 73, K1-K9. (DOI: 10.1190/1.2816650)

Fayek, M., T. M. Harrison, R. C. Ewing, M. Grove and C. D. Coath, 2002a. O and Pb isotope analyses of uranium minerals by ion microprobe and U-Pb ages from the Cigar Lake deposit, Chemical Geology, 185, p. 205- 225.

Fayek, M., and Kyser, K.K., 1997, Characterization of multiple fluid events and rare-earth-element mobility associated with formation of unconformity-type uranium deposits in the Athabasca Basin, Saskatchewan: The Canadian Mineralogist, v. 35, p. 627-658.

Fitterman D. V., and Labson V. F., 2005, 10. Electromagnetic Induction Methods for Environmental Problems. Near-Surface Geophysics: pp. 301-356.

Fowler, C. M. R., 2005, The solid earth: an introduction to global geophysics, Cambridge University Press, 726p.

Fraser, D., 1986, Dighem resistivity techniques in airborne electromagnetic mapping in Airborne Resistivity Mapping, ed. G.J. Palacky; Geological Survey of Canada, Paper 86-22, p. 49-54.

Fulton, R. J., 1995, Geological Survey of Canada, "A" Series Map 1880A, 1 sheet, https://doi.org/10.4095/205040

Fugro Airborne Surveys Corp., 2006, DIGHEM survey for Osisko Exploration Ltd. in Malartic/Cadillac area, Quebec, Canada, 203p.

Gandhi, S.S., 1989, Geology and uranium potential of the Thelon Basin and adjacent basement in comparison with the Athabasca Basin region: Uranium Resources and Geology of North America, Technical Committee Meeting, Saskatoon, Vienna, 1-3 September, 1987, Proceedings, p. 411-428.

Gandhi, S.S., 1995, An overview of the exploration history and genesis of Proterozoic

uranium deposits in the Canadian Shield: Exploration and Research for Atomic Minerals, v. 8, p. 1-47.

Geddes, R.S., 1982, The Vixen Lake indicator train Northern Saskatchewan; in Prospecting in Areas of Glaciated Terrain – 1982, (ed.) P.H. Davenport; Canadian Institute of Mining and Metallurgy, p. 264–283.

Geosoft, 2006, Gravity and magnetic software, user manual. Oasis Montaj v 6.4, Geosoft Inc.

Geosoft, 2007, 2-D frequency domain processing of potential field data; user's guide. Oasis Montaj v.6.4. Geosoft Inc.

Geotech Ltd., 2013, Report on a helicopter-borne versatile time domain electromagnetic (VTEM max) and aeromagnetic geophysical survey, Read Lake project, McArthur river mine, Saskatchewan, Canada, 150p.

Gill, P.E., W. Murray & M.H. Wright, 1981. Practical Optimization, Academic Press, London.

Goldak Airborne Surveys, 2007, Technical report on a fixed wing magnetic gradiometer survey over McArthur River and Read Lake in the Athabasca Basin, Saskatchewan, Canada, 22p.

Grant, F. S., and West, G. F., 1965, Interpretation Theory in Applied Geophysics. McGraw-Hill Co., New York.

Griffiths, D. J., 1999, Introduction to Electrodynamics, third edition: Prentice-Hall inc.

Györfi, I., Hajnal, Z., White, D.J., Takács, E., Reilkoff, B., Annesley, I.R., Powell, B., and Koch, R., 2007, High-resolution seismic survey from the McArthur River region: contributions to mapping the complex P2 uranium ore zone, Athabasca Basin, Saskatchewan, in Jefferson, C.W., and Delaney, G., eds., EXTECH IV: Geology and

Uranium EXploration TECHnology of the Proterozoic Athabasca Basin, Saskatchewan and Alberta: Geological Survey of Canada, Bulletin 588, (also Geological Association of Canada, Mineral Deposits Division, Special Publication 4; Saskatchewan Geological Society, Special Publication 18), p. 397-412.

Haber, E., 1997, Numerical Strategies for the Solution of Inverse Problems, Ph.D. thesis, University of British Columbia.

Haber, E., and Oldenburg, D.W., 2000, A GCV based method for nonlinear ill-posed problems, Computational Geosciences, 4, 41–63.

Hajnal, Z., E. Takács, D. J. White, I. Györfi, B. Powell, and R. Koch, 2007, Regional seismic signature of the basement and crust beneath the McArthur River mine district, Athabasca Basin, Saskatchewan, in C. W. Jefferson, and G. Delaney, eds., EXTECH IV: Geology and uranium exploration technology of the Proterozoic Athabasca Basin; Saskatchewan and Alberta: Geological Survey of Canada, Bulletin, 588, 389–396.

Hauck, C., Kneisel, C., 2008, Applied Geophysics in Periglacial Environments, Cambridge University Press, 240 pp.

Hinze, W. J., Von Frese, R. R. B., and Saad, A. H., 2013, Gravity and Magnetic Exploration: Principles, Practices and Applications, Cambridge Univ. Press, New York.

Hodges, G., 1999, A world of applications for helicopter electromagnetics to environmental and engineering problems, Proceedings of 12th Annual Symposium on the Application of Geophysics to Environmental and Engineering Problems (SAGEEP).

Hodges, G., 2013, The power of frequency domain: when you should it: AEM 2013, 6TH International AEM Conference and Exhibition, Expanded Abstracts, 5 p.

Hoeve, J., and Quirt, D.H., 1984, Mineralization and Host Rock Alteration in Relation to Clay Mineral Diagenesis and Evolution of the Middle- Proterozoic, Athabasca Basin, northern Saskatchewan, Canada: Saskatchewan Research Council, SRC Technical

Report 187, 187 p.

Hoeve, J., and Quirt, D.H., 1987, A stationary redox front as a critical factor in the formation of high-grade, unconformity-type uranium ores in the Athabasca Basin, Saskatchewan, Canada: Bulletin de Minéralogie, v. 110, p. 157-171.

Holladay, S., and Lo, B., 1997, Airborne Frequency-Domain EM- Review and Preview Proceedings of Exploration 97: Fourth Decennial International Conference on Mineral Exploration, pp 505-514.

Hsu, S. K., Sibuet, J.C., Shyu, C.T., 1996, High-resolution detection of geologic boundaries from potential-field anomalies: An enhanced analytic signal technique: Geophysics, 61, 373–386.

Irvine, R. and Witherly, K., 2006, Advances in airborne EM acquisition and processing for uranium exploration in the Athabasca Basin, Canada, SEG/New Orleans 76th Annual Meeting.

Jahandari, H., and Farquharson, C.G., 2014, A finite-volume solution to the geophysical electromagnetic forward problem using unstructured grids. Geophysics 79, E287–E302.

Jahandari, H., 2015, Three-dimensional numerical modelling of gravity and electromagnetic data using unstructured tetrahedral grids, PhD thesis, Memorial University of Newfoundland, St. John's, NL, Canada, 183 p.

Jahandari, H., Ansari, S., and Farquharson, C.G., 2017, Comparison between staggered grid finite–volume and edge–based finite–element modelling of geophysical electromagnetic data on unstructured grid. Journal of Applied Geophysics, V 138, 185-197.

Jain, S., 2014, Fundamentals of Physical Geology, Springer Geology, P 350, DOI: 10.1007/978-81-322-1539-4_1.

Jefferson, C. W., G. Delaney, and R. A. Olson, 2003, EXTECH IV: Athabasca uranium multidisciplinary study of northern Saskatchewan and Alberta, Part 1: Overview and impact: Geological Survey of Canada Current Research, C18, doi: 10.4095/214200.

Jefferson, C. W., D. J. Thomas, S. S. Gandhi, P. Ramaekers, G. Delaney, D. Brisbin, C. Cutts, P. Portella and R. A. Olson, 2007. Unconformity associated uranium deposits, in Jefferson, C.W., and Delaney, G., eds., EXTECH IV: Geology and Uranium EXploration TECHnology of the Proterozoic Athabasca Basin, Saskatchewan and Alberta: Geological Survey of Canada, Bulletin 588 (also Saskatchewan Geological Society, Special Publication 18; Geological Association of Canada, Mineral Deposits Division, Special Publication 4).

Jin, J., 2002, The finite element method in electromagnetics, 2nd ed.: John Wiley & Sons Inc.

Jones, D., Ansari, S., Farquharson, C. and Hearst, R., 2016, Synthesizing time-domain electromagnetic data for graphitic fault zones and associated uranium deposits in the Athabasca Basin, Canada. SEG Technical Program Expanded Abstracts 2016: pp. 2206-2210.

Juhojuntti, N., Wood, G., Juhlin, C., O'Dowd, C., Dueck, P. and Cosma C., 2012. 3D seismic survey at the Millennium uranium deposit, Saskatchewan, Canada: Mapping depth to basement and imaging post-Athabasca structure near the orebody. GEOPHYSICS, 77(5), WC245-WC258.

Kearey, P., Brooks, M., Hill, I., 2002, An introduction to geophysical exploration. Blackwell Science.

Kornik, L.J., 1983, Vertical magnetic gradiometer survey and interpretation, NEA/IAEA Athabasca Test Area; in Uranium Exploration in Athabasca Basin, Saskatchewan, Canada, ed. E.M. Cameron; Geological Survey of Canada, Paper 82-11, p. 147-150.

Kuhn, S.; Cracknell, M.J.; Reading, A.M., 2018, Lithologic mapping using Random Forests applied to geophysical and remote-sensing data: A demonstration study from the Eastern Goldfields of Australia, Geophysics,, 83, B183–B193.

Kyser, K., Hiatt, E., Renac, C., Durocher, K., Holk, G., and Deckart, K., 2000, Diagenetic fluids in Paleo- and Mesoproterozoic sedimentary basins and their implications for long protracted fluid histories, Chapter 10 in Kyser, K., ed., Fluids and Basin Evolution, Short Course Series Volume 28 (Series editor Robert Raeside): Mineralogical Association of Canada, p. 225-262.

LaFehr, T. R., and Nabighian, M. N., 2012, Fundamentals of Gravity Exploration, Geophysical Monograph Series: Society of Exploration Geophysicists, http://dx.doi. org/10.1190/1.9781560803058.

Lankston, R., 1990, High Resolution Refraction Seismic Data Acquisition and Interpretation. In: Geotechnical and Environmental Geophysics, Vol 1, Reviewer and Tutorial, S. Ward (ed.), Investigations in Geophysics No. 5, Society of Exploration Geophysicists, Tulsa, OK, pp. 45–73.

Legault, J.M., Prikhodko, A., Kumar, H., and Tishin, P., 2011, An improved early-channel VTEM helicopter system for near-surface applications, a paper presented at 24TH SAGEEP symposium and annual meeting of Environment and Engineering Geophysical Society, EEGS, Charleston, SC.

Legault, J.M., 2015, Airborne electromagnetic systems — state of the art and future directions: CSEG Recorder, 40, 38–49.

Lelièvre, P. G. and Oldenburg, D. W., 2009, A comprehensive study of including structural orientation information in geophysical inversions, Geophys. J. Int., 178, 623–637.

Lelièvre, P. G., C. G. Farquharson, and Hurich, C. A., 2011, Computing first-arrival seismic traveltimes on unstructured 3D tetrahedral grids using the fast marching method:

Geophysical Journal International, 184, 885–896, doi: 10.1111/gji.2011.184.issue-2.

Lelièvre, P.G., Farquharson, C.G., Hurich, C.A., 2012. Joint inversion of seismic traveltimes and gravity data on unstructured grids with application to mineral exploration. Geophysics 77, K1-K15.

Lelièvre, P. G., and Farquharson, C. G., 2015, PODIUM: a suite of software utilities for Preparation of Data for Inversion on Unstructured Meshes.

Li, Y., and Oldenburg, D. W., 1998, 3-D inversion of gravity data: Geophysics, 63, 109–119.

Li, Y., and Oldenburg., D. W., 2000b, Joint inversion of surface and three–component borehole magnetic data. Geophysics 65(2):540–552.

Lim, B.K., Jones, S.J., 1989, Some applications and problems of the seismic refraction technique in civil engineering projects in Malaysia, Geol. Soc. Malaysia, 15, pp95-121.

Macnae, J., 2007, Developments in broadband airborne electromagnetics in the past decade In "Proceedings of Exploration 07: Fifth Decennial International Conference on Mineral Exploration" edited by B. Milkereit, 387-398.

Macnae, J., and Baron-Hay, S., 2010, Reprocessing strategy to obtain quantitative early time data from historic VTEM surveys: ASEG, Extended Abstracts, 4 p.

Madsen, N. K., and R. W. Ziolkowski, 1990, A three-dimensional modified finite volume technique for Maxwell's equations: Electromagnetics, 10, 147–161, doi: 10.1080/02726349008908233.

Marlatt, J., McGill, B., Matthews, R., Sopuck, V., and Pollock, G., 1992, The discovery of the McArthur River uranium deposit, Saskatchewan, Canada, new developments in uranium exploration, resources, production and demand: International Atomic Energy Agency - Nuclear Energy Agency of the OECD, Vienna, 26-29 August, 1991, Technical

Committee Meeting, Proceedings, IAEA TECDOC-650, p. 118-127

Matthews, R., Koch, R., Leppin, M., Powell, B., and Sopuck, V., 1997, Advances in integrated exploration for unconformity uranium deposits in Western Canada; in Proceedings of Exploration 97: Fourth Decennial International Conference on Mineral Exploration, (ed.) A.G. Gubins; GEO F/X, 993-1001, 1068 p.

Maus S. and Dimri V.P., 1996, Depth estimation from the scaling power spectrum of potential field. Geophysical J. International, v. 124, pp. 113–120.

Mavko, G., Mukerji, T., Dvorkin, J., 2009, The Rock Physics Handbook. 2nd ed. Cambridge: Cambridge University Press. p 522.

McCracken, K. G., Pik, J. P., and Harris, R. W., 1984, Noise in EM exploration systems: Explor. Geophys., 15, 169-174.

McGill, B.D., Marlatt, J.L., Matthews, R.B., Sopuck, V.J., Homeniuk, L.A., and Hubregtse, J.J.,1993, The P2 North uranium deposit Saskatchewan, Canada; Exploration Mining Geology, v. 2, p. 321–331.

McMullan, S. R., R. B. Matthews and P. Robertshaw, 1987. Exploration geophysics for Athabasca uranium deposits: Exploration ’87 Proceedings, Ontario Geological Survey, Geophysical Methods: Their application to ore exploration, 3, 547 – 566.

Millard, M.J., 1988, Quaternary geology and drift prospecting Dawn Lake area, northern Saskatchewan; M.Sc. thesis, University of Saskatchewan, Saskatoon, Saskatchewan, 171 p.

Milsom, J., 1989. Field Geophysics, John Wiley & Sons, New York.

Moosavi, V., Packmann, S., Vallés, Iván, 2014, SOMPY a Python Library for Self-Orgenizing Map (SOM), github website, https://github.com/sevamoo/SOMPY

Mwenifumbo, C. J., B. E. Elliott, C. W. Jefferson, G. R. Bernius and K. A. Pflug, 2004. Physical rock properties from the Athabasca Group: designing geophysical exploration models for unconformity uranium deposits, Journal of Applied Geophysics, 55, 117-135.

Mwenifumbo, C.J., Percival, J.B., Bernius, G., Elliott, B., Jefferson, C.W., Wasyliuk, K., and Drever, G., 2007, Comparison of geophysical, mineralogical and stratigraphic attributes in drill holes MAC 218 and RL 88, McArthur River uranium camp, Athabasca Basin, Saskatchewan, in Jefferson, C.W., and Delaney, G., eds., EXTECH IV: Geology and Uranium EXploration TECHnology of the Proterozoic Athabasca Basin, Saskatchewan and Alberta: Geological Survey of Canada, Bulletin 588, (also Geological Association of Canada, Mineral Deposits Division, Special Publication 4; Saskatchewan Geological Society, Special Publication 18) p. 507-520.

Nabighian, M. N. and Macnae, J. C., 1991, Time-domain electromagnetic prospecting methods, in Electromagnetic Methods in Applied Geophysics. Vol. 2, pp. 427-479, ed. Nabighian, M. N., Soc. Expl. Geophys., Tulsa.

Nabighian, M. N., and Macnae, J. C., 2005, Electrical and EM methods, 1980–2005 The Leading Edge, 24, 42-45.

Naidu, P. S., 1968, Spectrum of the Potential Field due to Randomly Distributed Sources. Geophysics, v. 33, pp. 337-345.

Naidu, P.S. and Mathew, M.P., 1998, Analysis of geophysical potential fields, A digital signal processing approach. Elsevier Science publishers, Amseterdam, 298p.

Newman, G. A., G. W. Hohmann, and W. L. Anderson, 1986, Transient electromagnetic response of a three-dimensional body in a layered earth: Geophysics, 51, 1608–1627, http://dx.doi.org/10.1190/1.1442212.

Nur, A., Mavko, G., Dvorkin, J., Galmudi, D., 1998, Critical porosity: a key to relating

physical properties to porosity in rocks. Leading Edge 17, 357-362.

O'Dowd, C. R., Wood, G. R., Brisbin, D., and Powell, B. W., 2006, Enhancing uranium exploration through seismic methods and potential field modeling at the McArthur River mine site, Saskatchewan, Canada: 76th Annual International Meeting, SEG, Expanded Abstracts, 1253–1257.

Okabe, M., 1979, Analytical expressions for gravity anomalies due to homogeneous polyhedral bodies and translations into magnetic anomalies. Geophysics, Vol. 44, No. 4; P. 730-741.

Okwueze, E.E., 1988, Mapping Bedrock Surface and Lithology with the Seismic Refraction Method in Basement Area. Physics, 26, pp 33-40.

Oldenburg, D. W., and Li, Y., 2005, Inversion for Applied Geophysics: A Tutorial. Near-Surface Geophysics: pp. 89-150. eISBN: 978-1- 56080-171-9

Paasche, H., and J. Tronicke, 2007, Cooperative inversion of 2D geophysical data sets: A zonal approach based on fuzzy c-means cluster analysis: Geophysics, 72, no. 3, A35–A39, doi: 10.1190/1.2670341.

Palmer, D., 1980, The Generalized Reciprocal Method of Seismic Refraction Interpretation, Soc. of Expl. Geophysicists, Tulsa, Oklahoma.

Palmer, D., 1981, An Introduction to the generalized reciprocal method of seismic refraction interpretation. Geophysics 46: 1508-1518.

Papoulis, A., 1962, The Fourier integral and its applications: McGraw-Hill.

Patterson Mining Geophysics Ltd., 2003, CREE extension project, geophysical field program grid at Moon Lake area, logistics report, Saskatchewan, Canada, 19p.

Pilkington, M., 1989, Variable-depth magnetization mapping: application to the Athabasca

Basin, northern Alberta and Saskatchewan, Canada: Geophysics, v. 54, p. 1164-1173.

Perrouty, S., Gaillard, N., Piette-Lauzière, N., et al., 2017, Structural setting for Canadian Malartic style of gold mineralization in the Pontiac Subprovince, south of the Cadillac Larder Lake Deformation Zone, Québec, Canada. Ore Geology Reviews 100. doi: 10.1016/j.oregeorev.2017.01.009

Powell, B., Wood, G., and Bzdel, L., 2007, Advances in geophysical exploration for uranium deposits in the Athabasca Basin, in Exploration 07 Proceedings Fifth Decennial Conference on Geophysics and Geochemistry of Minerals, ed. B. Milkereit, p. 771-790.

Rainbird, R. H., R. A. Stern, N. Rayner and C. W. Jefferson, 2007. Age, provenance, and regional correlation of the Athabasca Group, Saskatchewan and Alberta, constrained by igneous and detrital zircon geochronology; in Jefferson, C.W., and Delaney, G., eds., EXTECH IV: Geology and Uranium EXploration TECHnology of the Proterozoic Athabasca Basin, Saskatchewan and Alberta: Geological Survey of Canada, Bulletin 588 (also Saskatchewan Geological Society, Special Publication 18; Geological Association of Canada, Mineral Deposits Division, Special Publication 4).

Ramaekers, P., 1981. hudsonian and Helikian basins of the Athabasca Region, northern Saskatchewan, in Proterozoic Basins of Canada, (ed.) F.H.A. Campbell, GSC, paper 81 – 10, 219 – 233.

Ramaekers, P., 1990, Geology of the Athabasca Group (Helikian) in northern Saskatchewan; Saskatchewan Geological Survey, Report 195, 49 p.

Ramaekers, P. and Catuneanu, O., 2004, Development and sequences of the Athabasca Basin, Early Proterozoic, Saskatchewan and Alberta, Canada; in The Precambrian Earth: Tempos and Events, (ed.) P.G. Eriksson, W. Altermann, D.R. Nelson, W.U. Mueller, and O. Catuneanu; Elsevier, Amsterdam, Netherlands, p. 705–723.

Ramaekers, P., Jefferson, C.W., Yeo, G.M., Collier, B., Long, D.G.F., Catuneanu, O.,

Bernier, S., Kupsch, B., Post, R., Drever, G., McHardy, S., Jiricka, D., Cutts, C., and Wheatley, K., 2007, Revised geological map and stratigraphy of the Athabasca Group, Saskatchewan and Alberta, in Jefferson, C.W., and Delaney, G., eds., EXTECH IV: Geology and Uranium EXploration TECHnology of the Proterozoic Athabasca Basin, Saskatchewan and Alberta: Geological Survey of Canada, Bulletin 588, (also Geological Association of Canada, Mineral Deposits Division, Special Publication 4; Saskatchewan Geological Society, Special Publication 18) p. 155-192.

Rayner, J.N. ,1971, An Introduction to Spectral Analysis. Pion, England.

Redpath, B.B., 1973, Seismic refraction exploration for engineering site investigations, National Technical Information Service, 63 pp.

Reynolds, J. M., 1997, An Introduction to Applied and Environmental Geophysics. John Wiley & Sons.

Ruzicka, V., 1996, Unconformity associated uranium, Geology of Canada, 8, 197 – 210.

Schön, J.H., 1996, Physical Properties of Rocks: Fundamentals and Principles of Petrophysics (Handbook of Geophysical Exploration Series). Pergamon Press, London.

Schön, J.H., 2011, Physical Properties of Rocks: A Workbook, Elsevier publications, p 494.

Schreiner, B.T., 1983, Quaternary geology of the NEA/IAEA Athabasca test area; in Uranium Exploration in the Athabasca Basin, Saskatchewan, Canada, (ed.) E.M. Cameron; Geological Survey of Canada, Paper 82-11, p. 27–32.

Schreiner, B.T., 1984a, Quaternary geology of the Precambrian Shield, Saskatchewan; Saskatchewan Energy and Mines Report 221, 106 p., 1 map, scale 1:1 000 000.

Shaw, J. and Kvill, D., 1984, A glaciofluvial origin for drumlins of the Livingston Lake area, Saskatchewan, Canadian Journal of Earth Sciences, v. 21, p. 1442–1459.

Sheriff, R. E., Geldart, L. P., 1995, Exploration Seismology (2nd ed.). Cambridge University Press. p. 292.

Shewchuk, J. R., 1996, Triangle: Engineering a 2D Quality Mesh Generator and Delaunay Triangulator, in "Applied Computational Geometry: Towards Geometric Engineering" (Ming C. Lin and Dinesh Manocha, editors), volume 1148 of Lecture Notes in Computer Science, pages 203-222, Springer-Verlag, Berlin.

Shi, D., Milkereit, B., and Sun, L. F., 2014, Elastic and viscoelastic modeling of seismic waves in the Athabasca Basin, Canada. In 2014 SEG Annual Meeting. Society of Exploration Geophysicists.

Si, H., 2015, "TetGen, a Delaunay-Based Quality Tetrahedral Mesh Generator". ACM Trans. on Mathematical Software. 41 (2), Article 11 (February 2015), 36 pages. DOI=10.1145/2629697 http://doi.acm.org/10.1145/2629697.

Simpson, M.A., 1997, Surficial geology of Saskatchewan; Saskatchewan Energy and Mines–Saskatchewan Research Council, scale 1:1 000 000.

Sjörgen, B., 1984, Shallow refraction seismics. Springer Netherlands. p. VII. 270. DOI: 10.1007/978-94-009-5546-2.

Smith, R. S., Thurston, J. B., Dai, T. F., and MacLeod, I. N., 1998, iSPI —- the improved source parameter imaging method: Geophysical Prospecting, 46, 141–151.

Sobczak, L.W., 1983, Gravity surveys in the NEA/IAEA Athabasca Test Area; in Uranium Exploration in Athabasca Basin, Saskatchewan, Canada, ed. E.M. Cameron; Geological Survey of Canada, Paper 82-11, p. 151-166.

Spector, A., and Grant, F.S., 1970, Statistical models for interpreting aeromagnetic data, Geophysics, v.35, no.2, pp. 293-302.

Sproule, J.C., 1939, The Pleistocene geology of the Cree Lake region, Saskatchewan;

Transactions of the Royal Society of Canada, third series, v. 33, sec. 4, p. 101–109.

Stoffa, P.L., and Buhl, P., 1979, Two-ship multichannel seismic experiments for deep crustal studies: expanded spread and constant offset profiles. J. Geophys. Res., 84, 7645–60.

Swift, C.M. (1988). Fundamentals of the electromagnetic methods, in: Nabighian, M.N. Ed., Electromagnetic methods in applied geophysics, Soc. Expl. Geophysisic.

Telford, W. M., Geldart, L. P., Sheriff, R. E., and Keys, D. A., 1976, Applied geophysics. Cambridge University Press.

Thomas, D.J., 1983, Distribution, Geological Controls and Genesis of Uraniferous Pegmatites in the Cree Lake Zone of northern Saskatchewan: M.Sc. thesis, University of Regina, Regina, Saskatchewan, 213 p.

Thomas, D.J., Jefferson, C.W., Yeo, G.M., Card, C., and Sopuck, V., 2002, Introduction; in Field Trip A1. The Eastern Athabasca Basin and its Uranium Deposits, (ed.) N. Andrade, G. Breton, C.W. Jefferson, D.J. Thomas, G. Tourigny, S. Wilson, and G.M. Yeo; Geological Association of Canada–Mineralogical Association of Canada Guidebook, Saskatoon, Saskatchewan, p. 1–22.

Thomas, M. D. and McHardy, S., 2007. Magnetic insights into basement geology in the area of McArthur River uranium deposit, Athabasca Basin, Saskatchewan, in Jefferson, C.W. and Delaney, G., eds., EXTECH IV: Geology and Uranium EXploration TECHnology of the Proterozoic Athabasca Basin, Saskatchewan and Alberta: Geological Survey of Canada, Bulletin 588 (also Saskatchewan Geological Society, Special Publication 18; Geological Association of Canada, Mineral Deposits Division, Special Publication 4).

Thomas, M.D. and Wood, G., 2007. Geological significance of gravity anomalies in the area of McArthur River uranium deposit, Athabasca Basin, Saskatchewan; in EXTECH

IV: Geology and Uranium EXploration TECHnology of the Proterozoic Athabasca Basin, Saskatchewan and Alberta, (ed.) C.W. Jefferson and G. Delaney; Geological Survey of Canada, Bulletin 588, p. 441–464.

Treitel, S., Clement, W.G. and Kaul, R.K., 1971, The spectral determination of depths of buried magnetic basement rocks. Geophysical Journal of the Royal Astronomical Society, v.24, pp. 415–428.

Tuncer, V., 2007, Exploration for unconformity type uranium deposits with audio-magnetotelluric data: A case study from the McArthur River Mine, Saskatchewan, Canada. M.Sc. Thesis, University of Alberta.

Van Wijk, K., J. A. Scales, W. Navidi, and L. Tenorio, 2002, Data and model uncertainty estimation for linear inversion: Geophysical Journal International, 149, 625–632.

Veillette, J. J., 2004, Geologie des Formations en Surface et Histoire Glaciaire, Cadillac, Quebec. Commission Geologique de Canada, Carte 2019A, Echelle 1/100 000.

Vibrometric Canada Limited, 2007, 3D seismic investigations at Millennium area, factual report, Saskatchewan, Canada, 40p.

Ward, S. M., and G. W. Hohmann, 1988, Electromagnetic Theory for Geophysical Applications, in Electromagnetic Methods in Applied Geophysics, Volume 1, Theory: Society of Exploration Geophysicists, 131–308.

Wares, R. & Burzynski, J., 2011. The Canadian Malartic Mine, Southern Abitibi Belt, Québec, Canada: Discovering and Development of an Archean Bulk-Tonnage Gold Deposit, s.l.: Osisko Mining Corporation.

Wasyliuk, K., 2002. Petrogenesis of the kaolinite-group minerals in the eastern Athabasca basin of northern Saskatchewan: Applications to uranium mineralization; M. Sc. Thesis, University of Saskatchewan, Saskatoon, Saskatchewan, 140 p.

Weiss, C. J., 2010, Triangulated finite difference methods for global-scale electromagnetic induction simulations of whole mantle electrical heterogeneity: Geochemistry, Geophysics, Geosystems, 11, 1–15, doi: 10.1029/ 2010GC003283.

Wessel, P. and W. H. F. Smith, 1991, Free software helps map and display data, EOS Trans. AGU, 72, 441.

West G. F., and Macnae J. C., 1991, 1. Physics of the Electromagnetic Induction Exploration Method. Electromagnetic Methods in Applied Geophysics: pp. 5-46.

White, D. J., Z. Hajnal, B. Roberts, I. Gyorfi, B. Reilkoff, B. Bellefleur, C. Mueller, S. Woelz, C. J. Mwenifumbo, E. Takacs, D. R. Schmitt, D. Brisbin, C. W. Jefferson, R. Koch, B. Powell and I. Annesley, 2007. Seismic methods for uranium exploration; an overview of EXTECH IV seismic studies at the McArthur River mining camp, Athabasca Basin, Saskatchewan; in Jefferson, C.W., and Delaney, G., eds., EXTECH IV: Geology and Uranium EXploration TECHnology of the Proterozoic Athabasca Basin, Saskatchewan and Alberta: Geological Survey of Canada, Bulletin 588.

Witherly, K., Irvine, R., and Morrison, E.B., 2004, The Geotech VTEM time domain helicopter EM system, SEG Expanded Abstracts, 23, 1217-1221.

Witherly, K., and Irvine, R, 2006, The VTEM airborne electromagnetic system – benchmarking continuous improvement via repeat surveys over time, SEG Expanded Abstracts, 25, 1273-1277.

Wood, G. and Thomas, M.D., 2002. Modelling of high-resolution gravity data near the McArthur River uranium deposit, Athabasca Basin; in Summary of Investigations 2002, Volume 2, Saskatchewan Geological Survey, Sask. Industry Resources, Misc. Rep. 2002-4.2, CD-ROM, Paper D-16, 9p.

Wright, C., Barton, T., Goleby, B.R., Spence, A.G. and Pester, D., 1990, The interpretation of expanding spread profiles: examples from central and eastern Australia. Tectonophysics, 173, 73–82.

Yeo, G.M., and Delaney, G., 2007, The Wollaston Supergroup, stratigraphy and metallogeny of a Paleoproterozoic Wilson cycle in the Trans- Hudson Orogen, Saskatchewan, in Jefferson, C.W., and Delaney, G., eds., EXTECH IV: Geology and Uranium EXploration TECHnology of the Proterozoic Athabasca Basin, Saskatchewan and Alberta: Geological Survey of Canada, Bulletin 588, p. 89-118.

Zhang, J. and Toksoz, M.N., (1998), "Nonlinear Refraction Traveltime Tomography," Society of Exploration Geophysicists, Geophysics, Vol. 63, No.5, pp. 1726-1737.

Appendix A: PODIUM software

PODIUM (Preparation of Data for Inversion on Unstructured Meshes; Lelièvre and Farquharson, 2015) is a package of software. It has many utilities for working with meshes. The package helps users to prepare data and models for running forward and inverse modelling programs, and for assessing the results of such modelling. Following are some programs in this package which I have frequently used in this research:

add_noise: It adds noise and/or assigns uncertainties to data (.node or .ele file).

combine_mesh: It combines up to 8 mesh files. Mesh file is made from ele and node files.

combine_node: It combines up to 8 node files.

combine_poly: It combines up to 8 poly files. "poly" file is an input for the "tetgen" and "triangle" codes.

convert_format: It is to convert different format of files to each other as follow:

Input file extensions are mandatory:
- Datamine (.pt .tr .ssv)
- Geomatic (.dat .txt etc)
- Geomview (.off)
- Medit (.mesh)
- Gocad solids (.ts .so)
- GSS xyz mag (.xyz etc)
- WSINV3DMT (.model)

Output file extension is optional:
- .node
- .ele
- .vtu

interpolate_topography: Topography interpolation at specified points.

make_obs: This code creates gridded observation locations and writes them to a "node" file.

mesh2poly: Converts .node and .ele files to a .poly file for use with meshing programs.

mesh2solid: Converts .node and .ele files to a .tsurf or .tvol file.

mesh2vtu: It generates “vtu” file (which is the input file for the “ParaView” software) using “node” and “ele” files.

node2vtu: It generates “vtu” file from a “node” file.

poly2mesh: It converts a .poly file to .node and .ele files.

poly2vtu: It generates “vtu” file from a “poly” file.

print_coordinates: Reads data from a file which can be a .node or .ele file, and prints coordinate and attribute range information (minimum, maximum values, etc.).

remove_trend: Removes a polynomial trend from (x, y, d) data in a .node file.

transform_coordinates: Coordinate transformation of data or a model.

Appendix B: A 2D forward gravity code

File: /home/mehrdad/Desktop/Forward_Code.f90 Page 1 of 2

```
Program Forward

!#################################################################
!2D gravity forward modelling
!by: Mehrdad Darijani
!    March 2014
!================================
!================================
!This code is written based on the Okabe's paper: "Okabe, M., 1979, Analytical  expressions for gravity
anomalies due to homogeneous polyhedral bodies and translations into magnetic anomalies, Geophysics, Vol.
44 No. 4, 730-741."
!The file "obspoints.txt" is observation point coordinates. At file "mesh.1.node"  the first column is
number of vertice and two next column are respectively x and z cordinates
!At file "mesh.1.ele" the first column to end are: number of cell and the numbers of its three vertices
!The z axis is considered negative downward while in plotting the mesh in the Paraview software it
consider positive. !The z axis is considered positive upward.(density=g/cm^3)
!The outputs are the coordinates of x-axes of observation points and gravity responces.
!The output, gravity, can be in mgal (by multipying original "gal" to 1000).
!The input coordinates are in meters which will be transformed to cm afterwards in the code.
!#################################################################

implicit none
real::g,temp1,temp2,temp3,temp4, temp5, temp6,temp7,temp8,temp9, temp10,sumg,pof
real,dimension(1000000)::xobs,zobs,xvert,zvert,grav,x,z,xx,zz,sinsai,cossai,kn,first,second,&
                         &third,ll,lll,u,gravity,dens
integer,dimension(100000,5)::vert
integer::status,nobs,nvert,h,i,j,k,f,r,ncell

!----------------------------------------
g=6.67384*1.0E-8          !! cm^3/gs^2
!----------------------------------------

!!   Read the observation point from file and count them
nobs=0
open(unit=1, file="obspoints.txt")
    do
    read(1,*,iostat=status)temp1,temp2
    if (status/=0) exit
    nobs=nobs+1
    xobs(nobs)=temp1
    zobs(nobs)=temp2
    end do
!----------------------------------------

!!   Reading the vertice values of cells and count them
open(unit=3, file="mesh.1.node")
do
read(3,*,iostat=status)temp9,temp3,temp4
if (status/=0) exit
nvert=temp9
xvert(nvert)=temp3
zvert(nvert)=temp4
end do
!----------------------------------------

!!   Reading the cell number and its vertices and density
open(unit=5, file="mesh.1.ele")
do
read(5,*,iostat=status)temp10,temp5,temp6,temp7
if (status/=0) exit
ncell=temp10
vert(ncell,1)=temp5
vert(ncell,2)=temp6
vert(ncell,3)=temp7
vert(ncell,4)=vert(ncell,1)
end do
!----------------------------------------
```

```
!!   Reading the density
open(unit=44, file="density.txt")
do f=1,ncell
read(44,*,iostat=status)temp8
if (status/=0) exit
dens(f)=temp8
end do
!----------------------------------------

!!   Find the answer for observation points
do k=1,nobs
  do r=1,ncell

    do i=1,4
      x(i)=(xvert(vert(r,i))-xobs(k))*100
      z(i)=(zvert(vert(r,i))-zobs(k))*100
    end do

    do i=1,4
      sinsai(i)=(x(i+1)-x(i))/sqrt((z(i+1)-z(i))**2+(x(i+1)-x(i))**2)
      cossai(i)=(z(i+1)-z(i))/sqrt((z(i+1)-z(i))**2+(x(i+1)-x(i))**2)
    end do

    do i=1,3
      kn(i)=-sinsai(i)
        do j=i,i+1
          zz(j)=z(j)*cossai(i)+x(j)*sinsai(i)
          xx(j)=-z(j)*sinsai(i)+x(j)*cossai(i)
          pof=zz(j)**2+xx(j)**2
          if (pof==0) then
            first(j)=0
            else
            first(j)=zz(j)*log(pof)
          end if
          if (xx(j)==0) then
            second(j)=0
            else
            second(j)=2*xx(j)*atan(zz(j)/xx(j))
          end if
            third=2*zz(j)
            ll(j)=first(j)+second(j)-third(j)
        end do
          lll(i)=ll(i+1)-ll(i)
        end do

        sumg=0
        do i=1,3
          u(i)=lll(i)*kn(i)
          sumg=sumg+u(i)
        end do
      grav(r)=g*dens(r)*sumg  !*(1.0E3)
      end do

    gravity(k)=0
  do i=1,ncell
    gravity(k)=gravity(k)+grav(i)
  end do
end do
!----------------------------------------

!! Writting the result file
open (unit=10,file="obsdata.txt")
Do h=1,nobs
 write(10,*)xobs(h),gravity(h)
end do
end program
```

Appendix C: 2D linear inversion of gravity data

A simple example: 2D linear inversion of gravity data

A simple example of inversion method is explained in this appendix. It is a 2D model in which the mesh is made from triangular cells. The 2D linear equation for the inversion of gravity data using the minimum structure method can be simply defined as (Oldenburg and Li, 2005):

$$\{J^T W_d^T W_d J + \beta W_z^T W_t^T W_t W_z\}\delta m = J^T W_d^T W_d\Big(d^{obs} - d(m)\Big) - \beta W_z^T W_t^T W_t W_z m_0$$

where $\delta m = m - m_0$, m is the unknown vector containing the density values for cells, and $m_0$is the initial model which can be zero (so the term $\beta W_z^T W_m^T W_m W_z m_0$ can be removed!). Matrix m is

$$m = \begin{bmatrix} m_1 \\ \vdots \\ m_M \end{bmatrix}.$$

The data-weighting, W_d, is

$(W_d)_{jj} = \frac{1}{\sigma_j \times d_j}$, where

$$W_d = \begin{bmatrix} \frac{1}{\sigma_1 \times d_1} & \cdots & 0 \\ \vdots & \ddots & \vdots \\ 0 & \cdots & \frac{1}{\sigma_N \times d_N} \end{bmatrix}$$

where W_d is an $N \times N$ diagonal matrix whose elements are the reciprocals of the estimates of the standard deviations of the noise (σ_j) in the observations times the observed data (jth observation station), and N is the number of observation points.

Matrix $\boldsymbol{W}_t$ contains model differences between adjacent grid cells. It is the first-order spatial finite-difference matrix in which each row has two non- zero elements with the same value but different signs that are the reciprocal of the distance between the centroids of two adjacent triangles. Hence, in this matrix, the number of rows would be the number of connections between the centroids and the number of columns is the number of triangles (i.e. M). The following equation shows the W_t matrix for a simple example in Figure C1.

$$W_t = \begin{bmatrix} \frac{1}{c_{12}} & \frac{-1}{c_{12}} & 0 & 0 \\ 0 & \frac{1}{c_{23}} & \frac{-1}{c_{23}} & 0 \\ 0 & \frac{1}{c_{24}} & 0 & \frac{-1}{c_{24}} \end{bmatrix}$$

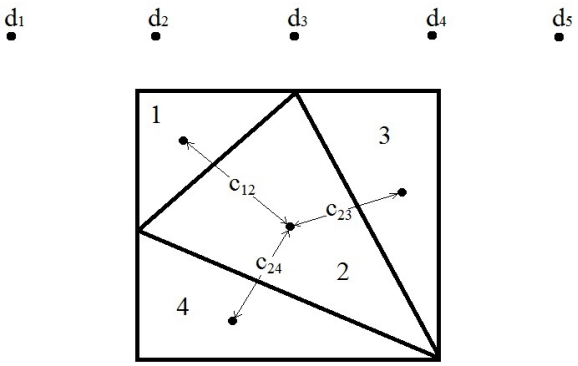

Figure C1: Simple triangular mesh and observation points.

In the potential methods (e.g. gravity and magnetic methods), to allow the code to generate models that have structure at depth, we have to consider a depth weighting. Otherwise, the structures will be reconstructed close to the surface. W_z is the depth

weighting function and an $M \times M$ diagonal matrix, where M is the number of cells, given by

$$(W_z)_{ii} = \frac{1}{(z+z_0)^{v/2}}$$

where z refers to the depth of the centroid of each triangle (ith triangle), v is a constant between 0 and 2, and the value of z_0 depends on the height of the observation points and size of mesh cells.

The Jacobian matrix, J, contains the first-order derivatives of the gravitational field with respect to all the model parameters at all the observation points. As you remember, we had the following equation in Chapter 3 for the gravity forward modelling:

$$U_k = \rho \left[G \sum_{i=1} k^T n_i I_i \right]$$

By comparing this equation with $d = Gm$ (general forward equation), it can be seen that U is the datum at an observation point, ρ is the model parameter (i.e. density) for a cell, and the remaining is the kernel matrix values that make up the Jacobian matrix for respective cell and observation point. Based on Figure 5.10, the following equations use the values in the Jacobian matrix.

$$d_1 = \rho_1 J_{11} + \rho_2 J_{12} + \rho_3 J_{13} + \rho_4 J_{14}$$

$$\vdots \qquad \vdots \qquad \vdots$$

$$d_5 = \rho_1 J_{51} + \rho_2 J_{52} + \rho_3 J_{53} + \rho_4 J_{54}$$

Therefore,

$$J = \begin{bmatrix} J_{11} & \cdots & J_{14} \\ \vdots & \ddots & \vdots \\ J_{51} & \cdots & J_{54} \end{bmatrix},$$

where J is an $N \times M$ matrix. Thus, the Jacobian matrix contains the forward problem.

The inversion equation is tested with synthetic data. The true model was a square anomaly with a density contrast of 1 g/cc. The gravity data were synthetized (using the code in Appendix B) along a 100 m profile with a station spacing of 5 m. The data is inverted using my code for the inversion equations given above over a 2D triangular mesh (see following for Fortran code). The reconstructed model obtained by the inversion, using parameters v=1, β=0.1 and z_0=0, is shown in Figure C2.

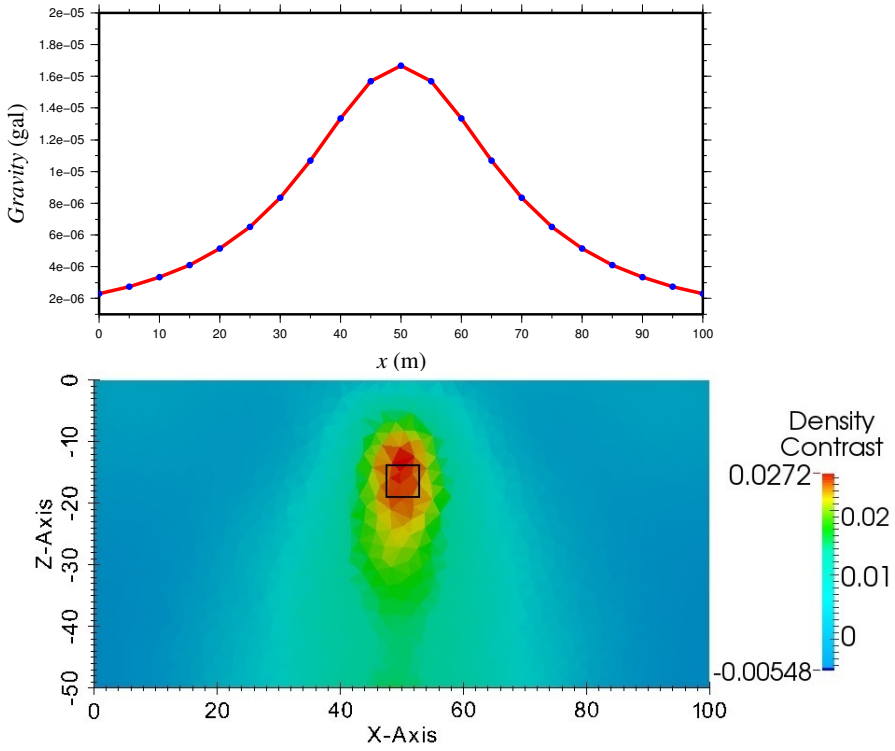

Figure C2: The observed data (blue points), calculated data (red curve) and 2D inversion result for v=1, β=0.1 and z_0=0. The black square shows the location of the true anomaly.

```
Program Inversion

!#####################################################################
!2D linear inversion of gravity data
!by: Mehrdad Darijani
!    2014-04-04
!============================
!============================
!This code is a linear code (without iteration) based on Minimun Structure method (Li and Oldenburg, 1996)
!The file "obspoints.txt" is observation point coordinates. At file "mesh.1.node"  the first column is
number of vertice and two next column are respectively x and z cordinates
!At file "mesh.1.ele" the first column to end are: number of cell and the numbers of its three vertices
!At file "mesh.1.neigh" the first column to end are: number of cell and the numbers of its three neighbors
!The z axis is considered negative downward while in plotting the mesh in the Paraview software it
consider positive.
!#####################################################################

implicit none

real(kind=8)::g,sumg,z0,beta,lambda,temp1,temp2,temp3,temp4,temp8,temp16,ooo,temp15,pof,pof1
integer::status,nobs,nvert,ncell,i,i1,i2,i3,i4,nne,i11,temp11,temp9,temp10&
         &,i6,i7,i8,i9,i10,temp5,temp6,temp7,nne1,p,q,i5,k,r,e,j,errorflag
integer,dimension(1000000)::n1,n2,n3
integer,dimension(100000,5)::vert
real(kind=8),dimension(1000000)::x,z,xx,zz,sinsai,cossai,kn,first,second,zobs,xobs&
         &,zvert,xvert,zcen,xcen,d,third,ll,lll,u,grav
real(kind=8),allocatable,dimension(:,:)::obsd,wd,wz,wt,rem,pred,jac,dd,A,B,OO,PP,QQ&
         &,RR,model,fmodel,IA

!----------------------------------------

!write (*,*)'Please enter a number for z0 , Beta and Lambda:
!read (*,*)z0,beta,lambda
z0=0
beta=1
lambda=0.1
!----------------------------------------

!!  Read the observation point from file and counting them
nobs=0
open(unit=1, file="obspoints.txt")
do
  read(1,*,iostat=status)temp1,temp2
  if (status/=0) exit
  nobs=nobs+1
  xobs(nobs)=temp1
  zobs(nobs)=temp2
end do
!----------------------------------------

!!  Reading the vertice coordinates of cells and counting them
open(unit=3, file="mesh.1.node")
do
  read(3,*,iostat=status)temp9,temp3,temp4
  if (status/=0) exit
  nvert=temp9
  xvert(nvert)=temp3
  zvert(nvert)=temp4
end do
!----------------------------------------

!!  Reading the cell number and its vertices
open(unit=5, file="mesh.1.ele")
do
  read(5,*,iostat=status)temp10,temp5,temp6,temp7
  if (status/=0) exit
  ncell=temp10
```

```
  vert(ncell,1)=temp5
  vert(ncell,2)=temp6
  vert(ncell,3)=temp7
  vert(ncell,4)=vert(ncell,1)
end do
!----------------------------------------

!!  Obtaining the centriod coordinates for each cell
do i=1,ncell
  xcen(i)=((xvert(vert(i,1))+xvert(vert(i,2))+xvert(vert(i,3)))/3)
  zcen(i)=((zvert(vert(i,1))+zvert(vert(i,2))+zvert(vert(i,3)))/3)
end do
!----------------------------------------

!!  Forming the Wz matrix
allocate(wz(ncell,ncell))
do i1=1,ncell
  do i2=1,ncell
    if (i1==i2) then
      wz(i1,i2)=1/((zcen(i1)+z0)**(beta/2))
    else
      wz(i1,i2)=0
    end if
  end do
end do
!----------------------------------------

!!  Reading the observed data (data unit:cm/s^2 or gal)
allocate(obsd(nobs,1))
i11=0
open (unit=7, file="obsdata.txt")
do
  read(7,*,iostat=status)temp8,temp16
  if (status/=0) exit
  i11=i11+1
  ooo=temp8
  obsd(i11,1)=temp16
end do
!----------------------------------------

!! Forming the Wd matrix
allocate(wd(nobs,nobs))
do i3=1,nobs
  do i4=1,nobs
    if (i3==i4) then
      wd(i3,i4)=1/(0.05*obsd(i3,1))
    else
      wd(i3,i4)=0
    end if
  end do
end do
!----------------------------------------

nne=0   !number of neighbors
open(unit=13, file="mesh.1.neigh")
do q=1,ncell
  read(13,*,iostat=status)temp11,n1(q),n2(q),n3(q)
  if (status/=0) exit
  if (n1(q)>temp11) then
    nne=nne+1
    d(nne)=sqrt((xcen(temp11)-xcen(n1(q)))**2+(zcen(temp11)-zcen(n1(q)))**2)
  end if
  if (n2(q)>temp11) then
    nne=nne+1
    d(nne)=sqrt((xcen(temp11)-xcen(n2(q)))**2+(zcen(temp11)-zcen(n2(q)))**2)
  end if
  if (n3(q)>temp11) then
```

```
    nne=nne+1
    d(nne)=sqrt((xcen(temp11)-xcen(n3(q)))**2+(zcen(temp11)-zcen(n3(q)))**2)
  end if
end do
!----------------------------------------

!! Forming the Wt matrix
allocate(wt(nne,ncell))
wt=0
nne1=0
do  p=1,ncell
  if (n1(p)>p) then
    nne1=nne1+1
    wt(nne1,p)= 1/(d(nne1))
    wt(nne1,n1(p))= -1/(d(nne1))
  end if
  if (n2(p)>p) then
    nne1=nne1+1
    wt(nne1,p)= 1/(d(nne1))
    wt(nne1,n2(p))= -1/(d(nne1))
  end if
  if (n3(p)>p) then
    nne1=nne1+1
    wt(nne1,p)= 1/(d(nne1))
    wt(nne1,n3(p))= -1/(d(nne1))
  end if
end do
!----------------------------------------

!! Reading the reference model 'rem' (density unit:g/cm^3)  >>>> it can be zero
allocate(rem(ncell,1))
open (unit=11, file="refmodel.txt")
do i5=1,ncell
  read(11,*,iostat=status)temp15
  if (status/=0) exit
  rem(i5,1)=temp15
end do
!----------------------------------------

!! Forming reference model data & jacobian [Forward Modelling Section]
g=6.67384*1.0E-8      ! cm^3/gs^2
allocate(pred(nobs,1),jac(nobs,ncell))
jac=0
do k=1,nobs
  do r=1,ncell
    do e=1,4
      x(e)=(xvert(vert(r,e))-xobs(k))*100
      z(e)=(zvert(vert(r,e))-zobs(k))*100
    end do
    do e=1,4
      sinsai(e)=(x(e+1)-x(e))/sqrt((z(e+1)-z(e))**2+(x(e+1)-x(e))**2)
      cossai(e)=(z(e+1)-z(e))/sqrt((z(e+1)-z(e))**2+(x(e+1)-x(e))**2)
               if (abs(cossai(e))<1.0e-8) then
               cossai(e)=0
               end if
    end do
    do e=1,3
       kn(e)=-sinsai(e)
       do j=e,e+1
          zz(j)=z(j)*cossai(e)+x(j)*sinsai(e)
          xx(j)=-z(j)*sinsai(e)+x(j)*cossai(e)
          pof=zz(j)**2+xx(j)**2
          if (pof==0) then
            first(j)=0
          else
            first(j)=zz(j)*log(pof)
          end if
```

```
          pof1=zz(j)/xx(j)
          if (xx(j)==0) then
            second(j)=0
          else
            second(j)=2*xx(j)*atan(pof1)
          end if
            third=2*zz(j)
            ll(j)=first(j)+second(j)-third(j)
        end do
        lll(e)=ll(e+1)-ll(e)
    end do
    sumg=0
    do e=1,3
    u(e)=lll(e)*kn(e)
    sumg=sumg+u(e)
    end do
    jac(k,r)=g*sumg  !Jacobian
    grav(r)=jac(k,r)*rem(r,1)
  end do
  pred(k,1)=0
  do e=1,ncell
  pred(k,1)=pred(k,1)+grav(e)
  end do
end do
!----------------------------------------

!!  Inversion equation calculations
allocate(dd(nobs,1))
do i6=1,nobs
  dd(i6,1)=obsd(i6,1)-pred(i6,1)
end do
allocate(A(ncell,ncell),OO(ncell,ncell),PP(ncell,ncell),B(ncell,1),QQ(ncell,1),RR(ncell,1))
OO=(matmul(matmul(matmul(transpose(jac),transpose(wd)),wd),jac))
PP=(lambda)*(matmul(matmul(matmul(transpose(wz),transpose(wt)),wt),wz))
QQ=(matmul(matmul(matmul(transpose(jac),transpose(wd)),wd),dd))
RR=(lambda)*(matmul(matmul(matmul(matmul(transpose(wz),transpose(wt)),wt),wz),rem))
do i7=1,ncell
  do i8=1,ncell
    A(i7,i8)=OO(i7,i8)+PP(i7,i8)
  end do
end do
do i9=1,ncell
  B(i9,1)=QQ(i9,1)-RR(i9,1)
end do

allocate(IA(ncell,ncell))
call FINDInv(A,IA,ncell,errorflag) !Finding the inverse of a square matrix
allocate(model(ncell,1),fmodel(ncell,1))

model=(matmul(IA,B))
do i10=1,ncell
  fmodel(i10,1)=rem(i10,1)+model(i10,1)
end do
!----------------------------------------

!! Writting the file of final model
open (unit=20, file="density.txt")
do i10=1,ncell
write(20,*)fmodel(i10,1)
end do

end program

!*****************************************************************************!
!*****************************************************************************!

!Subroutine to find the inverse of a square matrix
```

```
!Author : Louisda16th a.k.a Ashwith J. Rego
!Reference : Algorithm has been well explained in:
!http://math.uww.edu/~mcfarlat/inverse.htm
!http://www.tutor.ms.unimelb.edu.au/matrix/matrix_inverse.html
SUBROUTINE FINDInv(matrix, inverse, n, errorflag)
        IMPLICIT NONE
        !Declarations
        INTEGER, INTENT(IN) :: n           ! n is size of square matrix (n*n)
        INTEGER, INTENT(OUT) :: errorflag  !Return error status. -1 for error, 0 for normal
        REAL(kind=8), INTENT(IN), DIMENSION(n,n) :: matrix   !Input matrix
        REAL(kind=8), INTENT(OUT), DIMENSION(n,n) :: inverse !Inverted matrix

        LOGICAL :: FLAG = .TRUE.
        INTEGER :: i, j, k, l
        REAL(kind=8) :: m
        REAL(kind=8), DIMENSION(n,2*n) :: augmatrix !augmented matrix

        !Augment input matrix with an identity matrix
        DO i = 1, n
            DO j = 1, 2*n
                IF (j <= n ) THEN
                        augmatrix(i,j) = matrix(i,j)
                ELSE IF ((i+n) == j) THEN
                        augmatrix(i,j) = 1
                Else
                        augmatrix(i,j) = 0
                ENDIF
            END DO
        END DO

        !Reduce augmented matrix to upper traingular form
        DO k =1, n-1
            IF (augmatrix(k,k) == 0) THEN
                FLAG = .FALSE.
                DO i = k+1, n
                        IF (augmatrix(i,k) /= 0) THEN
                                DO j = 1,2*n
                                        augmatrix(k,j) = augmatrix(k,j)+augmatrix(i,j)
                                END DO
                                FLAG = .TRUE.
                                EXIT
                        ENDIF
                        IF (FLAG .EQV. .FALSE.) THEN
                                PRINT*, "Matrix is non - invertible"
                                inverse = 0
                                errorflag = -1
                                return
                        ENDIF
                END DO
            ENDIF
                DO j = k+1, n
                        m = augmatrix(j,k)/augmatrix(k,k)
                        DO i = k, 2*n
                                augmatrix(j,i) = augmatrix(j,i) - m*augmatrix(k,i)
                        END DO
                END DO
        END DO

        !Test for invertibility
        DO i = 1, n
                IF (augmatrix(i,i) == 0) THEN
                        PRINT*, "Matrix is non - invertible"
                        inverse = 0
                        errorflag = -1
                        return
                ENDIF
        END DO
```

```
        !Make diagonal elements as 1
        DO i = 1 , n
                m = augmatrix(i,i)
                DO j = i , (2 * n)
                        augmatrix(i,j) = (augmatrix(i,j) / m)
                END DO
        END DO

        !Reduced right side half of augmented matrix to identity matrix
        DO k = n-1, 1, -1
                DO i =1, k
                m = augmatrix(i,k+1)
                        DO j = k, (2*n)
                                augmatrix(i,j) = augmatrix(i,j) -augmatrix(k+1,j) * m
                        END DO
                END DO
        END DO

        !store answer
        DO i =1, n
                DO j = 1, n
                        inverse(i,j) = augmatrix(i,j+n)
                END DO
        END DO
        errorflag = 0

!RETURN
END SUBROUTINE FINDinv
```

Appendix D: Gravity gradiometry and the terrain effect

Gravity gradiometry theory

Gravity gradiometry measures the variations in the three orthogonal directions of the components of the acceleration due to gravity. The unit of gravity gradient is the Eötvös (E), which is a unit of acceleration divided by distance, and it is equivalent to 10^{-4} mGal/m (or 10^{-9} s^{-2}; LaFehr and Nabighian, 2012). All gradient elements (tensors) are shown in Figure D1. For example, the vertical gravity gradient (G_{zz}) represents the rate of change of vertical gravity (g_z) with height (z), i.e.,

$$G_{zz} = \frac{\partial g_z}{\partial z}.$$

Therefore, the gravity field (g_z) can be calculated from the gradient tensor by means of integration in the z direction. The output of any integration process lacks an unknown constant of integration, therefore, the absolute value of the gravity field can not be calculated from the gradient tensor (Bell Geospace Limited, 2007). In the airborne gravity, the absolute measure of g_z cannot be acquired to the same precision as on the ground because of the aircraft acceleration. But, airborne gravity gradiometry can remove the aircraft motion effects, and deliver relative gravity data to an accuracy comparable with ground gravity data (CGG, 2014).

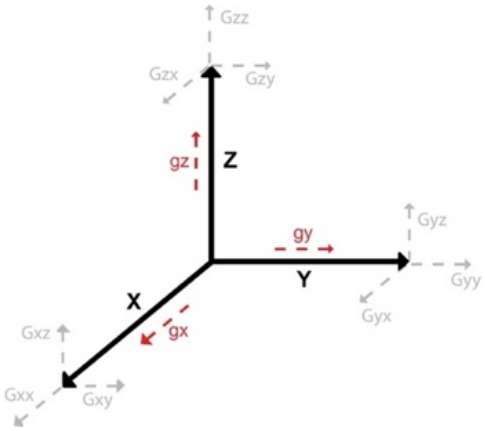

Figure D1: The relationships of the various gravity gradiometry elements (grey colour; adapted from www.wikipedia.org).

The modelled data considered here are compared with real HeliFALCON data (CGG, 2014) from the McArthur-Millennium area. The HeliFALCON gradiometer instrument acquires two elements of the gravity gradient tensor, namely G_{xy} and G_{uv} where $G_{uv}=(G_{xx} – G_{yy})/2$. G_{xy} and G_{uv} data can be transformed into other components as well as the vertical component of gravity (g_z; derived by integrating G_{zz}) which can be done in the Fourier domain. The G_{xy} and G_{zz} data are selected for plotting here. The directly measured G_{xy} data is appropriate for inversion to reconstruct the Earth model, and G_{zz} data is more sensitive to small and shallow structures and has greater spatial resolution than g_z (adapted from CMIC-Footprints project; CGG HeliFALCON gradiometry data report).

Terrain correction for gravity gradiometry data

Before moving on to consider different models of different degrees of realisticness and complexity, the terrain correction for gradiometry data is investigated. For this purpose, six components of the gradiometry tensor are synthetized using forward modelling for a model with a uniform density of 1 g/cc. The model is generated for a 6x6 km area below the

HeliFALCON survey (Figure D2). The forward modelling is done using an unstructured tetrahedral mesh, the advantage of which is that it can honour the topography to as fine a resolution as the topography is known. The model starts from an elevation of 450 m to a surface which includes a 10x10 m dense/refined topography of the Millennium area (Figure D3). These synthetized gradiometry data can be considered as the terrain effect.

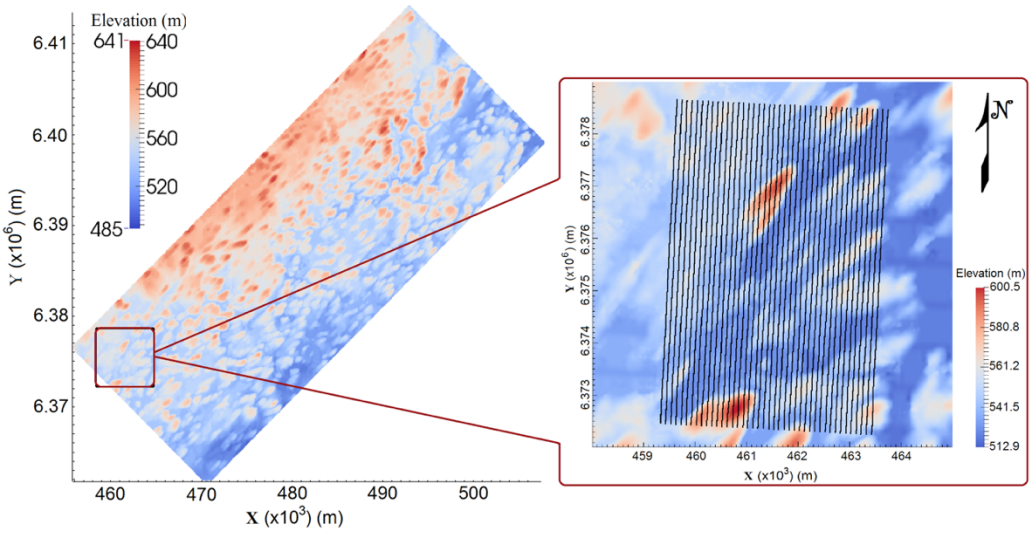

Figure D2: Topography of McArthur-Millennium corridor. Inset shows location of HeliFALCON survey lines (black) over the Millennium area. Tie lines are not shown.

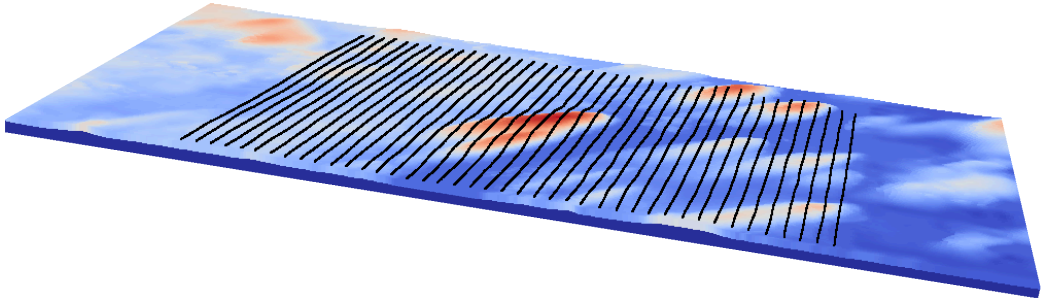

Figure D3: A part of model and HeliFALCON survey lines (black). Color scale is topography.

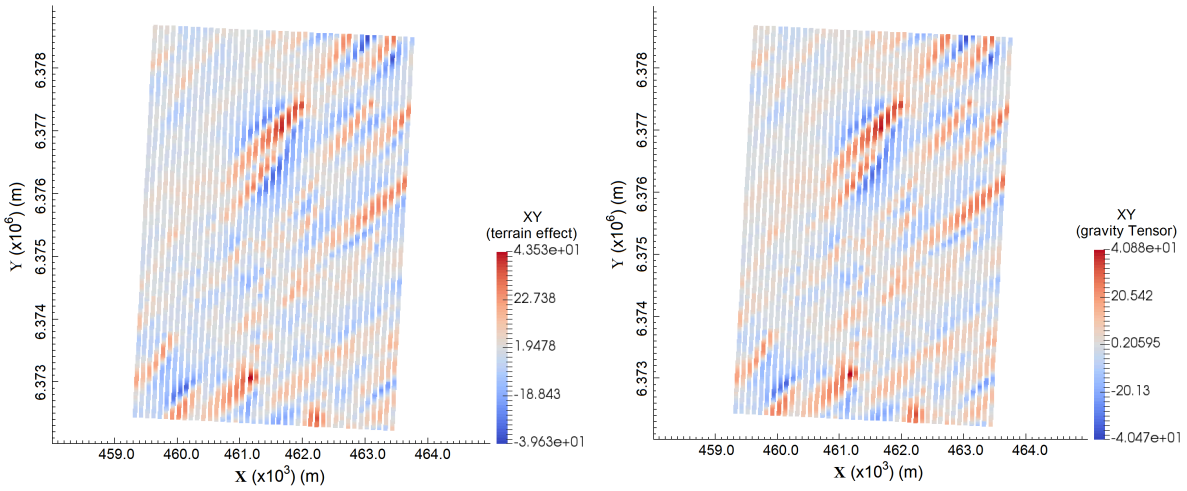

Figure D4: Terrain effect calculated for G_{xy} (left; CGG data) and gravity tensor synthetized for G_{xy} (right) for a density of 1g/cc (i.e. for the model in Figure D3). Unit: Eötvös.

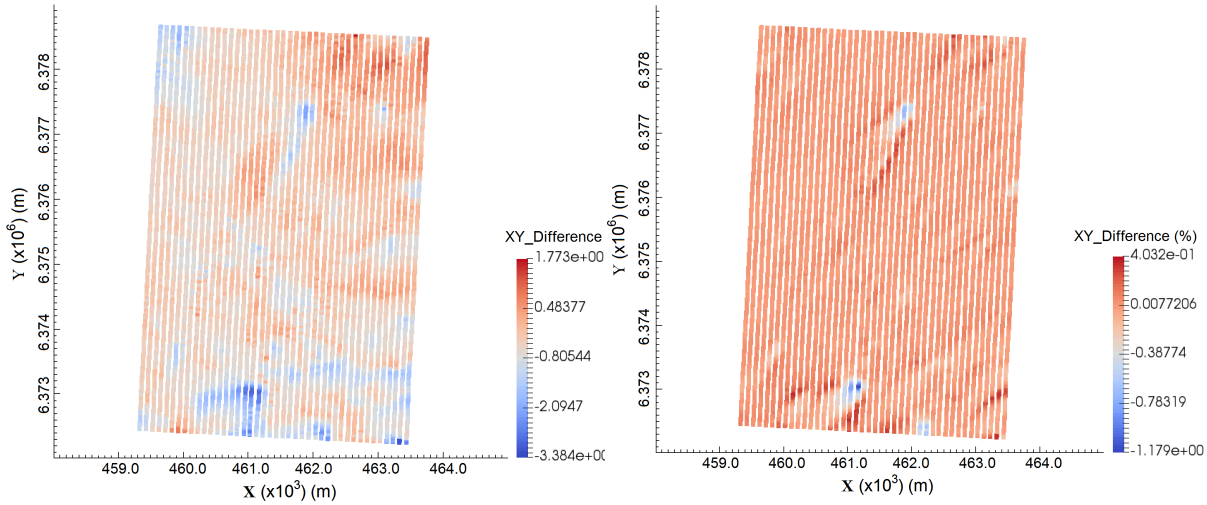

Figure D5: Difference (left) and percentage difference (right) between calculated terrain effect and synthetized gravity tensor for G_{xy} shown in Figure D4. Unit: Eötvös.

For two components G_{xy} and G_{zz}, the synthetized data are compared with terrain-effect data which is calculated using a Fourier-based technique by CGG (CMIC-Footprints project; CGG HeliFALCON gradiometry data report) for a terrain density of 1g/cc (Figures D4, D5, D6 and D7). Results on this and the next pages show around 5E (i.e. 2%) and 12E (i.e. 8%) differences for G_{xy} and G_{zz} components, respectively.

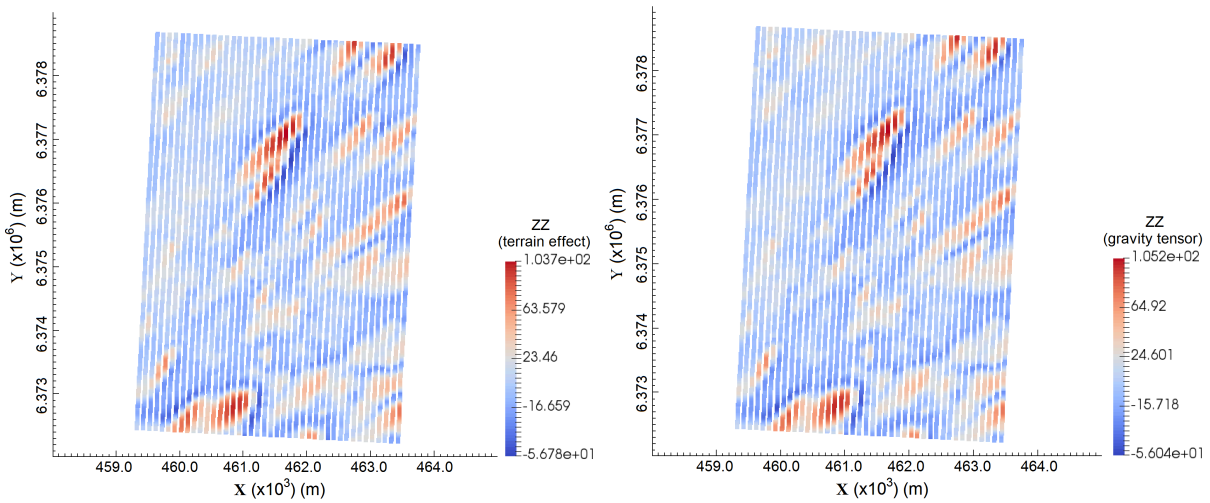

Figure D6: Terrain effect calculated for G_{zz} (left; CGG data) and gravity tensor synthetized for G_{zz} (right) for a density of 1g/cc (i.e. for the model in Figure D3). Unit: Eötvös.

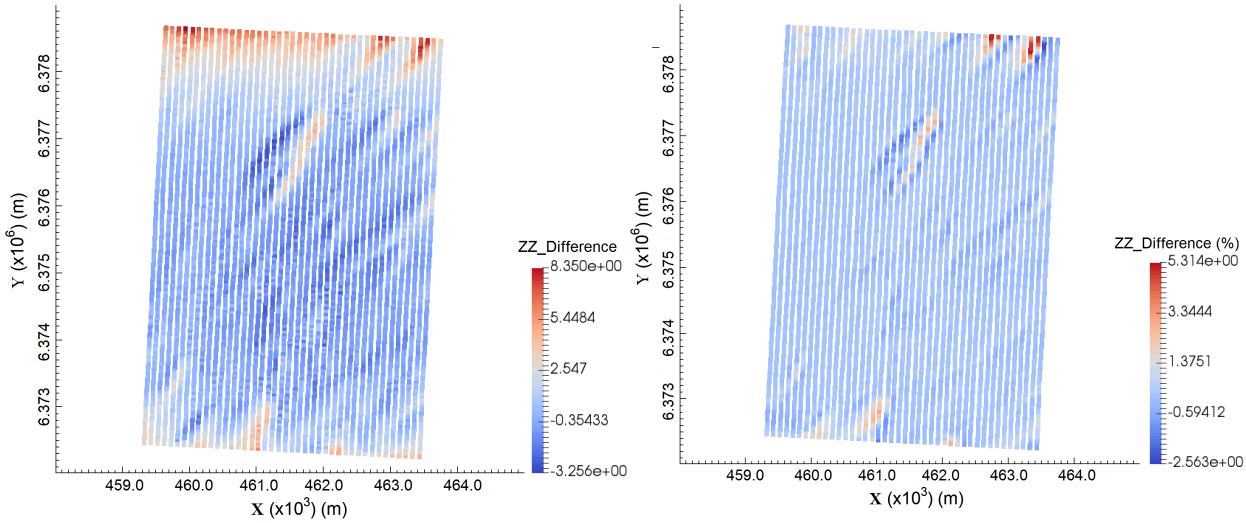

Figure D7: Difference (left) and percentage difference (right) between calculated terrain effect and synthetized gravity tensor for G_{zz}. Unit: Eötvös.

A density of 1 g/cc was used to compute the terrain effects and to synthetized the gravity tensors, which can then be simply multiplied by a chosen appropriate density and subtracted from the data. In this research a terrain density of 2 g/cc is chosen. Thus, synthetized G_{xy} and G_{zz} data are multiplied by 2. The results are used as the terrain correction that is applied to the synthetized data-set in the remainder of this section. They will be subtracted from CGG's Fourier derived G_{xy} and G_{zz} data, that is shown on Figures D8 and D10.

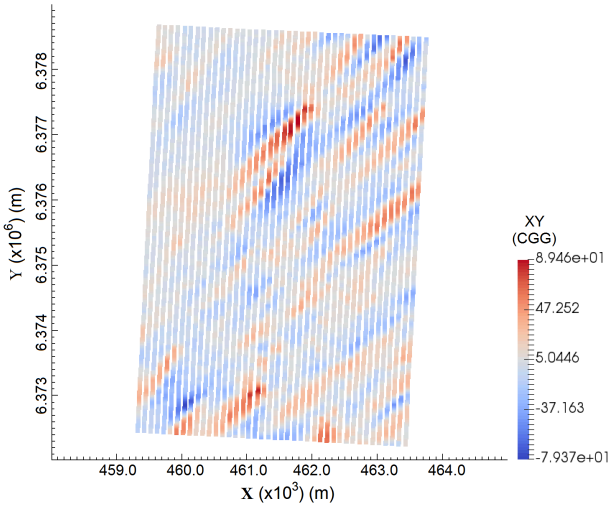

Figure D8: CGG's G_{xy} gradiometry data (no terrain correction applied). Unit: Eötvös.

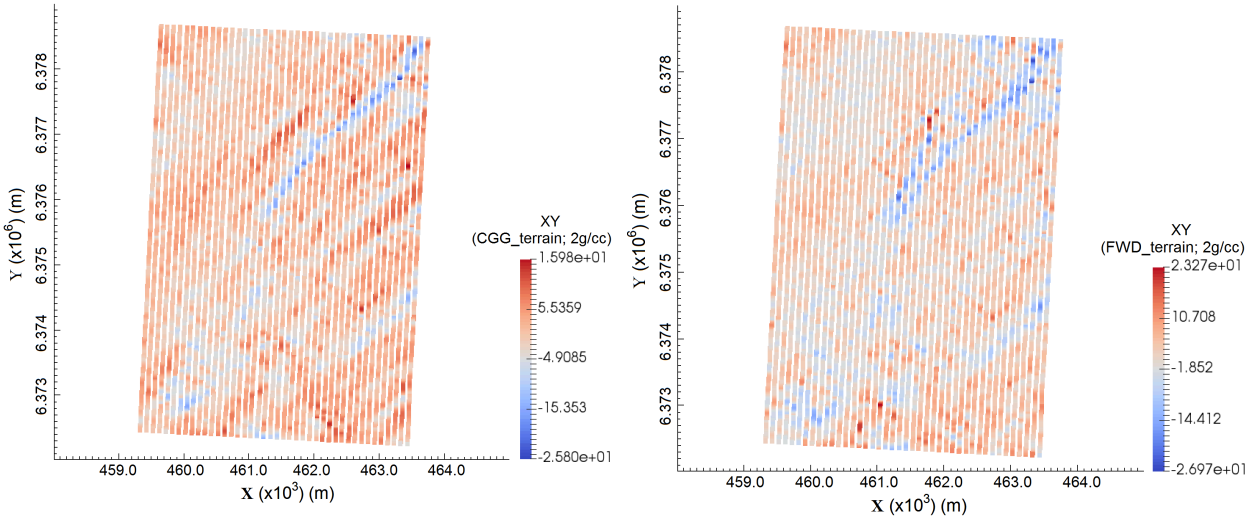

Figure D9: Left: G_{xy} gradiometry data after applying terrain correction using a Fourier-based technique by CGG. Right: G_{xy} gradiometry data after applying terrain correction using synthetized (forward modelling) terrain data in this research. Unit: Eötvös.

The final results will be compared with the (CGG's Fourier derived) terrain-corrected G_{xy} and G_{zz} data in which the terrain correction were computed by a common correction technique (Figures D9 and D11). It can be seen that the gradiometry data before the terrain correction are highly dominated by the topography signature. By comparing the terrain corrected results, it can be seen that the topography signature in the data which is corrected by our method is highly reduced in comparison with the CGG's data which is corrected by

a common terrain correction technique.

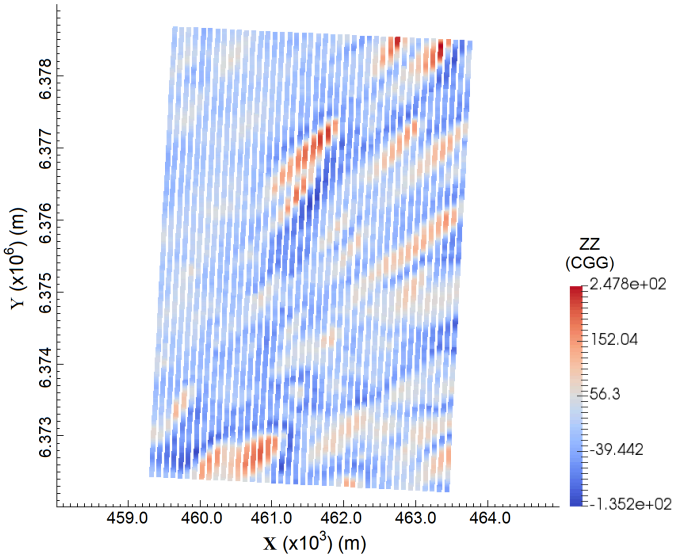

Figure D10: CGG's G_{zz} gradiometry data (no terrain correction applied). Unit: Eötvös.

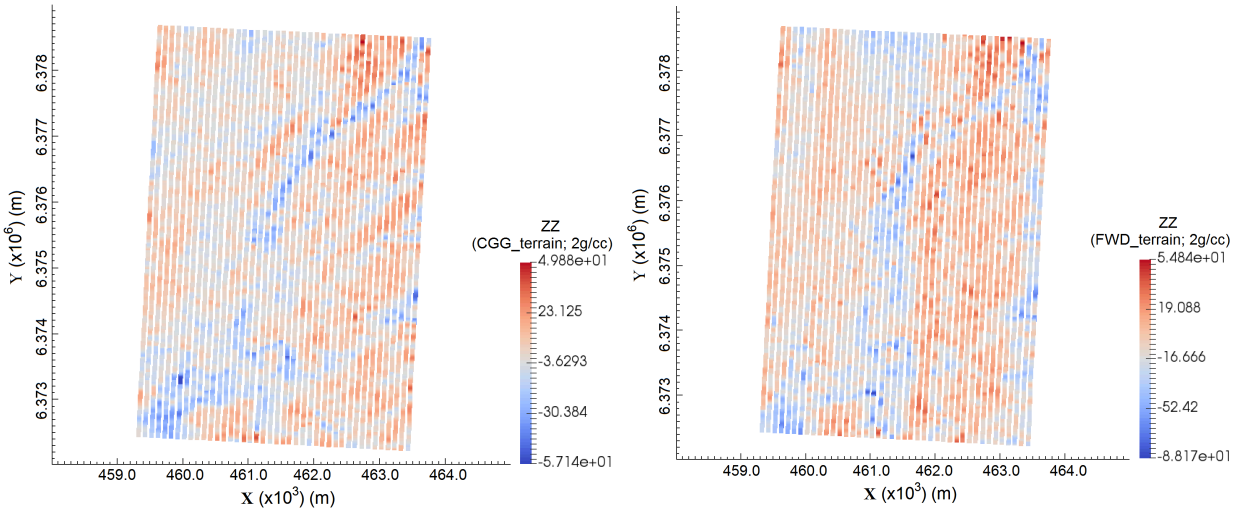

Figure D11: Left: G_{zz} gradiometry data after applying terrain correction using a Fourier-based technique by CGG. Right: G_{zz} gradiometry data after applying terrain correction using synthetized (forward modelling) terrain data in this research. Unit: Eötvös.

Appendix E: 1D inversion of real DIGHEM data for the Malartic area

Geological setting

The Canadian Malartic Gold Mine is an open pit mine which is located in Malartic near Val d'Or, Quebec. It is considered as a large-tonnage, low-grade Archean gold deposit in which the mineralization occurs in clastic metasedimentary rocks of the Pontiac Group and in porphyry monzodiorite intrusions. The main ore minerals are native gold accompanied by pyrite as a result of hydrothermal alteration (Wares & Burzynski, 2011). Sedimentary rocks of the Pontiac Group are cut by intrusive rocks including porphyritic quartz monzodiorite and granodiorite, intermediate and felsic dykes, and widespread lamprophyre dykes which are known to show some evidence of hydrothermal alteration (Figure E1). Also, sedimentary rocks are covered by subglacial till, coarse glaciofluvial sediments, and glaciolacustrine fine sediments (Veillette, 2004; Figure E2).

The DIGHEM system

A DIGHEM airborne geophysical survey was carried out (and processed) by Fugro Airborne Surveys Corp. for Osisko Exploration Ltd. over the Canadian Malartic Gold Mine in August 2006. Survey coverage consisted of north-south lines of approximately 2485 line-km with a line spacing up to 100 metres and a station spacing of around 3 m. This was accomplished using a DIGHEM electromagnetic system, supplemented by a high

sensitivity cesium magnetometer, a spectrometer and a GPS which were installed in an AS350B(2) turbine helicopter. The helicopter flew at an average of 136 km/h with an EM sensor height of approximately 30 metres (Fugro Airborne Surveys Corp., 2006). The DIGHEM system uses five frequencies from 877Hz to 56110Hz with two coil configurations: coaxial (horizontal dipole; 1128Hz and 5087Hz) coil pairs and coplanar (vertical dipole; 877Hz, 7166Hz and 56110Hz) coil pairs. Coil separation (between receiver and transmitter) is 8 m except for 55840Hz which is 6.3 m. Receiver and transmitter coils have a diameter of about half a metre. The system measures both in-phase and quadrature parts. I had access to the DIGHEM data-set as "Au site" is another research project of the large Canadian Mining Innovation Council (CMIC; www.cmic-footprints.ca) Footprints project.

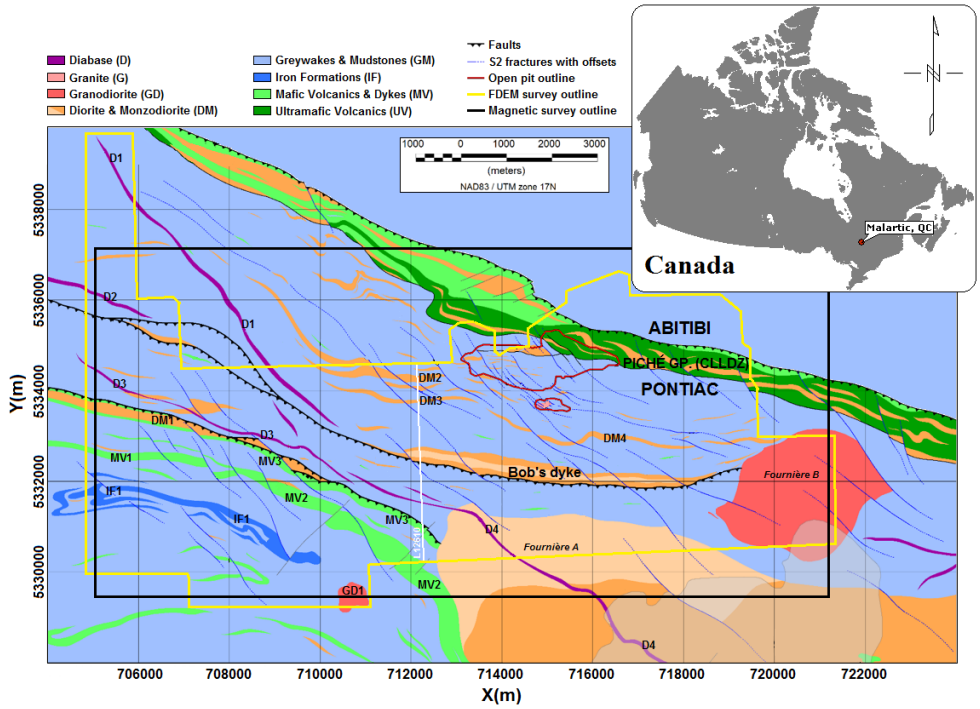

Figure E1: Geology map of the Malartic area. The red outlines show the pit and mining operation areas. The DIGHEM survey area is overlaid in yellow. White line shows the survey line L12610 which is inverted (adapted from Perrouty et al., 2017).

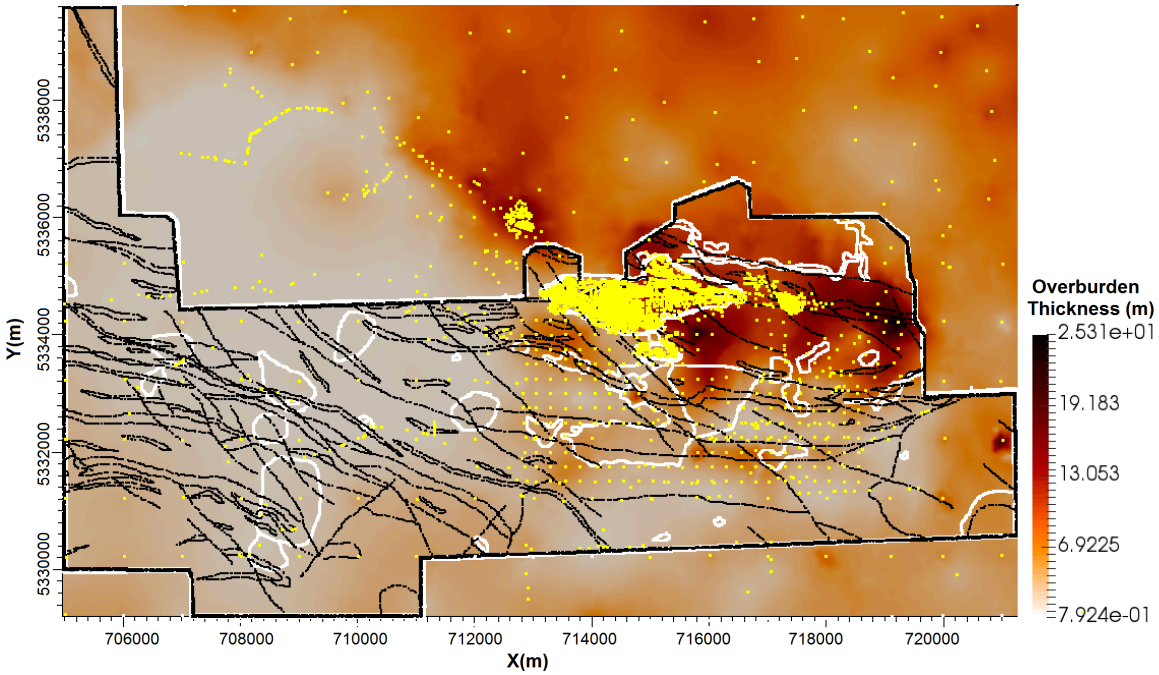

Figure E2: Map of the overburden thicknesses estimated from drill-hole data. Yellow dots show the location of drill-holes. The black outlines the DIGHEM survey area (mapped by Reza Mir; taken from CMIC-Footprints project).

1D inversion

Data were slightly filtered by Reza Mir (taken from CMIC-Footprints project). The 1D inversion using EM1DFM (which uses an L2-norm; Farquharson and Oldenburg, 2000) was applied to the filtered real DIGHEM data along a part of a profile (L12610) with 1050 stations over the Malartic area (Figure E3). Vertical dipole data (877Hz, 7166Hz and 56110Hz) were used for the inversion. Also, a 5% noise was used as an estimation of the data uncertainty. Magnetic data along the (inverted) survey line are shown in Figure E4. Figures E5 and E6 respectively show the 1D inversion model and the convergence curves for one of the stations.

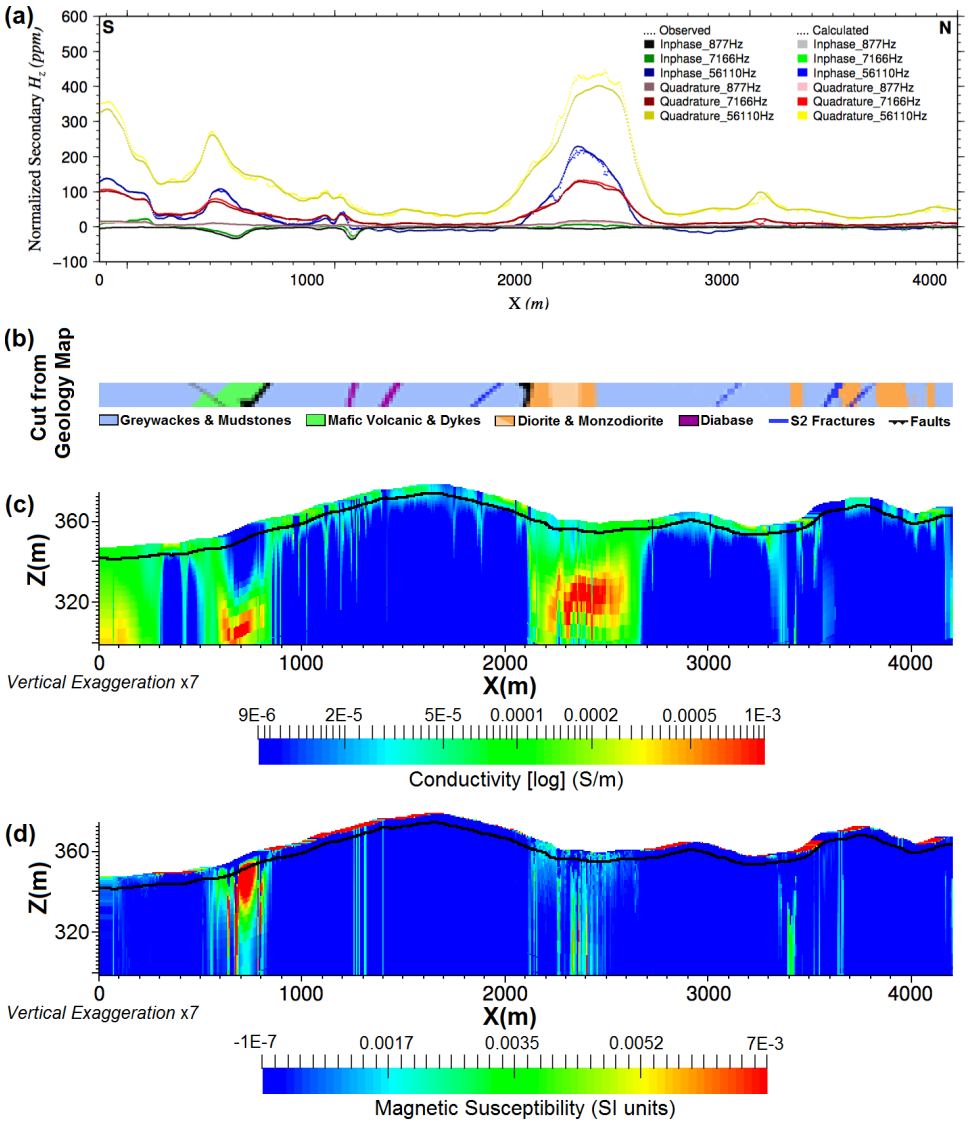

Figure E3: Observed and calculated data (a) as well as the conductivity (c) and magnetic susceptibility (d) models along the profile L12610 obtained from the 1D inversion of FDEM data over the Canadian Malartic area. Black lines show the base of overburden estimated from the drill-hole data. A cut of the geology map (b) under the profile is shown to ease the interpretation.

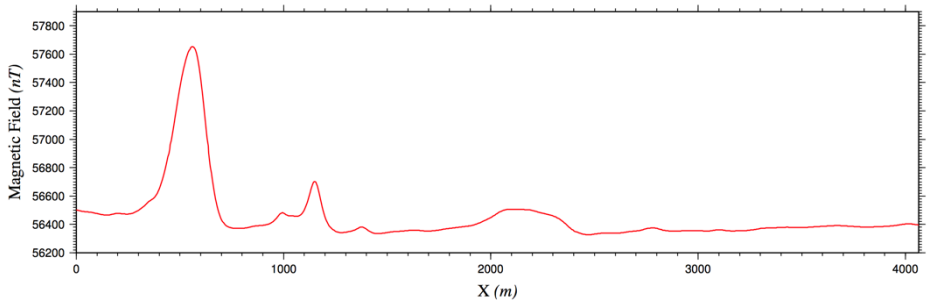

Figure E4: Magnetic data along the (inverted) survey line.

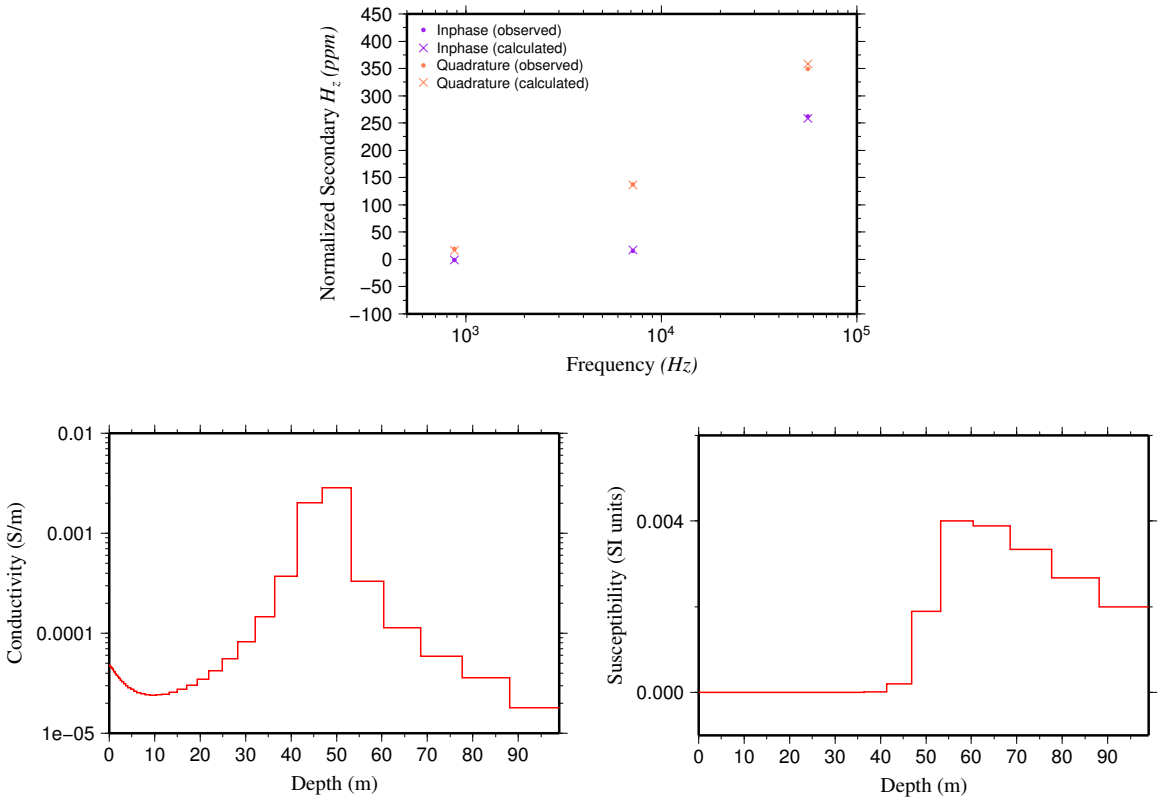

Figure E5: Top: observed and calculated data for a station of real DIGHEM data. Bottom: conductivity and susceptibility models obtained from the 1D inversion of DIGHEM data.

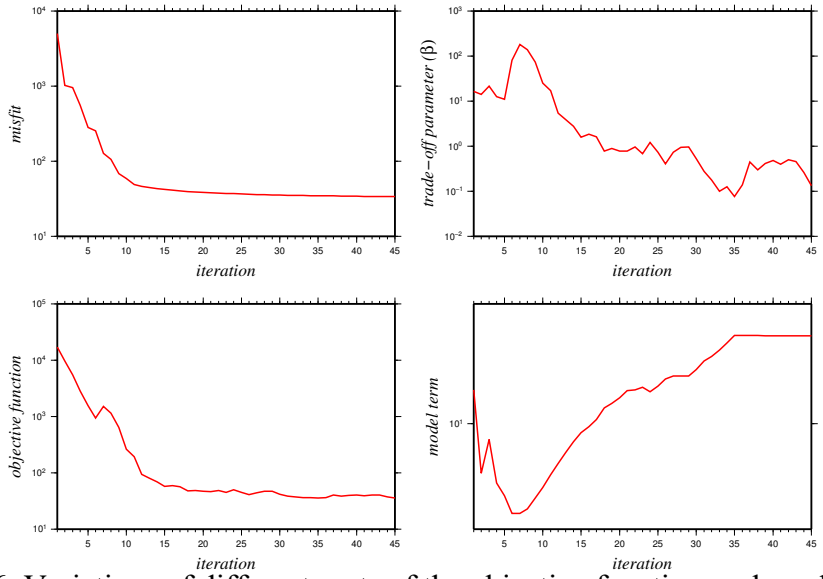

Figure E6: Variations of different parts of the objective function such as data misfit (ϕ_d; top-left), trade-off parameter (β; top-right), objective function (Φ; bottom-left) and model term (ϕ_m; bottom-right) at inversion iterations for the model in Figure E5.

The 1D inversion results show a good match with the geology map (see Figures E1 and E3) and the magnetic data (Figure E4). A good fit between the observed and calculated data is achieved. The profile goes over the mafic volcanic (MV3) and diabase (D4) dykes as well as diorite and monzodiorite rocks (DM2 and DM3). The conductivity and susceptibility models show some conductive and magnetic structures along the profile especially in the south and the center. The overburden is reconstructed better in the conductivity model than the magnetic susceptibility model as the conductivity of the overburden is more uniform than the magnetic property. The susceptible structures along the profile are the mafic volcanic (MV3) and diabase (D4) dykes as well as the diorite-monzodiorite rocks (DM2, DM3 and Bob's dyke). Mafic volcanic dykes (MV3) show the most magnetic responses. Two conductive and susceptible structures are shown in the south of the profile. The one from 0 to 300 m does not match with the geology map, but can be interpreted as a deep mafic volcanic rock belonging to the MV2 which is covered by the meta-sedimentary rocks. It shows that the MV2 in that part is extended toward the east at depth. From 500 to 900 m, the mafic volcanic rock of MV3 show strong magnetic response as well. From 1200 to 1400 m, some small structures are made which are related to diabase dykes (D4) in the area. The main conductive and magnetic structure in the center of the profile is the diorite and monzodiorite rock of Bob's dyke. A group of monzodiorite rocks (DM2 and DM3) shown in the northern part of the geology map can be seen as shallow structures in the inversion results. However, there are a few deep structures in the southern part (from 3300 to 3700 m) of this group some of which are not shown in the geology map. The meta-sedimentary rocks are reconstructed as resistive and non-magnetic structures in the inversion models (the blue background zone).

Appendix F: Spectral analysis and filtering for separation of overburden and deep signals

Methodology

Different sources at different depths (and of different scales) can give signals of different wavelengths/wavenumbers. Hence this might be a possible way to separate out overburden effect and deeper structures. For example, gravity and magnetic measurements are a combination of several sources at different depths; however, the separation of the contributions of each source is not always easily possible (Telford et al., 1976; Blakely, 1995). But, there is a relationship between the wavenumber/wavelength and the depth of the source and this relationship can help when estimating the depth as well as the vertical separation of sources (Blakely, 1995; Naidu and Mathew, 1998). Therefore, differences in wavenumber/wavelength content could potentially be used to identify deep alteration.

For this purpose, the data must be transformed from the space (or time) domain to the frequency domain using the mathematical method of the Fourier transform (Papoulis, 1962; Bracewell, 1965). Spectral analysis and frequency filtering are used in this research. Spectral analysis can separate sources (under certain assumptions and simplification) and represent each source contribution as well as the the depth to the source in the frequency domain if all sources have the same size and geometry (Naidu, 1968; Spector and Grant, 1970; Rayner, 1971; Treitel et al., 1971). Frequency filters (e.g. low-pass, high-pass and band-pass) are employed as each source has different frequency characteristics and can

therefore be separated on this basis (Cowan and Cowan, 1993; Hsu et al., 1996; Naidu and Mathew, 1998; Smith et al., 1998). Low-pass filters pass signals with a frequency lower than a certain cut-off frequency, and attenuate signals with frequencies higher than the cut-off frequency. In the high-pass filter, high frequencies are passed, and low frequencies are attenuated. Also in the band-pass filter, only frequencies in a specified frequency range are passed.

For the spectral analysis, 2D power spectrum (2DPS) and radially averaged power spectrum (RAPS) are investigated here. Spectral analyses are undertaken using Oasis Montaj software (Geosoft, 2006) over different grid cell sizes. The idea is to investigate the various contributions of gravity data in the wavenumber domain based on the power spectra. "Aliasing" and "*sinc* function" are two undesired effects which can be seen in the wavenumber domain especially in the 2D power spectrum.

Also, frequency filtering (such as low-pass, high-pass, band-pass and derivatives) are applied to the real data. For the filtering, two consecutive filters were applied using Oasis Montaj software (Geosoft, 2006): Directional cosine filter and Gaussian regional/residual filter. The directional cosine filter is useful for removing directional features from a grid. The cosine function makes the filter smooth, so directional ringing effects are usually avoided. The Gaussian filter is another smooth filter that is often used for low-pass or high-pass applications (Geosoft, 2006).

A 2D power spectrum represents the spectral content of data along with the azimuth of sources at all wavenumbers. It does not give quantitative information on the number of

sources with a particular frequency (Spector and Grant, 1970; Clement, 1972). Figure F1 shows the basic principle of the 2D power spectrum between space domain and wavenumber domain. Patterns in the space domain show a rotation by 90˚ (i.e. a phase shift of π/2 radians) in the wavenumber domain. The spectrum (power) of gravity data has a unit of $mGal^2$.

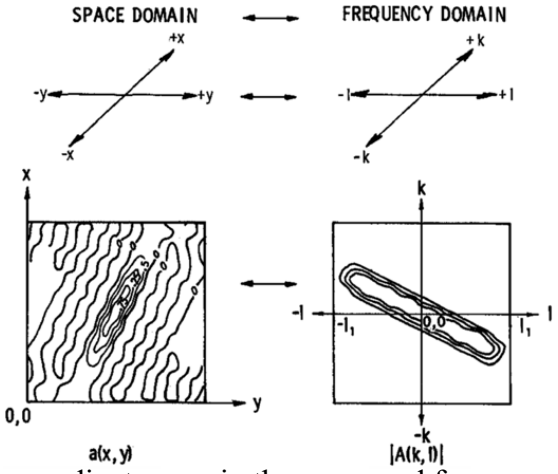

Figure F1: Top: coordinate axes in the space and frequency/wavenumber domains. Bottom: the two dimensional continuous function and its continuous spectrum (Clement, 1972). In this figure, instead of *u* and *v*, the symbols *k* and *l* refer to the frequency components in the *x* and *y* direction, respectively.

A 2D power spectrum can be converted to a one dimensional plot as a radially averaged power spectrum (RAPS) in order to allow the presentation on an x-y plot. It means that each point in the RAPS is an average of all points lying on a circle with a fixed radial frequency (or wavenumber). RAPS can give a more quantitative insight, and it gives averages over the spectral window (Bhattacharya, 1966; Spector and Grant, 1970; Maus and Dimri, 1996). The RAPS decreases with increasing depth to source (*d*) by a factor *exp(-2dk)*, where $k=\sqrt{u^2+v^2}$ is the wavenumber. Therefore, if the shape of the power spectrum is dominated by the depth factor, the logarithm of the power spectrum would be proportional to *-2dk*, and *d* can be obtained from the slope of the log radially averaged

power spectrum. The RAPS should be preferably applied on relatively homogenous structures so that the slope breaks are evident in the spectrum (Spector and Grant, 1970). The spectrum can be fit with a series of straight line segments where each line's slope (m) is related to the depth of density anomalies ($d = -m / 4\pi$; Spector and Grant, 1970). A RAPS of a large area may show multiple linear sections on the graph with distinct slopes that could be interpreted to show up to five depth values. Potential field power spectra possess limited depth information (Connard et al. 1983; Maus and Dimri, 1996). The radially averaged power spectrum is plotted as the natural log of power versus wavenumber. Line segments corresponding to the lower frequencies (wavenumbers) have information from deeper anomalies. In this study, I have plotted the line segments for each RAPS. Where the slope changes, that point (wavenumber) is considered as a cut-off point. These cut-off points can be used for designing filters (low-pass and high-pass). Wavenumber (k) is equal to 2π/wavelength (l). Therefore, using cut-offs obtained from RAPS I can find the wavelength belonging to the various contributions.

Spectral analysis and filtering of real gravity data

Many synthetic models are tested, but they are not shown here. In this section, I will investigate the spectral analysis and filtering on a part of the real airborne Bell gravity data (Figure F2; Bell Geospace Limited, 2007; see Section 7.1). I assume that the interface between the overburden and the sandstone constructed using drill-hole data is the best estimation. So, I will calculate the gravity data related to the overburden part at the actual gravity stations. And, then I subtract it from the real free-air data in order to generate the real estimated FwOB (free-air data without overburden signature) data (Figure F2).

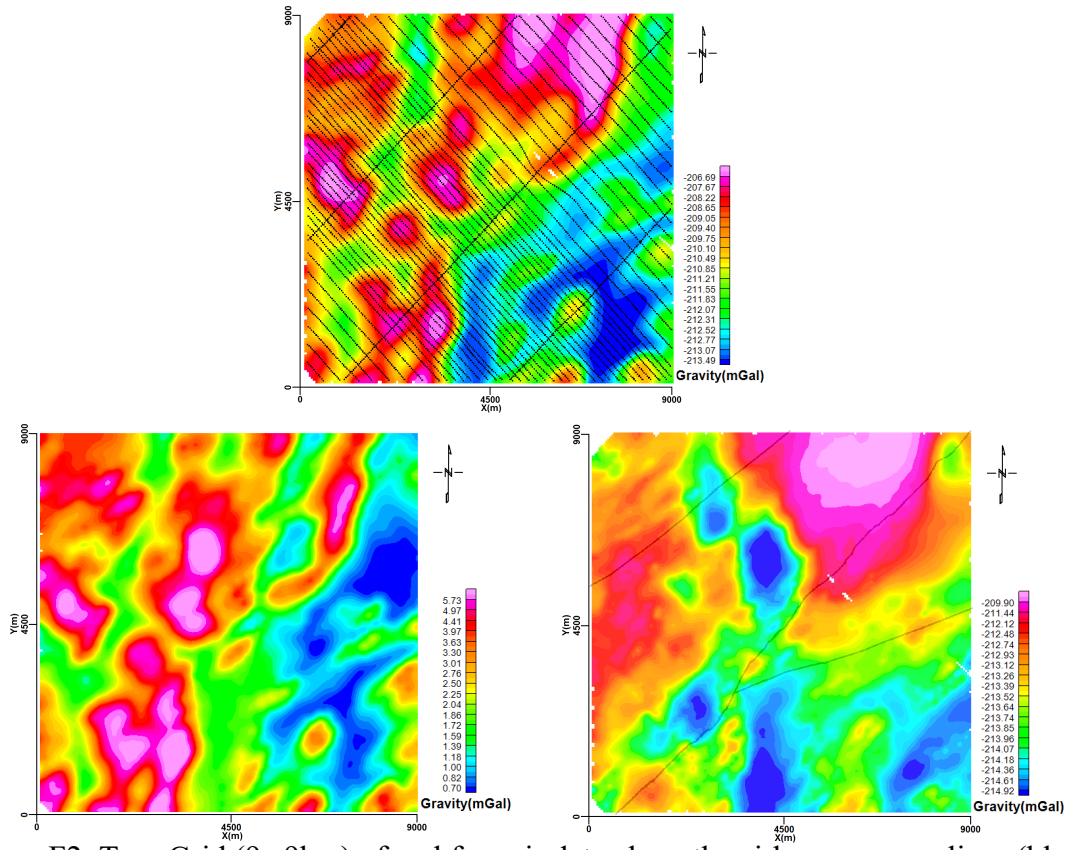

Figure F2: Top: Grid (9×9km) of real free-air data along the airborne survey lines (black dots). Number of stations: 7719. Bottom-left: Grid of overburden signature gravity data. Bottom-right: Grid of real gravity free-air data after removing overburden signature (FwOB). Faults are shown by the black lines. Main fault (P2 fault; adapted from CMIC-Footprints project) is shown by a diagonal line started from the bottom left to the top right (gridded by Oasis Montaj).

Figures F3 to F5 show the 2D power spectrum as well as the RAPS of the real free-air data and real estimated FwOB data. “Low-pass” filter and spectral analysis on the free-air data (Figures F3 to F6) as well as both “high-pass” and “derivative in Z-direction” filters on the real FwOB data (Figures F7 and F8) were applied. Some of the faults in the basement have been indicated on these images (using Global Mapper software) to indicate possible locations and trends of alteration zones.

For a grid cell size of 5 m, the linear pink parallel zones (high power; northeast to southwest trending) in the centre of the whole 2D power spectrum correspond to the direction of the survey lines (Figures F3 and F4). This indicates that there is a lot of power and hence a lot of structure in the data-set in that direction. For a grid cell size of 20 m, the linear pink zone (high power; northwest to southeast trending) in the centre of the 2D power spectrum of the free-air gravity data possibly corresponds to the direction of overburden streamlined deposits, and the linear pink zones in FwOB is due to variations (e.g. alteration zones) aligned with the faults. But, most likely the northwest-southeast trending features in the power spectra is still due to the survey lines because the larger cell size averages out (aliases) the variation along the flight lines that is happening at the measurement spacing, which is closer than 20 m.

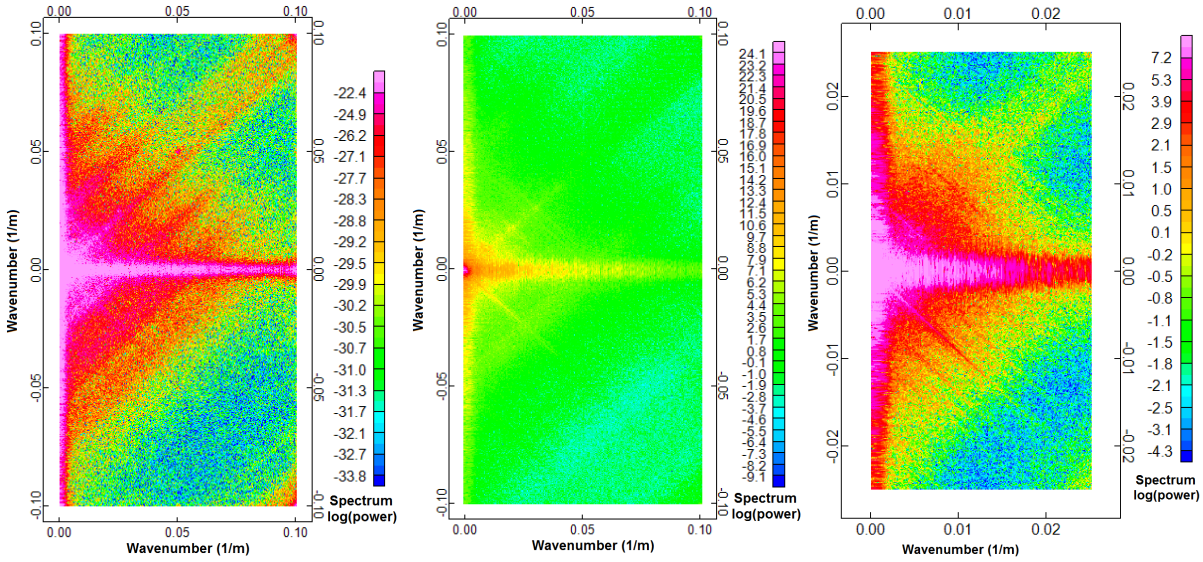

Figure F3: 2D power spectra for free-air data for grid cell sizes of 5 m (left), for grid cell size of 5 m with a larger range of "Spectrum log (power)" (middle), and for a grid cell size of 20 m (right; gridded by Oasis Montaj).

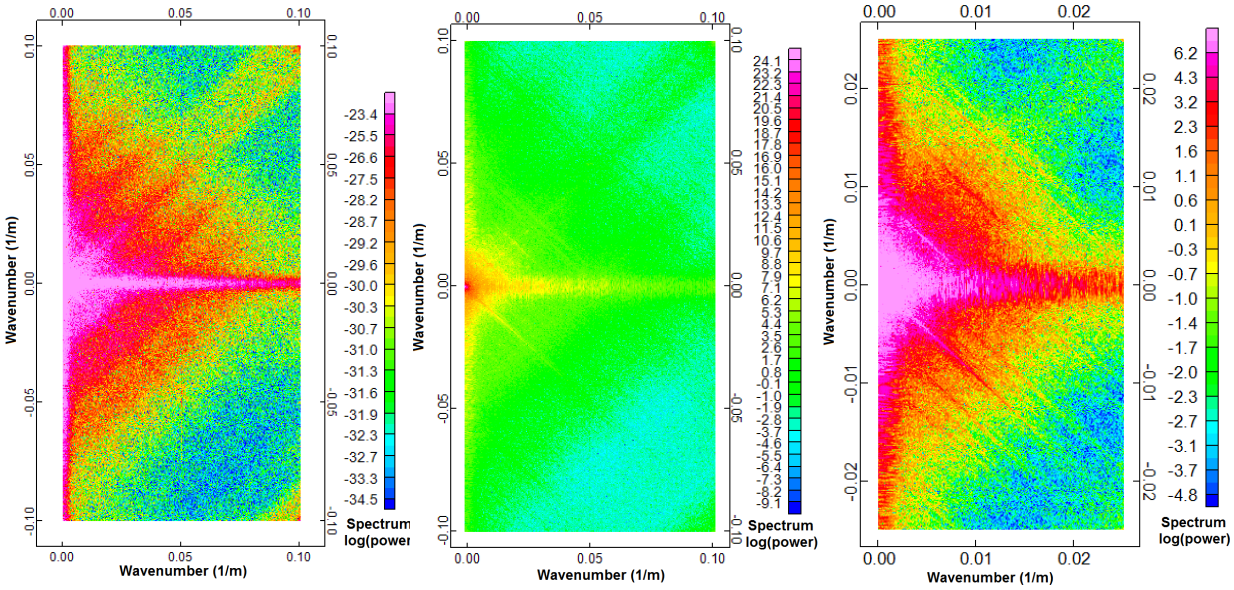

Figure F4: 2D power spectra for FwOB data for grid cell sizes of 5 m (left), for grid cell size of 5 m with a larger range of "Spectrum log (power)" (middle), and for a grid cell size of 20 m (right; gridded by Oasis Montaj).

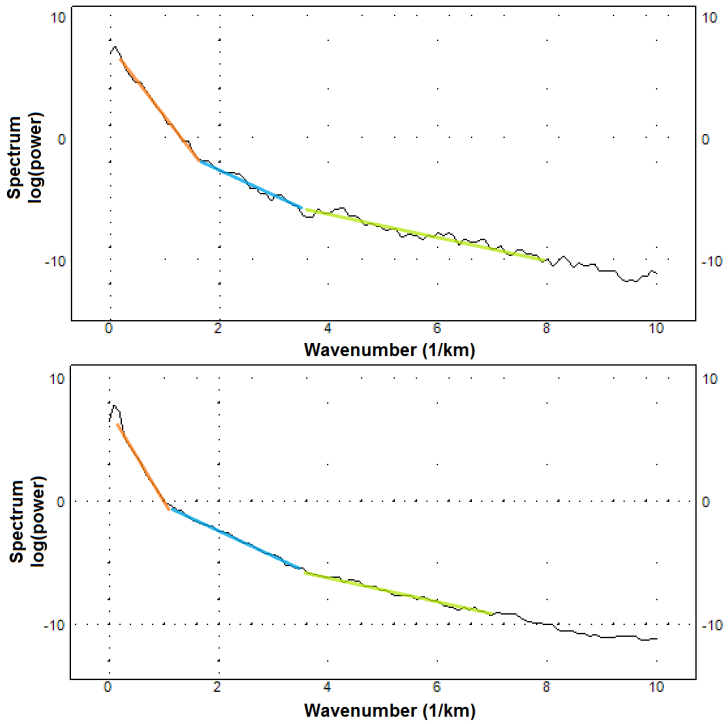

Figure F5: Top: RAPS from free-air data for grid cell sizes of 50 m. Colored lines are drawn and fitted in order to find the cut-offs (here 1.5, 3.2 and 8 km^{-1}). Bottom: RAPS from FwOB data for grid cell sizes of 50 m. Colored line are drawn and fitted in order to find the cut-offs (here 1.3, 3.3 and 7 km^{-1}; gridded by Oasis Montaj).

The following shows information inferred from the RAPS results for the free-air and FwOB data. Wavenumber (k) is equal to 2π/wavelength (l). Therefore, using cut-offs obtained from RAPS, I can find the wavelength belonging to the various contributions.

Free-air:

k=1.5 => l=4.2km (probably belonging to the basement)
k=3.2 => l=2km (probably belonging to the alteration)
k=8 => l=0.8km (wavelengths less than 2km are belonging to the overburden)

FwOB:

k=1.3 => l=4.8km (probably belonging to the basement)
k=3.3 => l=1.9km (probably belonging to the alteration)
k=7 => l=0.9km (probably belonging to the interface between overburden and sandstone)

The estimated depths (d: distance below observation stations) are obtained from the lines' slopes (m) using equation $d=-m/4\pi$ as follows:

Free-air:

orange line => d=-(3/-0.4)/4π=0.6km (probably belonging to the basement)
blue line => d=-(3/-1)/4π=0.24km (probably belonging to the alteration)
green line => d=-(2/-2)/4π=0.08km (probably belonging to the overburden)

FwOB:

orange line => d=-(5/-0.6)/4π=0.66km (probably belonging to the basement)
blue line => d=-(5/-1.9)/4π=0.2km (probably belonging to the alteration)
green line => d=-(1.5/-1)/4π=0.12km (probably belonging to the interface between overburden and sandstone)

In Figure F6, the low-pass filter results for the "real free-air data" for a value of 10000 m shows good correlation with the faults in the area. Figure F7 shows derivatives in the Z-direction for a number of differentiation orders. For these data, the tie-lines were removed from the dataset prior to gridding. The high-pass filter on the real FwOB data for cut-off

values more than 3000 m show variations which have good correlation with the faults (Figure F8).

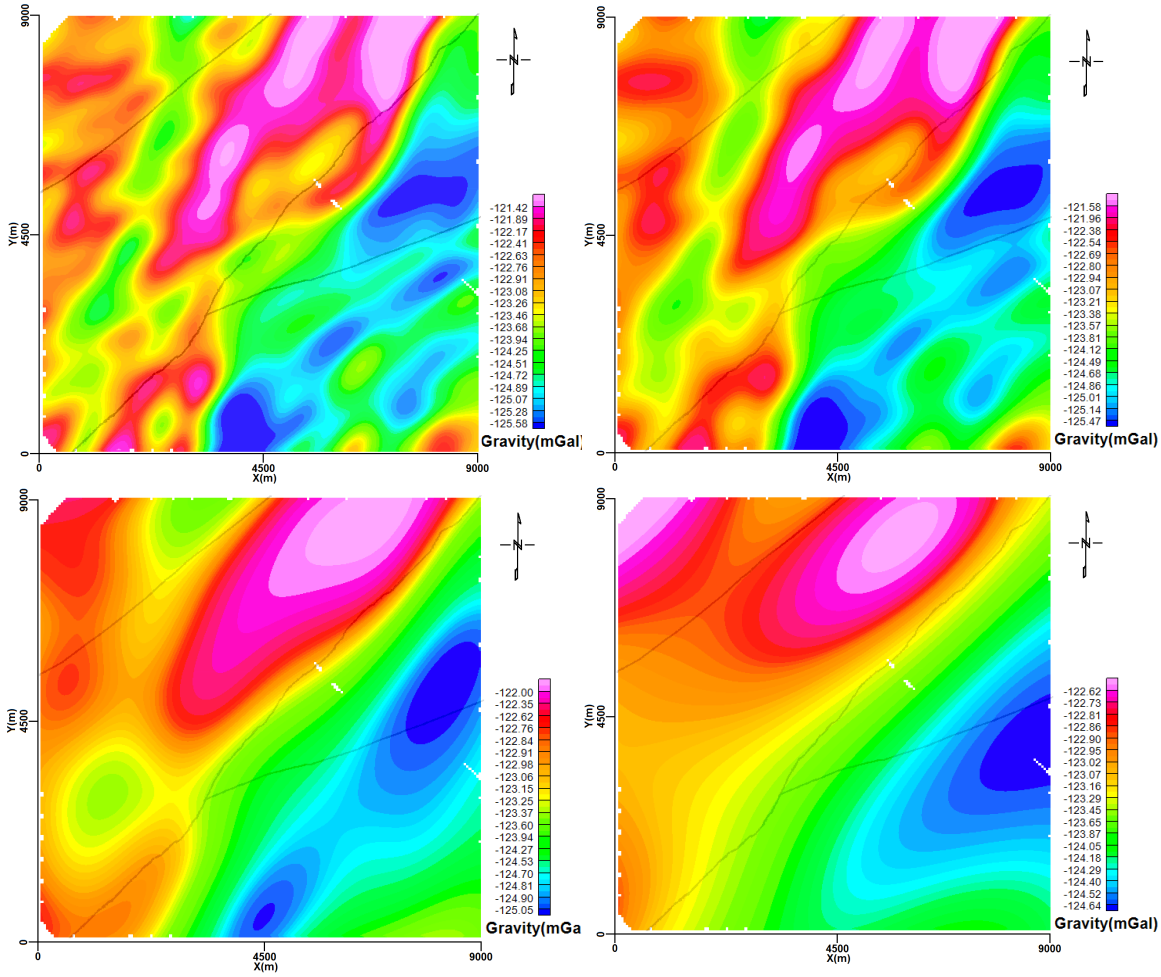

Figure F6: Grid of real gravity free-air data after applying low-pass filters 1000 m (top-left), 2000 m (top-right), 5000 m (bottom-left) and 10000 m (bottom-right). Faults are shown by the black lines (gridded by Oasis Montaj).

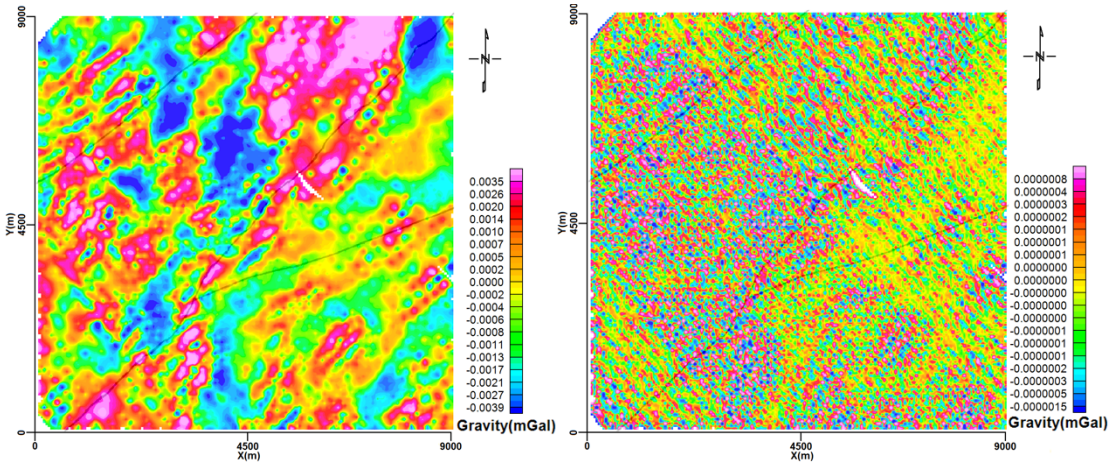

Figure F7: Grid of real FwOB data after applying derivative filter in Z-direction for differentiation orders of 1 (left) and 3 (right). Faults are shown by the black lines (gridded by Oasis Montaj).

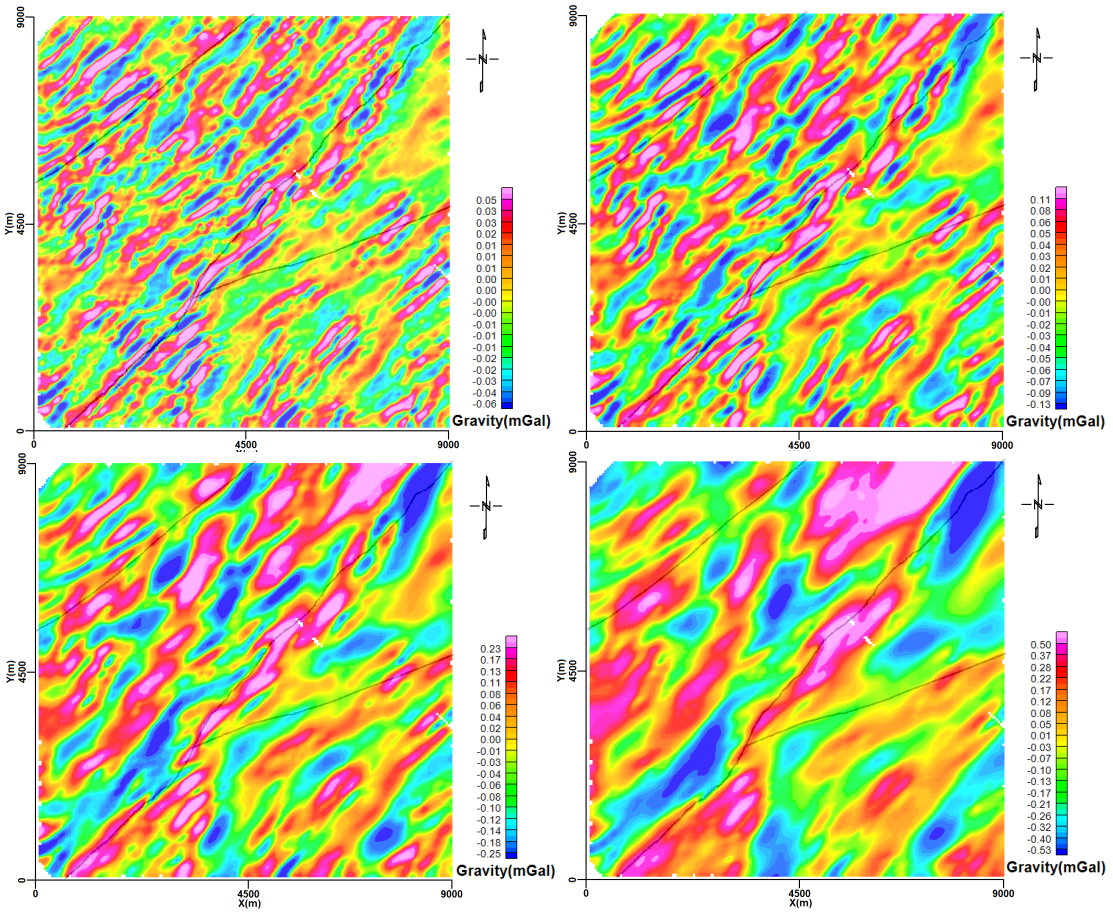

Figure F8: Grid of real FwOB data after applying high-pass filters of 500 m (top-left), 1000 m (top-right), 2000 m (bottom-left) and 5000 m (bottom-right). Faults are shown by the black lines (gridded by Oasis Montaj).